A Window into Terrestrial Paleoclimate:

Soil Carbonate Formation Processes and Climate Proxy Applications

Landon K. Burgener

A dissertation

submitted in partial fulfillment of the

requirements for the degree of

Doctor of Philosophy

University of Washington

2018

Reading Committee:

Katharine W. Huntington, Chair

Gerard H. Roe

Gregory D. Hoke

Program Authorized to Offer Degree:

Earth and Space Sciences

University of Washington

Abstract

A Window into Terrestrial Paleoclimate:

Soil Carbonate Formation Processes and Climate Proxy Applications

Landon K. Burgener

Chair of the Supervisory Committee:

Katharine W. Huntington

Department of Earth and Space Sciences

The isotopic composition of pedogenic (formed in soil) carbonates provides a geologically abundant archive of terrestrial climate change and the interactions between Earth's climate, geologic, and biologic systems. However, early paleoclimate reconstructions based on the carbon and oxygen isotope composition of soil carbonates were largely limited to qualitative estimates of change in key climate and environmental parameters such as surface temperature, precipitation, and soil biologic activity. The development of carbonate clumped isotope geothermometry has made it possible to make quantitative estimates of carbonate formation temperatures, and to relate those temperatures to changes in the Earth's climate. The application of carbonate clumped isotope geothermometry to studies of soil carbonate systematics has shown that the

seasonality of soil carbonate formation is closely linked to the timing of the local wet season, which has important implications for how the clumped isotope formation temperatures of soil carbonates relate to more meaningful climatologic parameters such as mean annual temperature. However, important questions remain regarding the impact of other climate and soil factors such as precipitation type (e.g., rain versus snow) and soil sediment grain size on the seasonality and mechanisms of soil carbonate formation.

This dissertation places new constraints on the effects these soil and climate factors have on the seasonality of soil carbonate formation, sheds new light on non-equilibrium formation processes affecting soil carbonates in freezing environments, and provides new, quantitative terrestrial paleoclimate reconstructions of seasonal variability in surface temperature during the Late Cretaceous greenhouse period. Chapter 2 presents soil carbonate clumped and stable isotope data from an approximately 4000 m elevation transect on the western flank of the Chilean Andes. The results from this first chapter provide evidence that the presence or absence of a winter snowpack plays a critical role in modulating soil wetting and drying cycles, which in turn dictate the seasonality of soil carbonate formation. Additionally, this work provides the first evidence of soil carbonate formation under conditions of isotopic disequilibrium in freezing environments. Chapter 3 builds on the results of Chapter 2 by presenting the analyses of a suite of cold-climate soil carbonates from soils with both fine grained (the High Arctic and the Tibetan Plateau) and coarse grained (the Chilean and Argentinian Andes and the Dry Valleys, Antarctica) inter-cobble matrices. The findings of this chapter show that in freezing soils, matrix grain size is an important control on promoting or inhibiting kinetic isotope effects during soil carbonate formation. Soils with coarse-grained matrices experience rapid CO_2

degassing associated with bicarbonate dehydration during soil freezing, which results in disequilibrium soil carbonate formation. In contrast, fine-grained matrices inhibit soil CO_2 degassing and promote equilibrium carbonate formation, even in freezing environments. Chapter 4 represents and application of cutting-edge soil carbonate paleoclimate reconstruction techniques to the long-standing issue of terrestrial seasonal temperature variability during greenhouse climates. The clumped isotope composition of paleosol carbonates from Late Cretaceous sedimentary outcrops in south-central Utah and northwest Montana, USA are used to reconstruct summer soil temperatures along the mid-latitude, western margin of the Western Interior Seaway. These summer temperatures are then paired with previous reconstructions of local mean annual temperature to reconstruct mean annual range in temperature for these two sites. The results of this work show better agreement with model simulations of Late Cretaceous seasonal temperature changes than previous estimates, and add to a growing body of work that suggests that seasonal temperature variations in greenhouse environments did not differ significantly from the modern. These findings have important implications not only for our understanding of greenhouse climate, but also for the impact of climate on the paleogeographic distribution of ancient faunal communities.

Table of Contents

List of Figures

List of Tables

Acknowledgments

I would like to recognize and express my appreciation to the numerous people who have supported me throughout my time at the University of Washington, and in my previous years of study as well.

My advisor, Katharine Huntington, has been an amazing source of support and guidance over the past six years. I am especially grateful that she gave me the space (and had the patience) to allow me to independently develop my own research questions and directions. Her example as a researcher has been a source of inspiration to me in my own work, and her advice and insight—with regard to both my research and career—has been immeasurably helpful.

My committee—Gregory Hoke, Ron Sletten, Gerard Roe, and Eric Steig—provided rigorous assessment of my research and provided interdisciplinary insight into the research questions I pursued. Special thanks go to Gregory Hoke for his experienced and enthusiastic leadership over two field seasons in the Chilean Andes, and to Ronald Sletten for his guidance as I explored soil carbonate formation processes in the Dry Valleys, Antarctica and the High Arctic.

My peers and friends in Johnson 423 made life as a graduate student bearable, providing the humor and commiseration I needed every day. Thanks guys!

And finally, thanks to my family. My wife Kylie has shown superhuman patience and unending support for the past eleven years as I have pursued my bachelor, masters, and doctoral degrees. Thank you Ky. I love you. And to my kids—Walter, Zuzu, and Linus, for making this entire effort worthwhile.

Dedication

To my family: Kylie, Walter, Isannah, and Linus

Chapter 1. Introduction

1.1. Motivation: Reconstructing Terrestrial Paleoclimate from the Clumped Isotope Composition of Pedogenic Carbonates

Pedogenic (formed in soil) carbonates have long been a focus of scientific study, due both to the insight they can provide regarding pedogenic processes in arid to semi-arid environments (Breecker et al., 2009; Birkeland, 1985; Gile et al., 1966), and their use as an archive of terrestrial paleoclimate conditions (Cerling and Quade, 1993). Indeed, because they are commonly preserved in continental sedimentary deposits (Cerling and Quade, 1993), soil carbonates have become one of the primary sources of information regarding the evolution of terrestrial climate during the Precambrian (e.g., Retallack, 2018, 1994; Retallack et al., 2016; Sheldon, 2006; Sreenivas et al., 2001; Ohmoto, 1996; Golani, 1989; Grandstaff et al., 1986; Gay and Grandstaff, 1980; Kalliokoski, 1975), Paleozoic (e.g., Michel et al., 2016; Retallack, 2013a, 2013b, 1999; Retallack et al., 1995; Feakes and Retallack, 1988), Mesozoic (e.g., da Silva et al., 2018; Schuurmans et al., 2015; Flaig et al., 2013; McCarthy and Plint, 2013; Retallack, 2013b, 1994; Retallack et al., 2011, 1987; Lee, 1999; Arndorff, 1994), early and middle Cenozoic (e.g., Raigemborn et al., 2018; Spinola et al., 2017; Cerling et al., 2011; Takeuchi et al., 2007; Retallack, 2009, 2007, 1995; Retallack et al., 2004; Terry, 2001; Wynn, 2000; Quade et al., 1995), and the Quaternary (e.g., Panin et al., 2018; Beverly et al., 2017; Li et al., 2017; Gallagher and Sheldon, 2016; Ringham et al., 2016; Hough et al., 2014; Peters et al., 2013; Zhou and Chaffetz, 2010).

Changes to local climate conditions are recorded in soil carbonates as variations in the calcite (or more rarely, aragonite or dolomite) carbon and oxygen isotopic

composition (Cerling and Quade, 1993; Cerling et al., 1991; Cerling et al., 1989; Salomons and Mook, 1986; Cerling, 1984; Magaritz et al., 1981). The carbon and oxygen isotope composition of soil carbonates is expressed as the ratio *R* of the heavy (rare) isotope to the light (common) isotope ($^{13}C/^{12}C$ and $^{18}O/^{16}O$, respectively), and is typically given in delta notation:

$$\delta^{13}C = 1000 \times (\frac{R_x}{R_s} - 1) \quad (1.1)$$

$$\delta^{18}O = 1000 \times (\frac{R_x}{R_s} - 1) \quad (1.2)$$

where R_x is the ratio of heavy and light isotopes for an unknown sample, and R_s is the ratio for a known laboratory standard. Soil carbonate $\delta^{13}C$ is controlled by the isotopic composition of soil CO_2, whose composition is in turn determined by local vegetation (Breecker et al., 2009; Cerling and Quade, 1993), and–in very arid climates–by the $\delta^{13}C$ of atmospheric CO_2. Past studies have leveraged this relationship between plant CO_2 respiration and soil carbonates to reconstruct changes to the composition of plant communities (e.g., the proportion of C3 and C4 vegetation; Liu et al., 2005; Ding and Yang, 2000; Quade et al., 1995; Wang et al., 1993; Cerling, 1992; Cerling et al., 1989), and to reconstruct changes in atmospheric CO_2 concentrations throughout the Phanerozoic (Myers et al., 2016; Tabor et al., 2013; Cotton and Sheldon, 2012; Mintz et al., 2011; Breecker et al., 2010; Retallack, 2009; Bowen and Beerling, 2004; Nordt et al., 2003; Ekart et al., 1999; Mora et al., 1996; Mora and Driese, 1993. In contrast, soil carbonate $\delta^{18}O$ values are controlled by the oxygen isotope composition of local meteoric waters and the temperature of calcite precipitation (Cerling and Quade, 1993). Past studies have used measurements of soil carbonate $\delta^{18}O$ to infer changes in local meteoric waters and/or local temperature (e.g., Sikes and Ashley, 2007; Fox and Koch, 2004;

Nordt et al., 2003; Garzione et al., 2000; Monger et al., 1998; Latorre et al., 1997; Liu et al., 1996; Wang et al., 1996; Koch et al., 1995; Smith et al., 1993; Cerling and Hay, 1986); however, these studies have largely been limited to qualitative assessments of these climate parameters, due to the difficulty of untangling the competing effects of varying local meteoric waters $\delta^{18}O$ values and changing temperatures on soil carbonate $\delta^{18}O$ values. The inability to calculate quantitative changes in soil water $\delta^{18}O$ values and/or carbonate formation temperatures has limited our ability to answer fundamental questions regarding soil carbonate formation (for example, what (if any) seasonal biases affect the timing of soil carbonate formation?), which has in turn hampered their application as a paleoclimate proxy.

The development of clumped isotope geothermometry over the past decade has provided a new tool for quantitatively measuring soil carbonate formation temperatures, and promises to enhance the use of paleosol soil carbonates as proxies of terrestrial climate change (Eiler, 2011). Clumped isotope geochemistry differs from traditional stable isotope geochemistry in that it measures the relative abundance of multiply substituted isotopologues (i.e. "clumped" isotope molecules) vs. singly substituted isotopologues (Eiler, 2007; Schauble et al., 2006; Eiler and Schauble, 2004; Wang et al., 2004). Isotopologues are the molecular equivalent to elemental isotopes: molecules of the same species that have differing atomic weights due to the presence of different isotopes in their chemical structure (Wang et al., 2004). For example, the isotopically normal carbonate molecule $^{12}C^{16}O_3$ has a mass of 60 amu, while the multiply substituted carbonate isotopologue $^{13}C^{18}O^{16}O_2$ has a mass of 63 amu (note that there are many other possible multiply substituted isotopologues of carbonate; Eiler and Schauble, 2004). Due

to subtle differences in the zero-point energy of multiply substituted isotopologues (see Eiler, 2007; Wang et al., 2004), the formation of clumped isotope molecules is favored at lower temperatures, such that the relative abundance of clumped isotope molecules in any given system increases with decreasing temperature (Eiler, 2007). Thus, if the relative abundance of clumped isotope molecules in a sample material can be measured, the formation temperature of the material can be calculated. With regard to carbonate, the isotopologue of interest is the mass-63 $^{13}C^{18}O^{16}O_2$ molecule, the abundance of which is measured by dissolving a carbonate sample in phosphoric acid to produce a CO_2 analyte. Dissolving the carbonate in acid removes an oxygen atom from the carbonate molecule; thus the CO_2 isotopologue of interest is the mass-47 molecule $^{13}C^{18}O^{16}O$. Similar to the δ notation of traditional stable isotopes, the clumped isotope ratio of a carbonate sample is expressed in capital delta notation (Δ), which is calculated as:

$$\Delta_{47} = 1000 \times \left(\frac{R_i}{R_{i*}} - 1\right) \quad (1.3)$$

where R_i is the abundance ratio of the mass-47 carbonate isotopologue relative to the isotopically normal mass-44 isotopologue, and R_{i*} is the calculated abundance ratio for a pool of molecules with the same bulk ($\delta^{13}C$ and $\delta^{18}O$) isotopic composition as the sample, but a stochastic distribution of isotopologues. Carbonate formation temperatures ($T[\Delta_{47}]$) can then be calculated from the measured carbonate Δ_{47} value via an emprical T-Δ_{47} calibration such as the Kelson et al. (2017) calibration below:

$$\Delta_{47} = \frac{0.0417 \pm 0.0013 \times 10^6}{T^2} + 0.139 \pm 0.014 \quad (1.4)$$

where Δ_{47} is the clumped isotope composition of the carbonate sample, and T is the carbonate formation temperature in Kelvin. For a complete explanation of carbonate

clumped isotope analysis methods, see Kelson et al. (2017), Schauer et al. (2017), Daëron et al. (2016), He et al. (2012), Dennis et al. (2011), and Huntington et al. (2009.

The application of clumped isotope geothermometry to soil carbonate formation processes has already resulted in significant new insights regarding the soil and climate factors that govern the timing of soil carbonate precipitation and the resulting clumped and stable isotope composition of soil carbonate accumulations. Early work on soil carbonates presented a fairly simple hypothesis regarding the seasonality of carbonate formation (Breecker et al., 2009), suggesting that carbonate precipitation occurred either year round or annually during the plant growing season (Cerling and Wang, 1996; Cerling and Quade, 1993; Cerling, 1992; Cerling, 1984), and that soil carbonate $\delta^{13}C$ and $\delta^{18}O$ values thus represent an annual or growing season average. In contrast, the $T(\Delta_{47})$ results from the first clumped isotope studies of soil carbonates, as well as modern soil carbonate stable isotope studies, suggested that rather than precipitating year-round or during the growing season, soil carbonates formation is typically restricted to the warm summer months (Quade et al. 2013; 2011, 2007; Breecker et al., 2009; Ghosh et al., 2006b). Based on these data, it was hypothesized that soil drying during the warm season led to calcite supersaturation of the soil water solution, resulting in soil carbonate precipitation (Breecker et al., 2009). Subsequent soil carbonate clumped isotope studies expanded on these initial findings, and revealed that other factors such as the timing of the wet season (e.g., winter or summer precipitation seasons; Peters et al., 2013) can also exercise an important control on the seasonality of soil carbonate formation and the resulting carbonate $\delta^{13}C$, $\delta^{18}O$, and Δ_{47} values. Despite this progress, important questions remain regarding how other soil processes or factors (e.g., changes in precipitation type

[snow vs. rain], radiative soil heating, variations in vegetation, elevation, local topographic relief) might influence the seasonality of soil carbonate formation. Additionally, intriguing clumped and stable isotope results from pedogenic carbonates collected near Kona, Hawaii provided the first evidence that kinetic isotope effects may modify the isotopic composition of certain soil carbonates (Quade et al., 2013), but it is unclear how common such kinetic isotope effects are in soils and what factors lead to their occurrence.

The goal of this dissertation is to advance the scientific understanding of soil carbonate formation processes and the application of their clumped and stable isotopic composition as quantitative paleoclimate proxies through a series of studies that focus on 1) constraining the effect of precipitation type (e.g., snow vs. rain) on the seasonality of soil carbonate formation along a ~4500 meter elevation transect on the western flank of the Andes in north-central Chile; 2) constraining the soil and climatologic factors that lead to kinetic isotope effects in the clumped and stable isotope composition of certain cold climate soil carbonates; and 3) reconstructing mean annual temperature range (MART) during the Late Cretaceous at two different terrestrial North American sites. My study of soil carbonates from north-central Chile, and from cold climates from various high-latitude and high-elevation sites, focuses on latest Pleistocene and Holocene soil carbonates pendants (carbonate rinds that form on the lower surface of gravel- to cobble-sized clasts in the soil column). Pendants are common in Quaternary soils with a coarse-grained component, and form the basis of many modern soil carbonate studies (Ringham et al., 2016; Hough et al., 2014; Peters et al., 2013; Quade et al., 2013; Breecker et al., 2009). In contrast, my work on Late Cretaceous MART makes use of soil carbonate

nodules preserved in fine-grained paleosol deposits from south-central Utah and northwest Montana in the western United States. Soil carbonate nodules occur in fine-grained calcareous soils, and are more commonly preserved in the geologic record than pendants (Gallagher and Sheldon, 2016).

1.2. Dissertation Organization and Chapter Overviews

The remainder of this dissertation is organized into three chapters that focus on the studies outlines above. Chapters 2 and 3 were previously published in *Earth and Planetary Science Letters* and *Geochimica et Cosmochimica Acta*, respectively. They are presented in their published form, save that the formatting has been adjusted for consistency with the remainder of the dissertation, and the literature cited in each chapter has been combined into a single bibliography at the end of this dissertation. Chapter 3 will be submitted for publication at *Palaeogeography, Palaeoclimatology, and Palaeoecology*, and its citations are also included in the final bibliography.

Chapter 2 presents the findings of my work in the Elqui Valley of north-central Chile, and tests the hypothesis that precipitation type exercises an important control the timing of soil carbonate precipitation, independent of the seasonality of precipitation. The Elqui Valley is ideally suited to test this hypothesis because it is dominated by a winter wet season at all elevations (~400 masl to 4700 masl), but experiences a distinct transition from winter rain below 3000 masl to winter snow at higher elevations. The clumped and stable isotope results from this study showed that the presence of a snowpack at high elevations during the spring and early summer prevents high elevation soils from drying out until the autumn, resulting in cooler $T(\Delta_{47})$ values that resemble local mean annual soil temperatures. At lower elevations dominated by rain, soils dry out

during the warm summer months and have T(Δ_{47}) values that are as warm or warmer than local mean summer soil temperatures. These findings have important implications for the interpretation of paleosol soil carbonates, suggesting that knowledge regarding not only the seasonality of precipitation, but also the type of precipitation is necessary for accurate reconstruction of paleoclimate parameters from soil carbonate T(Δ_{47}) values.

In addition to providing constraints on the effect of precipitation type on the seasonality of soil carbonate formation, my work in Chile also showed that in cold environments where soils regularly freeze during the winter months, the clumped and stable isotope composition of soil carbonates can be affected by kinetic isotope effects associated with cryogenic soil processes. The third chapter of my dissertation builds on these findings by analyzing a suite of cold-climate soil carbonates from the Chilean and Argentinian Andes, the High Arctic, the Tibetan Plateau, and the Antarctic Dry Valleys, in order to test the hypothesis that the sediment grain size of the inter-cobble soil matrix plays a key role in inhibiting or promoting kinetic isotope effects in cryogenic soil carbonates. The results of this study showed that the higher porosity and permeability of cold-climate soils with coarse-grained inter-cobble matrices facilitates soil CO_2 degassing during freezing-induced bicarbonate dehydration, resulting in large negative Δ_{47} anomalies and large positive $\delta^{13}C$ and $\delta^{18}O$ in precipitated cryogenic carbonates. In contrast, the reduced porosity and permeability of cold-climate soils with fine-grained inter-cobble matrices inhibits soil CO_2 degassing, and soil carbonates in these soils form under normal conditions of isotopic equilibrium. These findings suggest that cold-climate soil carbonates from coarse-grained soils or paleosols should not be used for paleoclimate

reconstructions, but that cold-climate soil carbonate from fine-grained soils should provide an accurate record of climate changes in high latitude or high elevation sites.

In the fourth and final chapter of the thesis, I present new estimates of Late Cretaceous MART based on paleosol soil carbonate T(Δ_{47}) reconstructions of warmest month mean soil temperatures, in an effort to help resolve the long-standing disagreement between proxy reconstructions and model simulations of seasonal equability during greenhouse climate periods. My work shows that Late Cretaceous MART in mid-latitude North America was similar in magnitude to modern MARTs, consistent with previous model simulations of Late Cretaceous climate. Additionally, my work provides new constraints on 1) the accuracy of MART calculations using only mean annual temperature and summer temperatures, as described in Snell et al. (2013); and 2) the extent of radiative soil heating (e.g., the degree of excess summer heating in soils versus air temperatures) that can be expected to have affect paleosol carbonate T(Δ_{47}) values based on the observed radiative heating in modern soils from the Soil Climate Analysis Network (SCAN). The findings of this study not only inform our understanding of greenhouse climate equability, but also provide new constraints on the proposed climate factors that contributed to floral and faunal endemism in western North America during the Late Cretaceous (Gates et al., 2010).

My dissertation work shows both the utility of carbonate clumped isotope thermometry in analyzing soil carbonate formation processes and in reconstructing paleoclimate conditions during soil carbonate formation, and highlights the importance of understanding how various soil and climate factors (e.g., sediment grain size and precipitation type) impact the timing of soil carbonate formation and the resulting soil

carbonate Δ_{47} values. Finally, my work on Late Cretaceous paleosols shows that carbonate clumped isotope thermometry can be paired with other paleoclimate proxies to provide important new information regarding climate factors such as mean annual range in temperature. Future studies of soil carbonates as paleoclimate proxies should focus on how different soil carbonate morphologies (e.g., nodules versus pendants) record similar climate conditions.

The exhaustive analytical results for all clumped isotope replicate analyses performed during the course of my dissertation research are included in Appendices A1, A2, B1, B2, and C1. Appendix A3 contains detailed geographic information for the Elqui Valley, Chile soil study sites, and Appendices C2 and C3 contain additional data regarding the measured Late Cretaceous paleosol sections and the SCAN soil climate data referenced in the last chapter of this dissertation.

Chapter 2: Variations in soil carbonate formation and seasonal bias over >4 km of relief in the western Andes (30°S) revealed by clumped isotope thermometry

This manuscript was published May 1, 2016 in Earth and Planetary Science Letters (EPSL)

Co-authored by: Katharine W. Huntington[a], Gregory D. Hoke[b], Andrew Schauer[a], Mallory C. Ringham[b], Claudio Latorre[c,d], Francisca P. Díaz[e]

[a] – Department of Earth and Space Sciences, University of Washington, Seattle, WA, United States

[b] – Department of Earth Sciences, Syracuse University, Syracuse, NY, United States

[c] – Departamento de Ecología, Pontificia Universidad Católica de Chile, Santiago, Chile

[d] – Institute of Ecology and Biodiversity, Santiago, Chile

[e] – Departamento de Microbiología y Genética Molecular, Pontificia Universidad Católica de Chile, Santiago, Chile

2.1. Abstract

Carbonate clumped isotope thermometry provides a new method for investigating long-standing questions regarding seasonal biases in soil carbonate formation and the relationship between soil carbonate formation temperatures recorded by clumped isotopes ($T(\Delta_{47})$) and surface temperatures. We address these questions by comparing C, O, and clumped isotope data from Holocene soil carbonates to meteorological and in situ soil monitoring data along a 170 km transect with >4 km of relief in Chile (30°S). This arid transect experiences a winter wet season, and a >20°C range in mean annual air temperature. We test the hypothesis that, regardless of soil moisture conditions, soil

carbonates from arid regions record warm season biases and form in isotopic equilibrium with soil water and soil CO_2. Below 3200 m, precipitation falls as rain and soil carbonate T(Δ_{47})values at depths >40 cm resemble summer soil temperatures. Above 3200 m, precipitation falls as snow and T(Δ_{47})values resemble mean annual soil temperatures. Soil carbonates from the highest site yield anomalous $\delta^{18}O$, $\delta^{13}C$, and T(Δ_{47})values indicative of kinetic isotope effects consistent with cryogenic carbonate formation. Our findings (1) demonstrate that soil carbonate T(Δ_{47})values from shallow (<40 cm) depths can be affected by short-term temperature changes following precipitation events; (2)suggest that only the largest precipitation events affect soil moisture at depths >40 cm; (3) highlight the role of the soil moisture regime in modulating the timing of soil carbonate formation, which affects the resulting carbonate T(Δ_{47})values; and (4) show that soil carbonates from high elevation or high latitude sites may form under non-equilibrium conditions. These findings underscore the importance of understanding past soil moisture conditions when attempting to reconstruct paleotemperatures using carbonate clumped isotope thermometry.

2.2. Introduction

The application of the carbonate clumped-isotope paleothermometer to pedogenic (formed in soil) carbonates has shed new light on a variety of paleoclimate and tectonic questions (Eagle et al., 2013; Garzione et al., 2008, 2014; Ghosh et al., 2006a; Leier et al., 2013;Passey et al., 2010; Quade et al., 2007a, 2007b, 2011; Snell et al., 2013, 2014; Suarez et al., 2011). Studies of modern soil carbonates provide context for paleoproxy interpretations by investigating the relationship between soil carbonate clumped isotope temperatures (hereafter T(Δ_{47})) and the environmental conditions under which the

carbonates formed (e.g., Hough et al., 2014; Passey et al., 2010; Peters et al., 2013; Quade et al., 2013). However, full utilization of soil carbonates as paleotemperature proxies has been hampered by several unresolved questions: (1) when does soil carbonate form? (2) How do soil carbonate formation temperatures relate to surface temperatures? (3) Are $T(\Delta_{47})$ values of soil carbonates from different environments (e.g., tropical versus high latitude) directly comparable? With regard to the first two questions, several studies (e.g., Breecker et al., 2009; Passey et al., 2010; Quade et al., 2013) suggest that carbonate formation is biased towards summer soil drying events, and that $T(\Delta_{47})$ values show a warm-season bias regardless of soil moisture conditions (Quade et al., 2013); however, some soil carbonates form under differing seasonal biases due to change in soil moisture (Peters et al., 2013), or under non-equilibrium conditions (e.g., Courty et al., 1994; Tabor et al., 2013), suggesting that comparing soil carbonates from different environments or determining the seasonal bias of ancient soil carbonates may not be a straightforward exercise.

We address these questions by collecting Holocene soil carbonates over >4 km of topographic relief on the western flank of the Andes, in north–central Chile (30°S). The range in environmental conditions along this transect allows us to investigate how soil carbonate $\delta^{18}O$, $\delta^{13}C$, and $T(\Delta_{47})$ values record environmental conditions under changing soil moisture and temperature regimes. At sites below the winter snow line carbonate $\delta^{18}O$, $\delta^{13}C$, and $T(\Delta_{47})$values are consistent with a warm season bias in carbonate formation. Carbonates from above the snow line yield $T(\Delta_{47})$ values similar to mean annual soil temperature (MAST). Our findings are consistent with the hypothesis that in hot arid environments, a warm-season bias in $T(\Delta_{47})$ values predominates, but that

significant changes in soil moisture conditions (e.g., effect of spring snowmelt on the timing of soil drying) can impact soil carbon-ate T(Δ_{47}) values. Additionally, we show that in high elevation or extremely arid climates, non-equilibrium processes can lead to anomalous $\delta^{18}O$, $\delta^{13}C$, and T(Δ_{47}) values that do not reflect local climate.

2.3. Background

2.3.1. Soil carbonate formation and isotopic composition

Pedogenic carbonates ($CaCO_3$) are common in arid to sub-humid environments (Landi et al., 2003). Carbonate precipitation follows the reaction:

$$Ca^{2+} + 2HCO_3^- \leftrightarrow CaCO_3 + CO_2 + H_2O \quad (2.1)$$

Calcium ions are introduced into the soil water solution via deposition of dust, dissolution of minerals, and rainwater infiltration (Gile et al., 1966; Machette, 1985; Monger and Wilding, 2006). Carbon is supplied by respired (vegetation and microbes) and atmospheric CO_2, and oxygen is derived from soil waters (e.g., Cerling and Quade, 1993). Precipitation and dissolution of soil carbonates are influenced by soil conditions, including temperature, moisture and pCO_2 (e.g., Breecker et al., 2009; Drever, 1988; Stern et al., 1999). Carbonate formation occurs when the soil solution becomes supersaturated in calcite due to dewatering, CO_2 outgassing, or an increase in Ca^{2+} or HCO_3^- in the solution (Breecker et al., 2009; Retallack, 2005).

Due to the slow rate of change in soil pCO_2 and temperature, carbonates are assumed to form in isotopic equilibrium with soil CO_2 and water (Cerling and Quade, 1993). The isotopic composition of soil carbonates therefore acts as a time-integrated record of local environmental changes over hundreds to thousands of years. Soil carbonate $\delta^{18}O$ and $\delta^{13}C$ values reflect soil water isotopic compositions and soil

productivity or vegetation type, respectively (Cerling and Quade, 1993; Meyer et al., 2014), whereas the clumped isotope (Δ_{47}) composition records soil temperature (Eiler, 2011; Peters et al., 2013; Quade et al., 2007a, 2007b, 2013).

Clumped-isotope thermometry provides a thermodynamics-based measurement of carbonate formation temperature (Eiler, 2007, 2011; Eiler et al., 2014; Ghosh et al., 2006b). Correlations between soil temperature data and soil carbonate T(Δ_{47}) values suggest that the dewatering/outgassing events driving soil carbonate formation typically occur during the summer months, leading to a warm-season bias in T(Δ_{47}) values (Hough et al., 2014; Passey et al., 2010; Peters et al., 2013; Quade et al., 2013; Suarez et al., 2011). However, it has been hypothesized that T(Δ_{47}) values that do not reflect summer soil temperatures are the result of unique soil moisture balance conditions that change the seasonality of soil drying events (Peters et al., 2013).

2.3.2. The Elqui and Turbio valleys, Chile

The study area is situated in the Elqui River catchment of north–central Chile (Fig. 2.1). The Elqui River and its tributary the Turbio River have headwaters in the western flank of the Andes and outlet into the Pacific Ocean. The study area is divided into three geomorphic regions: 1) between 0 and ~750 m, the valley is a wide (500 m to 4 km) cultivated fluvial plain with alluvial fans prevalent near the valley walls; 2) between ~750 and 3200 the valley narrows (100 m to ~1 km) and is characterized by large debris fans and fluvial terraces; 3) above 3200 m, the valley widens and glacial landscapes dominate. We examine sites from 400 to 4700 m that exhibit a range of soil moisture conditions and a >20 °C range in MAST.

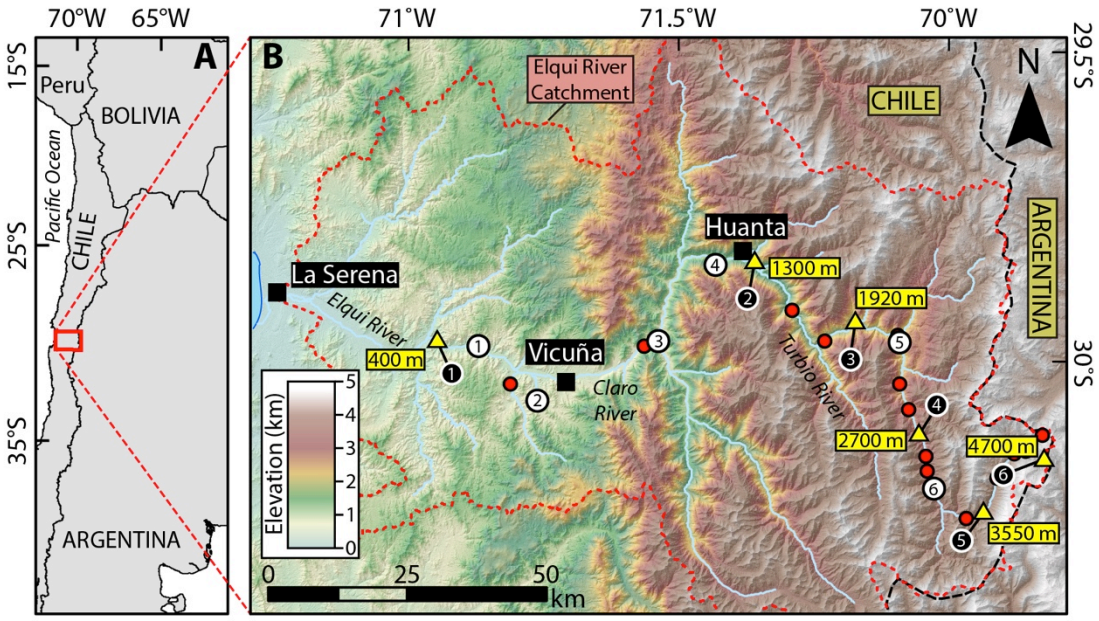

Figure 2.1. (A) Map shows the location of the study area. (B) Shaded relief map showing the location of the 1 m soil pits (yellow triangles), single 50 cm samples (red circles), weather stations maintained by the Chilean government (numbered white circles), and the weather stations installed for this study (numbered black circles). The upper regions of the Elqui River catchment (red dashed line) lie along the Chile–Argentina border (black dashed line).

Precipitation is controlled by the intensity and position of the South Pacific Subtropical High (Garreaud et al., 2009; Grosjean et al., 1998) and is characterized by a winter wet season and low mean annual precipitation (MAP) at all elevations (Fig. 2.2, Supplemental Fig. A1). The Dirección General de Aguas (DGA; http://www.dga.cl/) maintains meteorological stations (Fig. 2.1 and Table 2.1) that provide daily precipitation data over much of the valley. From 1990 to 2014, MAP at elevations from 0 to 820 m averaged 90 mm yr^{-1}, and MAP at the Huanta (1240 m) and La Laguna (3160 m) stations averaged 60 mm $yr^{-1}$and 140 mm yr^{-1}, respectively. MAP at La Serena declined over the last century from 200 mm yr^{-1}in 1900 to 80 mm yr^{-1} in 2000 (Fiebig-Wittmaack et al., 2012), and DGA data show that the area experienced a 40% decrease in MAP between the 2000–2004 and 2005–2010 periods.

The large range in mean annual air temperatures (MAAT) along the transect (Fig. 2.2) results in rain at elevations <3200 m, and snow at higher elevations. Cool Pacific waters generate a thermal inversion resulting in a small surface temperature lapse rate between 0 and ~2000 m. Above the thermal inversion (>2000 m) the surface temperature lapse rate is −6.2 °C km^{-1}. This pattern results in MAATs that decrease from ~17 °C at 370 m (Station 1, Table 2.1) to 8 °C at 3160 m (Station 6). MAAT reaches subzero temperatures at ~4500 m. Seasonal variations in air temperatures range from 7 °C on the

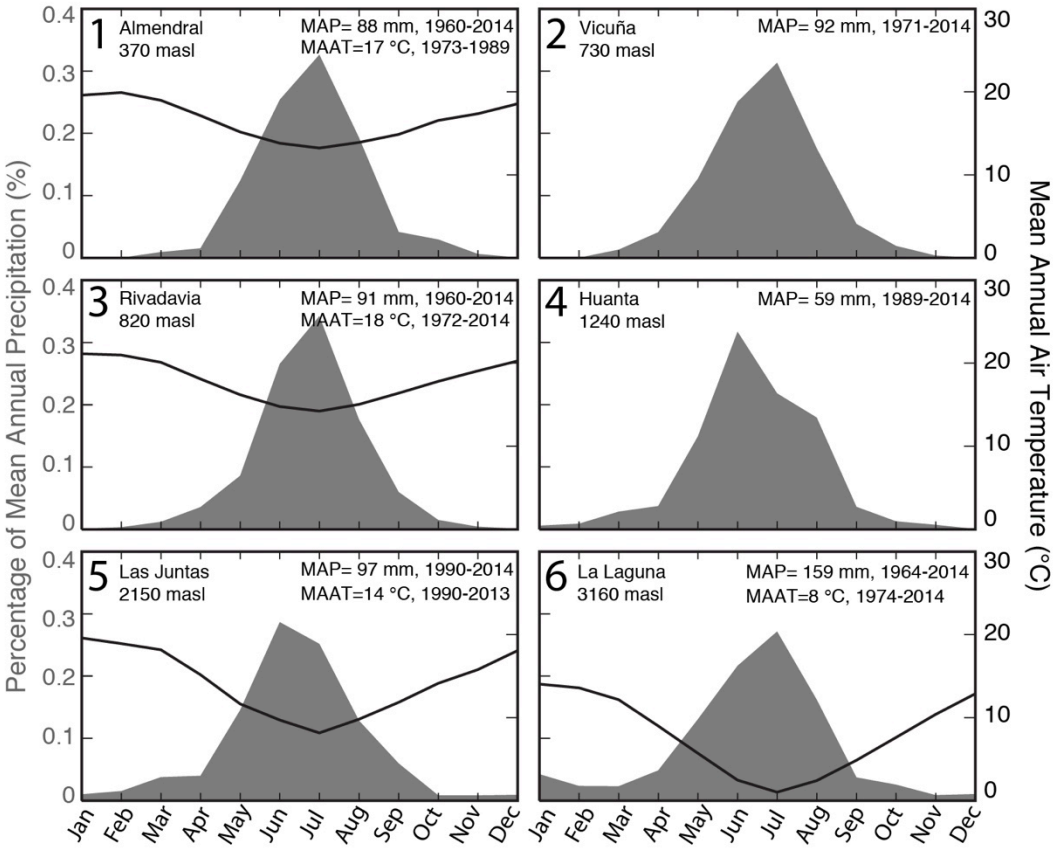

Figure 2.2. Monthly percent mean annual precipitation (MAP, shaded area), and mean annual air temperature (MAAT, black line) for the weather stations maintained by the Chilean government in the Elqui valley. Years of record from DGA are labeled on the figures. At all stations, more than 60% of the total annual precipitation falls during the austral winter (JJA).

Table 2.1. Weather stations maintained by the Direccíon General de Aguas (DGA)

Station[a]	Station Name	Lat (°N)	Lon (°E)	Elevation (m)	Data Type
1	Almendral	-29.982	-70.919	370	Air T (1973-1989), Precip (1960-2014)
2	Vicuña	-30.057	-70.717	730	Precip (1971-2014)
3	Rivadavia	-29.977	-70.562	820	Air T (1972-2014), Precip (1960-2014)
4	Huanta	-29.848	-70.385	1240	Precip (1989-2014)
5	Las Juntas	-29.977	-70.094	2150	Air T (1990-2013), Precip (1990-2014)
6	La Laguna	-30.203	-70.042	3160	Air T (1974-2014), Precip (1964-2014)

a. Station number corresponds to the white numbered circles in Figure 2.1.

coast to 13 °C at 3200 m. The large range in MAAT observed along the transect affects soil moisture balance, making it possible to compare the formation mechanisms affecting soil carbonates under a variety of temperature and soil moisture conditions.

2.4. Methods

2.4.1. Field methods

Surface water and carbonate samples were collected during January of 2013 and 2014. Water samples were collected from streams with flowing water with no evidence of flow contributed from upstream irrigation. All samples were collected in 15 ml centrifuge tubes with PTFE taped sealed threads and caps secured with electrical tape. Precipitation collectors consisting of 1 L HDPE Nalgene bottles fitted with ceramic Buchner funnels and filled with a 1–2 cm layer of oil were deployed at DGA-maintained meteorological stations. Any precipitated water that had accumulated in the bottle was collected on a monthly basis and the collector was redeployed after cleaning and adding fresh oil.

The 1 m soil pits were excavated at six elevations (Fig. 2.1), and sampled at ~20 cm intervals beginning at 20 cm depth. Individual carbonate samples were collected at 50 cm depth from an additional fourteen sites (Fig. 2.1). At all elevations, soil development was weak to absent, with the substrate composed of conglomerates. We surveyed the main

plant species present to within 100 m around each sample site and estimated the plant % cover. The plant species were identified based on a local vegetation catalogue (Marticorena et al., 2001). Below 3550 m, samples were collected from debris cone (~11–5.5ka) or fluvial terrace surfaces (5.5 ka); higher elevation samples were collected from a debris cone, terrace, or moraine surfaces (17–12 ka). The ages of glacial deposits in the Elqui/Turbio valleys were estimated from ^{10}Be exposure ages of glacial features in the nearby Encierro Valley (Zech et al., 2006). The ages of debris cones and fluvial gravels in the Elqui valley were determined from radiocarbon ages on organic matter-rich layers (Riquelme et al., 2011). We targeted non-carbonate clasts bearing discontinuous carbonate pendants, which Gile et al. (1966) identified as the initial form of carbonate growth in a rocky substrate. This allowed us to focus on Holocene and modern soil carbonates that should have integrated a limited number of climate fluctuations during their formation. To ensure the carbonate pendants had formed in situ, we only collected clasts with pendant formation on their underside. We note that most paleoclimate reconstructions make use of nodular carbonate collected from paleosols in sedimentary basins; however, mountainous regions with coarse-grained deposits are the only regions where we can explore such a large range of elevations over a short distance within a consistent moisture regime.

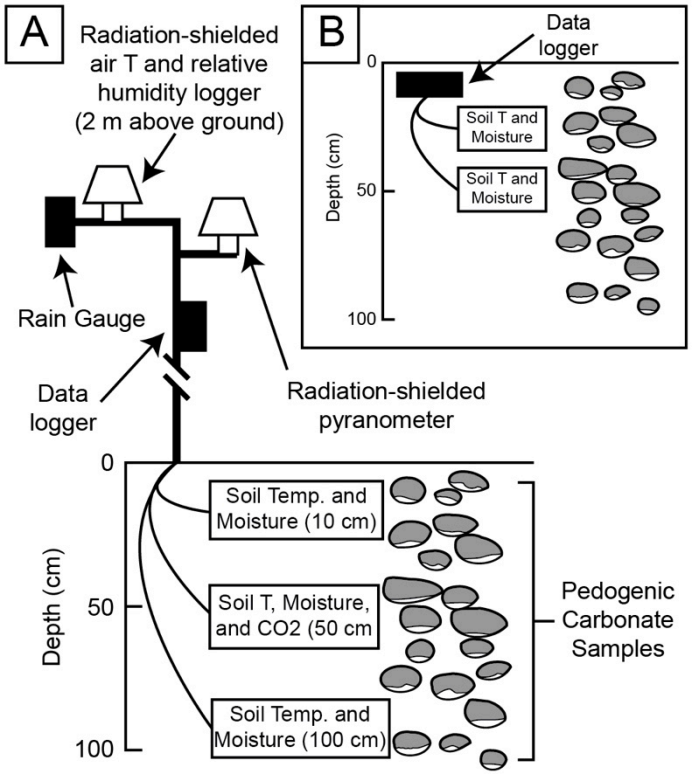

Figure 2.3. Diagram of (A) the air and soil weather stations installed at 400, 1300, 1900, 2700, and 3550 masl (modified from Peters et al., 2013), and (B) soil temperature and moisture monitoring station installed at 4700 masl (modified from Ringham et al., 2016).

During the 2014 field season, meteorological stations were installed at each 1-m soil pit (Fig. 2.3). Onset data loggers (HOBO U30/NRC) were installed at monitoring sites at 400, 1300, 1900, 2700, and 3550 m. Soil temperature sensors (S-TMB-M006) were placed at depths of 10, 50, and 100 cm. One local soil moisture sensor (S-SMC-M005, 0.3 L volume of influence) was placed at 10 cm depth, and wide-area soil moisture sensors (S-SMD-M005, 1.0 L volume of influence) were placed at 50 and 100 cm depth. A Vaisala CO_2 probe (GMM220 with CARBOCAP adaptor) was installed at 50 cm, powered by an independent 30 W solar panel and 44 A-h battery. A tipping bucket rain gauge (S-RGB-M002), air temperature/relative humidity (S-THB-M002, installed within radiation shield), and insolation sensors (S-LIB-M003) were mounted 2 m above the ground. Data were recorded at 15 min intervals by the U30/NRC units. One

Onset microstation data logger (model H21-002) was installed at 4700 m with soil temperature sensors (S-TMB-M006) and soil moisture sensors (S-SMD-M005) at depths of 10 and 50 cm.

2.4.2. Laboratory methods

In preparation for radiocarbon dating and stable isotope analysis, pedogenic carbonate samples were cleaned with a fine brush and DI water to remove soil/organic matter. The carbonate pendants were sampled using a rotary drill with a diamond-tipped bit. The powder from multiple clasts collected from the same depth was homogenized using a mortar and pestle.

Radiocarbon dating of soil carbonate samples was performed by Direct AMS (www.directams.com). Samples were digested in 85% phosphoric acid under vacuum, and the evolved CO_2 was transferred to a reaction vessel containing zinc and an inner vial of iron dust using a disposable manifold. Graphite formed after heating to 550 °C and baking for ~5h. The accelerator mass spectrometer analyses were performed on a National Electrostatics Corporation 1.55DH-1 Pelletron Accelerator, which produces measurements at 0.3% precision and accuracy.

Clumped isotope analyses ($\delta^{18}O$, $\delta^{13}C$ and Δ_{47}) were done at the University of Washington's IsoLab. Carbonate samples (6–8 mg) were digested in a common bath of phosphoric acid (specific gravity 1.9–1.95) held at 90 °C. The evolved CO_2 was cryogenically separated from water on an automated stainless steel vacuum line using an ethanol-dry ice slush trap, isolated in a liquid N_2 trap, and passed through a Porapak Q trap (50/80 mesh, 15 cm long, 4.5 mm ID, 0.635 mm OD) held between −10 °C and −20 °C. The CO_2 was transferred through the Porapak Q trap using He carrier gas, isolated

cryogenically and transferred into a Pyrex break seal. Every 4–5 carbonate sample unknowns, a carbonate standard (NBS-19, or C64 reagent-grade calcite intralaboratory standard) or CO_2 reference frame gas was purified on the vacuum line and transferred into a Pyrex break seal. The reference frame gases were created by equilibrating CO_2 in Pyrex break seals with water of different isotopic composition held at 4 °C or 60 °C, or by heating CO_2 in quartz break seals in a muffle furnace at 1000 °C. Break seals containing purified CO_2 were loaded into an automated 10-port tube cracker inlet system on a Thermo MAT 253 configured to measure m/z 44–49 inclusive.

Δ_{47}, $\delta^{13}C$, and $\delta^{18}O$ values were calculated from the mass spectrometer data using established methods (Huntington et al., 2009 and reference therein). Δ_{47} values were corrected to the Absolute Reference Frame (ARF) of Dennis et al. (2011) using heated gas and CO_2-water equilibration lines constructed during the corresponding analysis period. $\delta^{13}C$ was referenced to the international standards NBS-19 and LSVEC, and $\delta^{18}O$ was referenced to NBS-18 and NBS-19. Samples with Δ_{48} values higher than 2‰, indicating contamination, were rejected. Following Zaarur et al. (2013), the Pierce outlier test was used to identify and remove statistical outliers in the Δ_{47}, $\delta^{13}C$, and $\delta^{18}O$ datasets.

Currently, multiple Δ_{47}–T calibrations exist and the choice of which calibration to employ can have a significant impact on the resulting carbonate T(Δ_{47}) values (Defliese et al., 2015). Because our clumped-isotope analyses are most similar to the methods used by Kluge et al. (2015) and references therein, we applied the 90 °C Kluge et al. (2015) calibration (Equation (5)) to calculate T(Δ_{47}); for reference, T(Δ_{47}) results calculated using the Zaarur et al. (2013) calibration are given in Table 2.2.

Table 2.2. Location, stable isotope, and clumped isotope data for samples collected between 50 and 100 cm depth.

Sample ID	Latitude (°N)	Longitude (°E)	Elevation (m)	Depth (cm)	n	δ^{13} (‰) VPDB[a]	±1 SE (‰)[c]	$\delta^{18}O_{carb}$ (‰) VPDB[a]	±1 SE (‰)[c]	$\delta^{18}O_{FW}$ (‰)[b] VSMOW	Δ_{47} (‰) ARF[a]	±1 SE (‰)[c]	T(Δ_{47}) (°C) Kluge	±1 SE (°C)[c]	T(Δ_{47}) (°C) Zaarur	Radiocarbon Age (BP)
Elq13-400-70	-29.9732	-70.9536	400	70	2	-7.50	0.09	-3.21	0.10	-0.55	0.619	0.030	26	11	25	7324±40
Elq13-400-95	-29.9732	-70.9536	400	95	4	-8.57	0.03	-3.39	0.07	-1.44	0.629	0.014	23	5	23	
Elq13-600-50	-30.0451	-70.8191	600	50	5	-5.91	0.03	-7.56	0.07	-3.82	0.602	0.012	32	5	29	
Elq13-850-50	-29.9876	-70.5694	850	50	7	-3.04	0.02	-6.37	0.06	-3.78	0.620	0.011	26	4	25	2873 ±30
Elq13-1300-60	-29.8576	-70.3649	1300	60	6	-3.57	0.03	-9.77	0.06	-7.26	0.621	0.011	26	4	25	1143 ±30
Elq13-1300-80	-29.8576	-70.3649	1300	80	4	-2.78	0.03	-10.46	0.07	-7.21	0.609	0.014	29	5	28	
Elq13-1300-100	-29.8576	-70.3649	1300	100	4	-3.26	0.07	-10.63	0.07	-6.68	0.599	0.014	33	5	30	
Elq13-1500-50	-29.9323	-70.2940	1500	50	6	-0.27	0.03	-9.68	0.06	-6.16	0.606	0.011	31	4	29	
Elq13-1700-50	-29.9828	-70.2333	1700	50	4	-3.31	0.04	-11.72	0.07	-8.83	0.615	0.014	28	5	26	
Elq13-1924-60	-29.9543	-70.1754	1924	60	5	-0.57	0.03	-10.24	0.07	-6.96	0.609	0.012	30	5	28	1452 ±30
Elq13-1924-80	-29.9543	-70.1754	1924	80	5	-1.57	0.03	-10.63	0.07	-6.38	0.595	0.012	35	5	31	
Elq13-1924-100	-29.9543	-70.1754	1924	100	4	-2.25	0.03	-11.07	0.07	-6.74	0.593	0.014	35	5	32	
Elq13-2100-50	-29.9747	-70.0984	2100	50	3	0.24	0.04	-11.49	0.09	-7.88	0.604	0.016	31	6	29	
Elq13-2300-50	-30.0532	-70.0954	2300	50	3	0.24	0.04	-13.42	0.09	-10.83	0.619	0.016	26	6	25	
Elq13-2700-60	-30.1372	-70.0624	2700	60	4	2.88	0.03	-12.65	0.07	-9.46	0.610	0.014	29	5	27	
Elq13-2700-80	-30.1372	-70.0624	2700	80	5	2.45	0.03	-13.47	0.07	-11.53	0.629	0.012	23	4	23	
Elq13-2700-100	-30.1372	-70.0624	2700	100	3	2.46	0.04	-13.47	0.09	-9.98	0.606	0.016	31	6	29	
Elq13-3100-50	-30.1939	-70.0459	3100	50	5	-4.29	0.04	-15.22	0.07	-9.31	0.570	0.012	44	5	38	
Elq13-3300-50	-30.2715	-69.9734	3300	50	4	5.81	0.03	-10.16	0.07	-11.91	0.688	0.014	6	4	10	
Elq13-3550-60	-30.2624	-69.9415	3550	60	6	1.19	0.13	-9.81	0.06	-10.78	0.675	0.012	9	4	13	5780 ±30
Elq13-3550-80	-30.2624	-69.9415	3550	80	4	3.93	0.09	-8.90	0.11	-9.43	0.668	0.014	11	4	14	
Elq13-3550-100	-30.2624	-69.9415	3550	100	4	0.61	0.06	-11.30	0.09	-10.25	0.643	0.014	19	5	20	
Elq13-3750-50	-30.2064	-69.9161	3750	50	5	0.87	0.03	-11.59	0.11	-13.24	0.686	0.012	6	4	10	2336 ±30
Elq13-4200-50	-30.1637	-69.8620	4200	50	4	6.87	0.04	-4.60	0.07	-6.47	0.689	0.014	5	4	10	9663 ±40
Elq13-4500-50	-30.1382	-69.8298	4500	50	6	9.12	0.05	-9.17	0.06	-12.67	0.717	0.012	-2	3	4	
Elq13-4700-60	-30.1766	-69.8295	4700	60	4	10.03	0.03	-4.20	0.07	-4.59	0.666	0.014	12	4	15	345 ±30
Elq13-4700-80	-30.1766	-69.8295	4700	80	4	10.46	0.03	-5.23	0.07	-6.15	0.674	0.014	10	4	13	
Elq13-4700-100	-30.1766	-69.8295	4700	100	5	9.31	0.05	-6.38	0.07	-6.66	0.664	0.012	12	4	15	

a. Carbonate $\delta^{13}C$, $\delta^{18}O$, and Δ_{47} reported as mean of *n* replicates

b. Soil water $\delta^{18}O$ was calculted following the method outlined in Kim and O'Neil (1997)

c. SE was calculated by choosing whichever was larger: σ of the sample replicate measurements, or σ of the long-term C64 in-house standard; the resulting σ was then divied by the square root of *n*; the T(Δ^{47}) SE estimate also includes a propagation of the uncertainties associated with the T-Δ^{47} calibration of Kluge et al. (2015) (Eq. 5).

To confirm the measurements of $\delta^{18}O$and $\delta^{13}C$ made during clumped isotope analysis, repeat analyses of some samples were conducted at IsoLab using an automated Kiel III carbonate device connected to a Thermo-Finnigan Delta Plus isotope ratio mass spectrometer, following the methods detailed in Tobin et al. (2011).

Surface water and precipitation samples were analyzed on a Picarro L2130-i at Syracuse University. The isotopic values of un-known samples are reported relative to in-house standards ("Syracuse Snow" and "boiled water") calibrated against SLAP and VS-MOW international standard material. Analytical uncertainty is ±2‰ for δD and ±0.2‰ for $\delta^{18}O$based on long-term, repeat measurement of in-house standards.

2.5. Results

2.5.1. Radiocarbon ages

Carbonate radiocarbon ages (n =7) for the soil carbonate samples range between 350 ±30 and 9660 ±40 yr BP (Table 2.2). We note that the mean radiocarbon age of soil carbonates typically underestimates the true age (Amundson et al., 1994; Wang et al., 1994), but errors in ^{14}C age estimates for soil carbonates from arid soils, such as those found in our study area, are generally smaller than the errors associated with soil carbonate from semi-humid areas (Wang et al., 1994). Our soil carbonate radiocarbon ages are younger than or coeval with the radiocarbon ages reported by Riquelme et al. (2011) for debris cones/fluvial terraces along the Elqui and Turbio rivers, and are consistent with the other geochronologic data that are available for the study area.

Table 2.3. Weather stations installed for this study. Data collected from Jan. 2014 to Jan. 2015.

Stations[ab]	Latitude (°N)	Longitude (°E)	Elevation (m)	Total Precip (mm)	Air Temp (°C)			10 cm Soil Temp (°C)			50 cm Soil Temp (°C)			100 cm Soil Temp (°C)		
					Mean Annual	Mean Summer	Mean Winter	Mean Annual	Mean Summer	Mean Winter	Mean Annual	Mean Summer	Mean Winter	Mean Annual	Mean Summer	Mean Winter
1	-29.9732	-70.9536	400	0.5	14.4	18.2	11.8	21.0	28.8	14.2	21.2	27.5	15.7	21.4	26.5	16.8
3	-29.9543	-70.1754	1924	0.3	16.1	21.2	11.6	20.8	29.1	13.2	20.9	27.8	14.6	21.0	26.2	16.2
4	-29.848	-70.385	2700	0.2	10.7	16.4	6.1	13.9	23.6	5.0	14.3	22.8	6.3	14.4	21.6	7.7
5	-30.2624	-69.9415	3550	0	3.7	9.7	0.1	6.7	16.1	0.8	7.4	14.8	2.2	8.0	13.7	3.7
6	-30.1766	-69.8295	4700	NA	NA	NA	NA	-0.7	9.1	-8.2	-0.3	7.8	-6.2	NA	NA	NA

a. Station 2 (at 1300 masl) was vandalized; the results from that station are not included in this table.

b. Station number corresponds to the black numbered circles in Figure 1.

2.5.2. Meteorological station temperature, precipitation, and CO_2 data, and vegetation survey

Mean temperatures from the weather stations installed in 2014 are within 2σ of the long-term averages measured by the DGA stations. We do not report results from the 1300 m station due to sensor malfunctions caused by vandalism. At all stations mean summer soil temperatures are elevated above MAAT (Table 2.3). Between the 400 and 3550 m stations mean summer soil temperature at 50 cm falls from 21 to 7 °C. The range in 2014 monthly average air temperatures ranges from ~6 °C at the 400 m station to ~10 °C at the 1900, 2700, and 3550 m stations. The range in monthly average soil temperatures is greatest at 10 cm (15–19 °C). At 100 cm, the range in monthly average soil temperatures is <14 °C. Diurnal variations in soil temperatures are greatest during the summer at shallow soil depths.

Total precipitation recorded by our stations in 2014 was extremely low compared to the long-term averages and 2014 values recorded by the DGA stations (Table 2.3). For sites >2700 m this discrepancy may be due in part to the type of rain gauge we used, which does not accurately measure snowfall. As shown in Fig. 2.4, the 400 m station received the most rain (0.5 mm; 3 events), while 0.3 mm (3 events) fell at 1900 m, 0.2 mm (2 events) fell at 2700 m, and no rain fell at the 3550 m station. The DGA rain gauges show rainfall events in the same months; however, the DGA stations recorded one to two orders of magnitude more precipitation (1–10 s of mm) than our rain gauges.

Soil pCO_2 was low at all stations, ranging from 22 to 451 ppm at the 2700 m station. The CO_2 sensors installed at the 3500 m site did not function properly and failed to log any measurements.

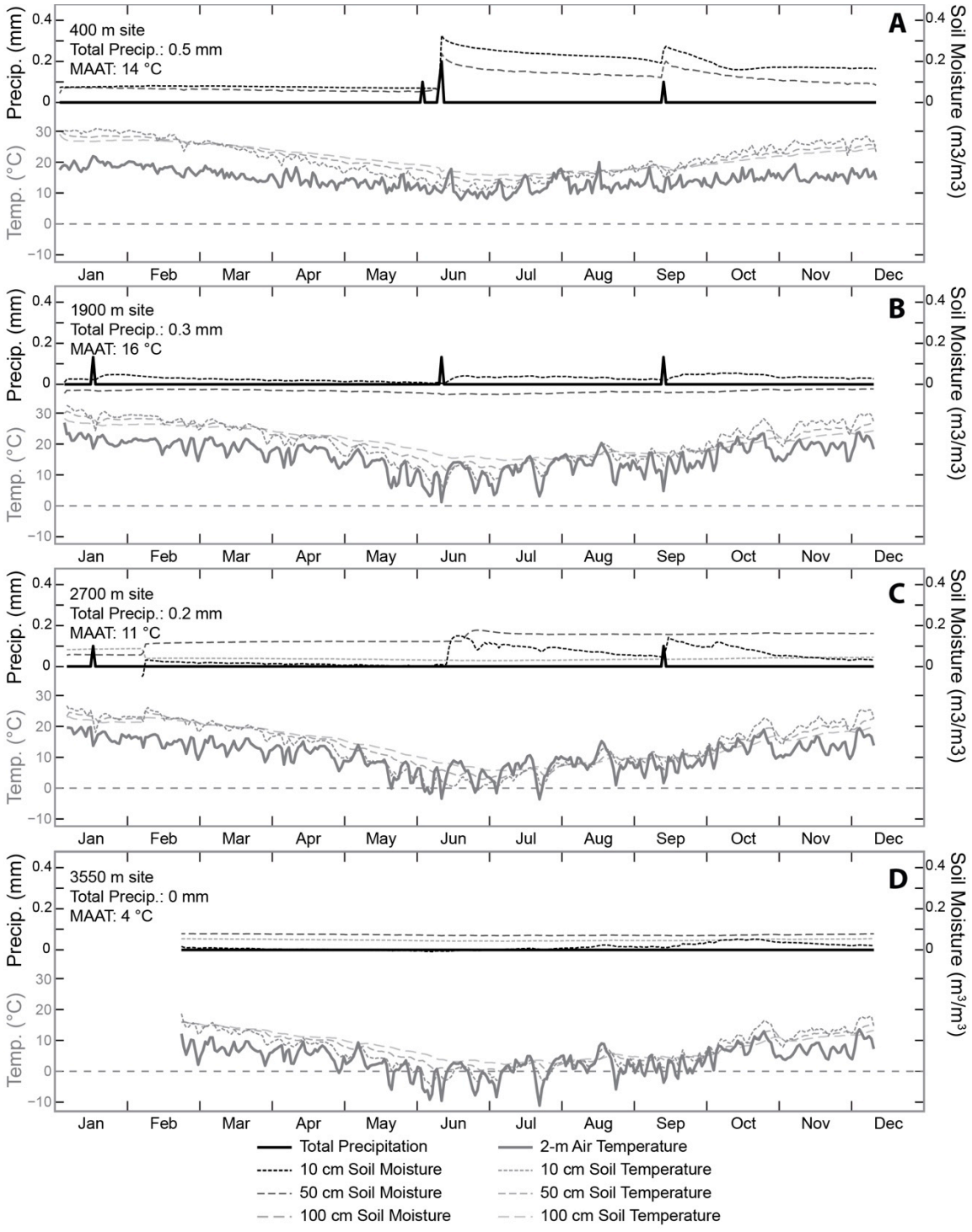

Figure 2.4. Weather station data for the six stations installed as part of this study at the 400, 1900, 2700 and 3550 masl sites. Data covers the period January 3 to December 11, 2014.

Our study area is dominated by C3 vegetation, with no significant C4 or CAM biomass (this study and Marticorena et al., 2001). The few CAM plants (e.g., *Echinopsiscacti*) found in the area are restricted to lower elevation sites (<2000 m). In general, vegetation richness decreases with elevation. Around 400 m *Eulychnia* and *Echinopsiscacti* dominate the xerophytic scrub. From 1000 to 2000 m the vegetation has low cover and is dominated by sub-shrubs such as *Encelia*, *Adesmia* and a few *Stipa* grasses. At 2700m, desert shrubs (*Ephedra*, *Fabiana*, *Atriplex* and *Adesmia*) dominate the landscape. Above 3500 m, the Andean steppe is characterized by grasses including *Stipa*, some sub-shrubs such as *Phacelia* and some cushion *Adesmia* and a 50% plant cover, until the vegetation limit at ~4300 m (0% cover).

2.5.3. $\delta^{18}O$, $\delta^{13}C$, and $T(\Delta_{47})$ results

Water isotope values from collectors mounted at DGA precipitation gauges, as well as streams and snowpack samples (Fig. 2.6A; Supplementary Table A1) range from −18.1 to −1.9‰ and decrease by ~1.9‰ km^{-1} with elevation. Amount-weighted means are calculated for rainfall isotope data; however, we note that the precipitation measurements represent just 2 years of data collection during a prolonged drought and are limited to a small number of samples below 3100 m and thus may not be representative of the long-term precipitation $\delta^{18}O$ values.

Soil carbonate $\delta^{18}O$, $\delta^{13}C$, and $T(\Delta_{47})$ results are reported in Table 2.2 and Supplementary Table A2 in the Supplementary Information. The $\delta^{18}O$ values (VPDB) of all samples range from −3.2 to −15.2‰, and $\delta^{13}C$ values (VPDB) range from −8.6 to 10.5‰, with a mean standard error (SE) of ±0.01‰. For the 1-m soil pits, $\delta^{18}O$ and $\delta^{13}C$

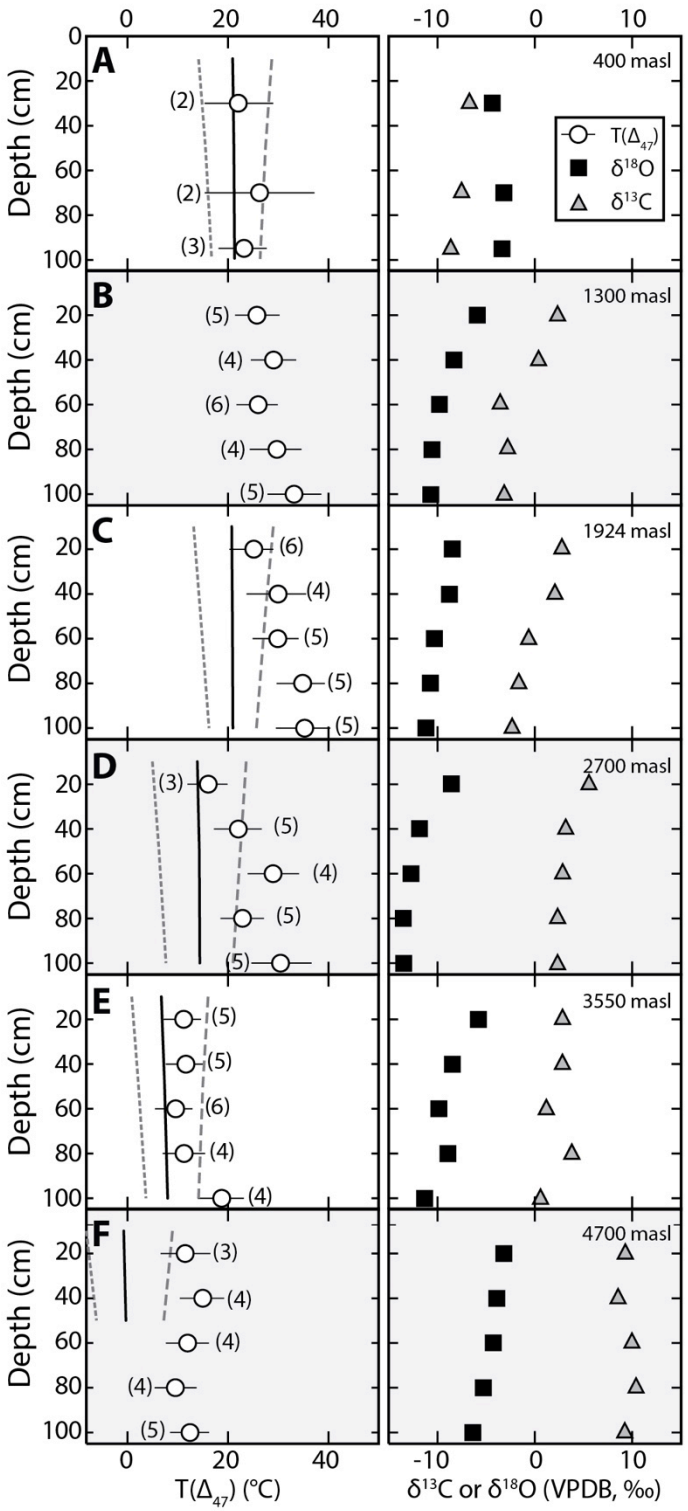

values increase towards the surface and are generally invariant below 40 cm depth (Fig. 2.5). The mean $\delta^{18}O$ values of samples collected at depths >40 cm range from −13.2‰ at the 2700 m soil profile, to −5.3‰ at the 4700 m profile. The mean $\delta^{13}C$ values of samples collected at >40 cm depth range from −8.0‰ at the 400 m soil profile, to 9.9‰ at 4700 m. We used the carbonate $T(\Delta_{47})$ and $\delta^{18}O$ values to reconstruct soil water $\delta^{18}O$ values (Kim and O'Neil, 1997). The calculated soil water $\delta^{18}O$ values are 0 to 5‰ higher than the $\delta^{18}O$ values of local surface water as measured in this study and in Strauch et al. (2006); as an exception, the

Figure 2.5. Depth profiles showing soil carbonate $T(\Delta_{47})$ (left column) and $\delta^{18}O$ and $\delta^{13}C$ (right column, VPDB) results for the five 1-m depth soil pits. The number of replicate analyses for each sample is indicated in parentheses. Lines show the mean annual (black), summer (dashed), and winter (dotted) soil temperatures from Jan. 2014 to Jan. 2015. Due to equipment failure, soil temperatures are not available for the 1300 masl site.

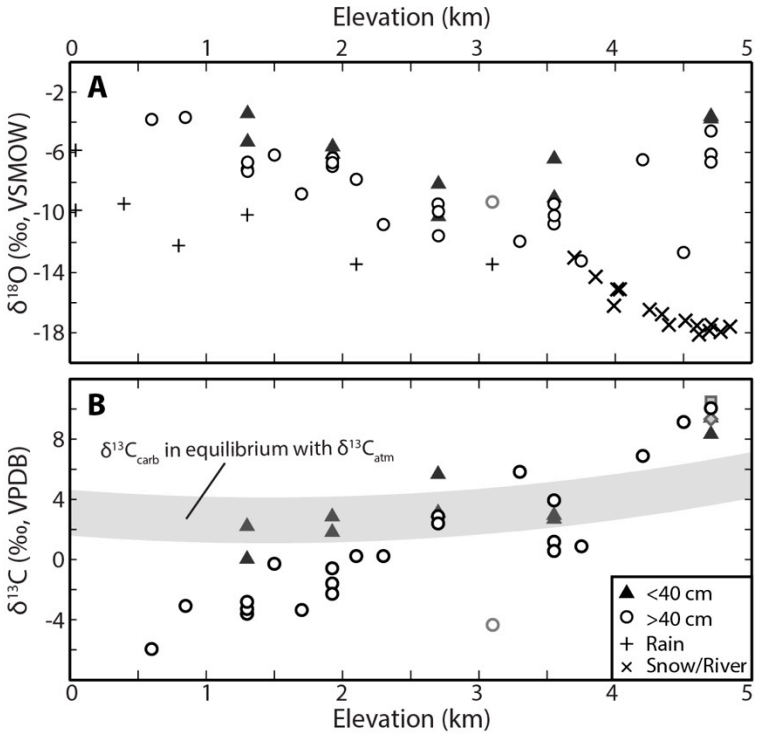

Figure 2.6. Calculated soil water $\delta^{18}O$and soil carbonate $\delta^{13}C$ results versus elevation. A) Calculated soil water $\delta^{18}O$ values are shown for samples collected at depths <40 (black triangles) and >40 cm (white circles). Measured $\delta^{18}O$ values of 2014 precipitation (white pentagons) are shown with ±1 SE error bars. Note that MAP in 2014 was extremely low, and these measurements represent a relatively small sample size. 2014 river, stream and snowpack samples are denoted by the white squares. Water samples were collected during the 2013 field season. River water samples collected by Strauch et al. (2006) are shown for comparison (gray squares). The black line represents a calculated precipitation fractionation pathway calculated using the model described in Rowley et al. (2001). Dashed gray lines mark the ±1 SE uncertainty in modeling results. B) Soil carbonate sample $\delta^{13}C$ values at <40 cm depth (black triangles) and >40 cm depth (white circles) are plotted vs. elevation; the shaded region marks the expected composition of carbonate that has formed in equilibrium with pure atmospheric CO_2 (based on Holocene atmospheric CO_2 values of −8.5 to −6.5‰), based on estimated mean annual air temperature variations over the past 20 kyr (Kaiser et al., 2008) and on the temperature-dependent fractionation between CO_2(g) and $CaCO_3$ at 25 and 0 °C (Romanek et al., 1992).

4700 m sample values are ~14‰ higher than local surface water $\delta^{18}O$ values (Fig. 2.6A).

Carbonate $\delta^{13}C$ values increase with elevation, from −8.6‰ at 400 m to 10.5‰ at 4700 m. Below 2500, most of the samples fall between the expected values of carbonates formed in isotopic equilibrium with atmospheric CO_2 (−6.5 to −8.5‰, pre-industrial and modern, respectively) and with CO_2 gas respired from C3/CAM plants (minimum $\delta^{13}C$ = approximately −25‰) (Breecker et al., 2009; Cerling and Quade, 1993; Diefendorf et al., 2010; Kohn, 2010; Quade et al., 2007a, 2007b). Above 2500 m, the $\delta^{13}C$ values of

several samples exceed the expected values of carbonates that formed in isotopic equilibrium with the pure atmosphere (Fig. 2.6B). The 50 cm sample collected at 3100 m has an anomalously low value (−4.3‰) compared to neighboring samples.

T(Δ_{47}) values range from −2 °C to 35 °C, with one outlier at 44 °C from the sample collected at 3100 m, which will be treated as an outlier for purposes of interpretation. After accounting for uncertainties in external replicate measurements and the Kluge et al. (2015) T−Δ_{47} calibration, the mean external error in temperature is ±5 °C (±1 standard error). Samples collected from below 3200 m elevation yield T(Δ_{47}) values greater than mean summer soil temperatures at all depths, although shallow samples (20 and 40 cm) are consistently colder than deeper samples. At elevations >3200 m, sample T(Δ_{47}) values fall within the expected range of Holocene MAST (Fig. 2.7). In contrast to the other high elevation samples, the samples collected at the highest site (4700 m) yielded an apparent T(Δ_{47}) value of 9 °C, which is within error of mean summer soil temperatures observed at that location.

2.6. Discussion

2.6.1. Comparing soil carbonate T(Δ_{47}), $\delta^{18}O$ and $\delta^{13}C$ to modern environmental parameters

To determine if changes to soil moisture conditions affect the seasonal biases of soil carbonate formation and the resulting T(Δ_{47}) values, we compare our sample T(Δ_{47}) values to modern temperature and precipitation records. Due to the limited temporal coverage of meteorological datasets compared to the long timescale of soil carbonate formation we discuss how soil temperatures varied over the past ~20 kyr. Since the Late

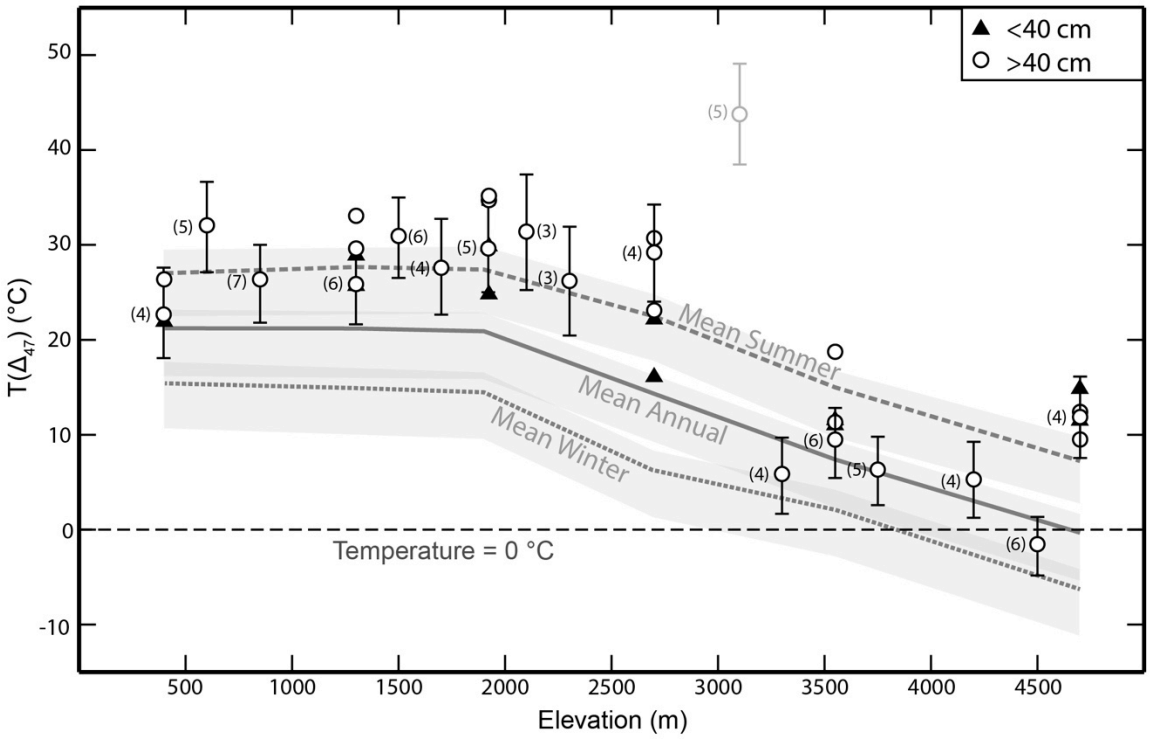

Figure 2.7. Mean T(Δ_{47}) results versus elevation for samples collected at depths <40 cm (gray triangles) and at depths >40 cm (black circles). The numbers in parentheses indicate the number of replicates per sample for the 50 and 60 cm samples. The error bars show the ±1 SE about the mean for the 50/60 cm samples (95 cm sample at the 400 m site). Grey lines show the mean annual (solid), mean summer (dashed), and mean winter (dotted) soil temperatures at 50 cm depth measured from Jan. to Dec. 2014; horizontal dashed black line marks 0 °C. The shaded regions around the mean summer, annual and winter lines show the expected range of Holocene mean, summer and winter soil temperatures (see text for explanation).

Pleistocene, regional MAAT was no more than 4 °C cooler and 2 °C warmer than the present (Kaiser et al., 2008), and we account for this expected range of Holocene soil temperatures in our figures by displaying uncertainties of −4 and +2 °C around the measured 2014 soil temperatures. Despite long-term increases and decreases in precipitation over the past 20 kyr, the region was consistently arid (Lamy et al., 1999). Dating on moraines north of the study area (29 °S), suggests that the equilibrium line altitudes of nearby glaciers have experienced a net change of <500 m since the Late Pleistocene (Grosjean et al., 1998). LANDSAT imagery since 1975 shows that above 3200 m winter precipitation falls predominantly as snow, while lower elevations receive mainly rain (LAND-SAT 1–5 MSS, 4–5 TM, and 7 ETM images courtesy of the USGS,

www.earthexplorer.usgs.gov). Together, these observations imply that the winter snow line elevation has probably varied <500 m during the Holocene.

The limited amount of precipitated water collected from the DGA weather stations during 2013 makes it difficult to determine if the low-elevation precipitation $\delta^{18}O$ values are representative of mean meteoric water $\delta^{18}O$; however the $\delta^{18}O$ values of river and stream samples at higher elevations are in line with isotopic measurements conducted by previous studies (Fig. 2.6A). Long-term measurements of precipitation measured at the La Serena Global Network of Isotopes in Precipitation (GNIP) station yield a mean $\delta^{18}O$ of −5.9‰ (Supplementary Table A1; IAEA/WMO, 2016) and provide a starting point for modeling a hypothetical fractionation pathway of precipitation using the model developed by Rowley et al. (2001), with an assumed starting temperature of 14 °C (mean temperature from May to August) and relative humidity = 81%. At elevations below ~3200 m the $\delta^{18}O$ values of reconstructed soil water are slightly enriched in ^{18}O above both meteoric water samples and the modeled precipitation $\delta^{18}O$ values, suggesting the soil waters experience at least some evaporative enrichment (Liu et al., 1996). Above 3200 m, the $\delta^{18}O$ value of river and stream samples continues to decrease, while the reconstructed soil waters display a high degree of variability.

Carbonate $\delta^{13}C$ values increase with elevation, and above 4000 m plot above the expected range of $\delta^{13}C$ values for hypothetical Holocene carbonates that formed in equilibrium with pure atmospheric CO_2 (Fig. 2.6B, dark gray band), taking into account the temperature-dependent fractionation between CO_2 and calcite (Romanek et al., 1992; Cerling and Quade, 1993). Even at the lowest elevation study sites, carbonate $\delta^{13}C$ values are higher than would be expected for pure C3 vegetation, suggesting that local aridity

and the presence of some CAM plants (e.g., *Echinopsis* cacti) leads to a more ^{13}C-enriched soil CO_2. At higher elevations the total vegetation cover decreases, causing atmospheric CO_2 to dominate the soil CO_2 composition and an increase in carbonate $\delta^{13}C$ values.

After accounting for the evaporative effect in this arid region (higher $\delta^{18}O$) and soil productivity that is low and decreases with increasing elevation (higher $\delta^{13}C$; Cerling and Quade, 1993; Kohn, 2010), most sample data are consistent with the soil carbonates having formed under apparent isotopic equilibrium with local soil water and soil CO_2 (Fig. 2.6). In contrast, samples from the highest site (4700 m) yield apparent T(Δ_{47}) values much higher than other nearby samples, calculated soil water $\delta^{18}O$ values up to 14‰ higher than local waters, and $\delta^{13}C$ values enriched by up to 4‰ above the estimated isotopic composition of Holocene atmospheric CO_2.

2.6.2. Systematic changes in soil carbonate T(Δ_{47}) due to changes in soil moisture

Soil carbonate T(Δ_{47}) values show a clear change in seasonal bias at ~3200 m (Fig. 2.7), coinciding with the mean position of the winter snow line. T(Δ_{47}) values below 2700–3200 m generally match or exceed the expected range of Holocene mean summer soil temperatures. T(Δ_{47}) values from elevations of 3200 to 4500 m are within error of Holocene MAST. The high T(Δ_{47}) values for samples collected below 3200 m at depths >40 cm agree with other studies that observed summer formation biases in soil carbonates collected from arid climates (Hough et al., 2014; Passey et al., 2010; Peters et al., 2013; Quade et al., 2013; Ringham et al., 2016). However, the T(Δ_{47})values of soil carbonates collected at depths <40 cm are more variable (Figs. 2.5 and 2.7), with samples generally yielding T(Δ_{47}) values cooler than mean summer soil temperature. We propose

that this discrepancy between shallow and deep soil carbonate T(Δ_{47})values is due to two mechanisms: 1) only the largest precipitation events lead to infiltration of meteoric water to depths >40 cm; once wet, these deeper soils only dry out during the hottest summer months; and 2) rapid growth of soil carbonates occurs at shallow depths during short-term periods of soil temperature depression following small precipitation events.

Recent work in Argentina has shown that small rain events are unlikely to penetrate deeply into arid soils (Ringham et al., 2016). Thus, deep horizons (>40 cm) in the soil profile may only be wetted infrequently, and once wet, these horizons may remain too moist for carbonate precipitation until drying occurs in the warm late spring and summer. This is consistent with soil moisture data from our 400 m and 1900 m sites, which both recorded a wetting event in early June 2014 (austral winter). At the 400 m site, the rainfall event was large enough to show increases in soil moisture at 10 and 50 cm depths, which remained elevated well into the summer months (Fig. 2.4); however, at the 1900 m site, the recorded rain event was smaller, and an increase in soil moisture was only recorded at 10 cm.

In light of these observations, we propose the following process for carbonate precipitation at elevations <3200 m: 1) winter rainfall causes increases in soil moisture, with the soil moisture of deeper soil horizons only increasing during the largest rain events; 2) relatively fast drying of shallow (<40 cm depth) soil horizons due to evaporation following smaller rain events leads to soil carbonate precipitation during the period of cooler shallow soil temperatures that are observed immediately after most precipitation events (Ringham et al., 2016), resulting in variable, cooler, soil carbonate T(Δ_{47}) values; 3) relatively slow drying of deeper soil horizons following larger rain

events causes calcite supersaturation of deeper soil waters only after prolonged periods of high temperature, resulting in soil carbonate T(Δ_{47}) values that are biased towards mean summer soil temperature.

The transition from warm-biased T(Δ_{47}) values below 2700–3200m to T(Δ_{47}) values that resemble MAST at higher elevations (Fig. 2.7) coincides with the average position of the winter snowline. The presence of winter snow could cause colder T(Δ_{47}) values via one of two mechanisms: 1) soil carbonate formation may be restricted to the brief period of time between soil wetting and drying. If this is the case, then soil carbonate formation at depths <40 cm in the soil profile may occur rapidly following the onset of melting, leading to T(Δ_{47}) values that are biased towards cold (near 0 °C) temperatures due to heat advection by melt water. 2) The presence of a snow layer and the initiation of snowmelt in the spring could affect the timing and rate of soil drying (Rodhe, 1998), causing a change in the seasonality of carbonate formation. We favor the second explanation for two reasons. First, the T(Δ_{47}) values of the >3200 m samples are generally warmer than 0 °C. Second, soil moisture data from the 3550 m site shows maximum drying during the austral autumn (Fig. 2.4D), and the expected range of Holocene autumn soil temperatures agrees well with MAST and the measured T(Δ_{47}) values.

We interpret our data to suggest that the timing of soil moisture wetting and drying events have a large impact on seasonal biases in soil carbonate formation and T(Δ_{47}) values. This is consistent with Peters et al. (2013), who suggested that changes to the seasonality of precipitation can lead to changes in the seasonal biases of soil carbonate T(Δ_{47}) values.

2.6.3. High-elevation cryogenic carbonate formation

There are several possible explanations for the anomalously high T(Δ_{47}), $\delta^{18}O$ and $\delta^{13}C$ values observed at the 4700 m sample site. Repeated cycles of carbonate dissolution and precipitation can lead to enrichment of carbonate $\delta^{13}C$ (Clark and Lauriol, 1992); however, low soil moisture values (<0.12 m^3 m^{-3}), and reports of persistent, high calcite activity values ($\alpha_{calcite}$< 1) from similar environments in Argentina (Ringham et al., 2016) suggest that dissolution of soil carbonates is rare. Aridity effects on soil respiration and evaporation can lead to significant increases in both $\delta^{18}O$ and $\delta^{13}C$ values of soil carbonate. Quade et al. (2007b) report estimated soil water $\delta^{18}O$ enrichments of up to 10‰ compared to local rainwater in the Atacama Desert (+700 km north of the Elqui Valley), and soil carbonate $\delta^{13}C$ values of up to +7.3‰; however, the high-elevation regions of our study area are less arid than the Atacama Desert but the calculated soil water $\delta^{18}O$ enrichment and $\delta^{13}C$ values of our 4700 m carbonates are even higher than carbonates collected from the Atacama. Sublimation of snow/ice prior to meltwater infiltration may be responsible for some of the observed $\delta^{18}O$ enrichment at the 4700 m site (Lechler and Niemi, 2011), but this does not explain the elevated carbonate $\delta^{13}C$ values.

We hypothesize that both the extremely high soil carbonate $\delta^{18}O$ and $\delta^{13}C$ values and relatively low Δ_{47} values at 4700 m can be explained by kinetic isotope effects (KIE) associated with cryogenic carbonate formation. Cryogenic soil carbonates precipitate when a soil water solution reaches calcite supersaturation due to the exclusion of solute ions from the ice matrix, and can form under non-equilibrium conditions with respect to soil water and soil CO_2 (Courty et al., 1994; Kluge et al., 2014; Lacelle, 2007).

Environmental conditions unique to the 4700 m site may explain why cryogenic carbonates are found at this site. The area is devoid of vegetation and the soil matrix is composed of ~3 cm unconsolidated clasts, which may affect the ability of the soil to retain moisture throughout the year. Perennial snow fields partially cover the area.

The KIE associated with cryogenic carbonate formation are the result of rapid CO_2 degassing via bicarbonate dehydration and dehydroxylation, induced by fast solution freezing (Clark and Lauriol, 1992; Guo, 2009). Due to the differences in zero-point energy levels, dehydration of bicarbonate isotopologues containing ^{12}C and ^{16}O proceeds faster than the dehydration of isotopologues containing ^{13}C and ^{18}O, resulting in a dissolved inorganic carbon (DIC) pool with higher $\delta^{13}C$and $\delta^{18}O$ values (degassed CO_2 with lower $\delta^{13}C$ and $\delta^{18}O$ values; Clark and Lauriol, 1992). This process causes lower carbonate Δ_{47} values (higher T(Δ_{47}) values) because degassing CO_2 from a bicarbonate solution acts as a "reverse" mixing problem (Guo, 2009). Previous studies have shown that mixing two end member CO_2 pools with distinct bulk isotope compositions but identical Δ_{47} compositions produces a combined CO_2 pool with a Δ_{47} composition that is not a simple linear mixture of the two original pools (Eiler and Schauble, 2004; Defliese and Lohmann, 2015). In a similar way, degassing isotopically light CO_2 results in a new, lower Δ_{47} value for the remnant DIC pool (Guo, 2009).

Our findings are consistent with experiments conducted by Tripati et al. (2015), which suggest that CO_2 dehydration and dehydroxylation lead to $\delta^{18}O$ enrichment and Δ_{47} depletion in the resulting carbonate. The data from the 4700 m site show that for every 1‰ increase in $\delta^{18}O$ with respect to local surface waters, Δ_{47} decreases by ~0.001‰ with respect to the expected Δ_{47} of carbonates formed under equilibrium conditions in the

same water. This Δ_{47}–$\delta^{18}O$ relationship is less than that reported by Guo (2009) (0.02 to 0.026‰ decrease in Δ_{47} for every 1‰ increase in $\delta^{18}O$), and nearer that reported by Kluge et al. (2014) for cryogenic cave carbonates (0.005‰). Our findings add to the body of evidence suggesting that the $\delta^{18}O$–Δ_{47} offset correlation in carbonates formed under non-equilibrium conditions can vary significantly (Kluge et al., 2014 and references therein).

The magnitude of kinetic fractionation observed in cryogenic carbonates depends on the rate at which the solution freezes. Clark and Lauriol (1992) suggest that freezing must occur nearly instantaneously in order for KIE to occur, but Guo (2009) observed KIE in carbonates that resulted from a bicarbonate solution that froze over the course of ~3h. We suggest that soil water freezing at our 4700 m site proceeds unusually fast due to the open nature of the soil matrix. Using a simple heat diffusion equation (Quade et al., 2013, Eq. (1)), we estimate that bare soil at 4700 m experiences winter diurnal temperature swings of up to 12 °C at 10 cm depth, consistent with our soil temperature observations. This suggests that rapid freezing is possible near the soil surface. Our observations show smaller diurnal temperature variations at depth, but the similarity in $T(\Delta_{47})$, $\delta^{18}O$, and $\delta^{13}C$ values among soil carbonates sampled at different depths suggests that at all depths >1m freezing still proceeds rapidly enough to produce KIE in soil carbonates.

The identification of cryogenic soil carbonates at high elevations has implications for anomalous $T(\Delta_{47})$ values from previously published datasets. Quade et al. (2011) presented $T(\Delta_{47})$ data for nine Tibetan soil carbonate samples that were collected at elevations >3800 m. Similar to our 4700 m samples, the $T(\Delta_{47})$, $\delta^{13}C$, and $\delta^{18}O$ values of

these carbonates are unexpectedly high. Based on our findings from the 4700 m site, we propose that these anomalously high T(Δ_{47})values may be due to cryogenic carbon-ate formation.

2.6.4. Biases in shallow soil carbonate T(Δ_{47})values

Our results suggest that the T(Δ_{47}) values of shallow soil carbonates are poor proxies of mean annual or carbonate growth season soil temperatures. Quade et al. (2013) suggested that T(Δ_{47}) values of soil carbonates formed during the warm season should systematically increase towards the surface; however, we observe the opposite: below 2700–3200 m, shallow (<40 cm) soil carbon-ate T(Δ_{47}) values are similar to or in some cases cooler than deeper carbonates. Our findings are consistent with observations in Argentina that show soil carbonate T(Δ_{47}) values on the eastern flank of the Andes are isothermal with depth (Peters et al., 2013; Ringham et al., 2016). Our soil temperature and moisture observations show that small precipitation events lead to short-term depression of soil temperatures at shallow depths in the soil pro-file, and taken together with the T(Δ_{47}) values are consistent with the hypothesis that shallow soil carbonates tend to form soon after precipitation events when shallow (<40 cm) soil temperatures are depressed (Ringham et al., 2016). These findings suggest that shallow carbonates are not appropriate for use as paleoclimate proxies.

2.7. Implications and conclusions

The Elqui and Turbio valleys in north–central Chile provide an opportunity to compare the $\delta^{18}O$, $\delta^{13}C$, and T(Δ_{47}) values of Holocene pedogenic carbonates collected from environments with different soil temperature and moisture conditions. At elevations <3200 m, soil carbonate T(Δ_{47}) values show a warm-season bias. Above 3200 m,

carbonate T(Δ_{47}) values resemble MAST. We pro-pose that the presence of snow during the winter months alters when and how rapidly soil drying occurs, resulting in cooler T(Δ_{47}) values for the >3200 m samples. At our highest elevation site (4700 m) we interpret anomalously high $\delta^{18}O$ and $\delta^{13}C$ and low Δ_{47} values to reflect KIE due to cryogenic carbonate formation.

Our findings have important implications for the use of soil carbonates as paleotemperature proxies. Building previous studies (e.g., Peters et al., 2013; Hough et al., 2014), we show that seasonal biases in T(Δ_{47}) are likely driven by soil moisture conditions, and that changes to seasonal soil moisture balance affect the relation-ship between T(Δ_{47}) and MAAT. Thus, when using soil carbonate T(Δ_{47}) as a paleoclimatic proxy, care should be taken to under-stand past soil moisture conditions.

Future work should focus on using the soil moisture indicators commonly preserved in paleosols (e.g., Mack et al., 1993; Hyland et al., 2015; Nordt and Driese, 2010; Retallack, 2005) to quantify how changes to soil moisture may have affected the T(Δ_{47}) of ancient soil carbonates. To better relate our work to ancient paleosol carbonates, the methods described in this study should be applied to carbonate nodules, which are more commonly preserved in the geologic record and typically integrate a longer climate signal than pendants. Finally, we show that at high elevations, cryogenic processes can affect the bulk and clumped isotope values of soil carbonates. Identifying cryogenic soil carbonates is especially relevant for paleoelevation studies, since KIE may bias these carbonates to high T(Δ_{47}) values, causing underestimates in elevation reconstructions.

2.8 Chapter Two Acknowledgements

The authors thank Carlos Galleguillos and Gustavo Freixas of the La Serena office of the Dirección General de Aguas (DGA) for permission to deploy rain collectors at DGA stations as well as providing station data. KWH and GDH were supported by NSF Grant EAR-1252064. KWH also received support from EAR-1156134. LKB was supported by a GSA research grant from the Geological Society of America (10615-14). The authors thank Nathan Sheldon and an anonymous reviewer for their insightful and constructive comments, and Heather Stoll for editorial support.

Chapter 3: Clumped isotope constraints on equilibrium carbonate formation and kinetic isotope effects in freezing soils

This manuscript was published August 15, 2018 in Geochimica et Cosmochimica Acta (GCA)

Co-authored by: Katharine W. Huntington[a], Ronald Sletten[a], James M. Watkins[b], Jay Quade[c], Bernard Hallet[a]

[a] – Department of Earth and Space Sciences and the Quaternary Research Center, University of Washington, Seattle, WA, United States

[b] – Department of Earth Sciences, University of Oregon, Eugene, OR, United States

[c] – Department of Geosciences, The University of Arizona, Tucson, AZ, United States

3.1. Abstract

The clumped and stable isotope (Δ_{47}, $\delta^{18}O$, and $\delta^{13}C$) composition of pedogenic (soil) carbonates from cold, arid environments may be a valuable paleoclimate archive for climate change-sensitive areas at high latitudes or elevations. However, previous work suggests that the isotopic composition of cold-climate soil carbonates is susceptible to kinetic isotope effects (KIE). To evaluate the conditions under which KIE occur in cold-climate soil carbonates, we examine the Δ_{47}, $\delta^{18}O$, and $\delta^{13}C$ composition of soil carbonate pendants from Antarctica (Dry Valleys, 77 °S), the High Arctic (Svalbard 79 °N), the Chilean and Argentinian Andes, and the Tibetan plateau (3800–4800 m), and compare the results to local climate and water $\delta^{18}O$ records. At each site we calculate the expected equilibrium soil carbonate Δ_{47} and $\delta^{18}O$ values and estimate carbonate Δ_{47} and $\delta^{18}O$ anomalies (observed Δ_{47} or $\delta^{18}O$ minus the expected equilibrium Δ_{47} or $\delta^{18}O$).

Additionally, we compare the measured carbonate $\delta^{13}C$ to the expected range of equilibrium soil carbonate $\delta^{13}C$ values. To provide context for interpreting the Δ_{47} and $\delta^{18}O$ anomalies, the soil carbonate results are compared to results for sub-glacial carbonates from two different sites, which exhibit large Δ_{47} anomalies (up to –0.29‰). The Antarctic and 4700 masl Chilean Andes samples have negative Δ_{47} anomalies and positive $\delta^{18}O$ anomalies consistent with KIE due to rapid bicarbonate dehydration during cryogenic carbonate formation. In contrast, the lower elevation Chilean Andes, Argentinian Andes, Tibetan Plateau and High Arctic results are consistent with equilibrium, summer carbonate formation. We attribute the differences in Δ_{47} and $\delta^{18}O$ anomalies to variations in inter-cobble matrix grain size and its effects on the effective soil pore space, permeability (hydraulic conductivity), moisture, and bicarbonate dehydration rate. The Antarctic and 4700 masl Chilean Andean soils have coarse-grained matrices that facilitate rapid bicarbonate dehydration. In contrast, the lower elevation Chilean Andes, Argentinian Andes, High Arctic and Tibetan Plateau soils have finer-grained matrices that decrease the soil pore space, soil permeability and CO_2 gas flux, promoting equilibrium carbonate formation. The sub-glacial carbonate samples yield highly variable Δ_{47} and $\delta^{18}O$ anomalies, and we propose that the differences between the two glacier sites may be due to variations in local sub-glacial drainage conditions, pCO_2, and pH. Our findings suggest that carbonates from soils with coarse-grained matrices may exhibit KIE in cold climates, making them poor paleoclimate proxies. Soils with fine-grained matrices are more likely to yield equilibrium carbonates suitable for paleoclimate reconstructions regardless of climate. Paleosol matrix grain size should

therefore be taken into account in the evaluation of carbonate stable and clumped isotope values in paleoclimate studies.

3.2. Introduction

Pedogenic (formed in soil) carbonates are spatially and temporally abundant in the geologic record, and their isotopic compositions provide a rich archive of past climatic, environmental, and tectonic changes. Numerous studies have used carbonate stable ($\delta^{18}O$, $\delta^{13}C$) and clumped (Δ_{47}) isotope compositions to reconstruct the formation temperature, soil respiration and biologic productivity of modern soils and paleosols from a variety of geologic time periods to answer outstanding questions regarding paleoclimatology (e.g., Passey et al., 2010; Snell et al., 2013) and paleoaltimetry (e.g., Ghosh et al., 2006; Garzione et al., 2014; Carrapa et al., 2014; Licht et al., 2017). Most past studies of modern and ancient soil carbonates have typically focused on samples collected from temperate or warm environments (e.g., Gile et al., 1966; Gunal and Ransom, 2006; Quade et al., 2007; Hough et al., 2014; Diaz et al., 2016; Gallagher and Sheldon, 2016; Ringham et al., 2016; Dietrich et al., 2017). In contrast, a much smaller number of recent studies have investigated the clumped and stable isotope compositions of pedogenic carbonates from cold-climate soils (here defined as soils that experience sub-zero mean monthly temperatures for two or more consecutive months per year; e.g., Quade et al., 2011, 2013; Peters et al., 2013; Burgener et al., 2016). These cold climate soil carbonates remain a largely untapped archive of climate information at high latitude and high elevation sites. Studies of cold-climate soil carbonates have the potential to expand the range of terrestrial environments that can be incorporated into paleotemperature reconstructions for a variety of applications. In particular, a better

understanding of the processes by which soil carbonates form in cold climates is needed to confidently reconstruct environmental conditions from such samples, and ultimately to provide insight into topics such as the uplift history of continental plateaus or how polar amplification has affected high latitude areas during previous episodes of climate change.

Carbonate-based temperature reconstructions operate on principles of thermodynamic equilibrium. Soil carbonates forming in warm and/or temperate soils are generally regarded as forming under conditions approaching isotopic equilibrium due to the slow precipitation of soil carbonates (Breecker et al., 2009). In contrast, it has been proposed that the stable isotope and Δ_{47} records of some soil carbonates in cold climates may be complicated by isotopic disequilibrium due to kinetic isotope effects (KIE) (e.g., Courty et al., 1994; Burgener et al., 2016). Such KIE have been invoked to explain temperature-independent effects in cryogenic cave carbonates (e.g., Kluge et al., 2014), and in other types of cryogenic carbonates (e.g., Lacelle, 2007), and have been suggested by Burgener et al. (2016) to account for anomalously warm clumped isotope temperatures from the Tibetan Plateau (Quade et al., 2011). It is not known, however, whether such processes are widespread among soil carbonates forming in cold climates, or among sub-glacially precipitated carbonates.

The main objective of this study is to explore the mechanisms for soil carbonate formation in cold-climate soils, and to evaluate the extent to which disequilibrium occurs in such soil carbonates. To this end, we document variations in Δ_{47}, $\delta^{18}O$, and $\delta^{13}C$ values in a suite of soil carbonate pendants collected from diverse cold-climate environments, and compare these values to available modern soil and meteorological data. These comparisons enable us to (1) assess whether the soil carbonates are precipitating via

"normal" processes typical of temperate soils (e.g., precipitation due to soil drying and subsequent $CaCO_3$ supersaturation of the soil solution), or via cryogenic processes (e.g., rapid soil water freezing leading to $CaCO_3$ supersaturation of the soil solution), and (2) evaluate how differences in environmental and soil conditions at the studied sites affect the magnitude of any observed KIE. The soil carbonates discussed in this study are pendant forms that precipitated on the underside of clasts collected from high-latitude sites in the Arctic and Antarctic, and from high-elevation sites in the Chilean and Argentinian Andes Mountains and the Tibetan Plateau (Fig. 3.1). To provide context for evaluating the magnitude of potential KIE for these samples, we compare the soil carbonate Δ_{47}, $\delta^{18}O$, and $\delta^{13}C$ values to the isotopic composition of cryogenic sub-glacial carbonates, which have well-constrained formation temperatures (between 0 and –1 °C) and host water $\delta^{18}O$ values.

Our findings suggest that cold-climate soil carbonates are more likely to form under conditions of isotopic disequilibrium in soils with relatively coarse (e.g., sand to gravel) inter-cobble matrices, whereas isotopic equilibrium can be established in carbonates formed in soils with fine-grained (e.g., silt to sand) inter-cobble matrices. By constraining the degree to which cold-climate soil carbonates can be affected by disequilibrium processes, this study adds to a growing body of work which suggests that both soil moisture and soil grain size are important factors in determining the kinetics of soil carbonate formation and interpreting the resulting isotopic record.

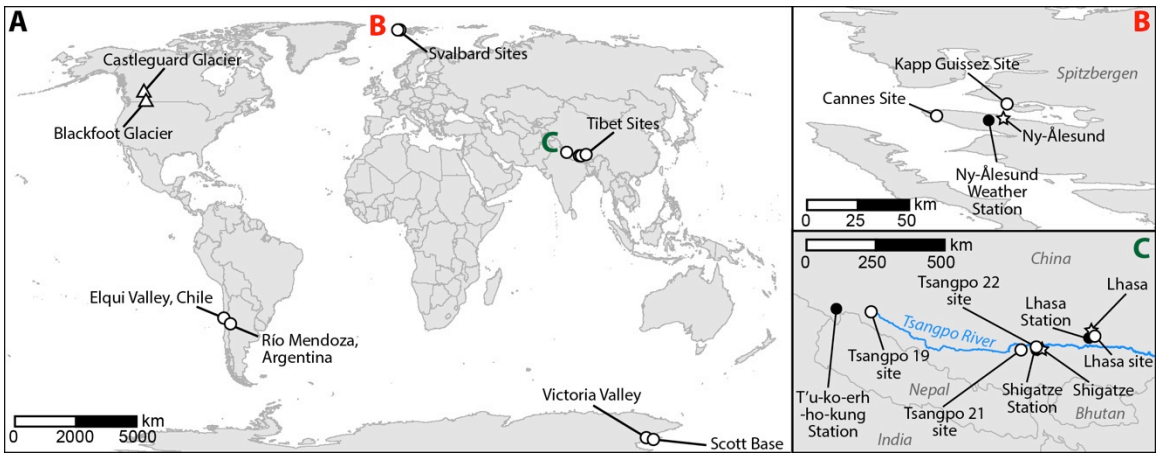

Figure 3.1. (A) Index map showing the location of the soil sample sites (circles) and sub-glacial carbonate sample sites (triangles). (B) Spatial relationship between the two Svalbard soil sample sites (Cannes and Kapp Guissez) and the Ny-Ålesund weather station used to calculate local climate conditions. (C) Spatial relationship between the various Tibet soil sample sites and weather stations used to calculate local climate conditions (see Table 3.3).

3.3. Background

3.3.1. Carbonate formation in cold-climate soils and sub-glacial environments

Pedogenic carbonates are common in cold climates (Lacelle, 2007), and have been identified at high latitude in the Arctic (Swett, 1974; Bunting and Christensen, 1978; Forman and Miller, 1984; Mann et al., 1986; Marlin et al., 1993; Courty et al., 1994; Kabala and Zapart, 2012) and Antarctic (Tedrow and Ugolini, 1966; McCraw, 1967; Vogt and Corte, 1996; Campbell and Claridge, 1998; Foley, 2005), as well as at high elevation sites (Quade et al., 2007, 2011, 2013; Hoke et al., 2009; Burgener et al., 2016). In this study, we define a “cold climate” site as one having at least two consecutive months where mean monthly air or soil temperatures are less than or equal to 0 °C. Carbonates from such cold climates are considered ‘‘cryogenic” when their precipitation is driven by the freezing of a calcium bicarbonate soil solution, which increases ion concentrations in the residual solution and leads to $CaCO_3$ supersaturation

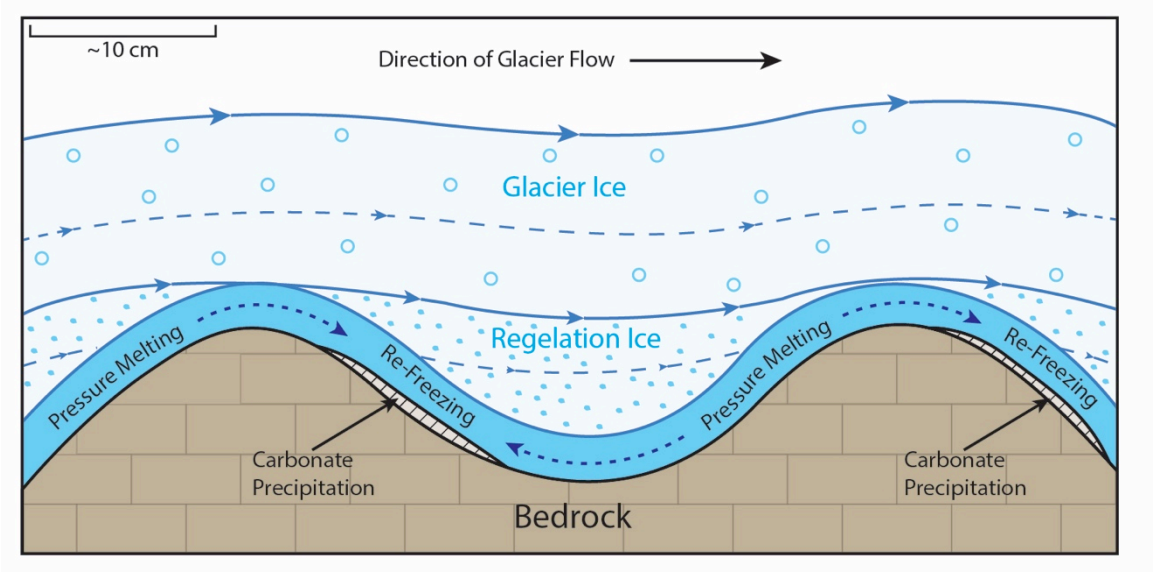

Figure 3.2. Schematic representation of carbonate precipitation in sub-glacial environments. Modified from Hanshaw and Hallet (1978).

(Hallet, 1976; Marlin et al., 1993; Courty et al., 1994; Vogt and Corte, 1996). Cryogenic soil carbonates typically form as pendants on the underside of coarse clasts embedded in the soil matrix. They form because carbonate-bearing soil water accumulates on the underside of clasts due to gravity and is retained there by surface tension; and subsequent freezing of the soil water leads to calcium carbonate supersaturation and carbonate precipitation (Courty et al., 1994). In addition to this cryogenic carbonate formation process, soil carbonate formation in cold climates can also occur via "normal" processes common in temperate and warm soils, involving supersaturation of a soil solution due to soil drying or CO_2 outgassing (see Breecker et al., 2009 for more detail). Unlike the cryogenic soil carbonates, these "normal" soil carbonates are thought to form under conditions of near-isotopic equilibrium, and may exhibit seasonal biases in their isotopic composition depending on individual soil characteristics (Breecker et al., 2009; Peters et al., 2013; Hough et al., 2014; Burgener et al., 2016; Ringham et al., 2016; Gallagher and Sheldon, 2016).

In contrast to pedogenic carbonates, which can potentially form in any soil that experiences suitable climate conditions, the occurrence of cryogenic sub-glacial carbonates is limited to areas of present or past glaciation. Subglacial carbonate precipitation is induced by pressure melting on the uphill (stoss) side of topographic bed obstacles, and subsequent refreezing on the downhill (lee) side of the obstacle (Hanshaw and Hallet, 1978; Souchez and Lemmens, 1985). As the water refreezes on the lee side of the obstacle, ions are excluded from the ice and concentrated in the remaining solution, until the solution reaches calcite supersaturation and calcite precipitation begins (Fig. 3.2); (Hallet, 1976; Hanshaw and Hallet, 1978; Souchez and Lemmens, 1985).

3.3.2. Non-equilibrium processes in cryogenic carbonates

There is an extensive body of literature investigating the various kinetic processes causing disequilibrium effects in carbonate clumped and conventional stable isotopic compositions (e.g., Clark and Lauriol, 1992; Zeebe and Wolfe-Gladrow, 2001; Watson, 2004; Ghosh et al., 2006; Dietzel et al., 2009; Guo, 2009; Lachniet, 2009; Watson and Müller, 2009; Dennis and Schrag, 2010; Tripati et al., 2010, 2015; Dae¨ron et al., 2011; DePaolo, 2011; Gabitov et al., 2012; Kluge and Affek, 2012; Saenger et al., 2012; Wang et al., 2013; Watkins et al., 2013, 2014; Affek et al., 2014; Affek and Zaarur, 2014; Kluge et al., 2014; Watkins and Hunt, 2015; Devriendt et al., 2017). The schematic diagram in Fig. 3.3 (modified after Tripati et al., 2015) summarizes the expected effects of the most relevant of these disequilibrium processes on carbonate Δ_{47}, $\delta^{18}O$, and $\delta^{13}C$ values. As discussed in the following sections, the primary disequilibrium processes associated with cryogenic carbonate formation are CO_2 degassing via bicarbonate dehydration, and pH-related effects.

3.3.2.1. CO_2 degassing via bicarbonate dehydration and dehydroxylation

Outgassing of CO_2 implies removal of dissolved inorganic carbon (DIC) from solution, and yet this process promotes calcium carbonate saturation by increasing the solution pH as well as the concentration of dissolved CO_3^{2-}. Degassing of CO_2 can proceed via two different reactions known as bicarbonate dehydration and dehydroxylation (Clark and Lauriol, 1992; Fairchild et al., 2007; Guo, 2009):

$$\text{Dehydration: } H^+ + HCO_3^-(aq) \rightarrow H_2CO_3 \rightarrow CO_2 + H_2O \quad (3.1)$$

$$\text{Dehydroxylation: } HCO_3^-(aq) \rightarrow CO_2 + OH^- \quad (3.2)$$

Bicarbonate dehydration is the dominant CO_2 degassing reaction at typical soil pH levels, and will thus be the focus of this discussion (Guo, 2009). Various studies have shown that kinetic isotope fractionations occur during bicarbonate dehydration (Marlier and O'Leary, 1984; Paneth and O'Leary, 1985; Clark and Lauriol, 1992; Zeebe and Wolfe-Gladrow, 2001; Guo, 2009; Affek and Zaarur, 2014; Tripati et al., 2015). Clark and Lauriol (1992) and Guo (2009) describe the following schematic reaction pathway between calcium carbonate and gaseous CO_2:

$$CaCO_3 \leftarrow Ca^{2+} + CO_3^{2-} \leftarrow CO_3^{2-} + H^+ \rightleftarrows HCO_3^- + H^+ \rightleftarrows H_2CO_3 \underset{kh}{\overset{kd}{\rightleftarrows}} H_2O + CO_{2(aq)} \rightleftarrows CO_{2(g)} \quad (3.3)$$

where the dotted arrows indicate reactions that are unimportant during rapid processes, and *kd* and *kh* are the rate constants for bicarbonate dehydration and hydration, respectively. When rehydration (*kh* in the above reaction) is insignificant, degassing of aqueous CO_2 to gaseous CO_2 is quantitative (e.g., all of the reactant is consumed) and non-fractionating (Clark and Lauriol, 1992). The precipitation reaction ($Ca^{2+} + CO_3^{2-} \rightarrow$

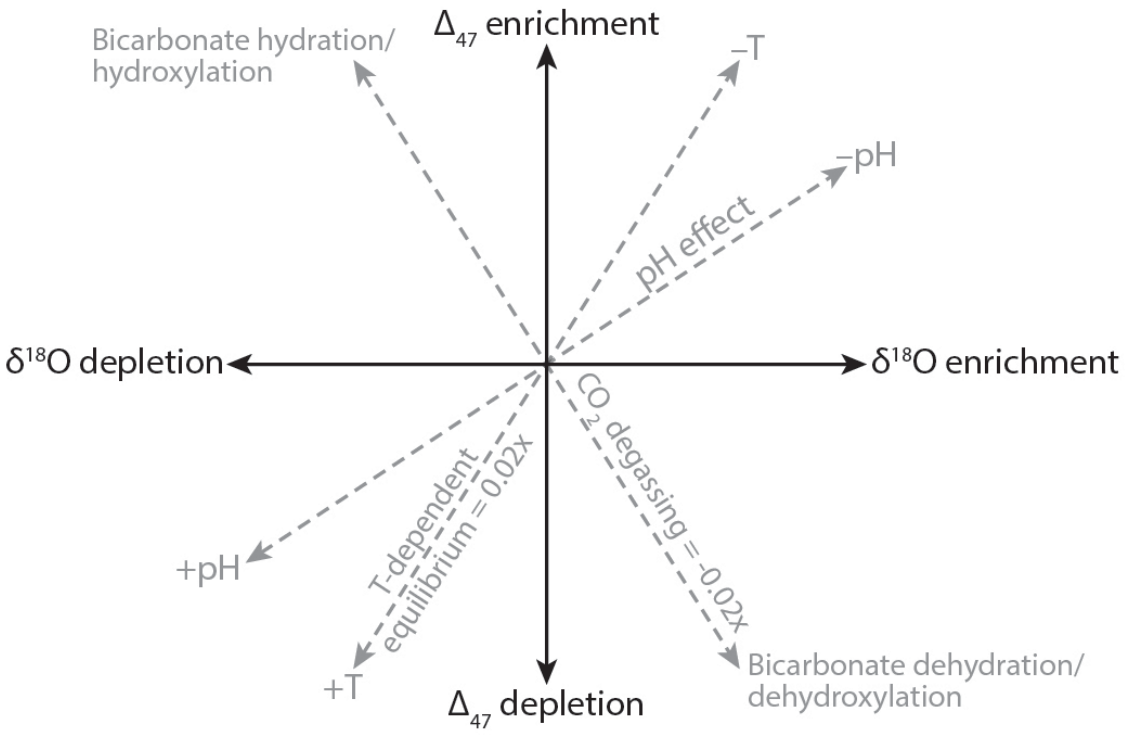

Figure 3.3. Schematic illustration of several carbonate equilibrium and disequilibrium fractionation processes and their effects on carbonate Δ_{47} and $\delta^{18}O$. +pH and –pH represent the isotopic effects of increasing or decreasing the pH of a bicarbonate solution, respectively. +T and –T show the isotopic effects of increasing or decreasing the temperature of a bicarbonate solution. Modified from Tripati et al. (2015).

$CaCO_3$) can give rise to small kinetic fractionations (<2‰; Watkins et al., 2014) that can partially offset the kinetic fractionations due to bicarbonate dehydration, but which are hereafter neglected due to their relatively small magnitude. Additionally, the equilibrium timescales for the various (de)protonation reactions (e.g., $CO_3^{2-} + H^+ \rightarrow HCO_3^-; HCO_3^- + H^+ \rightarrow H_2CO_3$) are several orders of magnitude lower (~10^{-7} s) than the bicarbonate dehydration reaction (~10 s) (Zeebe and Wolfe-Gladrow, 2001), making the decomposition of carbonic acid ($H_2CO_3 \rightarrow CO_2(aq) + H_2O$) the rate limiting step in the reaction pathway, and the control on kinetic isotope fractionations during bicarbonate dehydration. Both Clark and Lauriol (1992) and Guo (2009) found that CO_2 degassing and associated bicarbonate dehydration during the formation of cryogenic carbonate powders results in calcites enriched in ^{18}O and ^{13}C relative to the expected equilibrium

isotope composition. Affek and Zaarur (2014) and Tripati et al. (2015) confirmed these findings and showed that bicarbonate dehydration also leads to lower calcite Δ_{47} values (high apparent carbonate formation temperatures) relative to the expected equilibrium Δ_{47} value. Burgener et al. (2016) hypothesized that this bicarbonate dehydration process was responsible for the hotter-than-expected apparent soil carbonate formation temperatures (low Δ_{47} values), and high $\delta^{18}O$ and $\delta^{13}C$ composition in soil carbonates collected at a cold (mean annual soil temperature ~1 °C), high elevation (4700 m) site in north-central Chile.

As shown in the schematic reaction Eq. (3.3), enrichment in carbonate ^{18}O and ^{13}C values and decreases in Δ_{47} values are due to kinetic isotope fractionations associated with the decomposition of carbonic acid during CO_2 degassing and bicarbonate dehydration. With respect to carbonate ^{18}O and ^{13}C, enrichment occurs because ^{12}C–O and C–^{16}O bonds are preferentially broken over ^{13}C–O and C–^{18}O bonds during H_2CO_3 decomposition, resulting in lower $\delta^{18}O$ and $\delta^{13}C$ values for the CO_2 gas and higher $\delta^{18}O$ and $\delta^{13}C$ values for the residual HCO_3^- pool (Clark and Lauriol, 1992). The high $\delta^{18}O$ and $\delta^{13}C$ DIC composition is then inherited by the precipitating calcite. The decrease in Δ_{47} values (reflecting depletion in the abundance of calcite CO_3^{2-} groups containing both ^{13}C and ^{18}O) occurs because degassing CO_2 from a bicarbonate solution acts as a non-linear, "reverse" mixing reaction (Eiler and Schauble, 2004). In a forward mixing reaction, if two populations of CO_2 (or HCO_3^-) with identical Δ_{47} compositions but unique $\delta^{13}C$ and $\delta^{18}O$ compositions are mixed together, the resulting mixed population will have a new Δ_{47} composition that is a non-linear combination of the two end-member populations (Defliese and Lohmann, 2015). In contrast, the separation of a carbon pool (the degassed

CO_2) with a distinct bulk $\delta^{18}O$ and $\delta^{13}C$ composition from the original carbon reservoir (the initial DIC pool) is essentially the reverse of the "forward" mixing reactions described by Eiler and Schauble (2004), and results in a final carbon pool (the remnant DIC pool) with a new bulk isotope composition and a Δ_{47} composition that is not a linear (e.g., mass balanced) product of the separated carbon pool and original reservoir (Guo, 2009). Guo (2009) modeled the kinetic isotope fractionations associated with bicarbonate dehydration, and predicted that at 0 °C, for every 1‰ increase in calcite $\delta^{18}O$, there should be a corresponding 1.1–3.2‰ increase in $\delta^{13}C$ and a 0.02–0.027‰ decrease in Δ_{47}. In contrast, empirical data from cryogenic carbonate powders collected from several caves in northwestern Germany show a 0.005 ± 0.003‰ decrease in Δ_{47} for every 1‰ increase in calcite $\delta^{18}O$ (Kluge et al., 2014), suggesting that either the Guo (2009) kinetic fractionation model is not completely correct, or that there may be some variability in the relationship between $\delta^{18}O$ enrichment and Δ_{47} depletion in natural carbonates.

3.3.2.2. pH effect

The equilibrium oxygen and clumped isotope composition of a carbonate is expected to be independent of pH; however under disequilibrium conditions pH affects the oxygen and clumped isotope composition of precipitating calcite (Hill et al., 2014; Watkins et al., 2014). The pH of a carbonate solution controls the relative abundance of the various DIC species (CO_2(aq), CO_3^{2-}, HCO_3^-) and each of these DIC species has a distinct equilibrium clumped and stable isotope composition (Usdowski and Hoefs, 1993; Zeebe, 1999, 2007; Beck et al., 2005; Tripati et al., 2010; Hill et al., 2014; Tripati et al., 2015). At a given pH, the isotopic composition of the DIC pool will be the weighted sum of the various DIC species. For calcite grown slowly, under near equilibrium conditions,

the oxygen isotope fractionation between calcite and water is independent of the oxygen isotope composition of the DIC pool. Additionally, slowly forming carbonate has time to reach a state of bulk isotopic equilibrium (e.g., isotopic equilibrium between the crystal surface boundary layer and interior crystal lattice), leading to a Δ_{47} value that depends only on the temperature of the formation water (Watson and Müller, 2009; Tripati et al., 2010; Hill et al., 2014). However, if carbonate precipitation occurs at a sufficiently high rate, the carbonate mineral will incorporate the Δ_{47} signature of the DIC pool (Hill et al., 2014). Under such rapid growth conditions, higher pH values will lead to lower ^{18}O and Δ_{47} values compared to the expected equilibrium calcite composition (Fig. 3.3; Tripati et al., 2010, 2015; Hill et al., 2014; Watkins et al., 2014; Watkins and Hunt, 2015).

Due to the temperature dependence of the equilibration rates between the DIC pool and water (with respect to oxygen isotopes) and the DIC pool and precipitating calcite (with respect to carbon isotopes), carbonates forming in cold environments are thought to be more susceptible to KIEs (Clark and Lauriol, 1992; Tripati et al., 2010). The time required for the DIC pool to reach isotopic equilibrium for both ^{13}C and ^{18}O is much longer at 0 °C than at 25 °C. For ^{13}C, the DIC equilibration time is approximately 24 s at 25 °C, and 440 s at 0 °C (Zeebe et al., 1999; Clark and Lauriol, 1992). The DIC equilibration times for ^{18}O are much slower, in the range of ~1 to 9 h at 25 °C, and ~6 to 150 h at 0 °C over the normal range of soil pHs (Uchikawa and Zeebe, 2012). Based on these considerations, Tripati et al. (2010) suggested that disequilibrium processes like bicarbonate dehydration are more likely to produce isotopic disequilibrium in carbonates forming in cold environments than in temperate environments, because at cold

temperatures (e.g., near freezing) carbonate precipitation may proceed more rapidly than isotopic equilibration in the DIC pool (see also Clark and Lauriol, 1992).

By sampling modern/Holocene soil carbonates from cold environments at high latitude and elevation, as well as sub-glacial carbonates, we explore potential disequilibrium processes during cryogenic carbonate formation, and investigate how varying soil environment characteristics (e.g., soil moisture, sediment grain size, etc.) affect the magnitude of any observed KIE.

3.4. Methods

We collected cold-environment soil carbonates from the Dry Valleys, Antarctica; Svalbard, Norway, in the High Arctic; the Chilean and Argentinian Andes; and Tibetan plateau, China; as well as sub-glacial carbonates from Montana, USA and British Colombia, Canada (Table 3.1). Sample analyses included Δ_{47}, $\delta^{18}O$, and $\delta^{13}C$ measurements of soil and sub-glacial carbonate, and XRD to determine mineralogy for select samples suspected of dolomite contamination. Context was established for the sample data using meteorological data and in-situ measurements of soil and sub-glacial conditions, as described in the following section.

3.4.1. Field methods and sampling procedures

Soil carbonate samples were collected from sixteen Early Holocene to recent sites representing a range of cold climate soils and two sub-glacial sites (Table 3.1) by different research groups using similar sampling methods at each soil site. In order to ensure that the sampled carbonates had formed in situ, care was taken at each soil site to collect only carbonate pendants that were found on the underside of in situ clasts (e.g.,

Burgener et al., 2016). Sampling methods and meteorological data for each site are described in the following paragraphs and summarized in Table 3.2.

The quality of soil temperature, soil moisture, and water $\delta^{18}O$ estimates varies from site to site due to a variety of factors, including the type of water sample collected, the distance between the meteorological stations and our soil sampling sites, and the temporal resolution of the dataset. For example, the meteoric water $\delta^{18}O$ data for the Svalbard sites comes from a Global Network of Isotopes in Precipitation (GNIP) station

Table 3.1. Sample location and environmental conditions.

Sample Name	Study Site	Latitude (° N)	Longitude (° E)	Elevation (m)	Depth in Soil (cm)	Age	Environment	Sample Source	Data Source	
									Clumped Isotopes	*Stable Isotopes*
Soil Carbonates										
Elq13-4700-20	Elqui Valley, Chile	-30.177	-69.829	4700	20	345±30[b]	High Elevation Desert	Burgener et al., 2016	Burgener et al., 2016[a]	Burgener et al., 2016
Elq13-4700-40	Elqui Valley, Chile	-30.177	-69.829	4700	40	345±30[b]	High Elevation Desert	Burgener et al., 2016	Burgener et al., 2016[a]	Burgener et al., 2016
Elq13-4700-60	Elqui Valley, Chile	-30.177	-69.829	4700	60	345±30[b]	High Elevation Desert	Burgener et al., 2016	Burgener et al., 2016[a]	Burgener et al., 2016
Elq13-4700-80	Elqui Valley, Chile	-30.177	-69.829	4700	80	345±30[b]	High Elevation Desert	Burgener et al., 2016	Burgener et al., 2016[a]	Burgener et al., 2016
Elq13-4700-100	Elqui Valley, Chile	-30.177	-69.829	4700	100	345±30[bc]	High Elevation Desert	Burgener et al., 2016	Burgener et al., 2016[a]	Burgener et al., 2016
Elq13-4500-50	Elqui Valley, Chile	-30.138	-69.830	4500	50	NA	High Elevation Desert	Burgener et al., 2016	Burgener et al., 2016[a]	Burgener et al., 2016
Elq13-4200-50	Elqui Valley, Chile	-30.164	-69.862	4200	50	9663±40[b]	High Elevation Desert	Burgener et al., 2016	Burgener et al., 2016[a]	Burgener et al., 2016
Elq13-3750-50	Elqui Valley, Chile	-30.206	-69.916	3750	50	2336±30[b]	High Elevation Desert	Burgener et al., 2016	Burgener et al., 2016[a]	Burgener et al., 2016
Elq13-3550-20	Elqui Valley, Chile	-30.262	-69.942	3550	20	5,780±30[bc]	High Elevation Desert	Burgener et al., 2016	Burgener et al., 2016[a]	Burgener et al., 2016
Peters-B15	Río Mendoza Valley, Argentina	-32.812	-70.064	3200	15	Holocene	Arid	Peters et al., 2013	Peters et al., 2013	Peters et al., 2013
Peters-B30	Río Mendoza Valley, Argentina	-32.812	-70.064	3200	30	Holocene	Arid	Peters et al., 2013	Peters et al., 2013	Peters et al., 2013
Peters-B45	Río Mendoza Valley, Argentina	-32.812	-70.064	3200	45	Holocene	Arid	Peters et al., 2013	Peters et al., 2013	Peters et al., 2013
Ant-1	Scott Base, Antarctica	-77.849	166.768	<10	surface	<12,000	Polar Desert	This Study	This Study	This Study
Ant-2	Victoria Valley, Antarctica	-77.377	161.814	361	surface	<12,000	Polar Desert	This Study	This Study	This Study
Ant-3	Victoria Valley, Antarctica	-77.377	161.814	361	surface	<12,000	Polar Desert	This Study	This Study	This Study
Ant-4	Victoria Valley, Antarctica	-77.377	161.814	361	surface	<12,000	Polar Desert	This Study	This Study	This Study

[a] Δ_{47} values recalculated using Brand et al. (2010) parameters, following Däeron et al., 2016 and Schauer et al., 2016

[b] Radiocarbon age (BP)

[c] Measured on a separate soil carbonate sample from the same soil profile

[d] Age estimated from Gile et al., 1966 definition of Stage I, II, and III soil carbonates

Table 3.1. Cont'd.

Sample Name	Study Site	Latitude (° N)	Longitude (° E)	Elevation (m)	Depth in Soil (cm)	Age	Environment	Sample Source	Data Source	
									Clumped Isotopes	*Stable Isotopes*
Soil Carbonates										
Tsangpo-19	Tibet	30.418	82.767	4800	110	Early Holocene to Latest Pleistocene[d]	Semi-Arid	Quade et al., 2011	This Study	This Study
Tsangpo-21a	Tibet	29.204	88.309	4016	60	Early Holocene to Latest Pleistocene[d]	Semi-Arid	Quade et al., 2011	This Study	This Study
Tsangpo-21b	Tibet	29.204	88.309	4016	60	Early Holocene to Latest Pleistocene[d]	Semi-Arid	Quade et al., 2011	This Study	This Study
Tsangpo-22	Tibet (near Shigatse)	29.317	88.942	3876	55	<5000[d]	Semi-Arid	Quade et al., 2011	This Study	This Study
Lhasa-4	Tibet (near Lhasa)	29.636	91.292	3809	60	Early Holocene to Latest Pleistocene[d]	Semi-Arid	Quade et al., 2011	This Study	This Study
Cannes-62	Cannes, Spitsbergen, Svalbard	78.937	11.455	60	62	11,750±430[b]	Polar Desert	Courty et al., 1994; Mann et al., 1986	This Study	This Study
KG-201a	Arrigetch, Spitsbergen, Svalbard	79.010	11.982	<10	unknown	9440±360 to 10,000±170[b]	Vegetated	Courty et al., 1994; Mann et al., 1986	This Study	This Study
KG-201b	Arrigetch, Spitsbergen, Svalbard	79.010	11.982	<10	unknown	9440±360 to 10,000±170[b]	Vegetated	Courty et al., 1994; Mann et al., 1986	This Study	This Study
Sub-Glacial Carbonates										
CG-1	Castleguard Glacier, British Columbia	52.080	-117.269	2100	-	NA	Sub-Glacial	This Study	This Study	This Study
CG-2	Castleguard Glacier, British Columbia	52.080	-117.269	2100	-	NA	Sub-Glacial	This Study	This Study	This Study
BF-1	Blackfoot Glacier, Montana	48.605	-113.662	2000	-	NA	Sub-Glacial	Hanshaw and Hallet, 1978	This Study	This Study
BF-2	Blackfoot Glacier, Montana	48.605	-113.662	2000	-	NA	Sub-Glacial	Hanshaw and Hallet, 1978	This Study	This Study
BF-3	Blackfoot Glacier, Montana	48.605	-113.662	2000	-	NA	Sub-Glacial	Hanshaw and Hallet, 1978	This Study	This Study

[a] Δ_{47} values recalculated using Brand et al. (2010) parameters, following Däeron et al., 2016 and Schauer et al., 2016
[b] Radiocarbon age (BP)
[c] Measured on a separate soil carbonate sample from the same soil profile
[d] Age estimated from Gile et al., 1966 definition of Stage I, II, and III soil carbonates

with nearly continuous measurements from 1990 to 2015, but the station (World Meteorological Organization [WMO] code: 100400) is located several kilometers away from the sample sites. In contrast, water $\delta^{18}O$ data for the Tsangpo-19 site was collected at the sample site, but comes from a limited number of individual samples collected by hand from local streams and snowpack.

At the two Antarctic soil sites, soil carbonate pendants were collected in 2015 as samples of opportunity from surficial, non-carbonate clasts. Scott Base soils are characterized by a weakly weathered, angular basaltic ash matrix dominated by gravel- to sand-sized particles, while soils in Victoria Valley are composed of weakly weathered sand and gravel that are ice-cemented below 40 cm, and capped by a 2 cm-thick, desert pavement (Hagedorn et al., 2010; see Supplementary Information Section 2). Snow, ice, and water samples were collected from Victoria Valley and their isotopic values analyzed as part of an earlier study (see Hagedorn et al., 2010, Section 2).

For the Chilean and Argentinian Andes samples, soil carbonate pendants and local snow, rain, and stream water samples were collected between 2009 and 2013 near the international border between Chile and Argentina (Peters et al., 2013; Burgener et al. (2016)). The Chilean samples include carbonates collected at 20, 40, 60, 80, and 100 cm depths at 4700 masl, samples collected at 50 cm depths for the 3750, 4200, and 4500 masl profiles, and a sample collected 20 cm below the ground surface from the 3550 masl profile (see Burgener et al. (2016), Section 3). For the Argentinian samples collected by Peters et al. (2013), only the upper 50 cm of the 3200 masl soil site experiences at least two consecutive months of sub-zero temperatures; thus, only the three samples collected between 15 and 45 cm depth are included in this study (see Peters et al. (2013), Section

Table 3.2. Temperature, $\delta^{18}O$, and Δ_{47} assumptions for each sample site.

Study Sites	Expected Carbonate Precipitation Temperatures (°C)[a]			Temperature Type	References	Expected Surface Water $\delta^{18}O$ (VSMOW)		References	Expected Equilibrium Carbonate Δ_{47} value (‰)[h]		
	Min	*MST*	*WMMT*			*Min*	*Max*		*-1 °C*	*MST*	*WMMT*
Elqui Valley, Chile 4700 m (10 cm)	-1	9	10	Soil	Burgener et al., 2016	-20	-15	Burgener et al., 2016	0.7336	0.6325	0.6289
Elqui Valley, Chile 4700 m (50 cm)	-1	7	9	Soil	Burgener et al., 2016	-20	-15	Burgener et al., 2016	0.7336	0.6398	0.6325
Elqui Valley, Chile 4500 m (50 cm)	-1	9	11	Soil	Burgener et al., 2016[b]	-20	-15	Burgener et al., 2016	0.7336	0.6325	0.6254
Elqui Valley, Chile 4200 m (50 cm)	-1	11	13	Soil	Burgener et al., 2016[b]	-17	-15	Burgener et al., 2016	0.7336	0.6254	0.6184
Elqui Valley, Chile 3750 m (50 cm)	-1	14	16	Soil	Burgener et al., 2016[b]	-16	-14	Burgener et al., 2016	0.7336	0.6150	0.6082
Elqui Valley, Chile 3550 m (10 cm)	-1	16	16	Soil	Burgener et al., 2016	-15	-12	Burgener et al., 2016	0.7336	0.6082	0.6082
Las Cuevas, Río Mendoza Valley, Argentina (10 cm)	-1	15	17	Soil	Peters et al., 2013[c]	-17	-9	Hoke et al., 2009	0.7828	0.7033	0.6938
Las Cuevas, Río Mendoza Valley, Argentina (30 cm)	-1	14	17	Soil	Peters et al., 2013[c]	-17	-9	Hoke et al., 2009	0.7828	0.7082	0.6938
Las Cuevas, Río Mendoza Valley, Argentina (50 cm)	-1	14	16	Soil	Peters et al., 2013[c]	-17	-9	Hoke et al., 2009	0.7828	0.7082	0.6985
Scott Base, Antarctica	-1	-1	2	Soil	NRCS Weather Station[d]	-33	-29	Hagedorn et al., 2010	0.7336	0.6705	0.6586
Victoria Valley, Antarctica	-1	0	3	Soil	NRCS Weather Station[d]	-33	-29	Hagedorn et al., 2010	0.7336	0.6665	0.6548

Table 3.2. Cont'd.

Study Sites	Expected Carbonate Precipitation Temperatures (°C)[a]			Temperature Type	References	Expected Surface Water $\delta^{18}O$ (VSMOW)		References	Expected Equilibrium Carbonate Δ_{47} value (‰)[h]		
	Min	*MST*	*WMMT*			*Min*	*Max*		*-1 °C*	*MST*	*WMMT*
Svalbard	-1	3	5	Soil	Mann et al., 1986; GTNP data repository[e]	-14	-8	GNIP[g]	0.7336	0.6548	0.6472
Lhasa, Tibet	-1	18	19	Air	Quade et al., 2013; ISD repository[f]	-14	-12	GNIP[g]	0.7336	0.6016	0.5983
Tsangpo Site 19, Tibet	-1	13	15	Air	Quade et al., 2013; ISD repository[f]	-17	-15	Quade et al., 2011	0.7336	0.6184	0.6116
Tsangpo Site 21, Tibet	-1	15	15	Air	ISD repository[f]	-19	-16	Quade et al., 2011	0.7336	0.6116	0.6116
Tsangpo Site 22, Tibet	-1	15	15	Air	ISD repository[f]	-18	-17	Quade et al., 2011	0.7336	0.6116	0.6116
Castleguard Glacier	-1	0	0	Meltwater	This Study	-20	-19	Hitchon and Krouse, 1972	0.7336	0.6665	0.6665
Blackfoot Glacier	-1	0	0	Meltwater	Hanshaw and Hallet, 1978	-15	-14	Hanshaw and Hallet, 1978	0.7336	0.6665	0.6665

a - Except where indicated, carbonate precipitation temperatures are calculated for -1 °C (minimum possible precipitation temperature), mean summer temperature (MST), and warmest mean monthly soil or air temperature (WMMT).

b - Soil temperatures interpolated from Burgener et al. (2016) 4700 and 3550 masl station data.

c - 30 cm soil temperature interpolated fromPeters et al. (2013) 10 and 50 cm data.

d - Data from USDA Natural Resources Conservation Services Program weatherstations

e - Data from the Global Terrestrial Network for Permafrost database (http://www.gtnpdatabase.org)

f - Data from the Integrated Surface Database repository (ftp://ftp.ncdc.noaa.gov/pub/data/noaa/)

g - Global Network of Isotopes in Precipitation (GNIP), Lhasa Station (http://www-naweb.iaea.org/napc/ih/IHS_resources_gnip.html)

h - All samples but Peters et al. (2013) samples calculated using Kelson et al. (2017) T-Δ_{47} calibration and the expected carbonate precipitation temperatures at each site. Peters et al. (2013) samples calculated using Ghosh et al. (2006) T-Δ47 calibration.

3.1). For both the Chilean and Argentinian samples, carbonate pendants on non-carbonate clasts were collected every 20 cm from the soil surface down to 1 m depth. The Chilean 4700 masl sample site is completely devoid of vegetation and is located less than 100 m from two small, perennial ice fields. The upper 100 cm of the local soil is composed of unconsolidated clasts with a mean diameter of ~3 cm (Burgener et al., 2016). In contrast, the 3550, 3750, 4200, and 4500 masl soil pits are located along small, upper tributaries of the Elqui River, and are composed of a consolidated, clast-supported conglomerate with a sandy inter-cobble soil matrix. The Argentinian 3200 masl soil was covered with relatively abundant vegetation and composed of much more fine-grained sediments (predominantly silt with thin mud and fine sand horizons). Both the Chilean and Argentinian samples were previously analyzed and their clumped and stable isotope compositions reported by Burgener et al. (2016) and Peters et al. (2013), respectively. The Burgener et al. (2016) samples were not re-analyzed for this study, but their Δ_{47} values were re-calculated using the ^{17}O correction parameters of Brand et al. (2010), following the recommendations of Daëron et al. (2016) and Schauer et al. (2016), and the T(Δ_{47}) values were recalculated using the T-Δ_{47} calibration of Kelson et al. (2017) (see Section 4.3). Due to a lack of material from the 3200 masl site, the Peters et al. (2013) samples could not be reanalyzed. Additionally, because these samples were analyzed at a different laboratory (Caltech) using older methods and T-Δ_{47} calibrations, their Δ_{47} and T(Δ_{47}) values could not be recalculated using modern methods. However, material collected at a lower elevation site in the Río Mendoza Valley was reanalyzed using the methods described in Section 3.4 of this paper and yielded similar results to the original Peters et al. (2013) values, suggesting that the Δ_{47}, $\delta^{18}O$, and $\delta^{13}C$ values of the

Argentinian Andes samples are directly comparable to the new results reported in this study.

Quade et al. (2011, 2013) collected soil carbonate pendants and water, snow, and ice samples from multiple locations across the southern Tibetan Plateau (Fig. 3.1C). The carbonate pendant samples re-analyzed in this study were collected at a variety of depths from three soil profiles along the Yarlung Tsangpo valley, and from one soil profile near Lhasa, Tibet (Table 3.1). The Tsangpo soils are characterized by significant loess deposits that either overlie or are incorporated into the soils. Minor gravels are common, but the soil is dominated by silt to sand-sized particles. The parent material for the Tsangpo-21 soil profile is calcareous sandstone and moderately calcareous siltstone; the parent material at the other three Tsangpo sites is non-calcareous. The uppermost horizon of the Lhasa soil is a ~0.75 m thick angular conglomerate that overlies a 1.5 m loess deposit. Clumped isotope analyses were conducted on some of these samples at the California Institute of Technology using early methodologies (Quade et al., 2011, 2013); to ensure consistency with the other datasets in this study, we reanalyzed the samples following the methods described in Section 3.3.

For the High Arctic samples, soil carbonate pendants were collected in the mid-1980s from two sites at Cannes and Kapp Guissez, near Ny-Alesund, Svalbard, Norway (Fig. 3.1B). The Cannes soil is characterized by a “polar desert” environment with less than 10% plant cover, while the Kapp Guissez soil site is characterized by 100% plant cover (Mann et al., 1986). The Cannes polar desert soil exhibits a well-developed, coarsening-upwards desert pavement composed of angular pebbles and pedogenic silt accumulations, which overlies a weakly developed A horizon and a Bk horizon

characterized by dolomitic silt accumulation and calcite pendants on the undersides of rocky clasts (Mann et al., 1986). In contrast, the vegetated Kapp Guissez soils are characterized by a lack of a desert pavement, and a well-developed O or A horizon overlying a Bk horizon with much thinner silt accumulations (Mann et al., 1986). The pendant samples from the Cannes site formed on dolomitic clasts, while the sample from Kapp Guissez formed on a non-carbonate igneous cobble. Due to the high concentration of dolomitic sediment in the Cannes profile (Mann et al., 1986), the mineral composition of the Cannes samples was determined by x-ray diffraction (XRD).

The sub-glacial carbonates analyzed in this study were collected at two sites: (1) Blackfoot Glacier, located in Glacier National Park in northwest Montana, and (2) Castleguard Glacier, in the Columbia Icefield ~160 km northwest of Banff, Alberta. Hanshaw and Hallet (1978) collected sub-glacial carbonate samples for stable oxygen and carbon isotope analysis from the surface of carbonaceous bedrock that had been recently exposed by the retreat of the Blackfoot Glacier in northwest Montana, USA, as well as meltwater and ice samples. The carbonate samples were reanalyzed for this study to determine their $\delta^{18}O$, $\delta^{13}C$, and Δ_{47} compositions. Samples from similar bedrock exposures at Castleguard Glacier, British Columbia, Canada were collected by the same researchers following the same methods, and the $\delta^{18}O$, $\delta^{13}C$, and Δ_{47} values for these samples are reported here for the first time. Details regarding the sources of weather station air and soil monitoring data and meteoric water $\delta^{18}O$ values are described in the online Supplementary Information.

3.4.2. X-Ray diffraction methods

The soil carbonate pendant samples from the Arctic Cannes site in Svalbard formed on the underside of dolomitic clasts (Mann et al., 1986). To assess whether detrital carbonate that had been incorporated into the pedogenic pendant was inadvertently sampled, the mineral composition of the carbonate pendant sample was determined via x-ray diffraction at the University of Washington's Materials Science and Engineering User Facility in the Department of Materials Science and Engineering. X-ray diffraction patterns were acquired using a Bruker D8 Focus Bragg-Brentano powder diffractometer with a scintillator type detector and nickel filter, operating at 40 kV and 40 mA with a Cu-Ka radiation source of 1.54A°. Scan data were collected between 20 and 90° 2θ with a 0.02° step size.

3.4.3. Clumped and stable isotope analysis laboratory methods

Clumped isotope analyses ($\delta^{18}O$, $\delta^{13}C$ and Δ_{47}) were conducted at the University of Washington's IsoLab following the methods of Burgener et al. (2016) and Kelson et al. (2017). In summary, 6–8 mg of each carbonate sample was digested in a common bath of phosphoric acid held at 90 °C and with an initial specific gravity of 1.904–1.970 g cm^3. The evolved CO_2 was cryogenically separated from water on an automated stainless steel and nickel vacuum line using an ethanol-dry ice slush trap, isolated in a liquid N_2 trap, and passed through a Porapaq Q trap using He as the carrier gas. Every 4–5 carbonate sample unknowns, a carbonate standard (intralaboratory standards: C64, C2, Coral; and interlaboratory standards ETH1, ETH2, ETH3 and ETH4; mean $\delta^{18}O$, $\delta^{13}C$ and Δ_{47} values for these standards are reported in Supplementary Table B1) was purified on the vacuum line and transferred into a Pyrex break seal. Sample and standard break

seals were then loaded into an automated 10-port tube cracker inlet system on a Thermo MAT 253 configured to measure m/z 44–49 inclusive.

Δ_{47}, $\delta^{13}C$, and $\delta^{18}O$ values were calculated for all samples following the methods of Huntington et al. (2009) with updated methods for (1) pressure baseline (PBL) measurement (He et al., 2012); (2) $\delta^{13}C$ value correction for ^{17}O interference using the parameters described in Brand et al. (2010), following the methods of Daëron et al. (2016) and Schauer et al. (2016); and (3) Δ_{47} correction to the Absolute Reference Frame (ARF) using heated gas and CO_2-water equilibration lines constructed during the corresponding analysis period (Dennis et al., 2011). Scripts for these calculations are provided by Schauer et al. (2016). $\delta^{13}C$ was referenced to the international standards NBS-19 and LSVEC, and $\delta^{18}O$ was referenced to NBS-18 and NBS-19. Samples with Δ_{48} values higher than 2‰, indicating contamination, were rejected. Following Ross (2003) and Zaarur et al. (2013), the Pierce outlier test was used to identify and remove statistical outliers (n = 4) in the Δ_{47}, $\delta^{18}O$, and $\delta^{13}C$ values for each of the samples.

3.4.4. Calculating Δ_{47}, $\delta_{18}O$, and $\delta^{13}C$ anomalies

We use the following methods to compare Δ_{47}, $\delta^{18}O$, and $\delta^{13}C$ observations to expected values for the environments of sample carbonate formation. For the purposes of this study we define the Δ_{47}, and $\delta^{18}O$ anomalies as the observed carbonate Δ_{47} and $\delta^{18}O$ values minus the expected equilibrium carbonate Δ_{47} and $\delta^{18}O$ values. Using this calculation, negative Δ_{47} and $\delta^{18}O$ anomalies show isotopic depletion with respect to the expected equilibrium carbonate composition, while positive anomalies show isotopic enrichment. In contrast to the Δ_{47} and $\delta^{18}O$ anomalies, exact $\delta^{13}C$ anomalies are difficult to calculate due to the lack of direct isotopic measurements of soil CO_2 at our study sites.

Instead, we compare the soil carbonate $\delta^{13}C$ values to the expected range of soil CO_2 $\delta^{13}C$ compositions.

Expected equilibrium carbonate Δ_{47} compositions are calculated for different temperatures selected to characterize the likely range of expected carbonate formation temperatures at each site. The minimum expected temperature of carbonate formation for all sites is taken to be –1 °C because carbonate precipitation requires the presence of liquid water, but high salinity solutions such as may be found in sub-glacial environments or hyper-arid soils can have a depressed freezing point. At the sub-glacial sites, the maximum carbonate formation temperature is assumed to be 0 °C. For soil carbonates, the warmest mean monthly air or soil temperature (WMMT or WMMST, respectively) is taken to characterize the maximum likely temperature of carbonate formation, and expected equilibrium carbonate Δ_{47} compositions are also calculated for local mean summer air or soil temperatures (MST or MSST, respectively). Local WMMT/WMMST and MST/MSST are calculated at each site from available meteorological records (see Table 3.2). Expected temperatures, expected equilibrium carbonate Δ_{47} compositions corresponding to these assumed formation temperatures are calculated using Eq. (1) in Kelson et al. (2017):

$$\Delta_{47} = 0.0417 \pm 0.0013 \times \frac{10^6}{T^2} + 0.139 \pm 0.014 \quad (3.4)$$

where T is the carbonate formation temperature in Kelvin. The expected equilibrium carbonate Δ_{47} compositions are calculated using the Kelson T-Δ_{47} calibration. This calibration is most appropriate for our samples because the methodologies of Kelson et al. (2017) are the same as this study (90 °C acid digestion, purification apparatus, mass spectrometry including pressure baseline measurements, use of updated ^{17}O correction

parameters, etc.). The Kelson T-D47 calibration is based on a larger sample size (n = 56) than previously published T-Δ_{47} calibrations, and is not different from other published calibration data that have been calculated using the updated ^{17}O correction (Kelson et al., 2017).

Expected equilibrium carbonate $\delta^{18}O$ values are calculated from local minimum and maximum expected carbonate formation temperatures (as described above) and local meteoric water $\delta^{18}O$ values using the temperature dependent calcite-water oxygen isotope fractionation factor, as defined in Watkins et al. (2014):

$$\Delta O_{c-w}^{eq} = \frac{17747}{T_K} - 29.777 \quad (3.5)$$

where ΔO_{c-w}^{eq} is equal to the per mil fractionation of oxygen isotopes between water and calcite (equal to $1000 \times \ln(\alpha)$), and T_K is the carbonate formation temperature in Kelvin.

Despite the lack of soil CO_2 $\delta^{13}C$ measurements, general constraints can be placed on expected equilibrium soil carbonate $\delta^{13}C$ values based on the $\delta^{13}C$ composition of the two reservoirs that contribute carbon to soil carbonates: soil CO_2 and atmospheric CO_2. Atmospheric CO_2 is assumed to have ranged between –6.5 (pre-industrial) and –8.5‰ (modern). Soil CO_2 $\delta^{13}C$ is largely determined by the abundance of C3 and C4 plants in the local environment (Cerling and Quade, 1993). The mean CO_2 value of C3 plants (–28.5‰) is more negative than that of C4 plants (–12‰), and thus acts as the lower bound to the expected range of soil CO_2 values (Cerling and Quade, 1993; Kohn, 2010). Because C3 plants are favored in colder, arid to sub-arid environments (Still et al., 2003), we assume that the mean CO_2 value of C3 plants is a reasonable lower bound for expected equilibrium carbonate $\delta^{13}C$ values. To estimate the $\delta^{13}C$ offset from equilibrium

(e.g., the approximate $\delta^{13}C$ anomaly) for our samples, we calculated the equilibrium carbonate $\delta^{13}C$ value at carbonate formation temperatures ranging from 0 to 30 °C using the atmospheric and soil CO_2 $\delta^{13}C$ values described above, and the temperature dependent ^{13}C equilibrium fractionation factors for $CO_2(g) - HCO_3^-$ (Mook et al., 1974), $CO_2(aq) - HCO_3^-$ (Mook et al., 1974), and $CO_2(g)$ – *calcite* (Bottinga, 1968), as summarized in Watkins and Hunt (2015), Table 1. Our measured carbonate $\delta^{13}C$ values are then plotted against this range of expected equilibrium carbonate $\delta^{13}C$ values in order to explore the general relationship between measured and expected values.

3.5. Results

3.5.1. Local climate and meteoric water $\delta^{18}O$

3.5.1.1. Scott base and Victoria Valley, Antarctica

At both Antarctic sites, seasonal soil temperature at depth varies significantly, driven by the annual cycle in air temperature (Table 3.3, Supplementary Information, and Supplementary Figure B1). At Scott Base, from 1999 to 2015 (excluding 2008, for which data was not available), MSST at 50 cm depth is –4 °C, and WMMST at the same depth is –2 °C. Near the surface (1 cm depth), MSST at Scott Base is +2 °C. At Victoria Valley, 50 cm MSST from 1999 to 2015 averages –7 °C, and WMMST is –5 °C. MSST at 7 cm depth is –1 °C. The weather station at Victoria Valley weather station failed to record accurate mean annual air temperatures between 1999 and 2015, but did record soil temperatures. Unlike the other soil sites, the samples collected at Scott Base and Victoria Valley were collected from the surface, so the 1 cm (Scott Base) and 7 cm (Victoria

Valley) MSST and WMMST values are used to calculate the Δ_{47}, $\delta^{18}O$ anomalies, rather than the 50 cm temperatures.

Soil moisture is extremely low at both Antarctic sites (Supplementary Figure B1, Table 3.3), with minima occurring during the winter due to freezing, and maxima occurring during the summer. The $\delta^{18}O$ of the soil water at Victoria Valley varies between –33 (fresh snow) and –29‰ VSMOW (interstitial ice) (Hagedorn et al., 2010). Measurements of the isotopic composition of soil water at Scott Base are unavailable, but are assumed to be similar to the Victoria Valley waters.

3.5.1.2. Chilean and Argentinian Andes

A soil monitoring station installed by Burgener et al. (2016) at the 4700 masl Elqui Valley, Chile site from January 2014 to January 2015 recorded MSST and WMMST values at 50 cm depth of 7 and 9 °C, respectively. The site is extremely arid, with most precipitation occurring during the winter months; however, soil moisture is highest during the summer months when the past winter's snow begins to melt. During the monitoring period, mean summer soil moisture was 0.08 $m^3\ m^{-3}$ and 0.019 $m^3\ m^{-3}$ at 10 and 50 cm depth, respectively. At the 3550 masl site, the 50 cm MSST and WMMST over the same period were 15 and 16 °C, respectively, and 50 cm soil moisture was 0.07 $m^3\ m^{-3}$. Burgener et al. (2016) reported $\delta^{18}O$ values ranging from –20 to –15‰ VSMOW for local snow and meltwater at the 4700 masl site, and –15 to –12‰ at the 3550 masl site. Temperature monitoring stations were not installed at the 3750, 4200, and 4500 masl sites; instead, soil temperature for the three sites were interpolated using data from the nearby 3550 and 4700 masl monitoring stations.

Table 3.3. Weather station location and climatologic data.

Weather Station Location	Lat. (° N)	Lon. (° E)	Elev. (m)	MAT[a] (°C)	MST[b] (°C)	WMMT[c] (°C)	50 cm MAST[d] (°C)	50 cm MSST[e] (°C)	50 cm WMMST[f] (°C)	MAP[g] (mm)	MASM[h] (m^3 m^{-3})	Corresponding Samples	Distance from Sample sites (km)	Reference
Elqui Valley, Chile 4700 m	-30.177	-69.829	4700	NA	NA	NA	0	7	9	89[i]	0.019	Elq13-4700 samples	same site	Burgener et al., 2016
Elqui Valley, Chile 3550 m	-30.262	-69.942	3550	5	10	10	8	15	16	89[i]	0.073	Elq13-3550-20	same site	Burgener et al., 2016
Río Mendoza Valley, Argentina 3200 m	-32.812	-70.064	3200	NA	NA	NA	8	14	16	NA	0.062	Peters samples	same site	Peters et al., 2013
Scott Base, Antarctica	-77.849	166.768	<10	-17	1	5	-18	-4	-2	NA	0.006	Ant-1	<1 km	NRCS Weather Station
Victoria Valley, Antarctica	-77.377	161.814	361	-22	3	12	-22	-7	-5	NA	0.003	Ant-2, Ant-3, Ant-4	<10 km	NRCS Weather Station
Ngangla Ring Tso/ T'u-ko-erh-ho-kung, Tibet	30.55	81.433	4650	4	14	15	NA	NA	NA	640	NA	Tsangpo-19	113/130 km	Quade et al., 2013/ ISD repository
Shigatse, Tibet	29.250	88.883	3880	7	15	15	NA	NA	NA	515	NA	Tsangpo-21a Tsangpo-21b Tsangpo-22	55 km 55 km 10 km	ISD repository
Lhasa, Tibet	29.667	91.133	3800	9	16	17	NA	NA	NA	575	NA	Lhasa	15 km	ISD repository
Ny-Ålesund, Svalbard	78.921	11.833	60	-3	7	9	-3	3	5	385	NA	Cannes Arrigetch	8 km 11 km	Mann et al., 1986; GTNP data repository

a - Mean Annual Temperature (MAT)
b - Mean Summer Temperature (MST)
c - Warmest Mean Monthly Temperature (WMMT)
d - Mean Annual Soil Temperature (MAST)
e - Mean Summer Soil Temperature (MSST)
f - Warmest Mean Monthly Soil Temperature (WMMST)
g - Mean Annual Precipitation (MAP)
h - 50 cm Mean Annual Soil Moisture (MASM)
i - MAP record from nearby station located at 3200 masl.

At the Argentinian Andes 3200 masl site, Peters et al. (2013) installed a soil monitoring station that recorded soil temperature and soil moisture data from February 2010 to January 2011. 50 cm MSST and WMMST at the site were 13 and 16.9 °C, respectively. Mean summer soil moisture at 50 cm depth was 0.09 m^3 m^{-3} over the same period. Oxygen isotope measurements at the sample site are limited. Peters et al. (2013) collected precipitation samples from the site sporadically between October 2008 and October 2010, but due to the limited sample set, the standard deviation for these measurements is large (±7‰). Hoke et al. (2009) collected additional precipitation samples in the same valley, as well as river water samples from the nearby Río Mendoza (elevations range from 3000 to 3300 masl). Based on the observed $\delta^{18}O$ values of this suite of samples, the range in soil water $\delta^{18}O$ at the 3200 masl site is assumed to be –17 to –9‰.

3.5.1.3. Tibet, China

The temperature and precipitation data for the Lhasa, Shigatse, and T'u-ko-erh-ho-kung, Tibet weather stations are summarized in Table 3.3. All three sites are influenced by the Indian monsoon and have a summer wet season, with Lhasa, Shigatse, and T'u-ko-erh-ho-kung receiving 63%, 71%, and 57%, respectively, of their annual rainfall between June and August. GNIP data show that between 1986 and 1992 the mean $\delta^{18}O$ of rainwater at Lhasa was 13‰ VSMOW, which compares favorably to nearby river and meteoric water samples collected by Quade et al. (2011), which have $\delta^{18}O$ values between –16 and –13‰. $\delta^{18}O$ values from stream and meteoric waters collected near the

Shigatze and T'u-ko-erh-ho-kung soils range from –19 to –15‰ (Table 3.2, Quade et al., 2011).

3.5.1.4. Svalbard, Norway, the High Arctic

The Ny-Ålesund, Svalbard weather station (which is located roughly 10 km from the Cannes and Kapp Guissez sample sites) records a MST of 7 °C for the period 1998 to 2014, (Fig. 3.1B). WMMT was 9 °C for the same period. Modern 50 cm MSST from a permafrost borehole near Ny-Ålesund is 3 °C, and WMMST at the same depth is 5 °C (Paulik et al., 2014), consistent with August soil temperatures between 0.5 and 10 °C measured at the Cannes site Mann et al. (1986). Soil moisture data were unavailable for the Svalbard study sites, but 1998–2014 weather station data show that there is strong autumn-winter bias in precipitation, with an average of 245 mm of precipitation falling between September and February, and an average of 140 mm falling between March and August. Courty et al. (1994) reported local snow $\delta^{18}O$ values of –8 to –6‰ for the Cannes site discussed in this study; however, this was a single measurement and probably does not capture local variability in precipitation $\delta^{18}O$. Additional long-term meteoric water $\delta^{18}O$ values were recorded at the Ny-Ålesund GNIP station from 1990 to 2015, and have a mean value of –11.6‰ with a standard deviation of 2.8‰. In order to make a conservative estimate of the carbonate $\delta^{18}O$ anomalies for the High Arctic samples, we used the longer term (15 years) GNIP mean $\delta^{18}O$ value of 11.6‰, and assumed that the range in local meteoric water $\delta^{18}O$ values was –14 to –8‰ (range encompasses the mean GNIP $\delta^{18}O$ value ± the standard deviation [2.8‰]).

3.5.2. X-ray diffraction results

X-ray diffraction analysis was performed on the Kapp Guissez (KG-201a, KG-201b) and Cannes (Cannes-30) High Arctic samples to assess the impact of the presence of dolomitic parent material in the soil profiles. X-ray diffraction analysis was not performed on the other samples either because there was no dolomitic parent material in the sampled soils, or (in the case of the sub-glacial carbonates) because previous studies had shown that the carbonate precipitates had little to no dolomitic inclusions (Hanshaw and Hallet, 1978). X-ray diffraction results show that the Cannes-30 sample is composed of 20% dolomite and 80% calcite. Mann et al. (1986) noted the presence of detrital dolomitic silt in the Cannes soil, suggesting that the dolomite in the Cannes-30 sample is likely detrital in origin. This sample was not analyzed further. In contrast, x-ray diffraction analysis showed that the Cannes-62 sample is composed of 70% aragonite and 30% calcite, with no measurable dolomite fraction. Because past studies (Schauble et al., 2006; Eagle et al., 2013; Henkes et al., 2013; Wacker et al., 2013) have shown that clumped isotope results for calcite and aragonite are indistinguishable under current analytic uncertainties, we proceeded with clumped isotope analysis for the Cannes-62 sample.

3.5.3. Δ_{47}, $\delta^{18}O$, and $\delta^{13}C$ results

Soil carbonate and sub-glacial $\delta^{18}O$, $\delta^{13}C$, and Δ_{47} values are reported in Table 3.4 and in Supplementary Table B2 in the Supplementary Information, along with calculated apparent T (Δ_{47}) values. The $\delta^{18}O$ values of the Cannes-62 sample were adjusted to account for the difference in $\delta^{18}O$ CO_2-carbonate fractionation factors (Kim et al., 2007) between calcite and aragonite (see Supplementary Information). $\delta^{18}O$ (VPDB) values

Table 3.4. Clumped and stable isotope data for all soil and sub-glacial carbonates.

Sample Name	*n*	$\delta^{13}C_{carb}$ (‰) VPDB	± 1 SE (‰)	$\delta^{18}O_{carb}$ (‰) VPDB	± 1 SE (‰)	mean $\delta^{18}O$ Anomaly (‰)						Δ_{47} (‰) ARF	± 1 SE (‰)	mean Δ_{47} Anomaly (‰)			$T(\Delta_{47})$ (°C)	± 1 SE (°C)
						-1 °C CFT[a]		*MST CFT*		*WMMT CFT*				*-1 °C CFT*	*MST CFT*	*WMMT CFT*		
						Low $\delta^{18}O$[b]	*High* $\delta^{18}O$	*Low* $\delta^{18}O$	*High* $\delta^{18}O$	*Low* $\delta^{18}O$	*High* $\delta^{18}O$							
Elq13-4700-20	3	9.43	0.06	-3.10	0.06	11.99	6.96	14.26	9.25	14.48	9.47	0.6391	0.0093	-0.063	-0.024	-0.020	16	3
Elq13-4700-40	4	8.52	0.03	-3.82	0.08	11.26	6.24	13.09	8.08	13.54	8.52	0.6245	0.0111	-0.077	-0.046	-0.038	20	3
Elq13-4700-60	4	10.00	0.02	-4.17	0.05	10.92	5.89	12.75	7.73	13.19	8.18	0.6321	0.0080	-0.070	-0.038	-0.031	18	2
Elq13-4700-80	3	10.36	0.04	-5.17	0.05	9.92	4.89	11.75	6.73	12.19	7.18	0.6462	0.0093	-0.056	-0.024	-0.017	14	3
Elq13-4700-100	5	9.25	0.04	-6.35	0.07	8.73	3.71	10.57	5.55	11.01	5.99	0.6323	0.0072	-0.070	-0.038	-0.031	18	2
Elq13-4500-50	7	9.14	0.05	-9.16	0.03	5.93	0.90	8.20	3.19	8.64	3.63	0.6803	0.0109	-0.022	0.018	0.025	5	3
Elq13-4200-50	5	6.88	0.04	-4.56	0.06	7.51	5.50	10.22	8.22	10.65	8.65	0.6581	0.0080	-0.044	0.003	0.010	10	2
Elq13-3750-50	6	0.87	0.03	-11.59	0.11	-0.52	-2.53	2.84	0.84	3.26	1.26	0.6671	0.0072	-0.035	0.022	0.029	8	2
Elq13-3550-20	5	2.92	0.14	-5.79	0.18	4.27	1.26	8.06	5.06	8.06	5.06	0.6463	0.0105	-0.056	0.009	0.009	14	3
Peters-B15	4	-2.08	0.04	-10.66	0.04	1.41	-6.63	4.98	-3.03	5.40	-2.61	0.6835	0.0139	-0.096	-0.010	0.000	17	3
Peters-B30	2	-5.37	0.04	-11.83	0.05	0.24	-7.80	3.60	-4.41	4.23	-3.78	0.6831	0.0215	-0.096	-0.015	0.000	17	4
Peters-B45	4	-4.67	0.04	-12.84	0.02	-0.77	-8.81	2.59	-5.42	3.01	-5.00	0.7076	0.0080	-0.072	0.010	0.019	12	2

a - CFT = carbonate formation temperature; see Table 2 for the MST and WMMT estimates for each site

b - See Table 2 for the high and low $\delta^{18}O$ estimates for each site

Table 3.4. Cont'd.

Sample Name	*n*	$\delta^{13}C_{carb}$ (‰) VPDB	± 1 SE (‰)	$\delta^{18}O_{carb}$ (‰) VPDB	± 1 SE (‰)	mean $\delta^{18}O$ Anomaly (‰)						Δ_{47} (‰) ARF	± 1 SE (‰)	mean Δ_{47} Anomaly (‰)			$T(\Delta_{47})$ (°C)	± 1 SE (°C)
						-1 °C CFT[a]		*MST CFT*		*WMMT CFT*				*-1 °C CFT*	*MST CFT*	*WMMT CFT*		
						Low $\delta^{18}O$[b]	*High* $\delta^{18}O$	*Low* $\delta^{18}O$	*High* $\delta^{18}O$	*Low* $\delta^{18}O$	*High* $\delta^{18}O$							
ANT-1	3	6.86	0.10	-14.41	0.15	13.75	9.73	13.75	9.73	14.44	10.42	0.6383	0.0093	-0.064	-0.064	-0.052	16	3
ANT-2	3	8.36	0.08	-17.81	0.14	10.34	6.32	10.57	6.55	11.26	7.24	0.6323	0.0093	-0.070	-0.066	-0.054	18	3
ANT-3	3	8.90	0.09	-17.87	0.20	10.28	6.26	10.51	6.49	11.20	7.18	0.6493	0.0093	-0.053	-0.049	-0.037	13	3
ANT-4	3	9.32	0.04	-20.34	0.17	7.81	3.79	8.04	4.02	8.73	4.71	0.6487	0.0093	-0.053	-0.049	-0.037	13	3
KG-201a	3	-0.42	0.01	-7.51	0.10	1.54	-4.49	2.48	-3.54	2.94	-3.08	0.6485	0.0093	-0.054	-0.037	-0.029	13	3
KG-201b	3	0.53	0.02	-7.11	0.17	1.94	-4.09	2.88	-3.14	3.34	-2.68	0.6305	0.0093	-0.071	-0.055	-0.047	18	3
Cannes-62	3	5.31	0.07	-5.03	0.06	4.03	-2.01	4.96	-1.06	5.42	-0.60	0.6779	0.0093	-0.024	-0.008	0.000	5	2
Tsangpo-19a	3	3.30	0.05	-14.71	0.10	-2.64	-4.65	0.72	-1.29	0.93	-1.07	0.6573	0.0093	-0.045	0.013	0.016	11	3
Tsangpo-19b	3	3.79	0.08	-14.21	0.04	-2.13	-4.14	1.23	-0.78	1.44	-0.57	0.6648	0.0093	-0.037	0.020	0.024	8	2
Tsangpo-21a	3	-2.91	0.03	-11.65	0.04	2.43	-0.59	5.99	2.99	5.99	2.99	0.6600	0.0093	-0.042	0.019	0.019	10	3
Tsangpo-21b	3	-2.94	0.05	-13.59	0.04	0.50	-2.52	4.06	1.06	4.06	1.06	0.6248	0.0133	-0.077	-0.016	-0.016	20	4
Tsangpo-22	4	-1.45	0.04	-15.74	0.06	-2.67	-3.67	0.90	-0.10	0.90	-0.10	0.6184	0.0080	-0.084	-0.023	-0.023	22	3
Lhasa-4	3	-3.98	0.05	-17.33	0.09	-8.28	-10.29	-4.49	-6.49	-4.28	-6.28	0.6355	0.0094	-0.067	-0.002	0.001	17	3
CG-1	3	0.53	0.09	-10.23	0.17	4.86	3.85	NA	NA	5.09	4.09	0.4451	0.0093	-0.257	-0.253	-0.253	96	6
CG-2	3	2.42	0.01	-11.16	0.02	3.93	2.92	NA	NA	4.16	3.16	0.4102	0.0112	-0.292	-0.288	-0.288	119	8
BF-1	3	-1.14	0.02	-18.26	0.03	-8.20	-9.20	NA	NA	-7.96	-8.97	0.6839	0.0108	-0.018	-0.014	-0.014	4	3
BF-2	4	-0.77	0.01	-17.06	0.09	-7.00	-8.01	NA	NA	-6.76	-7.77	0.5969	0.0104	-0.105	-0.101	-0.101	29	4
BF-3	3	-0.87	0.04	-16.61	0.11	-6.55	-7.56	NA	NA	-6.31	-7.32	0.5790	0.0093	-0.123	-0.119	-0.119	35	3

a - CFT = carbonate formation temperature; see Table 2 for the MST and WMMT estimates for each site

b - See Table 2 for the high and low $\delta^{18}O$ estimates for each site

range from –3.1 to –20.3‰ for the soil carbonate samples, and –18.3 to –10.2‰ for the sub-glacial carbonate samples. The mean external error (1 standard error) for all carbonate $\delta^{18}O$ measurements is ±0.09‰. $\delta^{13}C$ values range between –5.4 and +10.4‰ for the soil carbonates and –1.1 and +2.4‰ for the sub-glacial carbonates, and yield a standard error of ±0.05‰. Observed sample average Δ_{47} values range from 0.618 to 0.680‰ for the soil carbonate samples analyzed in the UW Isolab, 0.683 to 0.708‰ for the Peters et al. (2013) samples (analyzed at Caltech), and 0.410–0.684‰ for the sub-glacial carbonates. The mean standard error for all Δ_{47} measurements is ±0.012‰.

For all samples except the Argentinian Andes soil carbonates, T(Δ_{47}) values were calculated from the Δ_{47}results using the Δ_{47}-T calibration of Kelson et al. (2017) (Eq. (1); 90 °C acid reaction, no acid correction). For the Argentinian Andes samples, see Peters et al. (2013) for complete methods description. Apparent T(Δ_{47}) values for the subglacial carbonates are highly variable, ranging from 96 to 119 ° C for the Castleguard Glacier samples (2 samples, 3 replicates each), to 4–35 °C for the Blackfoot Glacier samples (3 samples, 3 to 4 replicates each). The mean standard error in T(Δ_{47}) estimates for the sub-glacial carbonates is ±5 °C. In contrast to the sub-glacial samples, the soil carbonates show a much smaller degree of variability in T(Δ_{47}) values. Apparent formation temperatures for individual samples range from 5 °C (Cannes-62) to 22 °C (Tsangpo-22), within the range of Earth-surface temperatures. The standard error in T(Δ_{47}) for the soil carbonate samples is ±3 °C. Mean T(Δ_{47}) is 15 °C for the Antarctica samples, 17 and 14 °C for the 4700 and 3550 masl Chilean Andes samples, 12 °C for the Arctic carbonates, and 16 °C for the Tibetan samples. Supplementary Figure B1 shows soil carbonate T(Δ_{47}), mean monthly air temperature and (where available) mean monthly soil

temperature, mean monthly precipitation, and mean monthly soil moisture for the soil sample sites in the Andes, Antarctica, the High Arctic, and Tibet.

The Tibetan Plateau samples analyzed for this study are distinct nodules collected from the same sites and soil horizons as the samples reported in Quade et al. (2013). The $\delta^{18}O$, $\delta^{13}C$, and Δ_{47} values for our new nodules are generally consistent with the Quade et al. (2013) samples, though they do display some heterogeneity. For all of the soil sites, the difference in measured $\delta^{13}C$ values is within 2‰, which is similar to the variability observed between the original Quade et al. (2013) samples (Supplementary Table B3). With respect to $\delta^{18}O$ and Δ_{47}, the differences for the Tsangpo-19, Tsangpo-22, and Lhasa-4 samples are less than 3‰ or 2 °C respectively; but the Tsangpo-21 site yields much larger differences (6‰ and 8 °C respectively). The differences between the samples analyzed for this study and those analyzed previously by Quade et al. (2013) appear to be due to natural variability in the isotopic composition of the carbonate pendants within any given horizon.

3.5.4. Δ_{47}, $\delta^{18}O$, and $\delta^{13}C$ anomalies

The calculated –1 °C, MST/MSST, and WMMT/ WMMST Δ_{47} anomalies for our soil carbonate samples exhibit a 0.1‰ range of values (Fig. 3.4), with some samples yielding values near the 0‰ expected for equilibrium carbonates, and other samples being significantly more negative suggesting disequilibrium processes. Some uncertainty in calculated anomalies is introduced depending on the assumed local carbonate formation temperature at each site (Table 3.4). For the colder Arctic and Antarctic sites, the difference between the minimum assumed carbonate formation temperature of –1 °C and the local MSST and WMMST is relatively small, leading to small uncertainty in

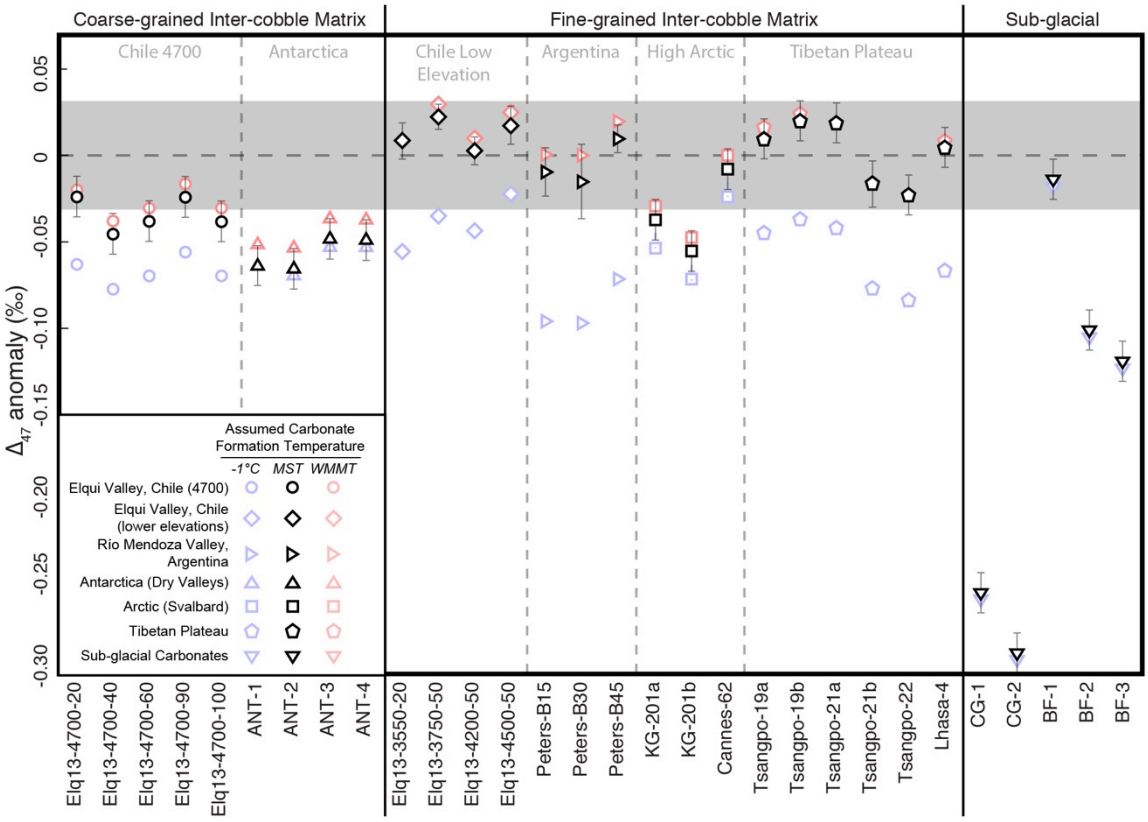

Figure 3.4. Calculated carbonate Δ_{47} anomalies arranged by soil matrix type. The dashed horizontal line marks a Δ_{47} anomaly of 0‰, and the dark gray band shows the 95% confidence interval (external error) around that line.

calculated Δ_{47} anomalies that are on the order of typical analytical uncertainty in Δ_{47}. The Chilean soil carbonates exhibit larger variations in Δ_{47} anomaly calculated using different assumed formation temperatures, reflecting the greater difference between –1 °C and the warmer local MSST and WMMST.

For those samples from soils with coarse grained inter-cobble matrices (n = 9; the Antarctic and 4700 masl Chilean samples), all of the calculated Δ_{47} anomalies are negative regardless of whether the soil carbonates are assumed to have formed at –1 °C, local MAT or MSST, or local WMMST (Fig. 3.4). The mean Δ_{47} anomaly for the Antarctic soil carbonates is –0.060‰ at –1 °C, –0.057‰ at local MSST, and –0.045‰ at local WMMST, and the 4700 masl Chilean soil carbonate samples have a mean Δ_{47} anomaly of –0.067‰ at –1 °C, –0.034‰ at local MST, and –0.027‰ at local WMMT. If the Chilean and Antarctic Δ_{47} anomalies are calculated using an assumed carbonate formation temperature of –1 °C, the resulting values are all significantly below 0‰ (e.g., they fall outside the 95% confidence interval (CI) for the expected Δ_{47} value for equilibrium carbonates). When MSST or WMMST are used to calculate the Δ_{47} anomalies, all of the Antarctic samples and one of the Chilean samples (Elq13-4700-40) are still significantly below 0‰.

In contrast, the sample from soils that have relatively fine grained inter-cobble matrices (n = 16; the 3550, 3750, 4200, and 4500 masl Chilean, Argentina, Svalbard, and Tibet samples) yield Δ_{47} anomalies calculated using mean summer air or soil temperatures and warmest mean monthly air or soil temperatures that are indistinguishable from 0‰ (i.e., they fall within the 95% CI of the expected equilibrium carbonate Δ_{47} composition; Fig. 3.4). The exception to this trend are the samples from

Kapp Guissez, Svalbard: the KG-201b sample has a significant negative Δ_{47} anomaly, and the Δ_{47} anomaly for sample KG-201a from the same locality falls slightly outside the 95% confidence interval when calculated using MST. When the fine-matrix samples (n = 16) Δ_{47} anomalies are calculated using a formation temperature of –1 °C, every sample except Cannes-62 falls outside the 95% CI for the Δ_{47} value of expected equilibrium carbonates Fig. 3.4).

The sub-glacial carbonate Δ_{47} anomalies yield a much wider range in values than observed in the soil carbonates, and only one of the sub-glacial samples has a Δ_{47} anomaly that falls within the 95% CI for the Δ_{47} value of expected equilibrium carbonates (Fig. 3.4). Sample BF-1 from Blackfoot Glacier falls within the 95% CI for the Δ_{47} value of expected equilibrium carbonates, while the Δ_{47} anomalies for the other two Blackfoot sub-glacial samples are much larger and negative (–0.105 to –0.123‰); as a result, individual samples from this site display a much wider range in Δ_{47} anomaly values than any of our other sample sites. The Δ_{47} anomalies for the Castleguard sub-glacial samples are –0.257 to –0.292‰ at –1 °C, which is an order of magnitude more negative than any of the soil carbonate samples.

The soil carbonate $\delta^{18}O$ anomalies for the samples with relatively coarse-grained inter-cobble matrices (i.e., 4700 masl Chilean Andes and Antarctic samples) are one to two orders of magnitude larger than the calculated Δ_{47} anomalies, but display a similar pattern in that they are consistently different from the expected equilibrium value regardless of assumed formation temperature. The $\delta^{18}O$ anomalies for the coarse-grained matrix samples are all large and positive (>3‰), and very high relative to all of the other soil and sub-glacial carbonate samples, except the lower elevation Chilean samples which

are comparable (Fig. 3.5). The range in Δ_{47} anomalies for the Antarctic and 4700 masl Chilean samples is too small (<0.025‰) to determine if there is a significant Δ_{47}–$\delta^{18}O$ correlation; however, these samples plot near the lower limit of the 0.005 ± 0.003‰ slope observed by Kluge et al. (2014) in coarse-grained cryogenic cave carbonates, and significantly above the 0.02‰ slope predicted by Guo (2009) (Supplementary Figure B2).

The $\delta^{18}O$ anomalies for the samples with relatively fine-grained inter-cobble matrices (i.e., 3550, 3750, 4200 and 4500 masl Chilean Andes, Argentinian Andes, High Arctic, and Tibet samples) yield mixed results. With values of 2.8‰ at –1 °C, 5.8‰ at MSST, and 6.2‰ at WMMST, the mean $\delta^{18}O$ anomaly for the lower elevation Chilean samples (3550, 3750, 4200, and 4500 masl) is positive and large, similar to the smallest anomalies from the coarse-grained matrix sample suite. The Argentinian Andes samples (n = 3) have relatively large ranges in possible $\delta^{18}O$ anomalies due to the large range in observed meteoric water $\delta^{18}O$ values at the 3200 masl sample site. Despite this large range, the Argentinian Andes anomalies cluster about the 0‰ line. The High Arctic sample $\delta^{18}O$ anomalies (n = 3) yield either negative or positive results depending on whether the $\delta^{18}O$ anomalies are calculated using the maximum or minimum local meteoric water $\delta^{18}O$ values, respectively. The Tibetan plateau sample $\delta^{18}O$ anomalies (n = 6) are small and scattered about 0‰.

The sub-glacial $\delta^{18}O$ anomalies yield different results, with the Castleguard glacier samples having large positive $\delta^{18}O$ anomalies, and the Blackfoot glacier samples yielding large negative $\delta^{18}O$ anomalies.

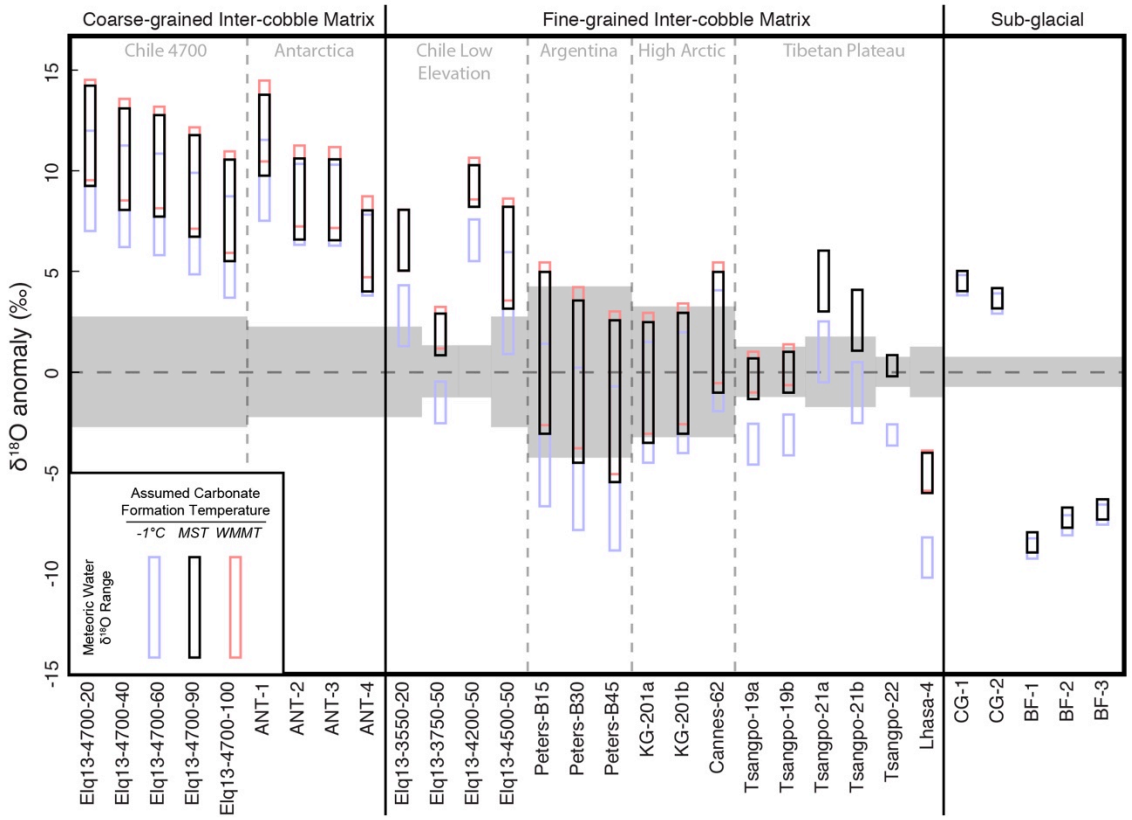

Figure 3.5. Calculated carbonate $\delta^{18}O$ anomalies arranged by soil matrix type. Black bars represent the range in $\delta^{18}O$ anomalies calculated for local mean summer air or soil temperature and the range of local meteoric water $\delta^{18}O$ values. Red bars represent the range in $\delta^{18}O$ anomalies calculated for local warmest mean monthly air or soil temperature. Blue bars represent the range in $\delta^{18}O$ anomalies calculated for –1 °C. The dashed horizontal line marks a $\delta^{18}O$ anomaly of 0‰, and the gray band shows the uncertainty around that line (calculated for each sample as the difference between the maximum and minimum local meteoric $\delta^{18}O$ values plus the analytical error [±1 SE]).

To test the dependence of our $\delta^{18}O$ anomalies on the choice of calcite-water $\delta^{18}O$ calibration, we recalculated the anomalies using the calibration of Kim and O'Neil (1997). For all of our samples, the Kim and O'Neil (1997) $\delta^{18}O$ anomalies are ~1.61‰ larger than the Watkins et al. (2014) $\delta^{18}O$ anomalies (Supplementary Figure B3). This difference is expected, since the Kim and O'Neil (1997) calibration is isotopically light relative to the Watkins et al. (2014) calibration. The difference between the Kim and O'Neil (1997) and Watkins et al. (2014) $\delta^{18}O$ anomalies does not change our interpretations of the data, and for the remainder of this paper only the Watkins et al. (2014) $\delta^{18}O$ anomalies will be discussed.

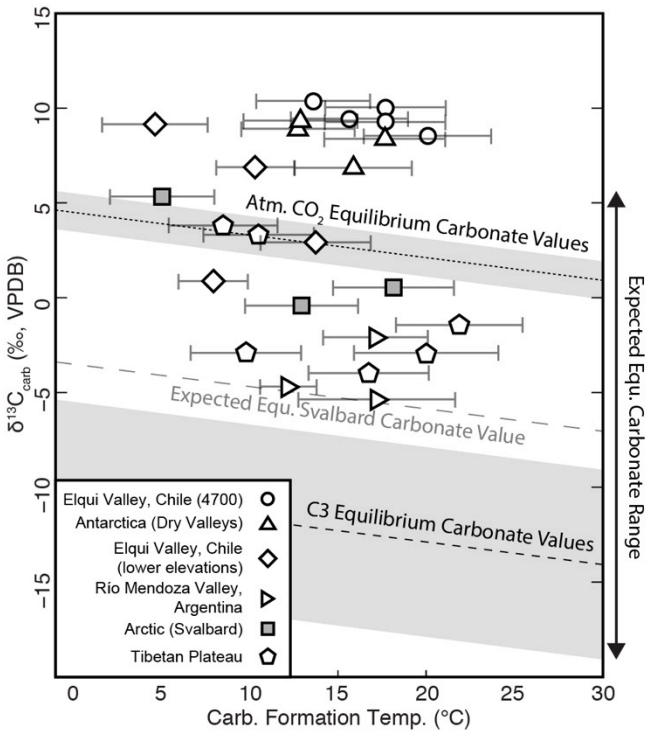

Figure 3.6. Carbonate $\delta^{13}C$ values plotted against carbonate formation temperature (°C). The dark dotted and dashed lines represent the mean $\delta^{13}C$ values of carbonates forming in equilibrium with atmospheric and C3 plant-respired CO_2 (Cerling and Quade, 1993), respectively, with the gray bands showing the uncertainty associated with these values. The dashed light gray line shows the soil CO_2 $\delta^{13}C$ values measured at the Cannes, Svalbard soil site by Marlin et al. (1993). The sample symbols are the same as in Fig. 5, save that the Svalbard High Arctic samples are highlighted as dark gray squares. The dark symbols plot the sample $T(\Delta_{47})$ versus sample $\delta^{13}C$, with the associated 1 SE error bars. Note that equilibrium soil carbonates would be expected to plot between the atmospheric and C3 equilibrium carbonates values (see range marked by arrows to the right of the graph).

The lack of soil CO_2 stable isotope data limits our ability to calculate precise $\delta^{13}C$ anomalies for most soil carbonate samples, but we can nevertheless compare the observed sample $\delta^{13}C$ values to the expected range of equilibrium soil carbonate $\delta^{13}C$ values. Fig. 3.6 shows the expected $\delta^{13}C$ values for soil carbonates precipitated in isotopic equilibrium with two separate CO_2 reservoirs: atmospheric CO_2 (lower gray band), and CO_2 respired by C3 plants (upper gray band) (Cerling and Quade, 1993; Kohn, 2010). As shown in Fig. 3.6, the coarse-grained inter-cobble matrix (i.e., Antarctic and 4700 masl Chilean Andes) carbonates plot at or above the upper limit of expected values for soil carbonates that have formed in isotopic equilibrium with atmospheric CO_2 (pre-industrial = –6.5‰; modern = –8.5‰), regardless of the assumed carbonate formation temperature. The $\delta^{13}C$ values of most of the fine-matrix samples (i.e., two of the lower elevation Chilean samples, and the Argentinian and

Tibetan Plateau samples) generally fall within the range of equilibrium carbonates forming from atmospheric and plant respired CO_2. In contrast, the carbonate $\delta^{13}C$ values of two of the lower elevation Chilean samples (4200 and 4500 masl samples) are higher than the upper limit of expected equilibrium carbonate $\delta^{13}C$ values. Similarly, the $\delta^{13}C$ values for the High Arctic samples (KG-201a, KG-201b, and Cannes-62) are higher than soil CO_2 $\delta^{13}C$ values measured by Courty et al. (1994) at the Cannes soil site.

3.6. Discussion

The calculated Δ_{47}, $\delta^{18}O$, and $\delta^{13}C$ anomalies enable us to assess equilibrium versus KIE processes in carbonate proxy archives from cold environments. We find that the Δ_{47}, $\delta^{18}O$, and $\delta^{13}C$ anomalies of the lower elevation Chilean Andes, Argentinian Andes, and Tibetan and High Arctic soil carbonates (collected from soils with a silt to sand matrix component) are consistent with summer formation of soil carbonate under conditions near isotopic equilibrium; however the isotopic composition of the lower elevation Chilean and High Arctic soil carbonates appear to have been affected by extreme aridity and dissolution/reprecipitation, respectively. In contrast, the Δ_{47}, $\delta^{18}O$, and $\delta^{13}C$ anomalies of the Antarctic and 4700 masl Chilean Andes soil carbonates (collected from soils that lack a silt or finer sand component in the soil matrix) are consistent with cryogenic carbonate formation and KIE due to rapid CO_2 degassing during bicarbonate dehydration. The sub-glacial carbonates from both glacier sites yield negative Δ_{47} anomalies, but distinctly different $\delta^{18}O$ anomalies that may be consistent with differences in sub-glacial plumbing and resulting variations in meltwater salinity and pH. We attribute the observed site-to-site variability in soil carbonate Δ_{47}, $\delta^{18}O$, and $\delta^{13}C$ anomalies to differences in inter-cobble soil matrix grain size and attendant

differences in soil moisture, and discuss the implications of our findings with respect to past and future paleoclimate studies based on soil carbonates from cold climates.

3.6.1. Isotopic equilibrium and disequilibrium in cold-climate soil carbonates

3.6.1.1. equilibrium soil carbonates from fine-matrix soils from the Tibetan Plateau, High Arctic, and the Chilean and Argentinian Andes

First we examine the isotopic results from soils with fine-grained inter-cobbles matrices, i.e., those samples collected from the 3550, 3750, 4200, and 4500 masl sites in the Chilean Andes, as well as the Argentinian Andes, Tibetan Plateau, and High Arctic sites. Due to the reduced pore space and permeability (e.g., hydraulic conductivity) in these soils, we expect them to experience slower rates of CO_2 degassing, which in turn should favor equilibrium soil carbonate formation. Equilibrium soil carbonates are predicted to have $T(\Delta_{47})$ values in the range of local soil temperatures: similar to local MAT, or local winter or summer soil temperatures if there is a seasonal bias to soil carbonate formation (Peters et al., 2013; Quade et al., 2013; Hough et al., 2014; Burgener et al., 2016; Gallagher and Sheldon, 2016; Ringham et al., 2016). Equilibrium soil carbonate $\delta^{18}O$ values should be consistent with the isotopic composition of local meteoric waters (after taking into account the temperature-dependent calcite-water fractionation factor), but may be more positive by ≤10‰ due to evaporative effects (Liu et al., 1996; Quade et al., 2007; Burgener et al., 2016). Equilibrium soil carbonate $\delta^{13}C$ should fall between the $\delta^{13}C$ values of atmospheric CO_2 and C3 plant-respired CO_2 (after taking into account the temperature dependent ^{13}C fractionation between CO_2 and calcite; see Fig. 3.6).

The Peters et al. (2013) Argentinian Andes samples all yield negligible Δ_{47} and $\delta^{18}O$ anomalies and $\delta^{13}C$ values that are consistent with equilibrium carbonate formation. Sample Δ_{47} values are consistent with measured local mean summer soil temperatures. The samples show a large range in $\delta^{18}O$ anomalies that are consistent with the range of meteoric water $\delta^{18}O$ values observed in this study area. It is interesting to note that the values of these anomalies decrease with depth, which is characteristic of soil profiles that have experienced enrichment of soil water $\delta^{18}O$ nearer the soil surface due to the effects of evaporation (Liu et al., 1996). We attribute the large ranges in the $\delta^{18}O$ anomalies of these samples to uncertainties in the long-term range of meteoric water $\delta^{18}O$ values. Because the $\delta^{18}O$ anomalies all center on the 0‰line (Fig. 3.5), we interpret them as being consistent with equilibrium carbonate formation. The soil carbonate $\delta^{13}C$ values plot well within the range of expected soil CO_2 $\delta^{13}C$ values.

In regard to the Tibetan Plateau samples, Quade et al. (2011) showed that most of the soil carbonates they analyzed from the Tibetan plateau exhibit a summer-season bias in their $\delta^{18}O$ values; therefore we expected that the Δ_{47} and $\delta^{18b}O$ anomalies calculated using local MST and WMMT would be small, consistent with equilibrium, seasonally biased carbonate formation. The $T(\Delta_{47})$ values of these samples are in line with local summer soil temperatures (Supplementary Figure B1 E, F, and G), and their average Δ_{47} anomalies calculated using MST/WMMT are smaller than our analytical uncertainties (0.002‰ and 0.003‰, respectively). Additionally, their $\delta^{13}C$ values fall between the ranges of expected $\delta^{13}C$ values for soil carbonates that formed in equilibrium with some mixture of atmospheric and soil CO_2 (Fig. 3.6), consistent with this hypothesis.

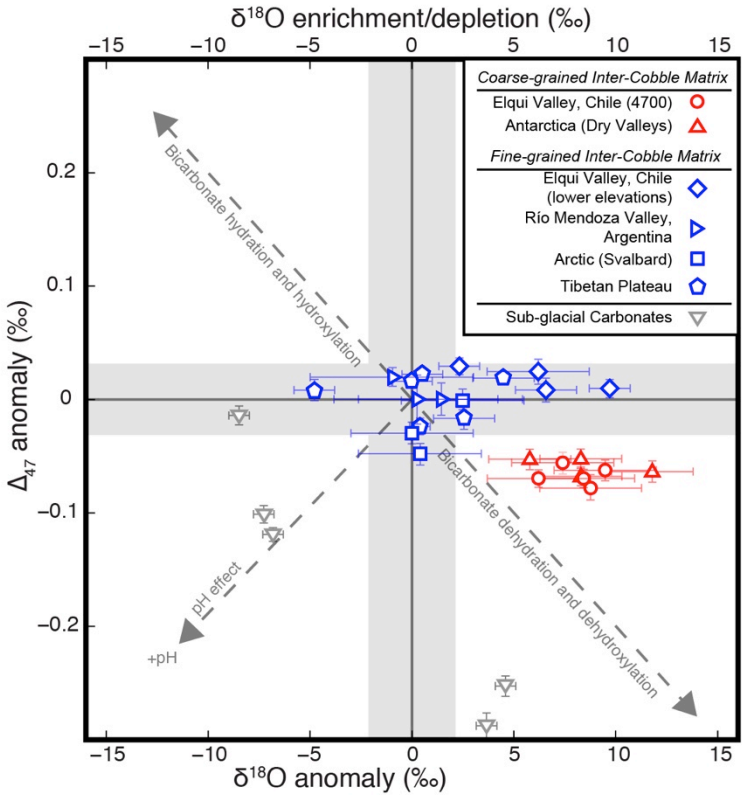

Figure 3.7. Estimated Δ_{47} and $\delta^{18}O$ anomalies for the coarse-grained inter-cobble matrix soils (red symbols), fine-grained inter-cobble matrix soils (blue symbols), and sub-glacial samples (gray symbols). All samples are plotted using the favored precipitation temperature as discussed in Section 5 of this study (e.g., –1 °C for the coarse-grained inter-cobble matrix samples, and local WMMT/ WMMST for the fine-grained inter- cobble matrix samples). Horizontal error bars show the range in $\delta^{18}O$ anomalies based on local meteoric water $\delta^{18}O$ values. Vertical error bars show the range in Δ_{47} anomalies based on local air or soil temperature uncertainties. The dark gray dashed lines show the disequilibrium tendencies of various disequilibrium carbonate precipitation processes, as in Fig. 3.2. Schematic modified from Tripati et al. (2015). The vertical gray band shows the 95% confidence interval about the 0‰ line for the Δ_{47} anomalies; the horizontal gray band shows the uncertainty around the 0‰ line for the $\delta^{18}O$ anomalies (calculated for each sample as the difference between the maximum and minimum local meteoric $\delta^{18}O$ values plus the analytical error [1 SE]).

We suggest that the differences from 0‰ (e.g., apparent equilibrium) observed for some of the Tibetan Δ_{47} and $\delta^{18}O$ anomalies (e.g., the Lhasa-4 $\delta^{18}O$ anomaly) calculated for local MST and WMMT (Figs. 3.5 and 3.7) can be explained by three factors, with no need to invoke disequilibrium processes. First, variable conditions in local soil and climate, as well as small differences in mean soil carbonate age, mean that our samples may include carbonate that precipitated at different times in the past and under slightly

different temperature and meteoric water $\delta^{18}O$ conditions. Second, due to the lack of long-term soil temperature measurements, we were forced to estimate mean soil temperature conditions at the sampling sites using data from meteorological stations that are located up to 130 km away (see Table 3.3), introducing unquantified uncertainties into our soil temperature estimates and the subsequent anomaly calculations. Third, our calculations of equilibrium carbonate $\delta^{18}O$ values also contain uncertainties due to (1) the distance between the sample soil sites and GNIP stations or individual water samples collected by Quade et al. (2011); (2) the short temporal coverage and data gaps in the available GNIP records; and (3) the fact that our calculations are based on meteoric and stream water $\delta^{18}O$ values that do not take into account evaporative effects that commonly enrich soil waters relative to local meteoric waters (Liu et al., 1996; Quade et al., 2007; Burgener et al., 2016).

After taking into account variations due to uncertainties in local temperature and meteoric water $\delta^{18}O$ values, we interpret the Δ_{47}, $\delta^{18}O$, and $\delta^{13}C$ results of the Tibetan Plateau soil carbonate samples as being consistent with calcite formation under conditions of apparent isotopic equilibrium. This interpretation is supported by the fact that no single process (e.g., bicarbonate dehydration or the pH effect) can account for the Δ_{47} and $\delta^{18}O$ anomalies observed in these samples. For example, KIEs associated with bicarbonate dehydration during cryogenic carbonate formation should result in enrichment in soil carbonate ^{18}O relative to the expected equilibrium carbonate composition (e.g. a positive $\delta^{18}O$ anomaly), and depletion in soil carbonate Δ_{47} relative to the expected equilibrium clumped isotope composition (e.g., a negative Δ_{47} anomaly) for all samples. This is not observed in our Tibetan samples, which instead have Δ_{47}

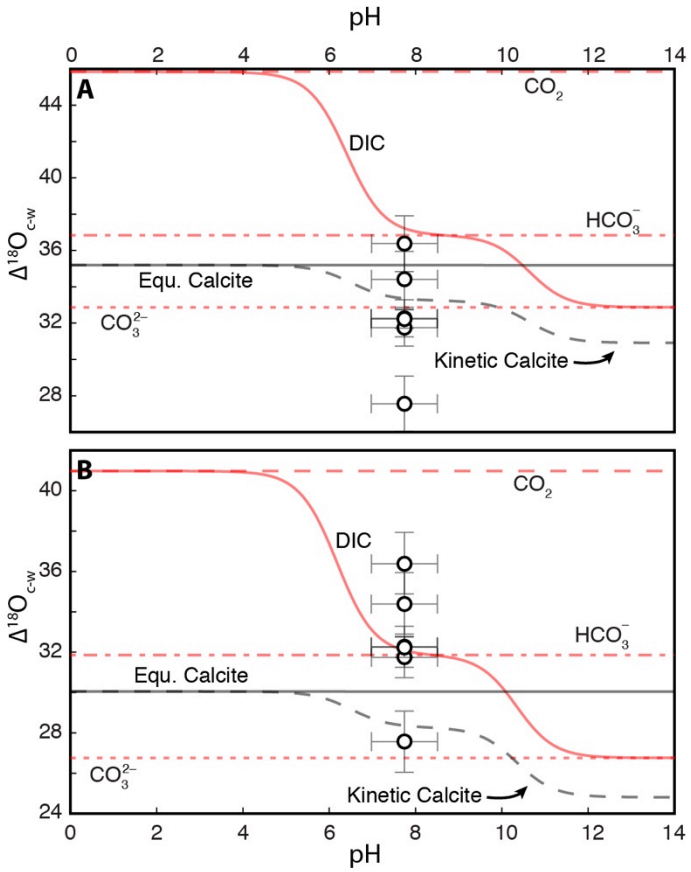

Figure 3.8. Modeled pH-dependence of disequilibrium calcite $\delta^{18}O$ values at 0 ° C (A), and mean Lhasa/Shigatse summer temperatures (23.5 °C; B). Circles show the calculated $\delta^{18}O$ disequilibrium values for the Tibet soil carbonates. Soil pH values were estimated using mean global soil pH values (Brady and Weil, 2010).

anomalies indistinguishable from expected equilibrium values, and variable (positive and negative) $\delta^{18}O$ anomalies. Alternatively, as shown in Fig. 3.8, if we assume a normal range in soil pH (7–8.5; Brady and Weil, 2010) for the Tibet soils, their carbonate $\delta^{18}O$ values do not appear to be in good agreement with $\delta^{18}O$ values for carbonates that have experienced the disequilibrium ‘‘pH effect”, as predicted using the process-based model developed by Watkins and Hunt (2015), which calculates Δ_{47}, $\delta^{18}O$, $\delta^{13}C$ values for non-equilibrium carbonates. Based on these observations, we deem it most reasonable to attribute the relationship between the observed carbonate isotope values (T(Δ_{47}), $\delta^{18}O$,

and $\delta^{13}C$) and local environmental conditions to equilibrium carbonate formation processes rather than to some combination of disequilibrium processes.

We also interpret the lower elevation Chilean Andes (i.e., 3550, 3750, 4200, and 4500 masl) Δ_{47} and $\delta^{18}O$ anomalies, and $\delta^{13}C$ values as being consistent with equilibrium carbonate formation in arid conditions, after taking into account the effects of evaporation on soil carbonate $\delta^{18}O$ values. The Δ_{47} anomalies for these four samples are indistinguishable from 0‰ at the 95% CI. The positive 5–8‰ $\delta^{18}O$ anomaly observed for this site can be explained by the large degree of evaporation observed in arid soils (Quade et al., 2007). Our calculation of the $\delta^{18}O$ anomaly was based on the maximum and minimum observed $\delta^{18}O$ composition of local meteoric waters, which do not experience as much evaporation and ^{18}O-enrichment as local soil water. Any soil carbonates that precipitate from soil water solutions that are evaporatively enriched in ^{18}O will inherit the heavy ^{18}O composition of the soil water, and should have a positive $\delta^{18}O$ anomaly relative to local meteoric waters. Quade et al. (2007) found that soil water in the Atacama Desert is evaporatively enriched relative to local meteoric waters by up to ~10‰. Because the low elevation Chilean study area is less arid than the Atacama Desert, we suggest that soil waters at these sites could have experienced ~6‰ evaporative enrichment. After taking this evaporative enrichment into account, we interpret the $\delta^{18}O$ value of these samples as being consistent with the expected equilibrium carbonate composition.

With respect to carbonate $\delta^{13}C$ values, two of the lower elevation Chilean Andes samples (Elq13-3550-20 and Elq13-3750-50) yield d13C values that fall within the range of expected carbonate d13C of soil carbonate forming in equilibrium with atmospheric

CO_2 gas; however, the samples from the 4200 and 4500 masl sites yield $\delta^{13}C$ values higher than the expected range of equilibrium carbonate $\delta^{13}C$ values and only slightly lower than the $\delta^{13}C$ values of soil carbonates collected from the coarse-grained soils at 4700 masl. There are several possible explanations for these high $\delta^{13}C$ values, including: (1) the soil carbonates at the 4200 and 4500 masl sites formed under equilibrium conditions, and the high $\delta^{13}C$ values are due to very low soil respiration rates (Quade et al., 2007); (2) the soils carbonates from these sites formed under equilibrium conditions but experienced multiple cycles of carbonate dissolution and precipitation resulting in higher $\delta^{13}C$ values (Nakai et al., 1975; Clark and Lauriol, 1992) or (3) the soil carbonates at these sites formed via cryogenic processes leading to very positive $\delta^{13}C$ values. While the available data does not allow us to conclusively determine whether the high $\delta^{13}C$ values from these samples are the result of low soil respiration rates, dissolution-precipitation cycles, or some combination of these processes, we do reject the latter explanation (e.g., KIEs associated with bicarbonate dehydration) because in addition to causing higher than expected $\delta^{18}O$ and $\delta^{13}C$ values, cryogenic carbonate formation should also cause negative Δ_{47} anomalies. Instead we observe Δ_{47} anomalies that are indistinguishable from 0‰ and consistent with equilibrium formation, and $\delta^{18}O$ anomalies that can be explained by evaporative enrichment. Due to these observations, we suggest that the 4200 and 4500 masl samples formed under conditions of isotopic equilibrium, and that the high $\delta^{13}C$ values are the result of some other process unique to these soil sites.

Like the Tibet samples, we interpret the High Arctic sample Δ_{47} and $\delta^{18}O$ anomalies to be consistent with equilibrium carbonate formation during the summer

season (Figs. 3.4, 3.5, and 3.7). These High Arctic samples have T(Δ_{47}) and $\delta^{18}O$ values that are consistent with local summer conditions, and Δ_{47} and $\delta^{18}O$ anomalies that—considering uncertainties in the local soil temperature and meteoric water $\delta^{18}O$ values—do not appear to be significantly different from our equilibrium soil carbonate Δ_{47} and $\delta^{18}O$ estimates. The sample from the Cannes site has Δ_{47} anomalies within error of zero; however, higher-than-expected clumped isotope temperatures (negative Δ_{47} anomalies) are observed for the Kapp Guissez samples. We suggest that these differences are likely due to two factors. First, the depth in the soil profile of the Kapp Guissez samples is unknown. The WMMT used to calculate the Kapp Guissez Δ_{47} anomalies (5 °C) is an estimate for 50 cm soil depth, but the Kapp Guissez samples may have come from shallower depths that would have experienced higher summer temperatures. Using a simple heat diffusion equation (e.g., Quade et al., 2013), we estimate that summer soil temperatures at 10 cm depth can be up to 11 °C warmer than 50 cm soil temperatures during the warmest part of the day. Second, the Kapp Guissez sample site is located ~10 km to the north of the Ny-Ålesund weather station that provides our soil and air temperature data, on a small peninsula with a south-facing aspect, exposing the soils there to more direct solar radiation than at the weather station site, which is characterized by a north-facing aspect. This difference in aspect likely results in higher surface and soil temperature at the Kapp Guissez site (Lambert and Roberts, 1976; Kang et al., 2000; Monteith and Unsworth, 2013). Taken together, we suggest that uncertainties in the exact soil depth of the Kapp Guissez samples, and variability in local climate conditions between the Kapp Guissez soil sites and the Ny-Ålesund weather station are sufficient to account for the differences between the measured Ny-Ålesund soil temperatures and the

Kapp Guissez soil carbonate T(Δ_{47}) values. The $\delta^{18}O$ anomalies fall within the uncertainty of the 0‰ line regardless of whether the anomalies are calculated using the maximum or minimum meteoric water $\delta^{18}O$ estimates (Fig. 3.5). Based on these observations, we interpret the High Arctic as being consistent with equilibrium summer season carbonate formation.

While we do not see evidence of the High Arctic T(Δ_{47}) and $\delta^{18}O$ being significantly and systematically different from the expected equilibrium carbonate values, $\delta^{13}C$ values are very enriched relative to the $\delta^{13}C$ of local soil CO_2 (Fig. 3.6; Marlin et al., 1993). Unlike the Δ_{47} and $\delta^{18}O$ values, the carbonate $\delta^{13}C$ values for the Svalbard samples are inconsistent with simple equilibrium carbonate formation. The samples from both the Kapp Guissez and Cannes sites are enriched by ~4 and ~10‰ respectively, relative to the –20‰ soil CO_2 $\delta^{13}C$ values reported at the Cannes site by Marlin et al. (1993) (Fig. 3.6). Courty et al. (1994) reported similarly high carbonate $\delta^{13}C$ values for their soil carbonate samples, and explained them by invoking the same KIE (bicarbonate dehydration during cryogenic CO_2 degassing) that we suggested for our Antarctic and 4700 m Chilean samples. However, if we use this cryogenic carbonate formation to explain these anomalous carbonate $\delta^{13}C$ values, we would expect the carbonates to also have a positive $\delta^{18}O$ anomaly. In fact we observe the opposite, with the High Arctic Svalbard samples having negative $\delta^{18}O$ anomalies regardless of the assumed carbonate formation temperature (Fig. 3.5). As shown by both Clark and Lauriol (1992) and Guo (2009), the KIE associated with bicarbonate dehydration should lead to enrichment in both carbonate ^{13}C and ^{18}O, which is inconsistent with the Courty et al. (1994) interpretation. Additionally, we cannot invoke low soil respiration rates to explain the

high $\delta^{13}C$ values, as we did for the 4200 and 4500 masl Chilean Andes samples, because mean annual precipitation at the High Arctic sample sites is an order of magnitude higher than at the Chilean Andes study area, which should lead to higher soil respiration rates.

Instead of invoking disequilibrium processes or low soil respiration rates, we propose that the High Arctic Svalbard soil carbonates precipitated under conditions of isotopic equilibrium, but that the carbonate $\delta^{13}C$ values for samples from both sites have been enriched in ^{13}C due to repeated cycles of dissolution and reprecipitation. Nakai et al. (1975) and Clark and Lauriol (1992) both proposed dissolution-precipitation cycles as a method for enriching carbonate ^{13}C. Using the model and equations described in Nakai et al. (1975) (see also Clark and Lauriol, 1992) we assume that an initial equilibrium carbonate precipitated in a Svalbard soil would have a carbonate $\delta^{13}C$ value of –4‰ based on measured soil CO_2 $\delta^{13}C$ value of –20‰ at the Cannes site and the $CaCO_3$-CO_2 fractionation factor of 16‰ of Bottinga (1968). The model assumes that the initial soil carbonate undergoes partial dissolution, producing 2 mol of HCO_3^- with a $\delta^{13}C$ value of –6.4‰. Subsequent precipitation of calcite produces 1 mol of CO_2 gas with a $\delta^{13}C$ value of –17.3‰, and 1 mol of $CaCO_3$ with a $\delta^{13}C$ value of –1.3‰. Repeated cycles of similar dissolution and reprecipitation would result in a final soil carbonate $\delta^{13}C$ value of +1.4‰. This is in good agreement with the ~0‰ $\delta^{13}C$ observed at the Kapp Guissez site, and slightly less than the 5‰ $\delta^{13}C$ at the Cannes site. Courty et al. (1994) describes the environment of the Cannes soil site as a polar desert, suggesting that lower soil respiration rates may explain the slightly higher $\delta^{13}C$ value of the Cannes-62 sample. Additional support for $\delta^{13}C$ enrichment through dissolution and reprecipitation comes from the common dissolution features noted by Courty et al. (1994) on the carbonate

pendants, suggesting that carbonate dissolution and reprecipitation is an active process in the Svalbard soils.

3.6.1.2. Disequilibrium effects in coarse-matrix cryogenic soil carbonates from Antarctica and the Chilean Andes

The coarse-matrix soil carbonates from Antarctica and the 4700 masl Chilean Andes site can be positively identified as cryogenic soil carbonates based on their isotopic anomalies. Regardless of the assumed temperature of carbonate formation, the estimated disequilibrium in the Antarctic and 4700 masl Chilean soil carbonates results in negative Δ_{47} anomalies and positive $\delta^{18}O$ anomalies, though one of the 4700 masl Chilean samples (Elq13-4700-20) plots very close to the Δ_{47} origin (Fig. 3.7). Similarly, at all estimated formation temperatures, the $\delta^{13}C$ values of these carbonates are higher than the expected $\delta^{13}C$ of carbonates formed in equilibrium with atmospheric CO_2, which should be the upper boundary for equilibrium soil carbonates. While arid climate processes such as evaporation and low soil respiration may be responsible for some of the observed enrichment in ^{18}O and ^{13}C (Liu et al., 1996; Quade et al., 2007), these processes are insufficient to completely explain the very positive soil carbonate $\delta^{18}O$ and $\delta^{13}C$. For example, in the Atacama Desert—which is more arid than our Chilean study area—Quade et al. (2007) observed soil carbonate $\delta^{18}O$ anomalies of up to 10‰, and soil carbonate $\delta^{13}C$ values up to 7.3‰. In contrast, in our Antarctic and 4700 masl Chilean Andes samples, we observe $\delta^{18}O$ anomalies as high as 14‰, and soil carbonate $\delta^{13}C$ values up to 10.4‰. Only kinetic fractionation processes associated with rapid bicarbonate dehydration during solution freezing can explain the large magnitude of the

highly positive $\delta^{13}C$ and $\delta^{18}O$, and the negative Δ_{47} anomalies observed in our coarse-grained matrix samples (Burgener et al., 2016).

We suggest that cryogenic carbonate formation occurs in the Antarctic and 4700 masl Chilean soils, but not at our other sample sites (3550, 3750, 4200, and 4500 masl Chilean Andes, Argentinian Andes, High Arctic, and Tibetan Plateau) due to differences in inter-cobble matrix grain size. While all of the soils described in this study have large cobbles, the Antarctic and 4700 masl Chilean soils are characterized by inter-cobble matrices that are coarse-grained (gravel-, pebble-, and sand-sized grains). In contrast, the inter-cobble matrices of the Argentinian, High Arctic and Tibetan Plateau soils all have a fine-grained component (silt sized or finer), and while the inter-cobble matrix of the lower elevation Chilean soils are dominated by sand-sized particles, they are all much more compacted than the 4700 m site. At the Arctic Svalbard site, this fine-grained component consists of dolomitic silt, while all of the Tibetan Plateau sites contain thick loess deposits that either cap the soils or form part of the inter-cobble matrix. These differences in grain size (and compaction for the four lower elevation Chilean sites) likely have a profound impact on variations in soil moisture fluctuations throughout the year, which in turn impacts the timing and style of carbonate precipitation.

It has been shown that soil sediment size plays a key role in facilitating or inhibiting CO_2 efflux out of a surface. Bouma and Bryla (2000) conducted experiments varying soil moisture and sediment size in three soil columns. They found that when irrigated, the CO_2 efflux from fine-textured soils declined drastically, and soil CO_2 concentration increased. In contrast, coarse-grained, sandy soils showed a smaller decrease in CO_2 efflux, a faster return to pre-irrigation CO_2 efflux levels, and total lower

soil CO_2 concentrations following irrigation (Bouma and Bryla, 2000). The authors attributed these differing soil CO_2 responses to two factors: (1) coarse-grained soils have a larger pore-space volume than fine-grained soils (the study reported that total porosity decreased from 51% for an experimental soil composed of 96% sand, to 40% for an experimental soil composed of 45% silt and 28% clay), and (2) coarse-grained soils tend to dry faster than fine-grained soils after a wetting episode. Because of their larger pore space, coarse-grained soils preserve more open, interconnected passages for CO_2 transport and efflux even when the soil is wet, while the smaller poor spaces of finer-grained soils tend to be clogged by soil water during wetting episodes, inhibiting CO_2 transport and efflux. This observation is consistent with a compilation of permeability values for a suite of soils with grain sizes ranging from gravel to clay, which shows that soil permeability ranges from a high of 5.0×10^{-2} m s^{-1} for graded gravels with little to no fines, to as low as 7.0×10^{-10} m s^{-1} for compacted silts (Leonards, 1962; Carter and Bentley, 1991; Swiss Standard SN 670 010b, 1999; West, 2010; Dysli and Steiner, 2011). Based on these findings, we suggest that the rate of bicarbonate dehydration—and associated CO_2 degassing in cryogenic soils—is limited by the soil pore space and permeability. Soils with coarse-grained inter-cobble matrices permit rapid CO_2 degassing, leading to the KIE observed in our Antarctic and Chilean carbonate samples. Soils with finer grained inter-cobble matrices, such as the Tibet, 3550 masl Chilean, and Svalbard High Arctic sites, inhibit CO_2 degassing by reducing CO_2 efflux from the soil and increasing CO_2 concentration within the soils. Carbonate formation at the latter soils would thus be restricted to “normal” equilibrium growth during the summer season.

We note that other processes related to, or independent of, soil sediment grain size, may also play a role in determining whether a particular cold climate soil produces cryogenic soil carbonates. For example, under equal climate conditions, fine-grained soils will be wetter than coarse-grained soils, due to their lower porosity and permeability. During freezing events, the temperature of wetter soils will take longer to drop below 0 °C due to the "zero curtain effect", which refers to the effect of latent heat in sustaining soil temperatures near 0 °C during freezing or thawing events (Romanovsky and Osterkamp, 2000; Outcalt et al., 1990). Importantly, the duration of this zero curtain effect is controlled in part by the amount of moisture in the soil (e.g., wetter soils experience a longer zero curtain effect; Kelley and Weaver, 1969). In some locations, the zero-curtain effect has been observed to keep soil temperatures near 0 °C for up to a month (Kelley and Weaver, 1969). It is possible that a delay in complete freezing of any soil water due to the zero curtain effect could provide sufficient time for the DIC pool in a fine-grained soil to reach clumped and stable isotopic equilibrium, meaning that any soil carbonates produced in such a soil would not record the KIEs associated with bicarbonate dehydration.

In contrast, the presence or absence of a winter snowpack over a soil is not dependent on the soil matrix grain size, but may still affect whether or not cryogenic carbonate formation occurs. The presence of an overlying snowpack increases soil CO_2 concentrations by acting as an impermeable barrier that traps gases within the soil (Hinkle, 1994). Solomon and Cerling (1987) developed a model that showed the soil CO_2 concentrations at 35 cm depth increased by 15 times due to the presence of a snowpack. Higher soil CO_2 concentrations would limit CO_2 degassing from the soil water DIC pool

and may even drive Eq. (3.3) to the left, resulting in calcite dissolution. Under such circumstances cryogenic carbonate formation would be unlikely to occur.

However, we note that potential snowpack effects are unlikely to be a factor in most of our study areas due to the local arid at those sites. Accurate, long-term measurements of snowfall at the Antarctic and 4700 masl Chilean site are unavailable (Hagedorn et al., 2007), but a review of Landsat imagery suggests that extended periods of snow cover at all of the Chilean soil sites are rare (LAND-SAT 1– 5 MSS, 4–5 TM, and 7 ETM images from the USGS Earth Explorer web page, www.earthexplorer.usgs.gov). In the Dry Valleys, Antarctica, snowfall is also rare and can be as low as 7 mm per year (Hagedorn et al., 2007), though some studies suggest long-term snowfall rates are 100–200 mm annually (Schwertferger, 1984). Additionally, weather station data from the three Tibetan Plateau sites (Lhasa, Shigatse, and T'u-ko-erh-ho-kung) record almost no snowfall over the period 1980 to 2000, which is consistent with the dry winter, wet summer climate systems that dominate the Tibetan Plateau. Landsat imagery from the three Tibetan Plateau sites largely agrees with the weather station data; while imagery from the T'u-ko erh-ho-kung region suggests that brief snowfall events are more common in that area, the snow typically melts within a matter of days. We suggest that at such arid sites, the impact of snow cover on cryogenic carbonate development is negligible. In contrast, over the period 2008–2015, weather station data from Ny-Ålesund shows mean winter snow depths of 27 cm (maximum: 43 cm, minimum: 10 cm, r = 16 cm), suggesting that snow effects could play a role in inhibiting the formation of cryogenic carbonates at the two Svalbard soil sites.

3.6.2. Isotopic disequilibrium in sub-glacial carbonates

We expected to observe evidence of KIE in sub-glacial carbonates due to the narrowly constrained, cryogenic temperature range of carbonate formation in the sub-glacial environment (–1 to 0 °C) as described in Section 3.3.1. Consistent with this hypothesis, the sub-glacial carbonates from Blackfoot and Castleguard glaciers both have large negative Δ_{47} anomalies. However, the $\delta^{18}O$ anomalies are more variable in terms of both magnitude and sign. Like the Antarctic and Chilean soil carbonates, the Castleguard glacier carbonates have a negative Δ_{47} anomaly and a positive $\delta^{18}O$ anomaly; however, the mean Δ_{47} anomaly of the Castleguard glacier carbonates is an order of magnitude larger than that of the coarse-matrix soil carbonates from Antarctica and the 4700 masl Chilean Andes site (–0.27‰ versus –0.023 to –0.060‰, respectively), while the $\delta^{18}O$ anomaly is slightly smaller (4.1‰ versus 9.1 to 11.2‰). The negative Δ_{47} anomaly and positive $\delta^{18}O$ anomaly observed in the Castleguard glacier carbonates are consistent with the direction of KIE associated with rapid CO_2 degassing via bicarbonate dehydration, as hypothesized for the coarse-matrix Antarctic and 4700 masl Chilean soil carbonates; however, the fact that the Castleguard glacier carbonate Δ_{47} anomalies are more than an order of magnitude larger than the coarse-matrix Antarctic and 4700 masl Chilean Δ_{47} anomalies suggest that there is some fundamental difference between cryogenic carbonate precipitation in the sub-glacial and soil environments.

In contrast to the Castleguard glacier carbonates, the Δ_{47} and $\delta^{18}O$ anomalies calculated for the Blackfoot glacier carbonates are both negative (–0.078 and –7.52‰ respectively for Δ_{47} and $\delta^{18}O$). The Δ_{47} and $\delta^{18}O$ anomalies are broadly consistent with the KIE associated with a high pH environment (Fig. 3.3), but we lack pH data for the

sub-glacial environment at Blackfoot glacier to confirm this possibility. Unlike the negative Δ_{47} and $\delta^{18}O$ anomalies, our Blackfoot glacier samples yield $\delta^{13}C$ values that are slightly more negative than those reported in Hanshaw and Hallet (1978), but that appear to be in isotopic equilibrium with the local carbonate bedrock.

We speculate that the difference in magnitudes of the Δ_{47} anomalies, and the different signs of $\delta^{18}O$ anomalies for the sub-glacial carbonates from the two different sites, is likely due to differences in meltwater salinity caused by variations in sub-glacial plumbing. Hanshaw and Hallet (1978) proposed that sub glacial meltwater flow could be divided into two different end-member states. (1) In the "local flow" model, the sub-glacial film (from which the sub-glacial carbonates precipitate) is isolated from the bulk of the subglacial meltwater, which is funneled to the glacial tongue via discrete channels and/or tunnels. (2) In the "throughflow" model, most of the sub-glacial meltwater is distributed throughout the sub-glacial film, and thus free to interact with the carbonate precipitating solution. We suggest that salinity levels in the "local flow" model may reach much higher levels than in the "through-flow" model, due to the isolated nature of the sub-glacial films. Hill et al. (2014), have shown that in solutions where salinity is at least 50 g kg^{-1}, KIEs that are typically associated with pH levels > 10 will manifest at lower pH levels (pH = 8–9). Hanshaw and Hallet (1978) argued that sub-glacial flow beneath Blackrock glacier is most similar to the "local flow" model. We propose that this local flow style resulted in higher salinity levels in the sub-glacial films and a lower pH threshold for the onset of KIEs, which explains why the Blackfoot sub-glacial carbonate Δ_{47} and $\delta^{18}O$ anomalies are consistent with the positive pH effect as illustrated in Fig. 3.7. In contrast, the sub-glacial flow beneath Castleguard glacier may be more characteristic

of the ‘‘through-flow” model, resulting in lower salinity levels that favor KIEs driven by cryogenic carbonate formation and bicarbonate dehydration (resulting in negative Δ_{47} anomalies and positive $\delta^{18}O$ anomalies) rather than KIEs associated with the pH effect. Future work should focus on testing this hypothesis by making direct measurements of glacier meltwater pH and investigating how different styles of sub-glacial water flow affect meltwater salinities and resulting carbonate records.

Despite their well constrained formation temperatures and expected equilibrium $\delta^{18}O$ values, the sub-glacial carbonates proved to have larger and more variable Δ_{47} and $\delta^{18}O$ anomalies than the soil carbonates, making it a challenge to meaningfully compare and contrast the two different carbonate types. It is clear that sub-glacial carbonates are affected by a variety of formation processes, as detailed in Fairchild et al. (1994), and that this in turn can have a dramatic impact on their isotopic compositions. The Δ_{47} compositions of sub-glacial carbonates likely will not be useful in paleoclimate reconstructions or in reconstructing the oxygen isotope composition of paleo-glaciers, but they do offer unique insight into the formation processes of sub-glacial carbonates—and may present the intriguing possibility that sub-glacial carbonate Δ_{47} and $\delta^{18}O$ anomalies can be used to identify differences in the sub-glacial plumbing of ancient glaciers.

3.6.3. Implications for paleoclimate and paleoaltimetry reconstructions from soil carbonates

The results of this study provide a benchmark for testing whether the findings of past studies of soil carbonates may have been affected by the inclusion of disequilibrium cryogenic soil carbonates. For example, Quade et al. (2011) reported apparent $T(\Delta_{47})$ values from nine soil carbonate samples that were higher than modeled soil temperatures

(e.g., the soil carbonate Δ_{47} values were lower than expected). They suggested that the discrepancy was simply the result of inaccurate modeling of local soil temperatures. Burgener et al. (2016) presented the alternative hypothesis that a cryogenic origin might explain the low Δ_{47} values, but did not attempt to calculate Δ_{47} and $\delta^{18}O$ anomalies for the Tibetan samples. The new Δ_{47}, $\delta^{18}O$, $\delta^{13}C$ values reported in this study, along with actual measurements of local summer temperatures, show that the Tibetan samples are not cryogenic in origin and are in fact consistent with the expected equilibrium carbonate isotope composition.

Our findings have important implications for terrestrial paleoclimate and paleoelevation studies. Soils with coarse-grained inter-cobble matrices in high latitude and high elevation sites are likely to produce disequilibrium soil carbonate pendants and should be avoided for quantitative paleoclimate and paleoelevation reconstructions. However, soil carbonates from high elevation sites may still provide important information about a region's tectonic and climate history. For example, soil carbonate-based paleoelevation studies typically rely on the well-known negative correlation between soil carbonate $\delta^{18}O$ and elevation, and the positive correlation between environmental temperatures estimated using Δ_{47} and elevation (Fig. 3.9A). Abrupt departures from that pattern (e.g., an abrupt increase in $\delta^{18}O$ and decrease in Δ_{47} with increasing elevation) may be evidence of a rapid shift to a cryogenic environment (Fig. 3.9B) due to uplift or climate change. Additionally, with regard to carbonate-bearing soils in deep time, the presence or absence of soil carbonate pendants that exhibit Δ_{47} and $\delta^{18}O$ anomalies indicative of cryogenic KIEs could provide constraints on the latitudinal limits of cold environments during greenhouse periods such as the Cretaceous and Eocene.

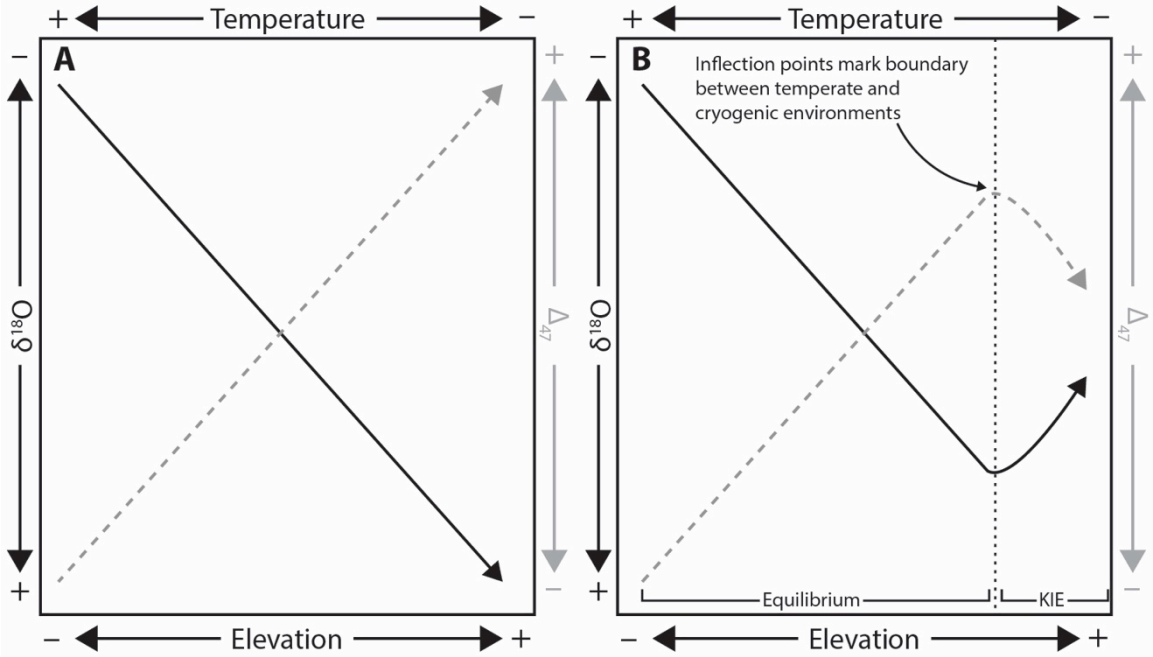

In contrast, high latitude and high elevation soils with a fine-grained inter-cobble matrix should produce equilibrium soil carbonates that are suitable for paleoclimate

Figure 3.9. Schematic illustration showing how kinetic isotope effects (KIE) associated with cryogenic carbonate formation can affect the relationship between $\delta^{18}O$, Δ_{47} and elevation. Panel A shows the typical negative correlation between soil carbonate $\delta^{18}O$ (black line) and elevation, and the typical positive correlation between soil carbonate Δ_{47} (dashed gray line) and elevation or temperature. Panel B illustrates how a transition from a typical warm or temperature climate to a cold climate at high elevation (marked by vertical dotted line) may result in high elevation soil carbonates that have increasing $\delta^{18}O$ values (positive $\delta^{18}O$ anomaly as calculated in this paper) and decreasing Δ_{47} values (negative Δ_{47} anomaly). Identification of such signals in paleoclimate datasets will help identify temporal or spatial transitions to cold climates.

reconstructions. Past studies (e.g., Vogt and Corte, 1996) have identified Pleistocene and Holocene calcic paleosols with fine-grained inter cobble matrices in current or former cold-climate environments. Such soils may offer an important window into how different terrestrial environments (e.g., mountains high elevation sites versus low elevation, high latitude sites) responded to rising temperatures and changing precipitation patterns following deglaciation at the Pleistocene/Holocene boundary.

Importantly, our findings suggest that carbonate-bearing soils that are appropriate for paleoclimate studies can be identified in the field using observations of soil matrix

grain size, which should enable fieldworkers to rapidly identify soil carbonates that are likely to yield equilibrium Δ_{47}, $\delta^{18}O$, $\delta^{13}C$ values. Our work also highlights the complementary nature of clumped and conventional stable isotope analyses to identify and understand disequilibrium processes in soil carbonates. For example, based on Δ_{47} or $\delta^{18}O$ values alone, it would be very difficult to determine whether our 4700 masl Chilean Andes samples represent equilibrium soil carbonates with a warm season bias, or cryogenic carbonates with lower-than-expected Δ_{47} due to KIEs; however, by using Δ_{47} and $\delta^{18}O$ anomalies in tandem, with supporting information from a comparison of expected and observed carbonate $\delta^{13}C$ values, we can positively identify the carbonates as having been affected by disequilibrium processes. Finally, our findings also point to the need for additional work to improve our understanding of how soil moisture and soil grain size interact to affect soil carbonate formation, both in terms of the timing of carbonate formation, and in terms of equilibrium versus disequilibrium isotope processes.

We note that other kinetic processes have been implicated as sources of disequilibrium isotope compositions in pedogenic carbonates from the Mojave Desert and Hawaii. McFadden et al. (1998) described carbonate ‘‘collars” that occur on large surficial clasts of Holocene and Pleistocene soils in the Mojave Desert and yield enriched $\delta^{18}O$ and $\delta^{13}C$ values relative to the isotopic composition of local waters and soil CO_2. They attributed these heavy carbonate $\delta^{18}O$ and $\delta^{13}C$ values to rapid soil water evaporation that preferentially removed ^{18}O and ^{13}C from the soil solution. Quade et al. (2013) reported very low Δ_{47} values (high $T(\Delta_{47})$ temperatures) for fissure-filling soil carbonates in Hawaii. They hypothesized that because these carbonates were exposed to advecting air, they might have been affected by kinetic isotope effects. Together with our

own study of cryogenic soil carbonates, these studies show that soil carbonates may be affected by any number of different kinetic, non-equilibrium processes depending on climatic and soil conditions. The same approach of paired clumped and stable isotope investigations employed in this study to identify and constrain cryogenic kinetic isotope effects can be used to better characterize the disequilibrium processes associated with the Mojave soil carbonate collars and the Hawaii fissure carbonates.

We suggest that future studies of kinetic isotope effects in cryogenic soil carbonates should focus on three key areas: First, do cryogenic soil carbonates have distinct crystal growth structures, grain sizes, and crystal forms that are distinct from the calcite morphology of equilibrium soil carbonates? Second, why do cryogenic soil (this study) and cave carbonates (Kluge et al., 2014) fall off the 0.02‰ Δ_{47}-$\delta^{18}O$ correlation line modeled by Guo (2009) for bicarbonate dehydration? Third, future studies should target soils and environments that will allow a rigorous study of how other processes beyond soil sediment grain size (e.g., soil moisture, presence/absence of snow cover) inhibit or promote cryogenic soil carbonate formation.

3.7. Conclusion

Our findings show that soil matrix grain size plays a critical role in determining whether soil carbonates from cold climates precipitate under conditions of isotopic equilibrium or disequilibrium (Fig. 3.7). Arid soils with coarse-grained inter-cobble matrices are more susceptible to KIEs associated with bicarbonate dehydration, due to rapid CO_2 degassing. In contrast, soils with high soil moisture levels and fine-grained inter-cobble matrices experience reduced rates of soil CO_2 degassing, which inhibits the KIEs associated with bicarbonate dehydration during carbonate precipitation. Our findings provide important

new information about (1) the importance of both annual changes to soil moisture and soil sediment size in controlling the timing and style of soil carbonate formation (e.g., Burgener et al., 2016; Gallagher and Sheldon, 2016); (2) the utility of paired clumped and stable isotope studies in identifying and describing disequilibrium processes in carbonate formation; and (3) guidelines for determining whether past studies of soil carbonates may have been influenced by the presence of disequilibrium carbonates.

The Δ_{47}, $\delta^{18}O$, $\delta^{13}C$, and calculated Δ_{47} and $\delta^{18}O$ anomalies of the Blackfoot and Castleguard glaciers are highly variable, and we attribute this observed variability to differences in sub-glacial water flow, as discussed by Hanshaw and Hallet (1978). In glaciers that experience "local flow" (e.g., channelized sub glacier meltwater flow), the isolated pockets of meltwater film may see increased salinity levels that result in a prominent pH effect that is manifested as negative Δ_{47} and $\delta^{18}O$ anomalies. Alternatively, in glaciers characterized by a "through-flow" regime (e.g., distributed meltwater flow across the entire base of a glacier) salinity levels likely remain low and bicarbonate dehydration associated with cryogenic carbonate formation is the dominant KIE process. Currently, no pH data exists for waters derived from the two glaciers analyzed in this study. In order to better characterize the clumped isotope composition of sub-glacial carbonates, and understand their formation processes, future modeling and sampling work should focus on constraining sub-glacial solution pH and solute chemistry at the many sites where subglacial carbonates have been identified.

Our results suggest that high latitude and high elevation soil carbonates from soils with a fine grained inter-cobble matrix are a useful archive of paleoclimate conditions in environments that are particularly vulnerable to climate change. Such soil carbonates

should be targeted in future studies to better understand how high latitude and high elevation regions responded to previous periods of climate change, such as the repeated transitions from glacial to interglacial climates that have occurred over the course of the Pleistocene and Holocene.

3.8 Chapter Three Acknowledgements

The authors thank Dr. Weifu Guo of the Woods Hole Oceanographic Institution for his contributions to the early development of this project, and Dr. Gregory Hoke for his collegial review of the manuscript. The authors acknowledge support from NSF Grants EAR-1252064 and EAR-1156134 to KWH.

Chapter 4: Revisiting the Equable Climate Problem During the Late Cretaceous Greenhouse Using Paleosol Carbonate Clumped Isotope Temperatures from the Campanian Western Interior Basin

Co-authored by: Ethan Hyland[a], Katharine W. Huntington[b], Julia R. Kelson[b], Jacob O. Sewall[c]

[a] – Department of Marine, Earth, and Atmospheric Sciences, North Carolina State University, Raleigh, NC, United States

[b] – Department of Earth and Space Sciences, University of Washington, Seattle, WA, United States

[c] – Department of Physical Sciences, Kutztown University of Pennsylvania, Kutztown, PA, United States

4.1. Abstract

Greenhouse climates such as the Late Cretaceous period provide important reference frames for understanding modern anthropogenic climate change. Late Cretaceous terrestrial climate proxies have been interpreted as evidence for "equable" climates with high-latitude mean annual temperatures consistently above 0 °C, reduced latitudinal temperature gradients, and reduced seasonal variations in temperature. However, climate models have largely failed to reproduce these reconstructions unless parameters such as atmospheric CO_2 concentrations are set to unreasonable values. To help resolve such model-proxy disagreements, we reconstruct mean annual range in temperature (MART) for the Campanian (~75 Ma) Kaiparowits (south-central Utah) and Two Medicine (northwest Montana) Formations using warmest mean monthly

temperature reconstructions from the clumped isotope composition of paleosol carbonate nodules, and previous reconstructions of local mean annual air temperatures. We also evaluate the validity of several common assumptions made in constructing MART in two novel ways. First, MART is commonly calculated as twice the difference between local mean annual air temperature and warmest mean monthly temperature, and we validate this method by estimating modern MART for a range of environments using climate reanalysis data. Second, we constrain the effect of radiative soil heating on our soil carbonated-based temperature estimates by reviewing paired soil and air temperature data from the Soil Climate Analysis Network (SCAN), and show that for most environments likely to be preserved in the geologic record, soil temperatures are <3 °C higher than air temperatures. Finally, we evaluate the use of the bulk elemental proxies (PWI and CIA-K) in certain paleosol environments. Our clumped isotope analysis of pedogenic carbonate nodules suggests that warmest mean monthly temperatures were 30 to 35 °C at both study sites, and that MART was 21 to 29 °C for the Kaiparowits Formation, and 21 to 27 °C for the Two Medicine Formation. Our findings suggest that mid-latitude Late Cretaceous MARTs were similar to modern ranges in mid-latitude seasonal temperature, and much (>15 °C) larger than previous estimates of Late Cretaceous MART based on other proxy records. These results add to a growing body of literature showing that terrestrial MART during ancient greenhouse periods was not significantly different from modern seasonal temperature variations.

4.2. Introduction

Periods of elevated earth surface temperatures (e.g., greenhouse episodes) like the Late Cretaceous are natural laboratories for studying how the Earth's climate system

behaves under elevated atmospheric CO_2 concentrations. However, our understanding of terrestrial climate conditions during these greenhouse periods is hampered by long-standing disagreement between proxy reconstructions and model simulations (e.g., Donnadieu et al., 2006; Huber, 2008; Sloan and Morrill, 1998; Sloan and Barron, 1990; Barron, 1987 and 1983). One of the most well known of these proxy-model discrepancies is the inability of climate models to simulate the mean annual range of temperature (MART) evidenced by terrestrial proxy records, which show above-freezing winter temperatures and warm mean annual temperatures at mid- to high-latitudes during the Late Cretaceous and Early Paleogene (Upchurch et al., 2015). This issue is a key component of the "equable climate problem", and is considered a classic unsolved question in paleoclimatology (Huber and Caballero, 2011; Spicer et al., 2008; DeConto et al., 2000).

The Campanian (~75 Ma) sedimentary record of western North America is an exceptional continental-scale record of climatic, geologic, and biologic changes during the Late Cretaceous, and provides an opportunity to constrain MART during a greenhouse period. The western margin of the Western Interior Seaway contains numerous well-dated and correlated formations that contain abundant carbonate-bearing paleosols (e.g., Foreman et al., 2015, 2011; Roberts, 2007; Nordt et al., 2006; Rogers, 1995). These carbonate-bearing paleosols are an archive of changing paleoclimate conditions, and can provide quantitative reconstructions of key climate parameters such as Earth-surface temperature and mean annual precipitation (Sheldon and Tabor, 2009). Importantly, these formations also contain an extensive, intensively studied fossil record (Gates et al., 2010), making it possible to not only reconstruct Late Cretaceous

paleoclimate conditions, but to examine the impact of climate parameters like MART on the evolution and distribution of terrestrial flora and fauna.

The main objective of this study is to revisit the question of seasonal equability in greenhouse climates and to place new constraints on MART during the Late Cretaceous by using carbonate clumped isotope paleothermometry of pedogenic (formed in soil) carbonate nodules. Specifically, we reconstruct warmest mean monthly soil and air temperatures using paleosols from two Campanian (~75 Ma) sedimentary deposits along the western margin of the Western Interior Seaway (WIS): the Kaiparowits Formation (KF), which crops out in modern south-central Utah, USA, and the Two Medicine Formation (TMF), in modern northwestern Montana, USA. These reconstructed summer temperatures are paired with previously reported estimates of mean annual air temperature (MAAT) to calculate MART based on the assumption that the annual distribution of air temperatures is symmetrical about the MAAT; these previous MAAT estimates are also used to test the applicability of bulk elemental proxies (PWI, CIA-K) to paleosols from KF and TMF. In addition to providing new constraints on climate in western North America during the Late Cretaceous, we also examine the errors and uncertainties associated with several common assumptions made when calculating summer air temperatures and MART with clumped isotope data. Taken together, our results provide a framework for more accurate estimates of paleo-MART during greenhouse periods, and more reliable climate interpretations of paleosol carbonates. Our MART reconstruction for the Late Cretaceous expands the available estimates of seasonality during greenhouse periods, providing a new point of comparison for similar work in the Paleocene and Eocene (e.g. Hyland et al., 2018; Snell et al., 2013).

4.3. Background

4.3.1 Global and North American climate during the Late Cretaceous

Previous proxy reconstructions have characterized Late Cretaceous global climate as warm and highly equable, with a reduced latitudinal temperature gradient and—of particular interest with respect to this study—reduced MART. Globally averaged mean annual air temperature (MAAT) was 6 to 14 °C warmer during the Late Cretaceous than the modern (Niezgodski et al., 2017; DeConto, 1999; Barron et al., 1995). Proxy reconstructions of terrestrial latitudinal temperature gradients during the Campanian and Maastrichtian (latest Cretaceous) range from 0.3 to 0.4 °C °latitude^{-1} (Amiot et al., 2004; Wolfe and Upchurch, 1987) and are much lower than the modern temperature gradient (~0.6-1.0 °C °latitude^{-1}; Hay, 2008; Greenwood and Wing, 1995). Quantitative estimates of Late Cretaceous MART are scarce, but suggest reduced MART (Hunter et al. 2013; Wolfe and Upchurch, 1987). However, these previous reconstructions in terrestrial and marine settings show little or no consistent trend with increasing latitude (de Winter et al., 2017; Wolfe and Upchurch, 1987), as would be expected based on modern climate observations.

In western North America, numerous studies have presented paleotemperature reconstructions during the Campanian. Some of these studies have focused on specific formations (e.g., Miller et al., 2013, Nordt et al., 2011; Nordt et al., 2003), and others focused on regional paleoclimate/latitudinal temperature trends (e.g., Wolfe and Upchurch et al., 1987). Miller et al. (2013) reported a MAAT of 20±2 °C for the KF based on leaf-margin analysis (LMA), and Foreman et al. (2011) estimated a MAAT of 16±4 °C for the TMF based on reconstructions from the climate leaf analysis multivariate

programe (CLAMP) by Wolf and Upchurch (1987). After accounting for the Late Cretaceous latitudinal temperature gradient of 0.3 to 0.4 °C °latitude^{-1}, temperature reconstructions from other coeval formations in relatively close proximity to the KF and TMF suggest that MAAT was between 17 and 21 °C for the KF (Upchurch et al., 2015; Miller et al., 2013; Wolfe, 1990), and 14 to 19 °C for the TMF (Barrick et al., 1999; Van Boskirk, 1998; Wolfe and Upchurch, 1987).

Precipitation rates are notoriously difficult to constrain, but some quantitative and qualitative proxy and model mean annual precipitation (MAP) estimates for Late Cretaceous North America do exist. Based on the distribution of leaf sizes from multiple North American fossil leaf assemblages, precipitation appears to have been fairly constant throughout the year below paleolatitude ~40 °N, but more seasonal at higher latitudes (Falcon-Lang, 2003, Wolfe and Upchurch, 1987). No quantitative estimates of MAP exist for the TMF; however, studies using evidence from Maastrichtian paleosols in Montana suggest that Late Cretaceous MAP was 900–1200 mm at ~49 °N (Falcon-Lang, 2003; Retallack, 1994). Miller et al. (2013) estimated MAP to be 1780 mm (1240 to 2550 mm) for the KF based on the leaf size distribution of multiple KF fossil leaf assemblages. Falcon-Lang (2003) showed that the TMF likely experienced large seasonal changes in precipitation based on an analysis of growth interruptions in fossil trees, which is consistent with modeling work done by Fricke et al. (2010) and Sewall and Fricke (2013) suggesting that there was a significant seasonal (monsoonal) pattern to North American precipitation during the Late Cretaceous.

4.3.2. Estimating Late Cretaceous MART in North America

Available proxy reconstructions for Late Cretaceous North America suggest MART values that are significantly smaller than modern MART at similar latitudes. Early leaf physiognomy studies suggested that MART in Late Cretaceous North America was just 8 °C at a paleolatitude of 52 to 55° N (Wolfe and Upchurch, 1987), and CLAMP analyses summarized by Hunter et al. (2013, see Tables 2 and 3) suggest a similarly small North American MART (~10 °C). These MART estimates are comparable to the mean MART of 13.5 °C reconstructed for Eocene North America (Greenwood and Wing, 1995), and much lower than the ~25 to 30 °C MART estimated for modern North America at 50 to 55° N from ERA-Interim climate reanalysis data. The low MARTs estimated for both the Late Cretaceous and Eocene appear to be consistent with qualitative evidence for winter temperatures above 5 °C based on the presence of fossil crocodilians and palms at high latitudes during these time periods (Markwick, 1998; Greenwood and Wing, 1995).

However, these proxy-based reconstructions of an equable Late Cretaceous/Eocene climate clash with model simulations that fail to reproduce such low MARTs. For example, Spicer et al. (2008) presented a detailed proxy-model comparison of Late Cretaceous Siberian seasonal temperatures, reporting CLAMP-derived MAAT, coldest mean monthly air temperature, and warmest mean monthly temperature values of 13.1, 5.8, and 21.1 °C (MART = 15.3 °C). They found that model simulations using a range of orbital configurations, atmospheric CO_2/CH_4 concentrations, oceanic heat transport schemes, and vegetation conditions underestimated proxy coldest month mean air temperature values by ~17 °C, and overestimated proxy warmest month mean air

temperature values by ~8 °C. Similarly, Hunter et al. (2013) conducted a model-proxy comparison of North American Late Cretaceous temperatures and showed that their model simulations underestimated CLAMP coldest month mean air temperature reconstructions by up to 12 °C depending on model parameters.

The inability of climate models to reproduce equable MART during greenhouse periods has been attributed to issues with both proxy records and climate models (Huber, 2008; Deconto et al., 1999). For example, leaf physiognomy proxies (LMA, CLAMP, and digital leaf physiognomy) of MAAT must take into account non-climate factors that affect leaf physiognomy (Peppe et al., 2011; Kowalski and Dilcher, 2003; Gregory-Wodzicki, 2000), as well as (in the case of CLAMP) methodological issues (Royer et al., 2012). However, despite these challenges, the relationship between MAAT and leaf margin morphology has been shown to be robust and statistically significant across geographic areas (Peppe et al., 2017; Royer et al., 2012). In contrast, leaf physiognomy reconstructions of coldest and warmest month temperatures suffer from all of the same challenges as MAAT reconstructions, and face additional problems as well. For example, coldest and warmest month temperatures are more likely to be regionally dependent than MAAT, and the two parameters are susceptible to covariation (Peppe et al., 2011, 2010; Jordan, 1996, 1997b). With respect to paleoclimate model simulations, the proposed issues appear to be less well defined, but are thought to include: 1) limited model spatial and temporal resolution (Snell et al., 2013; Sewall and Sloan, 2006); 2) unrealistic or undefined land cover schemes (Thrasher and Sloan, 2010); and 3) inaccurate or poorly resolved boundary conditions (e.g., the presence of oceanic gateways; Hunter et al., 2013; Donnadieu et al., 2006).

Previous terrestrial proxy-model comparison studies of the Late Cretaceous and Eocene relied almost exclusively on leaf or animal fossils (e.g., Hunter et al., 2013; Spicer et al., 2008; Barrick et al., 1999; Barron, 1983). To build on past estimates of seasonal temperature during the Late Cretaceous, we reconstruct MART from the clumped isotope composition of pedogenic carbonates, the geochemical composition of paleosol Bt horizons, and previously published floral/faunal proxy reconstructions. Following Snell et al. (2013), we calculate Late Cretaceous MART as twice the difference between previous MAAT estimates and soil carbonate clumped isotope formation temperatures. Additionally, we provide important new constraints on this method's accuracy by: 1) constraining the errors associated with calculating MART from just warmest month air or soil temperatures and MAAT; and 2) employing long term modern soil and air temperature datasets to estimate the typical range of radiative soil heating (ST_{RH}) caused by direct solar radiation, allowing for more accurate conversion of soil temperatures to air temperatures.

4.3.3. Geologic setting

The Late Cretaceous non-marine sedimentary rocks of the TMF and KF are part of a large, north-south trending clastic wedge that was deposited into the subsiding Cordilleran foreland basin (e.g., the Western Interior Basin) by eastward-flowing fluvial systems beginning in the middle Jurassic and extending through the Eocene (Fig. 4.1; Foreman et al., 2011; Roberts, 2007; Kauffman and Caldwell, 1993). This body of sedimentary rocks formed a broad alluvial and coastal plain between the fold-and-thrust belt and the western margin of the WIS that stretched from the southern United States into northern Canada. Broadly speaking, both the TMF and the KF represent alluvial

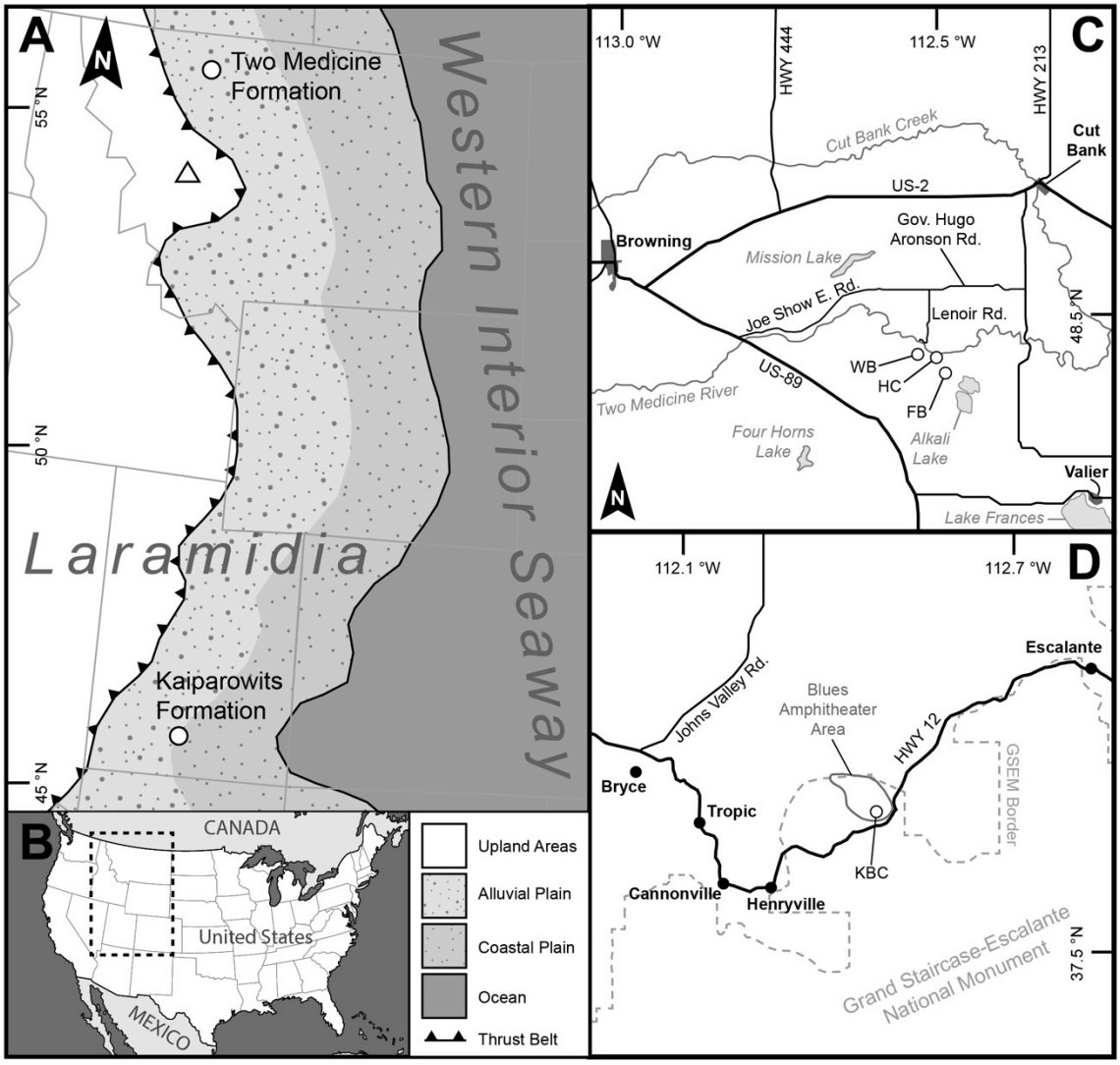

Figure 4.1. A) The western margin of the Western Interior Seaway during the late Campanian (~75 Ma). The Kaiparowits Formation and Two Medicine Formation study areas are marked with white circles. White triangles show the position of active volcanic centers. Paleolatitudes from Miller et al. (2013). B) Locator map; dashed black line shows the location of A. C) Two Medicine Formation study area near Cut Bank and Browning, Montana. D) Kaiparowits Formation study area near Bryce and Escalante, Utah.

plain depositional environments; however, the TMF was characterized by relatively lower sedimentation rates and a semi-arid environment (Rogers, 1995), while the KF is notable for having the highest calculated sedimentation rates of any formation along the Late Cretaceous WIS, and is characterized by an extremely humid, wet environment (Roberts, 2007). Evaluation of seasonality in these two distinct environments allows us to explore the sensitivity of our proxies to pedotypes, and make robust MART estimates.

The TMF is composed of alluvial sediments that were deposited during two third-order regressive/transgressive cycles (R7-T8 and R8-T9) of the WIS (Foreman et al., 2011, 2008; Rogers, 1998). The formation is characterized by laterally extensive fluvial fine- to medium-grained sandstones (braided and meandering channel facies) that alternate with siltstone interfluvial facies characterized by well-developed paleosols and rare lacustrine units (Foreman et al., 2011; Rogers, 1998). The paleosols are relatively well developed and are characterized by meter scale red horizons that are typically mottled and contain root traces (Foreman et al., 2011). Numerous bentonitic ash layers are intercalated between the TMF paleosols. These bentonites were described and dated by Rogers et al. (1993) and Foreman et al. (2008), yielding $^{40}Ar/^{39}Ar$ ages ranging from 79.72±0.03 Ma at 80 m above the base of the TMF, to 77.52±0.03 Ma at 265 m above the base of the TMF. The latter age comes from a bentonite sample collected from the Hagan's Crossing locality measured and sampled as part of this study (Fig. 4.1).

The KF is characterized by freshwater and terrestrial depositional environments, as well as a minor section of tidally influenced environments (Roberts, 2007) that were deposited under high sediment accumulation rates (~40 cm ka^{-1} compared to ~7 cm ka^{-1} for the TMF). The KF paleosols are typically weakly developed, with drab gray colors,

Table 4.1. Basic information for the measured Kaiparowits and Two Medicine sections.

Formation	Section Name	Section Abreviation	Lat.[a] (°N)	Lon. (°W)	Paleolat.[b] (°N)	Number of Paleosols
Kaiparowits	Blue Ceratopsion	KBC	37.625	111.887	46.2	19
Two Medicine	Flag Butte	FB	48.441	112.489	56.5,53.4	12
Two Medicine	Hagan's Crossing	HC	48.455	112.502	56.5,53.4	15
Two Medicine	Western Butte	WB	48.461	112.527	56.5,53.4	16

a - Coordinates mark the location of the section base.
b - Paleolatitude from Miller et al. (2013)

incipient horizon development, and various pedogenic features typical of hydromorphic soils (e.g., gleying, siderite/pyrite accumulations). Roberts (2007) classified most of the KF paleosols as early Entisols, with rare calcite-nodule bearing Inceptisols suggestive of more prolonged pedogenic activity. These poorly developed paleosols are consistent with the high sedimentation rates, high water table, and overall humid conditions estimated for the KF. Age constraints for the KF come from four bentonite ash layers sampled by Roberts et al. (2005), which yielded $^{40}Ar/^{39}Ar$ ages ranging from 75.96±0.02 Ma at 80 m above the base of the KF, to 74.21±0.11 Ma at 790 m above the base of the KF.

4.4. Methods

4.4.1. Paleosol mapping and sampling methods

At both the KF and TMF sampling sites (Table 4.1), individual paleosols were identified and their depth profiles described based on pedogenic features such as horizonation, grain size, color, and clay accumulation, as well the as presence/absence of specific features such as carbonate nodules, mottling, root traces, and slickensides. Paleosols were characterized within the context of previously measured stratigraphic

sections (see Roberts, 2005, for a detailed description of the KF stratigraphy and Rogers, 1995, for the TMF stratigraphy). Each paleosol profile was measured and described after trenching to expose fresh material and avoid modern sediment and soil contamination. Paleosol types were classified based on the descriptive schemes of Mack et al. (1993) and Retallack et al. (1993). Where present, multiple carbonate nodules were collected to ensure adequate characterization of the clumped and stable isotope variability in each paleosol. Additionally, samples of bulk soil sediment were collected from the identified soil horizons (e.g., A, Bt, Bk, etc.) for whole rock geochemistry analysis. The KF samples were collected from the formation's proposed lectostratotype section (KBC section) as identified by Roberts (2007), while the TMF samples were collected from three sections (Hagan's Crossing, Flag Butte, and West Butte) that were previously correlated by Rogers (1995) based on the stratigraphic position of a through-going regional unconformity, and a distinct, widespread interval of lacustrine deposits.

4.4.2. Clumped and stable isotope analyses

Carbonate clumped-isotope thermometry is a thermodynamics-based measurement of carbonate formation temperature based on the ratio of multiply substituted isotopologues in a carbonate sample (e.g., the number of carbonate molecules that contain both a heavy ^{13}C and heavy ^{18}O isotope; Ghosh et al., 2006; Eiler, 2007, 2011; Eiler et al., 2014). Using this method, the clumped isotope composition (written as Δ_{47}) of soil carbonates can be used to estimate the carbonate formation temperature ($T[\Delta_{47}]$).

Clumped and stable isotope analyses (Δ_{47}, $\delta^{18}O$, and $\delta^{13}C$) of carbonate nodules (53 samples) were conducted at the University of Washington's IsoLab (detailed methods

in Burgener et al., 2016; Kelson et al., 2017; and Schauer et al., 2016). Micritic carbonate was sub-sampled from each nodule using a Merchantek micro-mill. For some of the diagenetically altered samples, only a single replicate measurement was performed. For the remaining samples, 2 to 6 replicate analyses were performed. Carbonate samples were digested in a common phosphoric acid bath at 90 °C, and the evolved CO_2 was then cryogenically separated from water and cleaned on an automated vacuum line. Carbonate standards or equilibrated CO_2 reference gases were processed between every 4-5 sample unknowns. The purified CO_2 was analyzed on a Thermo MAT253 configured to measure m/z 44-49 inclusive.

Δ_{47}, $\delta^{13}C$, and $\delta^{18}O$ values were calculated for all samples following the methods of Huntington et al. (2009) and He et al. (2012), and were corrected for ^{17}O interference using the parameters described in Brand et al. (2010) (see Daëron et al., 2016 and Schauer et al., 2016). The carbonate Δ_{47} values were calibrated to the Absolute Reference Frame (ARF) following the methods of (Dennis et al., 2011). $\delta^{13}C$ was referenced to international standards NBS-19 and LSVEC, and $\delta^{18}O$ was referenced to NBS-18 and NBS-19. The Pierce outlier test was used to identify and remove statistical outliers in the Δ_{47} values for each of the samples (Ross, 2003; Zaarur et al., 2013). Carbonate formation temperatures (T[Δ_{47}]) were calculated from the Δ_{47} results using the Δ_{47}-T calibration of Kelson et al. (2017), which was produced in the same laboratory using the same methods:

$$\Delta_{47} = \frac{0.0417 \pm 0.0013 \times 10^6}{T^2} + 0.139 \pm 0.014 \quad (1)$$

where T is temperature in Kelvin.

4.4.3. Diagenetic screening methods

Alteration of the primary clumped and stable isotope compositions of soil carbonate nodules via diagenesis can potentially destroy or modify any climate signals preserved in the samples. To avoid sampling altered material, the carbonate nodules collected for this study were assessed for alteration based on textural, cathodoluminescence (CL), and isotopic evidence. We assigned each thin-sectioned nodule to one of three categories (micritic, mixed, or sparry) based on the observed abundance, spacing (e.g., distributed evenly throughout the nodule or restricted to isolated veins), and luminescence of diagenetic sparry calcite (Fig. 4.2). Optical and CL observations of the thin sections were made using a Nikon Optiphot-2 microscope and Luminiscope ELM-3R CL system. Nodules were assigned to the micritic category if they were composed of homogenous micrite with a low luminescence. Nodules containing high luminescence spar were assigned to the mixed category if the spar was restricted to isolated veins or zones and the remaining micrite was easily sub-sampled, or to the sparry category if the nodule was composed completely of highly luminescent spar or if spar was pervasive throughout the nodule.

4.4.4. Mean annual temperature and precipitation calculations from whole rock geochemistry

The major-element composition of 25 bulk paleosol sediment samples from 12 individual Bt horizons and 5 well-developed soil profiles were measured by X-ray fluorescence (XRF) at the ALS Chemex Laboratory in Reno, Nevada. The Bt horizon compositions were used to calculate estimates of the time-averaged mean annual temperature (MAT) and mean annual precipitation (MAP) for each sample. MAT was

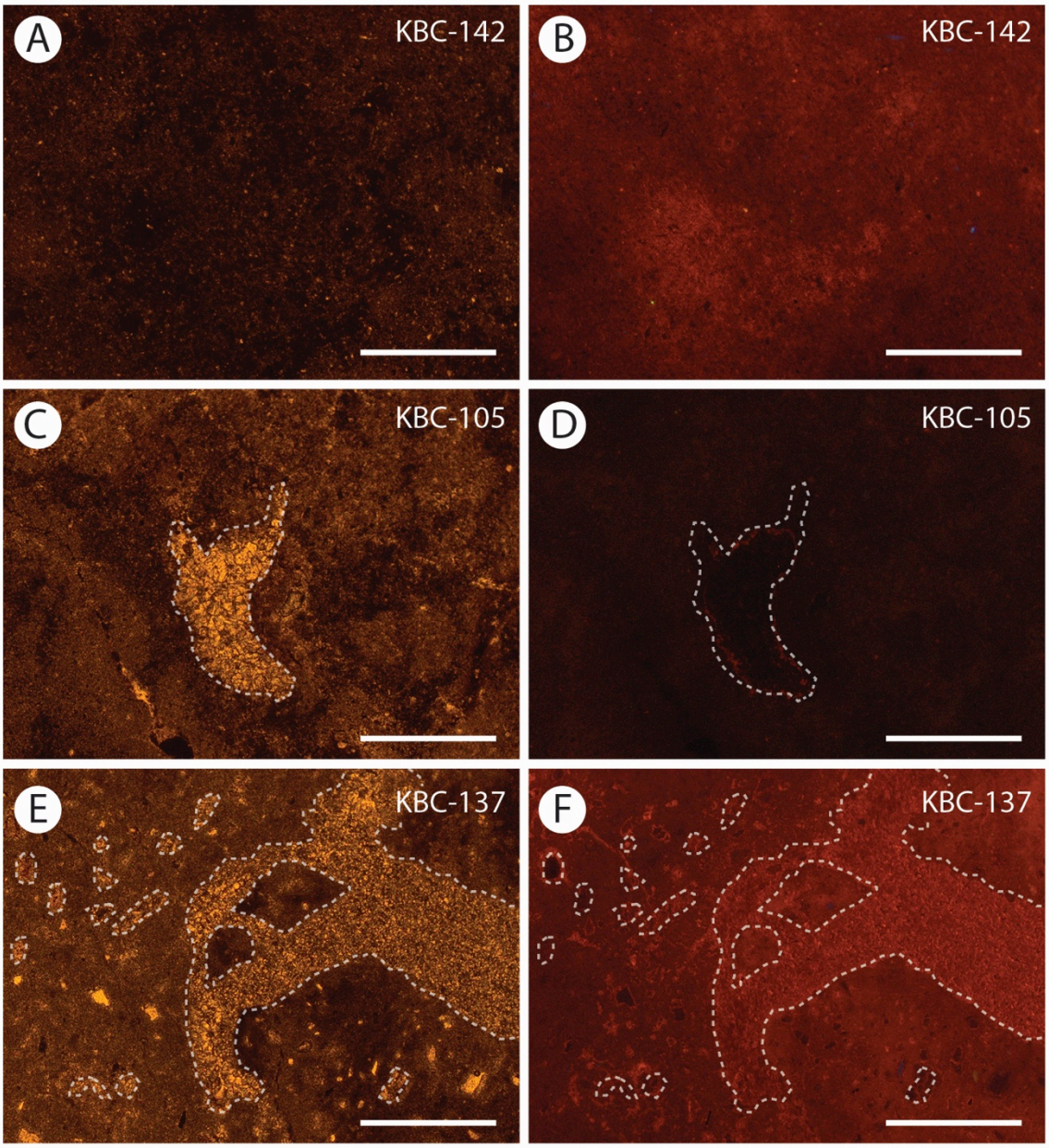

Figure 4.2. Optical (left) and cathodoluminescence (right) thin section images for micritic (A, B), mixed (C, D) and sparry (E,F) samples. Scale bars are 500 μm. White dashed lines highlight spar-filled voids and fractures in the mixed and sparry samples.

calculated using the paleosol weathering index (PWI) method described by Gallagher and Sheldon (2013). The PWI is a modified version of the index of weathering developed by Parker (1970) that estimates the extent of soil weathering based on the abundance of two cations that are highly susceptible to leaching during chemical weathering (Na and K) and two resistant cations (Mg and Ca). To calculate PWI, the relative molar abundance of each of these cations is divided by the cation's bond strength and percent ionic character, and the resulting values are then summed, resulting in the following equation:

$$PWI = 100 \times [(4.20 \times Na) + (1.66 \times Mg) + (5.54 \times K) + (2.05 \times Ca)] \quad (1)$$

The PWI value of a Bt horizon can then be related to MAT by the following empirically-derived expression:

$$MAT(°C) = -2.74 \times \ln(PWI) + 21.39 \quad (2)$$

The PWI paleothermometer should not be applied to paleosol horizons with a PWI over 60, because such high PWI values indicate little to no chemical weathering has taken place (Gallagher and Sheldon, 2013).

MAP was calculated using the chemical index of alteration without potassium (CIA-K), which was first developed by Maynard (1992). This proxy is based on the observation that modern soils that receive higher MAP also experience higher degrees of chemical weathering (Sheldon et al., 2002). CIA-K is calculated based on the molar ratio of Al_2O_3 to Al_2O_3, CaO, and Na_2O as follows:

$$CIA - K = 100 \times \left(\frac{Al_2O_3}{Al_2O_3 + CaO + Na_2O}\right) \quad (3)$$

The Bt horizon CIA-K value can then be related to calculate MAP using the equation:

$$MAP(mm\ yr^{-1}) = 221.1e^{0.0197(CIA-K)} \quad (4)$$

4.4.5. Modern climate reanalysis output and SCAN soil and air temperature data

In order to evaluate the accuracy of our Late Cretaceous MART reconstructions, we analyzed modern climate reanalysis output and soil and temperature data from the soil climate analysis network (SCAN). To calculate modern MART, we used mean monthly 2-meter air temperature output (1981 to 2016) from the ERA-Interim climate reanalysis project (spatial resolution = 0.75°; Dee et al., 2011; https://www.ecmwf.int/en/forecasts/datasets/reanalysis-datasets/era-interim). We calculated soil radiative heating (ST_{RH}) by taking the difference between SCAN station soil and air temperatures for three different summer periods: 1) mean summer temperature (June, July, August); 2) warmest-month mean temperature; and 3) warmest-month mean maximum daily temperature. We used long-term soil and air data from 199 SCAN weather stations in the continental United States and Alaska (Table SI 3; SCAN is maintained and distributed as a joint project of the National Water and Climate Center and the Natural Resources Conservation Service; https://www.wcc.nrcs.usda.gov/scan/). We note that there is a significant bias to the location of the SCAN weather stations, with just seven states (Alaska, Alabama, California, Mississippi, Nevada, Texas, and Utah) containing 59% of all stations. Despite this, the stations cover a latitudinal range from 20 to 66° N, with a gap from 48 to 59° N.

4.5. Results

4.5.1. Paleosol mapping results

We identified 19 individual paleosols (2 truncated) from the type stratigraphic section in the KF, and 43 paleosols (13 truncated) from three correlated stratigraphic sections (Figures 4.3 and 4.4; Supplementary Table C1) in the TMF. The KF section

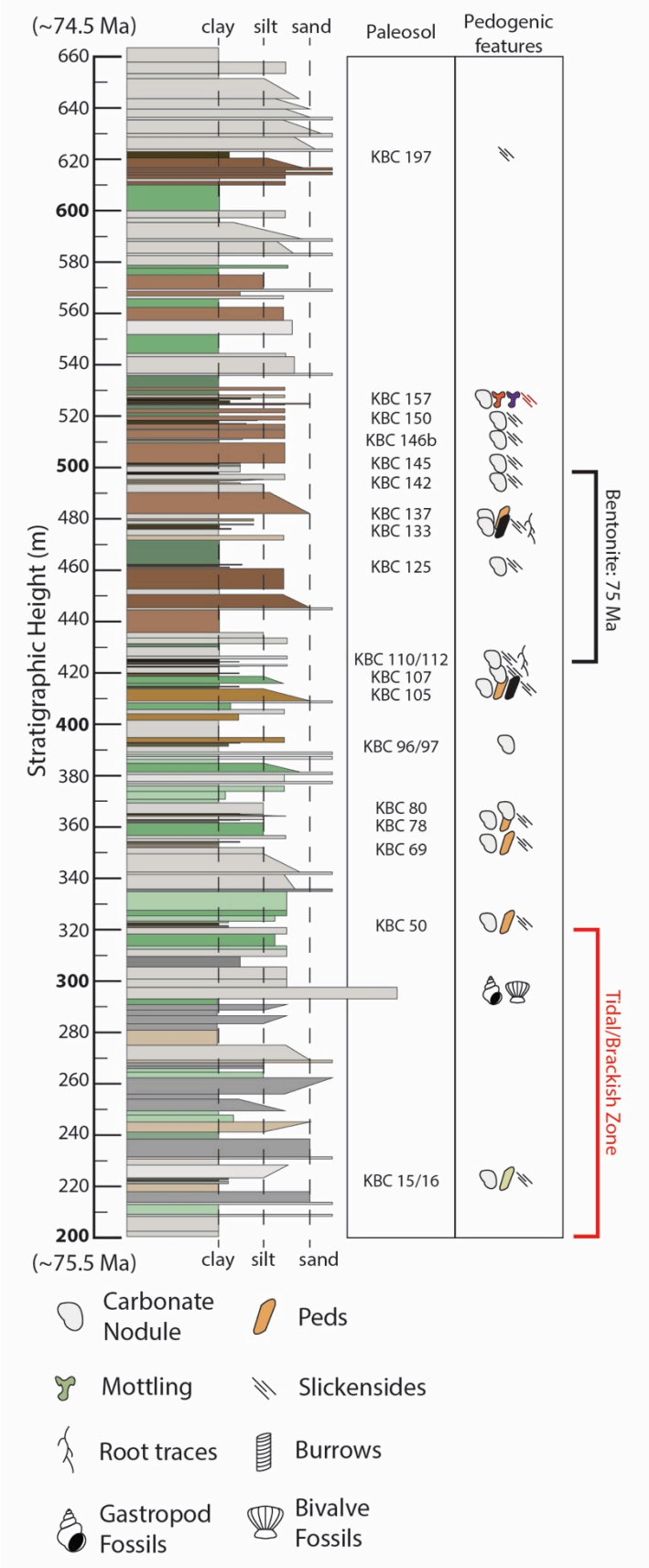

Figure 4.3. Stratigraphic column for the Kaiparowits Formation Blue Ceratopsian (KBC) section. Non-paleosol stratigraphic data from Roberts, 2005. Colors correspond to Munsell soil colors for fresh bulk sediment samples.

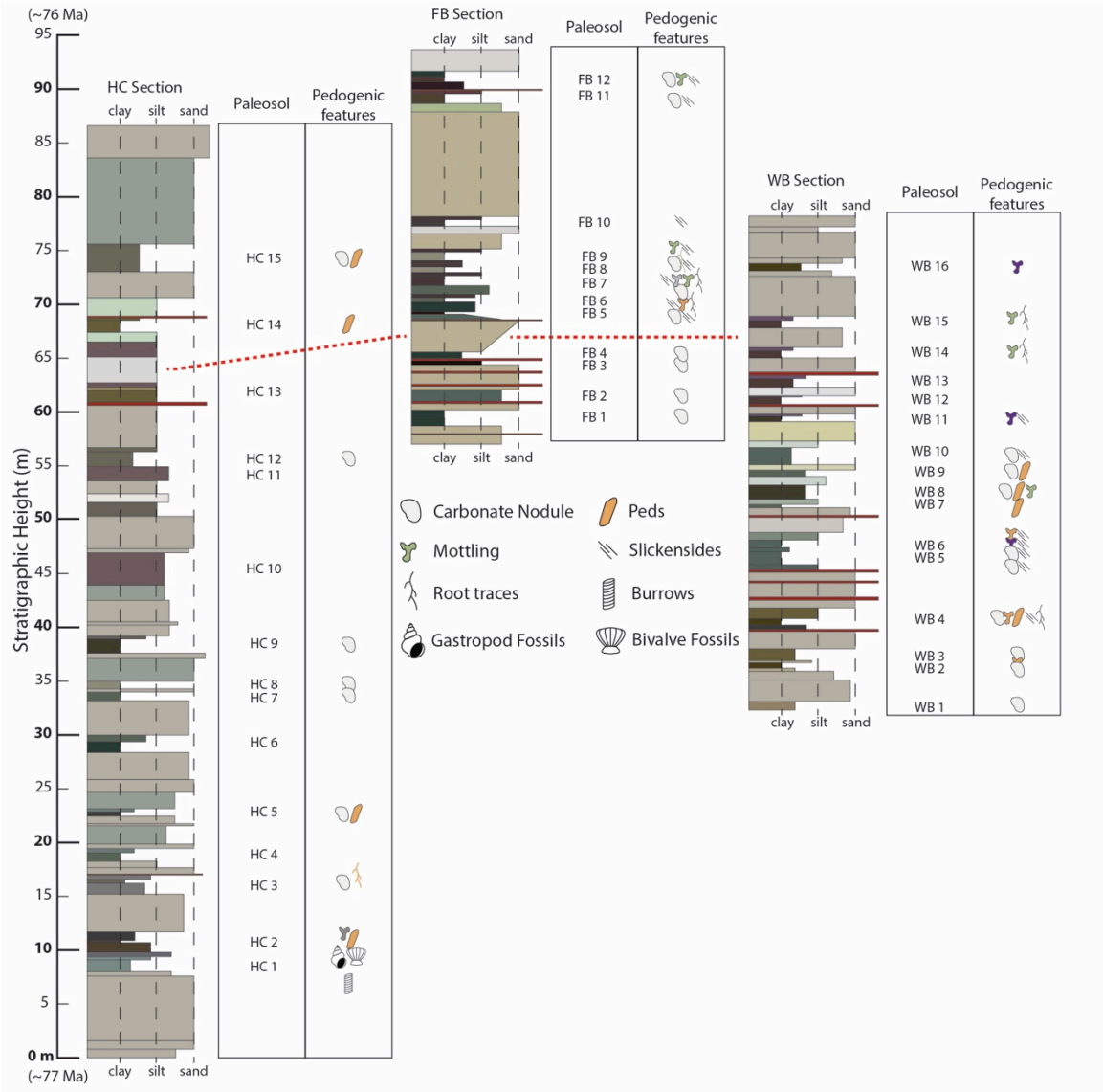

Figure 4.4. Stratigraphic column for the Two Medicine Formation Hagan's Crossing (HC), Flag Butte (FB), and Western Butte (WB) sections. Colors correspond to Munsell soil colors for fresh bulk sediment samples.

shows a distinct evolution in paleosol morphology with stratigraphic height. The first paleosol-bearing portion of the section (221 to 355 m) is ~130 m thick and contains just three widely spaced but well-developed paleosols that are relatively thick (>200 cm), and contain distinct A, Bt, and Bk horizons. The middle 65 m of the section (361 to 426 m) are typified by much thinner paleosols (~120 cm) with 10 to 20 cm A horizons and Bk or Bkt horizons characterized by weak or completely absent clay accumulation. The upper paleosol-bearing portion of the section is ~68 m thick (460 to 528 m), and shows a return to well-developed paleosols with A, Bt, and Bk horizons, though these upper paleosols are generally thinner (~150 cm) than the lowermost KF paleosols. All of the KF paleosols are drab gray or gray-green in color, contain abundant but small (maximum size <1.5 cm) carbonate nodules, rare mottling and root traces, and rare ped development (though ped surfaces are commonly oxidized). Based on these observations, we organize the KF paleosols into two taxonomic groups: the Powell Point (Calcic Argillisol/Calcic Alfisol) and Blues Amphitheater (Calcic Protosol/Calcic Inceptisol) pedotypes (Fig. 4.5A and B; Retallack, 1994). Qualitative minimum age estimates based on the average size of the carbonate nodules recovered from these paleosols yield ages of 3 to 4 ka for the KF paleosols (e.g., Retallack, 2005).

The TMF section is distinguished by abundant truncated paleosols (30% of the identified TMF paleosols), and by a higher proportion of non-calcic paleosols compared to the KF section (~40% of TMF paleosols versus ~10% of the KF paleosols). The first 25 meters of the Western Butte section are characterized by three well-developed carbonate bearing paleosols with distinct A, Bt, and Bk/Bkt horizons interspersed with five truncated Bk/Bkt horizons and a single thin argillic paleosol. The section abruptly

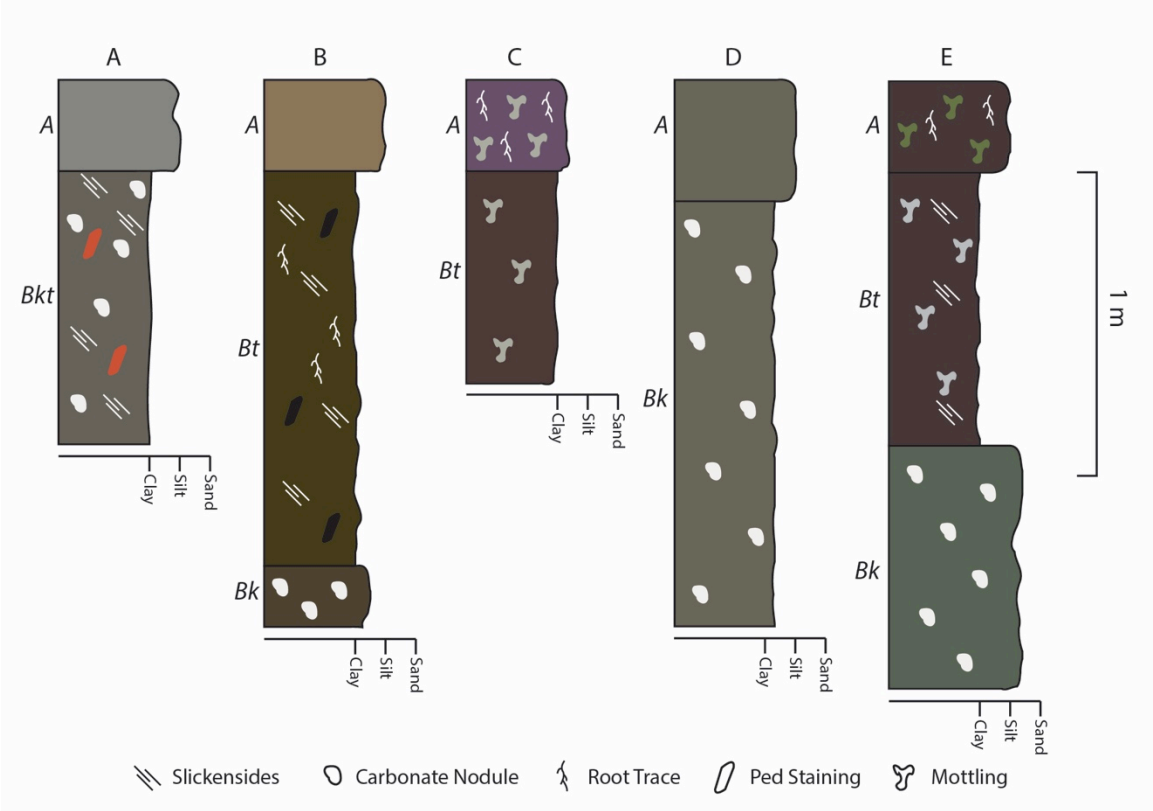

Figure 4.5. Type paleosol profiles for the Blues Amphitheatre Protosol/Inceptisol (A), Powell Point Argillisol/Alfisol (B), Western Butte Argillisol/Alfisol (C), Hagan's Crossing Calcisol/Aridisol (D), and Flag Butte Argillisol/Alfisol (E) pedotypes. Thicknesses displayed are averages for each pedotype.

transitions from this carbonate nodule-rich section to a 17 m sequence of predominantly purple argillic paleosols with complete A and Bt horizons. The lower 30 meters of the Hagan's Crossing section contain alternating carbonate-bearing and clay-rich paleosols topped by two truncated Bkt horizons. The upper portion of the Hagan's Crossing section contains predominantly carbonate-bearing paleosols, as well as two relatively thick Histosols. The first four paleosols in the Flag Butte section are truncated Bk or Bkt horizons, while the remainder of the section is characterized by relatively well-developed paleosols with distinct A, Bt, and Bk horizons, usually argillic paleosols with either Bt or Bk horizons. At all three TMF sections, the Bk and Bkt horizons are particularly well developed and yield abundant carbonate nodules that are typically much larger than those

found in the KF paleosols (<2.4 cm). Slickensides and organic plant matter are relatively rare in the TMF paleosols, while mottling, ped development, and root traces are more common than in the KF paleosols. We classify the TMF paleosols into three taxonomic groups: the Western Butte (Argillisol/Alfisol), Hagan's Crossing (Calcisol/Aridisol), and Flag Butte (Calcic Argillisol/Calcic Alfisol) pedotypes (Fig. 4.5C, D, and E). Qualitative minimum age estimates based on the average size of the carbonate nodules recovered from TMF paleosols range from 2 to 5 ka.

4.5.2. Clumped and stable isotope results

Based on the diagenetic assessment described in Section 3.5 of this study, we assigned the KF and TMF carbonate nodules to one of three categories: micritic, mixed, or sparry (Table 4.2 and Supplementary Table C2 and Supplementary Table C3). The micritic KF (n=4) and TMF (n=12) paleosol carbonate $\delta^{18}O$ (VPDB) values range from -7.7 to -7.5‰ (±0.1‰) and from -11.9 to -9.0‰ (±0.1‰), respectively (Table 4.2). Their $\delta^{13}C$ (VPDB) values range from -9.6 to -8.5‰ (±0.1‰) and from -8.6 to -6.7‰ (±0.1‰), respectively. These values are indistinguishable from $\delta^{18}O$ and $\delta^{13}C$ values reported for KF and TMF paleosol carbonates by Foreman et al. (2011, 2015). The mean $T(\Delta_{47})$ value for the micritic KF is 35±4 °C, and 33±4 °C for the micritic TMF. With only four pristine carbonate samples, the KF record is too sparse to determine if there is a temporal trend in the data, and the TMF $T(\Delta_{47})$ values for the micritic nodules (n = 12) show little variation with stratigraphic height (Supplementary Figures C1 and C2). The KF and TMF carbonates classified as mixed or sparry samples yield $\delta^{18}O$ (VPDB) values that range from -9.1 to -7.3‰ (±0.1‰) and -11.4 to -9.8‰ (±0.2‰), respectively, while the $\delta^{13}C$ (VPDB) values range from -9.4 to -7.4‰ (±0.1‰) and -9.1 to -7.1‰ (±0.1‰),

respectively. The mixed samples yield a mean T(Δ_{47}) value of 43±6 °C and 40±5 °C for the KF and TMF samples, respectively. The mean T(Δ_{47}) value of the KF sparry samples is 41±5 °C, and 42±6 °C for the TMF sparry samples (Supplementary Figure C3).

Table 4.2. Clumped and stable isotope results.

Sample Name	Formation	Section	Stratigraphic Height	n	Fabric Classification	$\delta^{13}C_{carb}$ (‰) VPDB	± 1 SE (‰)	$\delta^{18}O_{carb}$ (‰) VPDB	± 1 SE (‰)	$\delta^{18}O_{water}$ (‰) VSMOW	± 1 SE (‰)	Δ_{47}	± 1 SE (‰)	$T(\Delta_{47})$	± 1 SE (‰)
TM-HC-1	Two Medicine	Hagan's Crossing (HC)	8.2	2	Sparry	-7.84	0.08	-9.83	0.03	-2.49	0.03	0.563	0.012	40	4
TM-HC-1b	Two Medicine	Hagan's Crossing (HC)	8.2	3	Mixed	-8.24	0.07	-9.99	0.47	-3.91	0.47	0.578	0.009	35	3
TM-HC-1s	Two Medicine	Hagan's Crossing (HC)	8.2	2	Spar	-6.39	0.13	-12.32	0.08	-0.21	0.08	0.556	0.052	45	20
TM-HC-3	Two Medicine	Hagan's Crossing (HC)	16.4	2	Mixed	-7.12	0.00	-9.88	0.00	-0.93	0.00	0.551	0.016	45	6
TM-HC-3b	Two Medicine	Hagan's Crossing (HC)	16.4	2	Sparry	-8.17	0.02	-9.92	0.06	-3.06	0.06	0.570	0.044	39	16
TM-HC-3c	Two Medicine	Hagan's Crossing (HC)	16.4	3	Micritic	-6.65	0.05	-9.53	0.46	-2.99	0.46	0.588	0.009	31	3
TM-WB-1a	Two Medicine	Western Butte (WB)	33	4	Micritic	-7.87	0.08	-10.04	0.07	-2.95	0.07	0.571	0.016	38	6
TM-WB-1b	Two Medicine	Western Butte (WB)	33	3	Micritic	-7.95	0.01	-10.03	0.06	-3.43	0.06	0.576	0.018	36	7
TM-HC-7	Two Medicine	Hagan's Crossing (HC)	33.2	3	Micritic	-8.06	0.01	-9.45	0.05	-3.72	0.05	0.578	0.009	35	3
TM-HC-7s	Two Medicine	Hagan's Crossing (HC)	33.2	2	Spar	-4.58	0.10	-15.77	0.12	7.90	0.12	0.465	0.012	85	6
TM-HC-9	Two Medicine	Hagan's Crossing (HC)	37.6	3	Sparry	-9.09	0.00	-10.08	0.09	-3.63	0.09	0.561	0.009	41	3
TM-WB-3	Two Medicine	Western Butte (WB)	37.6	3	Micritic	-7.66	0.01	-8.97	0.08	-4.67	0.08	0.599	0.009	28	3
TM-WB-5	Two Medicine	Western Butte (WB)	46	1	Sparry	-7.92		-11.42		-0.68		0.535		51	
TM-WB-6	Two Medicine	Western Butte (WB)	47.7	4	Mixed	-8.59	0.05	-9.91	0.15	-2.30	0.15	0.549	0.008	46	3
TM-WB-6s	Two Medicine	Western Butte (WB)	47.7	2	Spar	-7.19	0.07	-13.21	0.14	0.86	0.14	0.524	0.012	56	5
TM-WB-8	Two Medicine	Western Butte (WB)	52.1	4	Micritic	-7.83	0.07	-9.89	0.10	-4.30	0.10	0.590	0.009	31	3
TM-FB-1	Two Medicine	Flag Butte (FB)	59.7	4	Micritic	-7.44	0.04	-9.55	0.02	-3.60	0.02	0.586	0.008	32	3
TM-HC-13	Two Medicine	Hagan's Crossing (HC)	60.9	2	Sparry	-7.96	0.02	-10.43	0.06	-1.67	0.06	0.549	0.014	46	5
TM-HC-13b	Two Medicine	Hagan's Crossing (HC)	60.9	2	Sparry	-8.22	0.27	-9.77	0.14	-1.61	0.14	0.545	0.018	48	7
TM-FB-3	Two Medicine	Flag Butte (FB)	64.4	3	Micritic	-7.21	0.02	-9.97	0.05	-3.13	0.05	0.582	0.014	34	5
TM-FB-5	Two Medicine	Flag Butte (FB)	68.6	2	Mixed	-8.56	0.09	-11.12	0.01	-4.25	0.01	0.579	0.024	35	8
TM-FB-5b	Two Medicine	Flag Butte (FB)	68.6	2	Sparry	-8.13	0.11	-11.33	0.03	-2.46	0.03	0.558	0.012	42	4
TM-FB-5c	Two Medicine	Flag Butte (FB)	68.6	2	Micritic	-8.46	0.25	-11.34	0.16	-3.92	0.16	0.575	0.012	36	4
TM-FB-7	Two Medicine	Flag Butte (FB)	70.9	2	Micritic	-8.53	0.13	-11.86	0.26	-5.69	0.26	0.601	0.012	27	4
TM-FB-7b	Two Medicine	Flag Butte (FB)	70.9	4	Micritic	-8.59	0.02	-11.89	0.24	-3.85	0.24	0.572	0.009	37	3
TM-HC-15	Two Medicine	Hagan's Crossing (HC)	73.1	3	Sparry	-7.48	0.03	-11.41	0.06	-3.70	0.06	0.587	0.009	32	3
TM-FB-11b	Two Medicine	Flag Butte (FB)	88.6	5	Micritic	-7.59	0.02	-11.10	0.03	-5.34	0.03	0.611	0.011	24	4

Table 4.2. cont'd.

Sample Name	Formation	Section	Stratigraphic Height	n	Fabric Classification	$\delta^{13}C_{carb}$ (‰) VPDB	± 1 SE (‰)	$\delta^{18}O_{carb}$ (‰) VPDB	± 1 SE (‰)	$\delta^{18}O_{water}$ (‰) VSMOW	± 1 SE (‰)	Δ_{47}	± 1 SE (‰)	$T(\Delta_{47})$	± 1 SE (‰)
KBC-15	Kaiparowits	Blue Ceratopsian (KBC)	222.8	2	Bulk	-6.40	0.12	-10.04	0.03	-0.23	0.03	0.551	0.012	45	4
KBC-15b	Kaiparowits	Blue Ceratopsian (KBC)	222.8	1	Mixed	-7.43		-9.04		-0.10		0.534		52	
KBC-50	Kaiparowits	Blue Ceratopsian (KBC)	321.6	2	Bulk	-9.87	0.00	-7.99	0.02	-3.85	0.02	0.553	0.012	44	4
KBC-69	Kaiparowits	Blue Ceratopsian (KBC)	353.5	2	Bulk	-9.01	0.04	-8.59	0.01	-4.17	0.01	0.571	0.012	38	4
KBC-69b	Kaiparowits	Blue Ceratopsian (KBC)	353.5	2	Mixed	-9.36	0.13	-7.61	0.18	-2.39	0.18	0.540	0.020	50	8
KBC-69c	Kaiparowits	Blue Ceratopsian (KBC)	353.5	2	Micritic	-9.33	0.06	-7.64	0.06	-4.95	0.06	0.577	0.012	35	4
KBC-80	Kaiparowits	Blue Ceratopsian (KBC)	365	2	Bulk	-8.25	0.46	-8.31	0.14	0.51	0.14	0.514	0.012	60	5
KBC-80b	Kaiparowits	Blue Ceratopsian (KBC)	365	2	Bulk	-8.37	0.04	-7.87	0.03	-2.75	0.03	0.559	0.012	42	4
KBC-96	Kaiparowits	Blue Ceratopsian (KBC)	392.6	4	Bulk	-8.96	0.01	-8.31	0.02	-3.57	0.02	0.563	0.014	41	6
KBC-105	Kaiparowits	Blue Ceratopsian (KBC)	414.4	3	Bulk	-9.67	0.04	-8.21	0.21	-5.51	0.21	0.581	0.009	34	3
KBC-105b	Kaiparowits	Blue Ceratopsian (KBC)	414.4	5	Micritic	-9.56	0.02	-7.74	0.04	-5.91	0.04	0.589	0.011	31	4
KBC-107	Kaiparowits	Blue Ceratopsian (KBC)	419.7	6	Bulk	-9.21	0.01	-9.13	0.13	-5.02	0.13	0.581	0.009	34	3
KBC-112	Kaiparowits	Blue Ceratopsian (KBC)	424.3	2	Sparry	-7.85	0.01	-9.06	0.09	-0.72	0.09	0.537	0.012	51	5
KBC-112b	Kaiparowits	Blue Ceratopsian (KBC)	424.3	3	Sparry	-8.28	0.01	-8.80	0.12	-2.64	0.12	0.559	0.010	42	4
KBC-125	Kaiparowits	Blue Ceratopsian (KBC)	461.3	4	Bulk	-9.02	0.06	-7.88	0.13	-4.27	0.13	0.574	0.020	37	8
KBC-125b	Kaiparowits	Blue Ceratopsian (KBC)	461.3	3	Sparry	-8.93	0.09	-7.27	0.04	-4.13	0.04	0.572	0.015	38	6
KBC-137	Kaiparowits	Blue Ceratopsian (KBC)	479.9	3	Sparry	-8.85	0.03	-8.38	0.03	-3.91	0.03	0.570	0.014	38	5
KBC-137b	Kaiparowits	Blue Ceratopsian (KBC)	479.9	3	Bulk	-9.05	0.12	-7.78	0.20	-4.06	0.20	0.569	0.015	39	6
KBC-137s	Kaiparowits	Blue Ceratopsian (KBC)	480.4	1	Spar	-8.56		-7.91		-4.58		0.583		33	
KBC-142	Kaiparowits	Blue Ceratopsian (KBC)	494	2	Micritic	-8.48	0.00	-7.55	0.03	-4.16	0.03	0.578	0.012	35	4
KBC-142b	Kaiparowits	Blue Ceratopsian (KBC)	494	4	Micritic	-8.50	0.14	-7.48	0.22	-3.90	0.22	0.574	0.009	36	3
KBC-145	Kaiparowits	Blue Ceratopsian (KBC)	501	3	Bulk	-10.53	0.01	-7.40	0.06	-8.20	0.06	0.609	0.009	25	3
KBC-146	Kaiparowits	Blue Ceratopsian (KBC)	510.5	2	Bulk	-9.13	0.02	-9.58	0.08	-2.61	0.08	0.546	0.019	47	7
KBC-150	Kaiparowits	Blue Ceratopsian (KBC)	517.2	3	Sparry	-7.84	0.05	-8.29	0.08	-3.37	0.08	0.577	0.016	36	6
KBC-150b	Kaiparowits	Blue Ceratopsian (KBC)	517.2	3	Mixed	-9.08	0.04	-8.20	0.09	-6.00	0.09	0.597	0.010	29	3
KBC-157	Kaiparowits	Blue Ceratopsian (KBC)	525.9	5	Bulk	-9.66	0.01	-8.15	0.06	-5.85	0.06	0.587	0.012	32	4

The spar from one KF and three TMF carbonate nodules (KBC-137s, TM-HC-1s, TM-HC-7s, TM-WB-6s) was subsampled to characterize its isotopic composition. The $\delta^{18}O$, $\delta^{13}C$, and $T(\Delta_{47})$ values of the KF spar sample was not distinguishable from those of the other KF samples. Due to the small size of the KF nodules and the observed heterogeneous mixture of micritic and sparry calcite in the KBC-137s nodule, we suspect that some micritic material was accidentally incorporated into this "spar" sample. In contrast, the TMF spar samples yield high $T(\Delta_{47})$ values (μ=61.9±10.4 °C) and show a clear pattern of decreasing $\delta^{18}O$ values and increasing $\delta^{13}C$ values relative to the micritic, mixed, and sparry TMF carbonates (Fig. 4.6).

4.5.3. Late Cretaceous MAAT and MAP from paleosol bulk geochemistry

The paleosol bulk geochemistry analyses for the KF and TMF paleosols yield Ti/Al ratios that are constant with stratigraphic height (KF: μ=0.05, σ=0.004; TMF = μ=0.03, σ=0.009), indicating that both locations experienced little or no provenance change over the measured interval (Hyland et al., 2017; Sheldon and Tabor, 2009). The PWI values for the measured KF and TMF Bt horizons range from 33.1 to 53.7 and 37.8 to 82.8, respectively. The mean and standard deviation of the PWI values are 40.9 and 6.9 for the KF, and 48.3 and 19.4 for the TMF. MAAT was calculated only for those Bt horizons that had PWI values that were both less than 60 and lower than the PWI of the underlying parent material (Gallagher and Sheldon, 2013). Based on these PWI values, both the KF and TMF yield a mean MAAT value of 11±2 °C (Table 4.3). CIA-K values

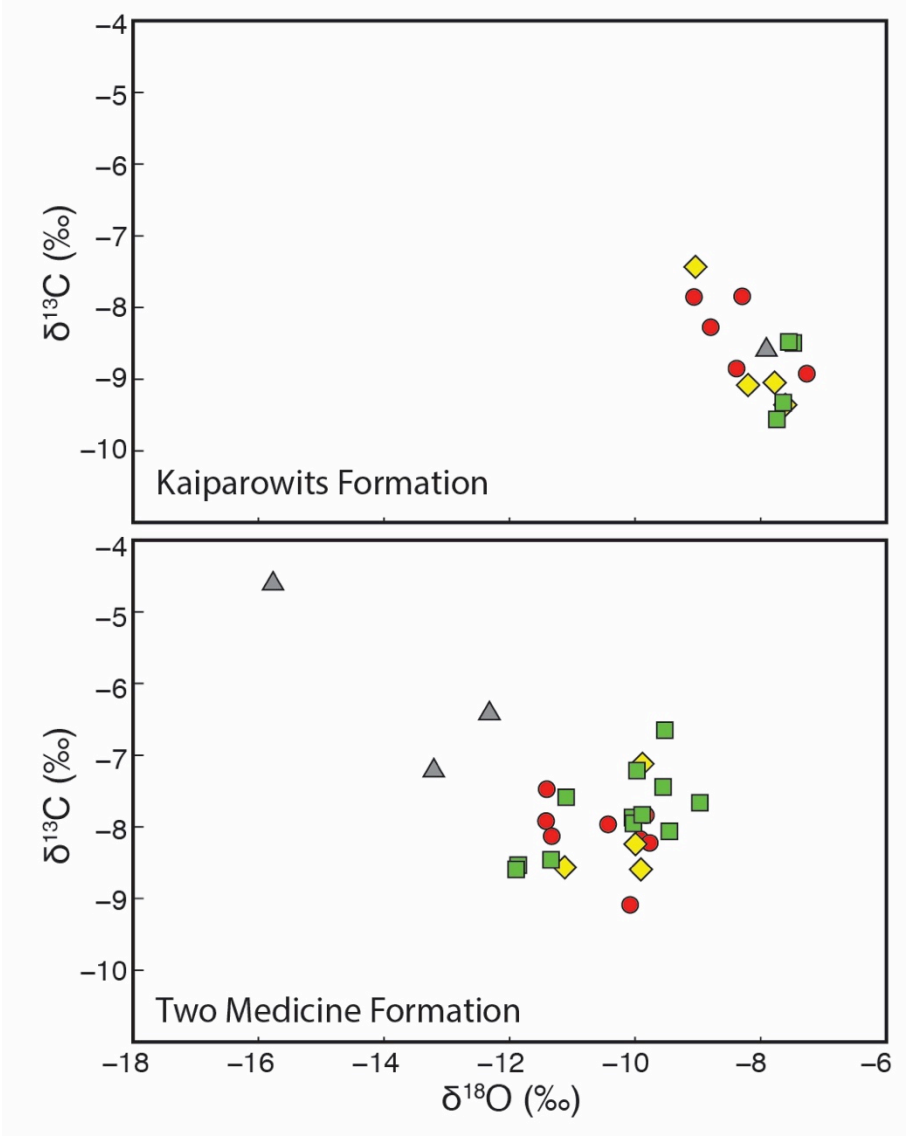

Figure 4.6. Paleosol nodule carbonate $\delta^{18}O$ versus $\delta^{13}C$ (VPDB), colored by fabric classification: micritic samples (green squares), mixed samples (yellow diamonds), sparry samples (red circles), and samples of exclusively void-filling spar (grey triangles).

Table 4.3. Kaiparowits and Two Medicine Formation bulk geochemistry results and paleoclimate reconstructions.

Sample Name	Horizon Type	Stratigraphic Height (m)	Soil Depth (cm)[a]	Al_2O_3 (wt %)	CaO (wt %)	Na_2O (wt %)	MgO (wt %)	K_2O (wt %)	Ti (wt %)	CIA-K[a]	MAP (mm yr^{-1})[a]	PWI	MAAT (°C)[a]
Kaiparowits Formation													
KBC-15-Bk	Bk	223	130	3.69	39.90	0.35	1.19	0.75	0.18	4.8		157.5	
KBC-15-Bt	Bt	223	70	13.06	2.89	1.06	3.34	2.23	0.57	65.1	797	44.6	11
KBC-50-Bt	Bt	322	60	15.10	2.11	1.62	2.50	2.02	0.61	69.9	876	40.9	11
KBC-69-Bk	Bk	354	30	12.52	9.76	1.22	3.64	1.98	0.58	38.8		70.6	
KBC-96-Bk	Bk	393	90	14.01	0.68	1.90	2.06	2.21	0.66	76.3		36.8	
KBC-107-Bk	Bk	420	75	14.61	2.08	1.95	3.07	2.31	0.61	67.6		47.0	
KBC-125-Bt	Bt	461	65	14.79	3.10	2.07	3.28	2.53	0.67	62.1	751	53.7	10
KBC-133-Bk	Bk	476	95	9.81	18.90	1.23	2.77	1.85	0.50	21.2		99.7	
KBC-133-Bt	Bt	476.3	170	16.13	0.72	1.72	2.58	2.66	0.75	79.6	1060	40.5	11
KBC-146B-Bt	Bt	511	60	15.77	0.32	1.45	2.01	3.11	0.73	84.2	1161	37.6	11
KBC-150-Bt	Bt	517	75	13.80	1.41	1.58	1.73	2.25	0.72	72.8	927	36.2	12
KBC-157-Bt	Bt	526	truncated	14.94	0.49	1.30	1.77	2.59	0.64	83.1	1137	33.1	12
										Mean MAP (mm yr^{-1})[a]	*960±190*	*MAAT (°C)[a]*	*11±2*
Two Medicine Formation													
TM-HC-2-C	C	10	100	18.89	1.67	3.28	4.25	0.48	0.32	69.1		48.7	
TM-HC-2-Bt	Bt	11	90	15.13	0.89	2.34	3.44	0.78	0.29	73.5		37.8	11
TM-HC-2-A	A	11	40	17.03	2.06	2.46	4.56	0.95	0.34	68.6		48.6	
TM-WB-4-Bkt	Bkt	41	180	11.83	8.97	1.53	2.92	2.48	0.47	38.6		69.7	
TM-WB-4-Bt	Bt	41	130	13.41	1.00	1.70	2.02	2.98	0.51	74.4	958	40.9	11
TM-WB-4-A	A	42	50	13.05	0.70	1.60	1.49	2.81	0.50	77.0		36.0	
TM-FB-1-C	C	59	185*	9.30	10.85	1.29	4.00	1.92	0.37	29.8		76.2	
TM-FB-1-Bkt1	Bkt	59	75*	14.02	2.41	1.46	2.89	3.24	0.55	67.4	834	49.6	
TM-FB-1-Bkt2	Bkt	60	25*	13.16	5.27	1.34	4.23	2.93	0.53	52.8		62.9	
TM-WB-13-Bt	Bt	63	70	13.06	1.08	1.53	2.17	3.09	0.49	74.5	959	41.4	11
TM-HC-14-Bt	Bt	67	75	12.25	8.94	0.50	7.58	2.64	0.55	41.8	503	82.8	
TM-FB-7-Bt	Bt	72	110	13.26	0.80	1.43	2.02	2.97	0.50	77.7	1022	38.4	11
TB-FB-11-Bkt	Bkt	89	75	14.02	4.13	0.92	3.29	4.28	0.53	60.8		60.1	
										Mean MAP (mm yr^{-1})[a]	*860±200*	*MAAT (°C)[a]*	*11±2*

range from 62.1 to 84.2 for the KF, and 41.8 to 77.7 for the TMF. The mean and standard deviation of the CIA-K values are 73.8 and 8.7 for the KF, and 68.4 and 15 for the TMF. One Bt sample from the TMF (TM-HC-2-Bt) yielded CIA-K values that were too similar to the underlying parent material (CIA-K difference <8), indicating that the soil had not experienced enough weathering to apply the CIA-K proxy. This sample was removed from further MAP calculations. For the remaining samples, the CIA-K calculated mean MAP values for the KF and TMF are 960±190 and 860±200 mm yr^{-1}, respectively.

4.6. Discussion

In the following sections, we present our interpretations of the paleosol carbonate and bulk geochemistry data and our subsequent estimates of Late Cretaceous MART. The T(Δ_{47}) values of our pristine (micritic) and altered (mixed and sparry) paleosol carbonate nodules are reviewed, and the SCAN data results are used to constrain the amount of radiative heating the KF and TMF paleosols likely experienced during soil carbonate formation. The unexpectedly low MAT and MAP estimates reconstructed by the PWI and CIA-K methods are compared to previous proxy reconstructions of KF and TMF temperature and precipitation, and possible causes for the differing values are discussed. We discuss the uncertainties associated with our Late Cretaceous MART and cold-month mean temperature estimates in light of modern MART estimates based on ERA-Interim climate reanalysis data. We compare our Late Cretaceous MART estimates to previous leaf physiognomy MART estimates and to model simulations for the same period. Finally, we compare these Late Cretaceous MART estimates to modern MART and discuss the implications of our findings for understanding greenhouse climates.

4.6.1. Interpreting Late Cretaceous summer air temperatures from paleosol carbonate $T(\Delta_{47})$ values

The mixed and sparry KF and TMF samples show textural and clumped isotopic evidence of being compromised to some degree by diagenetic alteration. In both the mixed and sparry samples, our petrographic analysis shows that void spaces and fractures have been filled to varying extents by coarse-grained, sparry calcite indicative of post-burial diagenesis. Supplementary Figure 3 shows that the mixed and sparry samples show more negative $\delta^{18}O$ values relative to the micritic samples, and more variability in $T(\Delta_{47})$ values. Additionally, the mixed and sparry KF and TMF samples yield high mean $T(\Delta_{47})$ values of 42.1±5.3 and 41.3±5.8 °C, respectively, which are 7 to 9 °C hotter than the mean $T(\Delta_{47})$ values of the micritic carbonates (Supplementary Figure C3E and F).

Based on the evidence presented above, we chose to treat all of the mixed and sparry KF and TMF samples as being compromised by some degree of diagenesis, and did not include those samples in our calculations of MART. In contrast, the remaining samples 1) have a fine-grained, micritic texture consistent with unaltered pedogenic carbonate, and 2) yield consistent, reasonable Earth-surface $T(\Delta_{47})$ values (<40 °C), which leads us to classify them as unaltered, pristine carbonate.

We interpret the mean KF and TMF $T(\Delta_{47})$ values of the micritic carbonates (35±4 °C and 33±4 °C, respectively) as being consistent with soil carbonate formation during the warmest month of the year (e.g., equivalent to warmest month mean soil temperature) for two reasons. First, multiple model simulations (Poulsen et al., 2007; Fricke et al., 2010; Kump and Singerland, 1999; Poulsen et al., 1999) have suggested that the western margin of the WIS experienced a pronounced monsoon-like climate in both

the middle and Late Cretaceous, with most precipitation falling during the warm season. The bulk oxygen isotope compositions of various carbonate materials (e.g., paleosol nodules, fossil bivalves, etc.) have been interpreted as consistent with this monsoon hypothesis (Dennis et al., 2013; Foreman et al., 2011; Fricke et al., 2010). In the modern, soil carbonate formation in hot monsoon climates is believed to occur in the warmest month just before the wet season begins (Breecker et al., 2009; Quade et al., 2013). We suggest that like modern soil carbonates in India or the southwestern United States, our Late Cretaceous paleosol nodules formed during the warmest month of the year just prior to the beginning of monsoonal precipitation, when soils were likely at their driest. Second, studies of modern plants show that at temperatures >35 °C, plants begin to die due to photorespiration dominating over photosynthesis (Huber et al., 2008; Matthews et al., 2007; Sharkey, 2000; Berry and Björkman, 1980), suggesting that in regions with well-established floral records such as the KF and TMF (Miller et al., 2013; Falcon-Lang, 2003), summer temperatures were likely <40 °C. Thus maximum surface temperatures at the KF and TMF could not have been much higher than the observed T(Δ_{47}) values from our paleosol carbonate samples.

Modern studies (Ringham et al., 2016; Hough et al., 2014; Quade et al., 2013; Passey et al., 2010) have suggested that the soil temperatures recorded by pedogenic carbonate clumped isotopes can be significantly higher than overlying air temperatures due to the effects of radiative soil heating. This has implications both for our interpretation of the KF and TMF T(Δ_{47}) values as well as for our calculations of MART. Past studies have either converted soil carbonate T(Δ_{47}) values to air temperatures by subtracting an assumed ST_{RH} value in order to account for radiant ground heating (e.g.,

Snell et al., 2013; Quade et al., 2007), or assumed that soil carbonate T(Δ_{47}) values are equivalent to air temperatures in certain locations because ST_{RH} is minimal due to vegetation shading (e.g., Hyland et al., 2018; Ghosh et al., 2016; Suarez et al., 2011). In their study of Paleogene Bighorn Basin paleosol carbonates, Snell et al. (2013) chose to subtract 5 °C from their T(Δ_{47}) values in order to convert carbonate formation temperatures to warmest month mean air temperatures. A ST_{RH} of 5 °C is near the upper limit of the range of ST_{RH} values (0 to 6 °C) assumed by Quade et al. (2013) for soil depths >50 cm, and may not be realistic for vegetated environments like the Paleogene Bighorn Basin or the Late Cretaceous WIS margin. Quade et al. (2013) based their estimates of ST_{RH} on modern soil profiles from arid to semi-arid environments with little vegetation cover, which should serve to amplify ST_{RH}. In contrast, multiple paleofloral studies (e.g., McInerney and Wing, 2011; Smith et al., 2007; Wing et al., 2005; Wing and Harrington, 2001; Wing, et al., 1995) have shown that during the Paleogene, the Bighorn Basin environment was semi-humid to humid and was likely characterized by open-canopied forests (McInerney and Wing, 2011) that would have shaded any carbonate-bearing soils. We suggest this in turn would have resulted in ST_{RH} values that are considerably lower than the maximum 6 °C assumed by Quade et al. (2013).

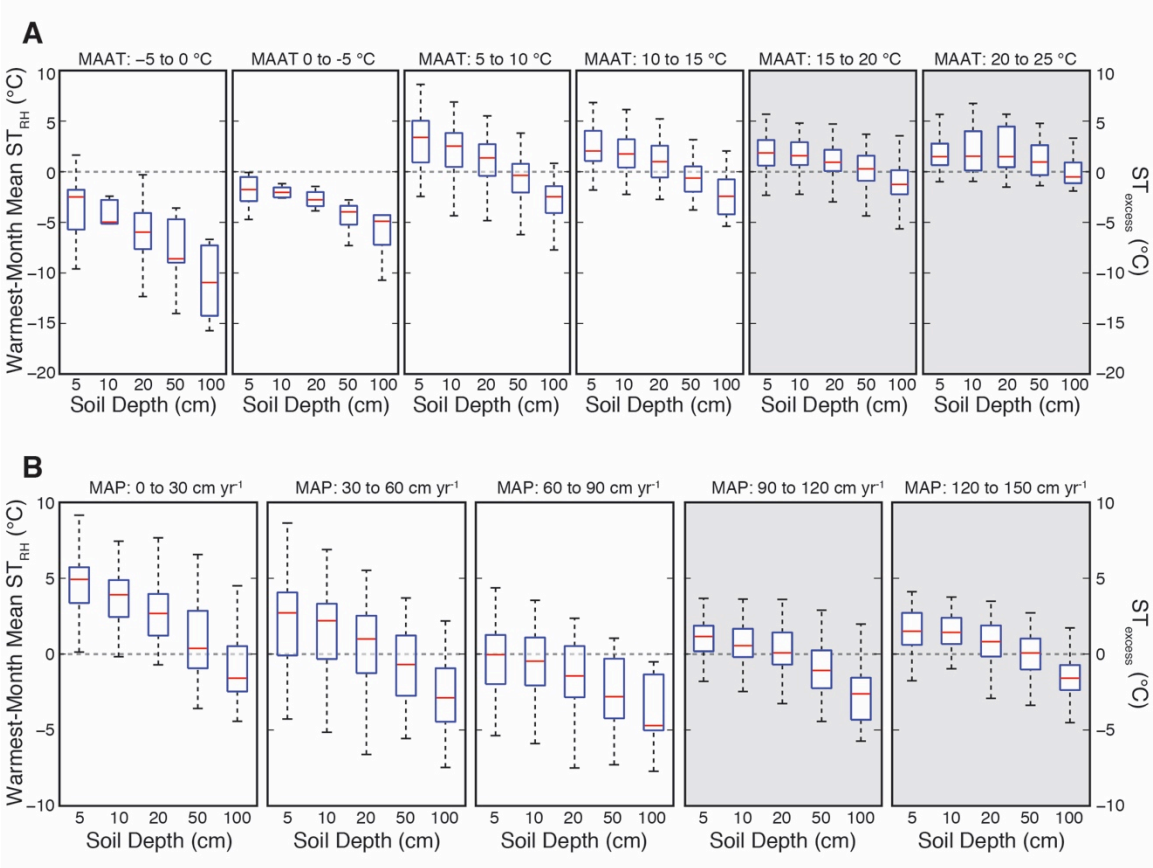

Figure 4.7. Soil excess temperatures from incident solar radiative heating (ST_{RH}) calculated from SCAN station (n = 205 stations) soil and air temperature data binned by: A) mean annual temperature (MAAT) and B) mean annual precipitation (MAP) at soil depths from 5 – 100 cm. In both A and B, the gray boxes indicate the MAAT and MAP conditions most similar to the climate conditions of the KF and TMF during the Late Cretaceous. Red lines represent median values for each bin, while blue boxes indicate 2σ and vertical dashed lines indicate full range of values. Horizontal dashed line indicates an ST_{RH} value of 0 °C (i.e., identical soil and air temperatures).

Our review of the SCAN soil and air temperature data show that in most environments, ST_{RH} is generally much smaller than has been assumed by previous studies like Quade et al. (2013) and Snell et al. (2013), regardless of whether it is calculated using mean summer, warmest month, or warmest-month maximum air and soil temperatures, particularly at depths relevant to carbonate proxy reconstructions. Mean ST_{RH} decreases with soil depth, and the maximum ST_{RH} observed for any station is 10 °C at 5 cm depth. At 50 cm depth—commonly cited as the minimum depth at which soil carbonate samples should be collected for paleoclimate analysis (Burgener et al., 2016;

Quade et al., 2013; Breecker et al., 2009)—75% of the SCAN stations have a mean warmest-mean month ST_{RH} of <0 °C, and 96% have a mean ST_{RH} <3 °C. Importantly, the SCAN data show that only soils from arid to sub-arid environments (MAP <600 mm yr^{-1}), where vegetation shading is limited, routinely experience warmest-month mean ST_{RH} values ≥5 °C, and this is typically limited to depths <50 cm(Fig. 4.7). Previously reconstructed MAP values for the KF and TM range from ~900 to ~1780 mm yr^{-1} are significantly higher than this threshold (Miller et al., 2013; Falcon-Lang, 2003; Buck and Mack, 1995; Retallack, 1994), and the SCAN data show that for soils experiencing a similar range of MAP (900 to 1500 mm yr^{-1}), ST_{RH} at 50 cm is negligible or actually negative (e.g., warmest summer month soil temperatures are slightly cooler than air temperatures; Fig. 4.7). We note that radiant heating cannot cause negative STRH values; rather, the negative STRH values we observed are the result of soil processes such as soil moisture effects, vegetation shading, or the time lag in the response of a soil at depth to surface temperature changes, which lead to cooler soil temperatures relative to air temperatures (Supplementary Figure C4).

Although some past clumped isotope-based studies of soil carbonates have assumed larger degrees of ST_{RH}, the relatively small degree of excess soil heating reported here is consistent with previous direct measurements of ST_{RH} (Supplementary Table C4). Passey et al. (2010) report ST_{RH} values of <3 °C from Narok, Kenya, and negative ST_{RH} values (-1.4 to -0.4 °C) for several sites in Ethiopia and California (soil depths not reported). Cermak et al. (2016) reported a maximum ST_{RH} of 3 °C at 2 cm soil depth for three different land cover types (bare clay, bare sand, and short grass). Finally,

Bartlett et al. (2006) reported long-term ST_{RH} values of <4 °C at 2.5 cm soil depth, and negative ST_{RH} values for vegetated soils at depths >10 cm.

Based on these findings regarding modern ST_{RH}, in addition to presenting our MART estimates assuming ST_{RH} = 0°C, we also calculate MART using the maximum ST_{RH} correction (3 °C) observed for modern soils at 50 cm during the warmest month, from environments with MAP values similar to the KF and TMF. Based on these two different assumptions regarding ST_{RH}, we suggest that the long-term warmest mean monthly air temperatures for the KF and TMF were 32 to 35±4 °C and 30 to 33±4 °C, respectively. These KF and TMF T(Δ_{47}) values show that summers along the western margin of the WIS—even at paleolatitudes as high as 53 to 56° N—were extremely hot, consistent with the global greenhouse conditions that existed at the time (Niezgodski et al., 2017). To put these summer temperatures in perspective, climate reanalysis data (ERA-Interim) shows that currently, less than 3% of the Earth's surface experiences warmest month mean air temperatures ≥35 °C.

4.6.2. Soil geochemistry estimates of MAT and MAP compared to previous reconstructions

The PWI and CIA-K estimates of MAT and MAP are significantly lower than previous estimates based on leaf physiognomy. For the KF, the paleosol PWI values equate to a mean MAT of 11±2 °C, which is ~7 to 11 °C colder than previous estimates (Table 4.4; Upchurch et al., 2015; Miller et al., 2013; Wolfe, 1990). Likewise, MAP predictions for the KF from the CIA-K method are 960 ± 190 mm yr^{-1}, which is nearly half the 1780 mm yr^{-1} predicted from fossil leaf size (Miller et al., 2013). Similarly, for the TMF the PWI method underestimates fossil-reconstructed MAT by ~3 to 8 °C

(Barrick et al., 1999; Van Boskirk, 1998; Wolfe and Upchurch, 1987). MAP estimates for the TMF are less well constrained, but our estimate of 860±200 mm yr^{-1} from CIA-K is at the lower end of the range of estimated values from fossil leaves (900 to 1200 mm yr^{-1}; Falcon-Lang, 2003). Gallagher and Sheldon (2013) note that high abundance of Ca in a Bt horizon will result in artificially low PWI-based MAT estimates. However, except for one Bt horizon from the KF, our paleosol Bt horizons have relatively low Ca abundances, suggesting that some other factor(s) is affecting paleoclimate estimates based on the Bt horizon geochemistry.

Table 4.4. Mean annual air temperature reconstructions for the Kaiparowits (KF) and Two Medicine (TMF) Formations.

Formation	Paleolatitude (°N)[a]	Distance from KF or TMF (°)[b]	Age	Proxy	MAAT (*C)[c]	Latitude-adjusted MAT (*C)[d]		Uncertainty (±°C)	Reference	Notes
						High	Low			
MAAT estimates for the Kaiparowits Formation										
Kaiparowits	46.2	0	Upper Campanian	LMA	20	20	20	2	Miller et al., 2013	
Vermejo	43.6	-2.6	Upper Campanian/ Lower Maastrichtian	CLAMP	18	17	17	1	Wolfe, 1990	
McRae	42.0	-4.2	Upper Campanian/ Lower Maastrichtian	LMA	22	21	20	2	Upchurch et al., 2015	
MAAT estimates for the Two Medicine Formation										
Two Medicine	55.0	0	Campanian	LMA	16	16	16	5	Foreman et al., 2011; Falcon-Lang, 2003; Wolfe and Upchurch, 1987	Based on the Late Cretaceous latitudinal temperature gradient reconstructed by Wolfe and Upchurch (1987) from multiple North American fossil leaf assemblages using leaf margin analysis. Uncertainty from Peppe et al. (2011)
Judith River	55.6	0.6	Upper Campanian	Turtle and Gar $\delta^{18}O$	14	14	14	1	Barrick et al., 1999	Late Cretaceous river temperature.
Judith River	55.6	0.6	Upper Campanian	Turtle and Gar $\delta^{18}O$	16	17	17	1	Barrick et al., 1999	Late Cretaceous river temperature.
Judith River	55.6	0.6	Upper Campanian	Turtle and Gar $\delta^{18}O$	19	19	19	1	Barrick et al., 1999	Late Cretaceous river temperature.
Eagle	50.9	-4.05	Lower Campanian	LMA	16	15	14	5	Van Boskirk, 1998	Uncertainty from Peppe et al. (2011)

a - Paleolatitudes from Upchurch et al. (2015) and Miller et al. (2013)

b - Calculated as straight-line north or south distance from the KF and TMF in degrees of latitude.

c - Mean annual air temperature (MAAT)

d - The latitude adjusted MAAT values for the KF and TMF were calculated using the Wolfe and Upchurch (1987) Late Cretaceous North American latitudinal temperature gradient of 0.3 to 0.4 °C.

We suggest that two factors influenced the KF and TMF soils during formation, leading to higher (lower) PWI (CIA-K) values and unrealistically low MAT and MAP estimates. First, the extremely high sediment accumulation rates during deposition of the KF (39 to 41 cm ka^{-1}; Roberts et al., 2005) may have provided a nearly continuous supply of fresh sedimentary material to the forming soils. If this input of fresh material (and the associated cations used to calculate PWI and CIA-K: Al, Ca, K, Mg, and Na) kept pace with soil weathering and leaching, the resulting PWI and CIA-K values would not reflect local MAT and MAP. Second, many of the paleosols in both the KF (11 of 19) and TMF (13 of 43) display vertic features such as well-developed slickensides and distinct clay accumulations. Buol et al. (2011) note that the presence of such features inhibits the leaching of cations from the soil, which would in turn result in high (low) PWI (CIA-K) values and unrealistically low MAT and MAP estimates.

Based on these considerations, we interpret the high (low) PWI (CIA-K) values from our paleosols as being caused by soil-forming factors rather than climate-dependent weathering conditions. Because of this, we choose to calculate MART based on previous estimates of MAT from the KF and TMF (see section 2.1). In order to provide a range of possible MART values we utilize latitude-adjusted MAT reconstructions from formations that formed coevally with, and in close proximity to, our study areas, and that represented similar alluvial or coastal plain settings along the WIS (see Table 4.4; Upchurch et al., 2015; Barrick et al., 1999; Van Boskirk, 1998; Wolfe, 1990). The MART estimates that result from using these ranges of MAT reconstructions are discussed in the following section.

4.6.3. Calculating Late Cretaceous MART and cold month mean air temperature

Modern MART is generally calculated by subtracting local winter temperatures from local summer temperature (Peppe et al., 2011); however, because quantitative winter temperature estimates are unavailable for the KF and TMF, we calculate Late Cretaceous MART as twice the difference between warm month mean air temperature (from our paleosol T(Δ_{47}) values) and MAAT from previous paleobotanical (Upchurch et al., 2015; Miller et al., 2013; Van Boskirk, 1998; Wolfe and Upchurch, 1987) and fossil phosphate oxygen isotope reconstructions (Barrick et al., 1999). The use of paleobotanical MAAT reconstructions is justified for two reasons: 1) LMA and CLAMP reconstructions of MAAT are considered more robust than paleobotanical reconstructions of warmest and coldest month mean temperatures (see section 2.2 and Jordan, 1996, 1997b); and 2) for both the KF and TMF, we estimate the range in MAAT from at least two studies using different proxy methods. In order to take into account the possible uncertainties associated with our various assumptions, we calculate four different MART and cold month mean air temperature values for each study area. First, we make use of the warmest and coldest MAAT estimates available for the KF and TMF formations, or for coeval formations in close proximity (Table 4.4), which provides a window of possible MAAT values. MAAT estimates for the various formations listed in Table 4.4 were adjusted based on the north/south latitudinal distance between the given formation and the KF or TMF, and the predicted Late Cretaceous latitudinal temperature gradient (0.3 to 0.4 °C °latitude^{-1}; Amiot et al., 2004; Wolfe and Upchurch, 1987). All of the formations used for these MAAT estimates come from coeval, low elevation, coastal or alluvial plain depositional environments along the WIS (Miller et al., 2013; Foreman et

al., 2011; Barrick et al., 1999; Van Boskirk, 1998; Wolfe, 1990; Lozinsky et al., 1984). For example, Upchurch et al. (2015) report a MAT of 22 °C for the late Campanian/early Maastrichtian McCrae Formation in southwestern New Mexico, which is located 4.2 degrees south of the KF. Thus, the adjusted MAT for the KF based on the Upchurch et al. (2015) MAAT reconstruction is 21 to 20 °C, consistent with the Miller et al. (2013) MAT estimate for the KF. We note that the latitudinal corrections made here are generally smaller than the uncertainty reported for the MAAT estimates, suggesting that these corrections are not a significant source of bias. Second, we assume two different values of warm month mean air temperature: first, we calculate MART and cold month mean air temperature assuming there is no radiative soil heating, such that warmest month mean air temperature is equal to warmest month mean soil temperature (e.g., our mean $T(\Delta_{47})$ values); second, we perform the same calculations, but we assume a maximum ST_{RH} value by subtracting 3 °C from our $T(\Delta_{47})$ values. For each of these calculations there are three sources of quantifiable uncertainty: 1) the mean analytical uncertainty of the sample $T(\Delta_{47})$ estimates (±4 °C for both the KF and TMF samples); 2) the uncertainty on the mean of the KF and TMF samples (±2 and ±4 °C, respectively); and 3) the analytical uncertainty of the MAAT estimates from each site, as reported in Table 4.4.

The initial MART estimates for the KF range from 21±5 to 35±4 °C, and from 21±4 to 37±6 °C for the TMF (Fig. 4.8; Table 4.5). Assuming a symmetrical annual temperature distribution, coldest month mean air temperature estimates based on these MART values are -1±4 to 10±5 °C for the KF, and -5±6 to 8±4 °C for the TMF. As

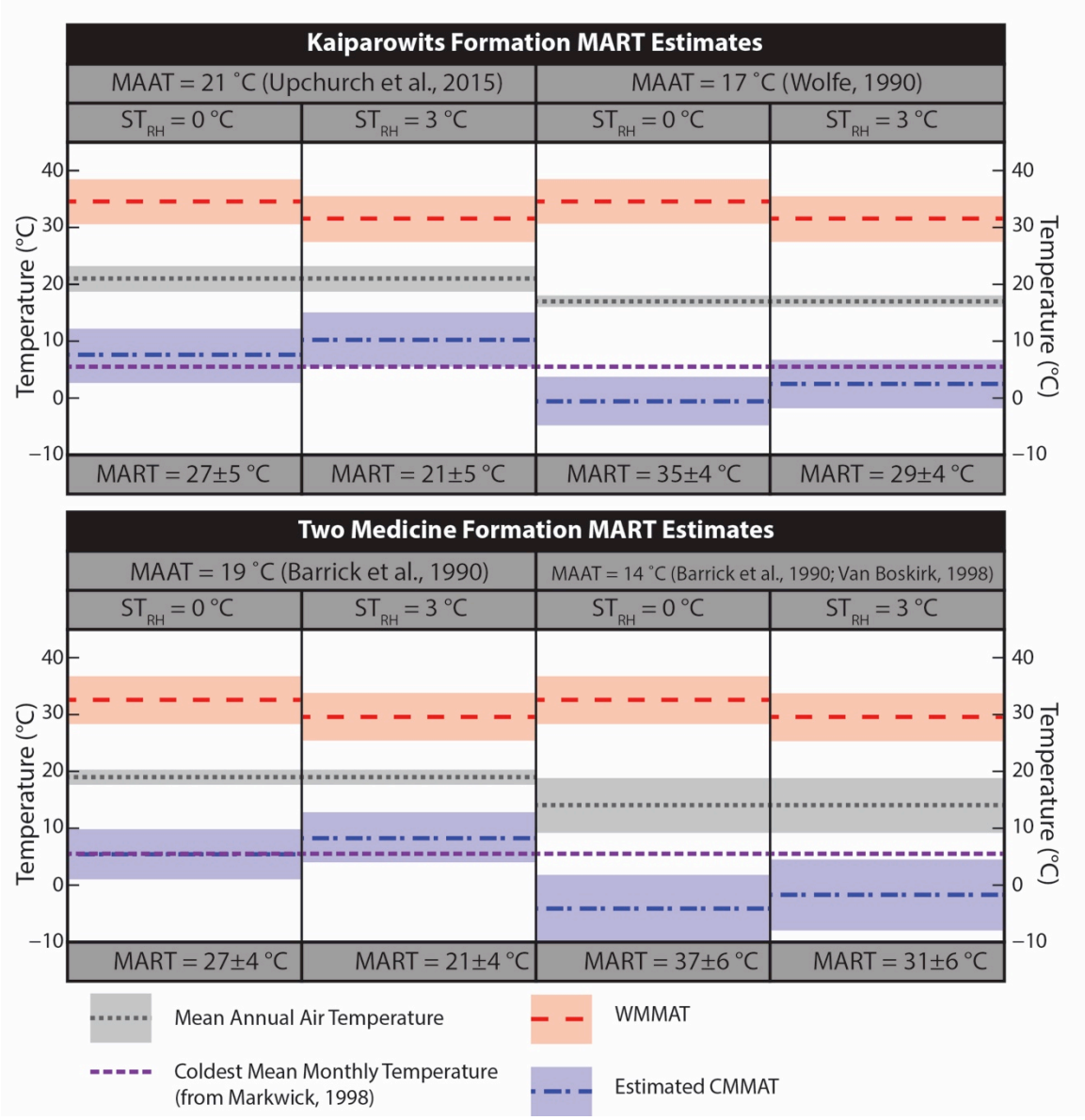

Figure 4.8. Mean annual range in temperature (MART) for the KF (upper panel) and TMF (lower panel). Winter cold temperature limit (purple small dashed line) from Markwick (1998). MAAT estimates for the KF and TMF denoted by the gray dotted line. Warmest month mean soil temperature reconstructed from paleosol carbonate T(Δ_{47}) (red large dashed line) calculated assuming an STRH of either 0 °C or 3 °C. Estimated coldest mean month temperature denoted with blue dot-dashed line.

discussed in Section 2.2, the presence of crocodilian fossils in both the KF (e.g., Farke et al., 2014; Boyd et al., 2013; Getty et al., 2010) and TMF (e.g., Horner et al., 2001; Varricchio, 1995) place a lower limit of ~5 °C (Markwick, 1998) on long term coldest month mean air temperature. If this temperature tolerance was conserved in Cretaceous crocodilians, it would indicate that our lowest coldest month mean air temperature estimates for the KF (-1±4 °C) and the lowest two estimates for the TMF (-5±6 and -2±6 °C) are likely too cold. This suggests that the best estimate of coldest month mean air temperature for the KF is ~2 to ~10 °C, and ~5 to ~8 °C for the TMF.

Ruling out those MART reconstructions that result in coldest month mean air temperature estimates below 5 °C leads to a narrower range of ~21 to ~29 °C for the KF MART values, and ~21 to ~27 °C for the TM MART values. Because our review of SCAN station soil and air temperature data shows that ST_{RH} values of 3 °C or higher are extremely rare in humid environments, we suggest that the high end of our range of MART estimates are the most plausible, since they assume no radiative soil heating.

The MART estimates for the KF and TMF are significantly larger than past reconstructions derived mainly from leaf physiognomy proxies (MART = 8 to 10 °C; Hunter et al., 2013; Wolfe and Upchurch, 1987), and suggest that mid-latitude seasonal temperature changes during the Late Cretaceous were of similar magnitudes to modern mid-latitude sites. The smaller MART estimates from leaf physiognomy could be due to the inaccuracies in warmest and coldest month temperature estimates from CLAMP and other leaf physiognomy proxies capable of reconstructing seasonal temperatures, as described by previous studies (e.g., Spicer et al., 2004, Jordan, 1996, 1997b). Such inaccuracies can be caused by a variety of climate, biologic, and geologic processes

Table 4.5. Mean annual, warmest mean month, coldest mean month, and mean annual range in temperature results.

MAAT Estimate (°C)[a]	±1 SE (°C)	Reference	ST_{RH} (°C)	WMMAT (°C)[b]	±1 SE (°C)	CMMAT (°C)[c]	±1 SE (°C)	MART (°C)[d]	±1 SE (°C)
Kaiparowits Formation									
21	2	Upchurch et al., 2015	0	35	4	7	5	27	5
21	2	Upchurch et al., 2015	3	32	4	10	5	21	5
17	1	Wolfe, 1990	0	35	4	*-1*	4	*35*	4
17	1	Wolfe, 1990	3	32	4	2	4	29	4
Two Medicine Formation									
19	1	Barrick et al., 1990	0	33	4	5	4	27	4
19	1	Barrick et al., 1990	3	30	4	8	4	21	4
14	5	Barrick et al., 1990; Van Boskirk, 1998	0	33	4	*-5*	6	*37*	6
14	5	Barrick et al., 1990; Van Boskirk, 1998	3	30	4	*-2*	6	*31*	6

a - Mean annual air temperature (MAAT)

b - Warmest month mean air temperature (WMMAT). Lower WMMAT values calculated by subtracting 3 °C from the mean paleosol carbonate T(Δ_{47}) results in order to account for maximum radiative soil heating.

c - Coldest month mean air temperature (CMMAT). Italicized values are interpreted as too cold to be reasonable based on the presence of crocodilian fossils in both the Kaiparowits and Two Medicine Formations.

d - Mean annual range in temperature (MART). Italicized values are interpreted as too cold to be reasonable based on the presence of crocodilian fossils in both the Kaiparowits and Two Medicine Formations.

including 1) taphonomic loss of leaf physiognomic characters (Spicer et al., 2005); 2) evapotranspiration cooling of forest canopies (Spicer et al., 2011); 3) the weak relationship between leaf size and warmest mean monthly temperature (Spicer and Yang, 2010); 4) high regional dependence of warmest and coldest month mean temperatures; or 5) covariance between warmest and coldest month mean temperatures, and a lack of independence between seasonal temperatures and MAAT (Jordan, 1996, 1997b) .

In order to further evaluate the uncertainties associated with these MART reconstructions, we used ERA-Interim climate reanalysis data to calculate modern MART in two different ways: first as the difference between modern warmest month mean air temperature and coldest month mean air temperature (hereafter referred to as $MART_{S\text{-}W}$), and second—following our method for calculating Late Cretaceous MART––as twice the difference between warmest month mean air temperature and MAAT. We then subtracted $MART_{S\text{-}W}$ from $MART_{S\text{-}MAT}$ such that a positive (negative) difference ($MART_{DIF}$) indicates that the $MART_{S\text{-}MAT}$ method is overestimating (underestimating) true MART, in order to compare the relative predictive power of the two methods. In both cases, we chose to use warmest month air and soil temperatures rather than mean summer air or soil temperatures, in order to be consistent with our interpretation of the paleosol carbonate $T(\Delta_{47})$ being representative of warmest month mean soil temperature.

Aside from deserts and high-latitude ice sheets, our calculations of modern $MART_{S\text{-}MAT}$ and $MART_{S\text{-}W}$ from ERA-Interim climate reanalysis output are in general agreement. Figure 4.9 shows that for all types of vegetated surfaces (as identified in MODIS imagery) mean $MART_{DIF}$ is -0.03 °C, with a maximum and minimum of 0.7 and -0.8 °C, respectively. In contrast, the mean $MART_{DIF}$ for ice and snow is 7.0 °C, and -1.8

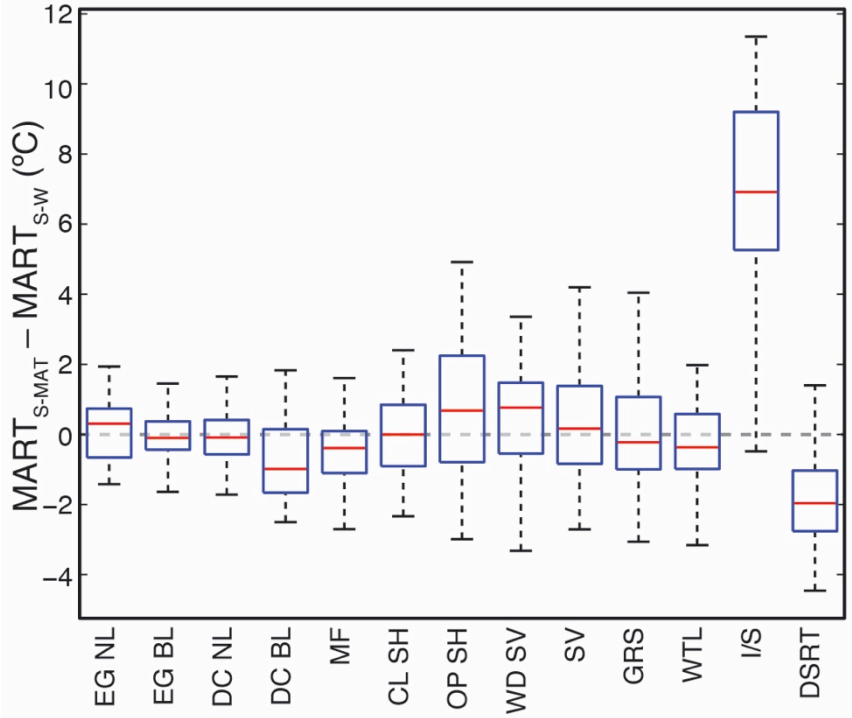

Figure 4.9. Mean $MART_{DIF}$ calculated from ERA-Interim climate reanalysis output, for thirteen different land cover types: evergreen needle leaf (EG NL), evergreen broad leaf (EG BL), deciduous needle leaf (DC NL), deciduous broad leaf (DC BL), mixed forest (MF), closed shrubland (CL SH), open shrubland (OP SH), woody savanna (WD SV), savanna (SV), grassland (GRS), WTL (wetland), ice and snow (I/S), desert (DSRT). Red lines represent median values for each bin, while blue boxes indicate 2σ and vertical dashed lines indicate full range of values. The boxplot symbology is the same as in Figure 6. Dashed line represents a $MART_{DIF}$ value of 0 °C (i.e., identical $MART_{S\text{-}MAT}$ and $MART_{S\text{-}W}$).

°C for desert and other barren land cover types. Our calculations of modern $MART_{S\text{-}MAT}$ and $MART_{S\text{-}W}$ are in general agreement; however, as shown in Figure 4.9 there are specific regions, such as the Antarctic and Greenland ice sheets, where $MART_{dif}$ can be quite large. High latitude (>60 °N/°S) $MART_{dif}$ values are much larger than mid- or low-latitude $MART_{dif}$ values, averaging 3.3 °C, with maximum and minimum differences of 11.4 and -4.5 °C, respectively. For the mid-latitudes, the mean $MART_{dif}$ value is 0.1 °C, with maximum and minimum differences of 3.6 and -5 °C, respectively. $MART_{dif}$ variability is nearly twice as large over the mid-latitude continents than over mid-latitude oceans (σ_{land}=0.45 °C, σ_{water}=0.24 °C). The magnitude of $MART_{dif}$ also varies with land cover type, and is especially large over ice sheets (Figures 4.10C, 4.10D, and 4.9). These

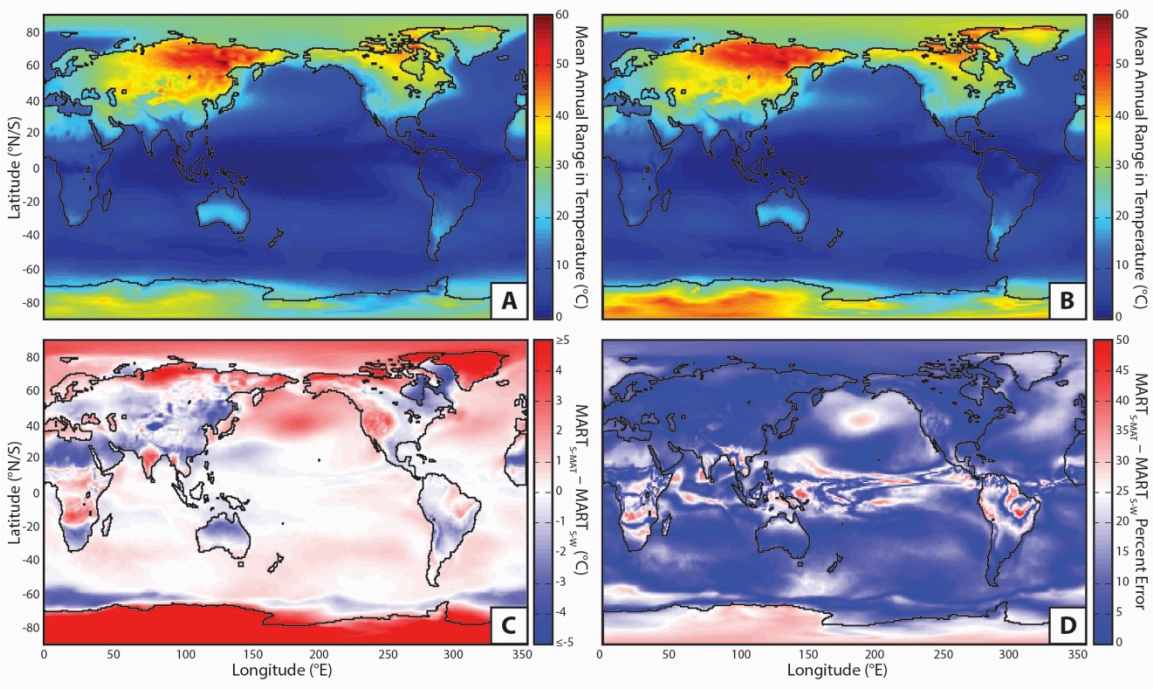

Figure 4.10. Mean annual range in temperature (MART) calculations, based on: A) summer minus winter temperatures ($MART_{S-W}$), and B) twice the difference between summer and mean temperatures ($MART_{S-MAT}$). Panel C shows the temperature difference between $MART_{S-MAT}$ and $MART_{S-W}$ ($MART_{DIF}$), and Panel D shows the percent error between the two methods of calculating MART. Temperature data from ERA-Interim reanalysis output.

$MART_{DIF}$ results suggest that calculating MART from just warmest month mean air temperature and MAAT should produce accurate estimates of the actual range in seasonal temperatures for nearly all mid-latitude terrestrial environments. These findings provide additional confidence that our Late Cretaceous MART calculations are accurately capturing the true range in seasonal temperatures.

We note that the potential error on our MART estimates are non-trivial (±4 to 6 °C) despite careful screening and a large number replicate carbonate analyses. In view of this fact, we suggest that future MART reconstruction studies will benefit from both a larger number of samples and replicate measurements than is traditionally collected for paleosol carbonate studies, and from the recalculation of older MAAT estimates from LMA (e.g., those presented in Wolfe and Upchurch (1987) and used in Foreman et al.

(2011) and this study) using modern methods (see Peppe et al., 2011) to reduce associated uncertainties.

4.6.4. Implications for seasonality in greenhouse climates

Having calculated Late Cretaceous MART values and evaluated their accuracy and associated uncertainties, we now compare the reconstructed MARTs to modern seasonal variability. This can be challenging because there are no perfect modern analogs for our study areas due to the fact that modern locations with similar MAAT and MAP (e.g., the Gulf Coast of the United States; Miller et al., 2013) are restricted to much lower latitudes than the Late Cretaceous paleolatitudes of the KF and TMF, and no major interior seaways exist in the modern. However, a comparison of our Late Cretaceous MART results to a suite of modern MART values shows that our estimates are consistent with the range of MART seen in North America today (Fig. 4.11). Lower-latitude environments like the Gulf Coast, which is thought to be analogous to the KF in terms of temperature and precipitation (Miller et al., 2013; Tidwell et al., 2007), experience significantly lower MART than our reconstructions due to their lower latitude positions, but modern sites within the same range of latitudes as our study area paleolatitudes have similar mean MART. These findings suggest that latitude has a larger impact on terrestrial seasonality than global mean surface temperatures, regardless of whether the climate is in a greenhouse or icehouse state (Sloan and Barron, 1990).

In addition to a comparison against modern MART values, we evaluate our KF and TMF MART, warmest month mean air temperature, and coldest month mean temperature estimates against MART values calculated from Late Cretaceous climate model output generated by Sewall and Fricke (2013). Due to differences in the

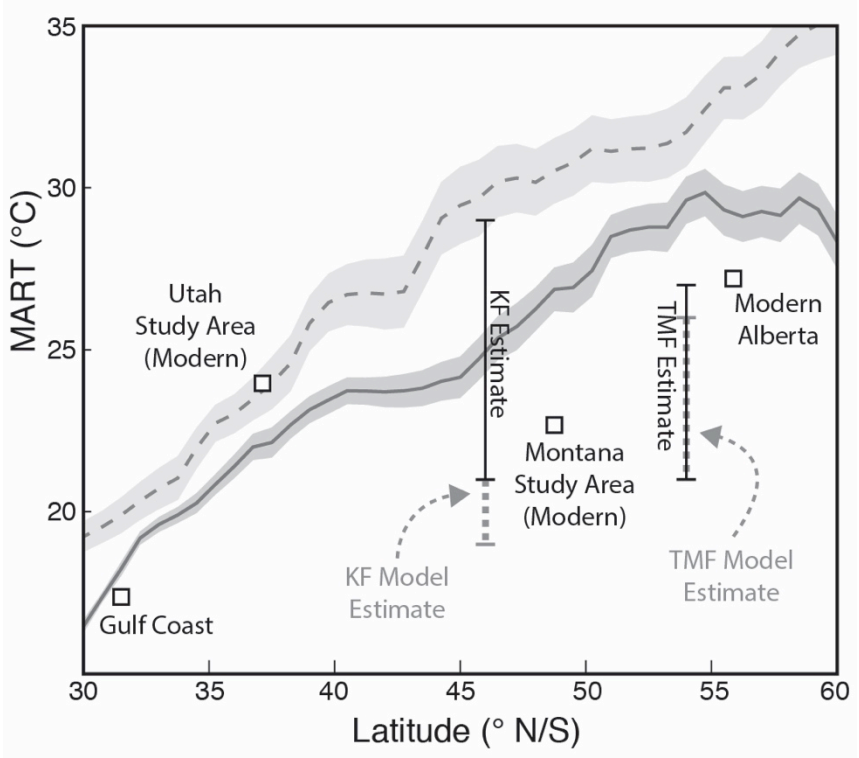

Figure 4.11. Mean annual range in temperature (MART) versus latitude. The thick gray line and dark gray band show North American mean MART at the 95% confidence interval. The thick dashed gray line and light gray band show global mean MART at the 95% confidence interval. Black error bars show MART reconstructions for the KF and TMF and the thick gray dashed bars are the simulated MART for the KF and TMF using model output from Sewall and Fricke (2013). White squares show modern MART for various related locations.

longitudinal position of the paleogeographic reconstructions used in this study versus the reconstruction used in the Sewall and Fricke (2013) model, we compare our results to the output from three model grid cells located around the KF study area, and four model grid cells around the TMF study area. Grid cells were chosen to avoid cooler upland and ocean areas (Figure 4.12). The mean model estimates of coldest month mean air temperatures for the KF study area are 3 °C warmer than our reconstructions, but our TMF coldest month mean air temperature estimates agree well with modeled winter temperatures, regardless of the exact MAAT and ST_{RH} values used in our MART calculations. The model underestimates warmest month mean temperature relative to our proxy reconstructions by ~4 °C at both sites—a common issue with model simulations of

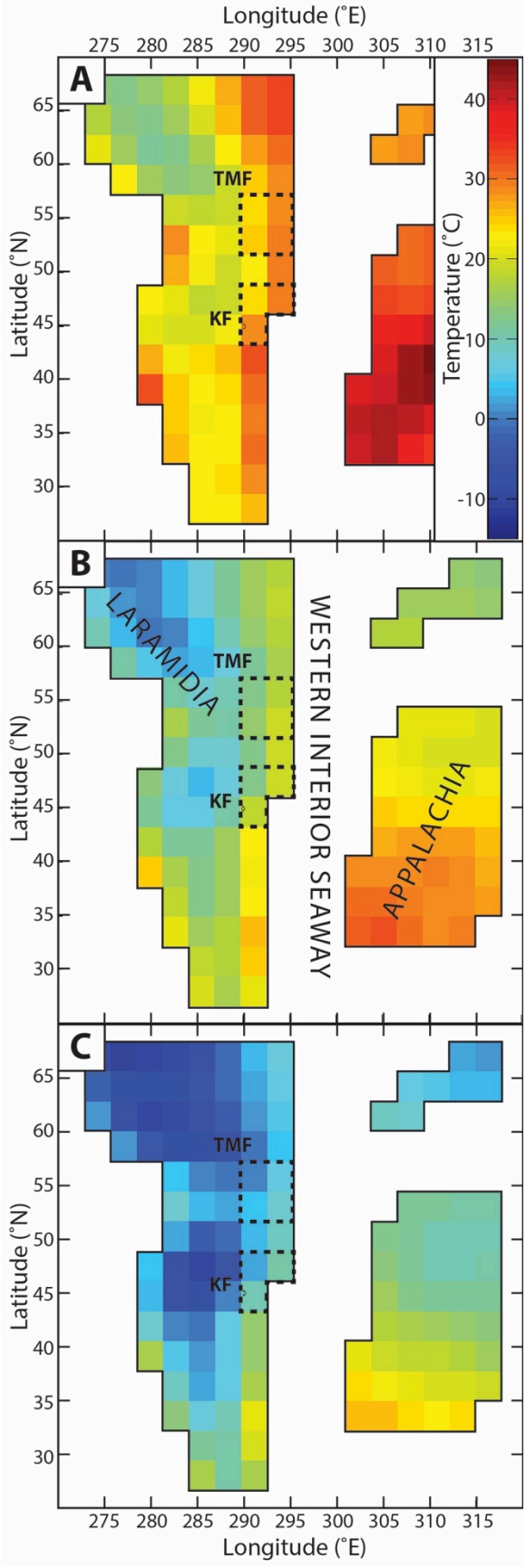

Figure 4.12. Visualization of Sewall and Fricke (2013) Late Cretaceous (Campanian) global climate model output. The grid cells used for comparison with our Kaiparowits (KF) and Two Medicine Formation (TMF) paleoclimate reconstructions are highlighted with dashed black lines. Panel A shows warmest mean monthly air temperatures (WMMAT), panel B shows mean annual air temperatures (MAAT), and panel C shows coldest mean monthly air temperatures (CMMAT). Additional text in panel B provides the name of relevant paleogeographic locations.

both the Late Cretaceous and Eocene greenhouse periods (Snell et al., 2013; Spicer et al., 2008). Calculations of MART using the model output yield mean values of 20±2 and 23±2 °C for the KF and TMF, respectively. Taking into account the associated uncertainties, the model MART estimates for the KF are consistent with the lower limits of our MART reconstructions for the KF and TMF, and the model MART estimates for the TMF are in very good agreement with our MART reconstructions.

We interpret the minor differences between the model simulations and our proxy reconstructions and estimates to be the result of some combination of: 1) spatial averaging of warmest and coldest month mean air temperatures due to the relatively coarse model resolution (~2.8° latitude × ~2.8° longitude; Sewall and Sloan, 2006); 2) the accidental inclusion of cooler upland regions in estimates of average model temperatures; and 3) uncertainty in the exact location of the KF and TMF study sites relative to the model grid due to differing paleogeographic reconstructions. We note that in addition to being consistent with the Sewall and Fricke (2013) simulation of Late Cretaceous North America, our results are in general agreement with past global or other regional modeling studies suggestive of a modern range in seasonality during the Late Cretaceous and other greenhouse periods (e.g., Hunter et al., 2013; Huber and Caballero, 2011; Valdes, 2011; Spicer et al., 2008; Deconto et al., 1999).

Our Late Cretaceous MART reconstructions add to a growing body of proxy evidence showing that terrestrial environments experience similar magnitudes of seasonal temperature change in both greenhouse and icehouse conditions (Hyland, 2018; Suarez et al., 2017; Snell et al., 2013). Additionally, our results provide evidence that during greenhouse periods like the Late Cretaceous and Paleogene, MAAT is shifted to higher

values, but MART remains essentially unchanged. Our MART reconstructions are similar in magnitude to model MART simulations (Sewall and Fricke, 2013; Snell et al., 2013; Sloan and Barron, 1990), which may indicate that disagreements between model simulations and proxy reconstructions of MART are likely due primarily to proxy shortcomings such as: 1) the effect of non-climate factors on leaf physiognomy proxies (e.g. Peppe et al., 2011), and 2) uncertainties regarding the climatic constraints of fossil plants and animals that are used as qualitative paleoclimate proxies. We note that uncertainties in model paleogeographic reconstructions may also limit the accuracy of proxy-model comparison studies (Kelson et al., *in revision*).

The presence of modern-magnitudes of MART in the Late Cretaceous also has implications for the geographic distribution and lifestyles of dinosaur and non-dinosaur faunal communities in western North America. There has been a long-standing debate regarding the degree of provincialism (e.g. regional partitioning) of northern and southern faunal communities along the western margin of the WIS during the Late Cretaceous (Leslie et al., 2018; Lucas et al., 2016; Morrone, 2014; Nydam et al., 2013; Gates et al., 2010; Sampson et al., 2010; Lehman et al., 2006; Lehman, 2001). Faced with a lack of known geographic barriers to animal migration, studies in favor of faunal provincialism have often cited latitudinal changes to climate as the driving force behind regionally discrete animal populations (e.g., Gates et al. 2010; Sampson et al., 2010). The approximate latitudinal position of this climate interface between the northern and southern provinces has been speculated to be near the present day northern borders of Utah and Colorado (Sampson et al., 2010). However, when paired with previous estimates of MAAT for both the KF and TMF, our warmest month mean temperature,

MART, and coldest month mean temperature reconstructions indicate that environmental conditions were similar in southern Utah and northwestern Montana during deposition of the KF and TMF, with only slightly cooler conditions characterizing the TMF during the winter. The difference in MAAT between the two sites was <5 °C, and MART was essentially identical. These findings suggest that there were no distinct temperature-related environmental changes between the KF and TMF that would have inhibited large terrestrial animals from inhabiting or migrating between the two areas during the Late Cretaceous. This may suggest that if some sort of climate "barrier" existed between the northern and southern provinces of the western margin of the WIS, that it was related to changes in precipitation and/or water availability (Fricke et al., 2010; Wolfe and Upchurch, 1987; Hallam, 1985, 1984; Parrish, et al., 1982).

4.7. Conclusions

Our findings show that Late Cretaceous MART along the mid-latitude region (paleolatitude: ~46 to 56 °N) of the western margin of the WIS was similar to mid-latitude MART in modern North America, and that no distinct change in MART or warmest and coldest month temperatures exists between the southern and northern limits of this area. Additionally, we show that: 1) reconstructing paleo-MART from warmest mean monthly temperatures and independent MAAT estimates should yield accurate results for most vegetated environments, and 2) in all but the driest environments, soil heating from incident solar radiation is typically <<3 °C (96% of SCAN stations) for commonly sampled soil types and depths (50–100 cm).

Modern-magnitude MARTs have now been reconstructed for two separate greenhouse periods using carbonate clumped isotope thermometry: the Late Cretaceous

(this study), and the Paleogene (Hyland et al., 2018; Snell et al., 2013), suggesting that modeling efforts to simulate greenhouse climates are more accurate than has previously been argued, and increasing confidence in future predictions of MART under predicted climate change scenarios. Future studies of Late Cretaceous MART should focus on true continental interior environments to provide a more complete picture of how MART varied between different Late Cretaceous sites, as well as providing additional evidence for the limited effect of climate on faunal provincialism in North America during this period.

4.8 Acknowledgements

The authors acknowledge support from the Quaternery Research Center and the UW Isolab, and thank the Grand Staircase-Escalante National Monument staff for access to the Kaiparowits Formation outcrops in Utah, and Robert Wellman for access to the Two Medicine Formation outcrops in Montana.

Chapter 5: References

Affek, H.P., Matthews, A., Ayalon, A., Bar-Matthews, M., Burstyn, Y., Zaarur, S., Zilberman, T., 2014. Accounting for kinetic isotope effects in Soreq Cave (Israel) speleothems. Geochim. Cosmochim. Acta 143, 303–318. https://doi.org/10.1016/j.gca.2014.08.008

Affek, H.P., Zaarur, S., 2014. Kinetic isotope effect in CO_2 degassing: Insight from clumped and oxygen isotopes in laboratory precipitation experiments. Geochim. Cosmochim. Acta 143, 319–330. https://doi.org/10.1016/j.gca.2014.08.005

Amiot, R., Lécuyer, C., Buffetaut, E., Fluteau, F., Legendre, S., Martineau, F., 2004. Latitudinal temperature gradient during the Cretaceous Upper Campanian-Middle Maastrichtian: $\delta^{18}O$ record of continental vertebrates. Earth Planet. Sci. Lett. 226, 255–272. https://doi.org/10.1016/j.epsl.2004.07.015

Amundson, R., Wang, Y., Chadwick, O., Trumbore, S., McFadden, L., McDonald, E., Wells, S., DeNiro, M., 1994. Factors and processes governing the ^{14}C content of carbonate in desert soils. Earth Planet. Sci. Lett. 125, 385–405. https://doi.org/10.1016/0012-821X(94)90228-3

Arndorff, L., 1994. Upper Triassic and Lower Jurassic palaeosols from southern Scandinavia. Lund Universitet.

Barrick, R.E., Fischer, A.G., Showers, W.J., 1999. Oxygen Isotopes from Turtle Bone : Applications for Terrestrial Paleoclimates? Palaios 14, 186–191.

Barron, E.J., Fawcett, P.J., Peterson, W.H., Pollard, D., Thompson, S.L., 1995. A "simulation" of mid-Cretaceous climate. Paleoceanography 10, 953–962.

Barron, E.J., 1987. Eocene equator-to-pole surface temperatures: a significant climate problem? Paleoceanography 2, 729–739.

Barron, E.J., 1983. A warm, equable Cretaceous: The nature of the problem. Earth Sci. Rev. 19, 305–338. https://doi.org/10.1016/0012-8252(83)90001-6

Bartlett, M.G., Chapman, D.S., Harris, R.N., 2006. A decade of ground-air temperature tracking at emigrant pass observatory, Utah. J. Clim. 19, 3722–3731. https://doi.org/10.1175/JCLI3808.1

Beck, W.C., Grossman, E.L., Morse, J.W., 2005. Experimental studies of oxygen isotope fractionation in the carbonic acid system at 15°, 25°, and 40° C. Geochim. Cosmochim. Acta 69, 3493–3503. https://doi.org/10.1016/j.gca.2005.02.003

Berry, J., Bjorkman, O., 1980. Photosynthetic Response and Adaptation to Temperature in Higher Plants. Annu. Rev. Plant Physiol. 31, 491–543. https://doi.org/10.1146/annurev.pp.31.060180.002423

Beverly, E.J., Peppe, D.J., Driese, S.G., Blegen, N., Faith, J.T., Tryon, C.A., Stinchcomb, G.E., 2017. Reconstruction of Late Pleistocene Paleoenvironments Using Bulk Geochemistry of Paleosols from the Lake Victoria Region. Front. Earth Sci. 5, 1–12. https://doi.org/10.3389/feart.2017.00093

Birkeland, P.W., 1985. Quaternary Soils of the Western United States. Geol. J. 20, 303–324.

Boskirk, V., Craig, M., 1998. The flora of the Eagle Formation and its significance for late Cretaceous floristic evolution. Yale University.

Bottinga, Y., 1968. Calculation of Fractionation Factors for Carbon and Oxygen Isotopic Exchange in the System Calcite-Carbon Dioxide-Water. J. Phys. Chem. 72, 800–808. https://doi.org/10.1021/j100849a008

Bouma, T.J., Bryla, D.R., 2000. On the assessment of root and soil respiration for soils of different textures: interactions with soil moisture contents and soil CO_2 concentrations. Plant Soil 227, 215–221. https://doi.org/10.1023/A:1026502414977

Bowen, G.J., Beerling, D.J., 2004. An integrated model for soil organic carbon and CO_2 : Implications for paleosol carbonate pCO_2 paleobarometry. Global Biogeochem. Cycles 18, n/a-n/a. https://doi.org/10.1029/2003GB002117

Boyd, C.A., Drumheller, S.K., Gates, T.A., 2013. Crocodyliform Feeding Traces on Juvenile Ornithischian Dinosaurs from the Upper Cretaceous (Campanian) Kaiparowits Formation, Utah. PLoS One 8. https://doi.org/10.1371/journal.pone.0057605

Brady, N.C., Weil, R.R., 2010. Elements of the Nature and Properties of Soils, 3rd Editio. ed. Pearson.

Brand, W.A., Assonov, S.S., Coplen, T.B., 2010. Correction for the ^{17}O interference in $\delta(^{13}C)$ measurements when analyzing CO_2 with stable isotope mass spectrometry (IUPAC Technical Report). Pure Appl. Chem. 82, 1719–1733. https://doi.org/10.1351/PAC-REP-09-01-05

Breecker, D.O., Sharp, Z.D., McFadden, L.D., 2010. Atmospheric CO2 concentrations during ancient greenhouse climates were similar to those predicted for A.D. 2100. Proc. Natl. Acad. Sci. 107, 576–580. https://doi.org/10.1073/pnas.0902323106

Breecker, D.O., Sharp, Z.D., McFadden, L.D., 2009. Seasonal bias in the formation and stable isotopic composition of pedogenic carbonate in modern soils from central New Mexico, USA. Geol. Soc. Am. Bull. 121, 630–640. https://doi.org/10.1130/B26413.1

Bunting, B.T., Christensen, L., 1978. Micromorphology of calcareous crusts from the Canadian High Arctic. Geol. Föreningen i Stock. Förhandlingar 361–367.

Burgener, L., Huntington, K.W., Hoke, G.D., Schauer, A., Ringham, M.C., Latorre, C., Díaz, F.P., 2016. Variations in soil carbonate formation and seasonal bias over >4 km of relief in the western Andes (30°S) revealed by clumped isotope thermometry. Earth Planet. Sci. Lett. 441, 188–199. https://doi.org/10.1016/j.epsl.2016.02.033

Campbell, I.B., Claridge, G.G.C., Campbell, D.I., Balks, M.R., 1998. The soil environment of the McMurdo Dry Valleys, Antarctica, in: Priscu, J.C. (Ed.), Ecosystem Dynamics in a Polar Desert: The McMurdo Dry Valleys, Antarctica; Antarctic Research Series 72. American Geophysical Union, p. 369.

Carrapa, B., Huntington, K.W., Clementz, M., Quade, J., Bywater-Reyes, S., Schoenbohm, L.M., Canavan, R.R., 2014. Uplift of the Central Andes of NW Argentina associated with upper crustal shortening, revealed by multiproxy isotopic analyses. Tectonics 33, 1039–1054. https://doi.org/10.1002/2013TC003461

Carter, M., Bentley, S., 1991. Correlations of Soil Properties. Pentech Press Publishers, Lond.

Cerling, T.E., Wynn, J.G., Andanje, S.A., Bird, M.I., Korir, D.K., Levin, N.E., MacE, W., MacHaria, A.N., Quade, J., Remien, C.H., 2011. Woody cover and hominin environments in the past 6-million years. Nature 476, 51–56. https://doi.org/10.1038/nature10306

Cerling, T., Quade, J., 1993. Stable carbon and oxygen isotopes in soil carbonates, in: Swart, P.K., Lohmann, K.C., McKenzie, J., Savin, S. (Eds.), Climate Change in Continental Isotopic Records. American Geophysical Union, pp. 217–231.

Cerling, T.E., Solomon, D.K., Quade, J., Bowman, J.R., 1991. On the isotopic composition of carbon in soil carbon dioxide. Geochim. Cosmochim. Acta 55, 3403–3405. https://doi.org/10.1016/0016-7037(91)90498-T

Cerling, T.E., Quade, J., Wang, Y., Bowman, J.R., 1989. Carbon isotopes in soils and palaeosols as ecology and palaeoecology indicators. Nature 341, 138–139. https://doi.org/10.1038/341138a0

Cerling, T.E., Hay, R.L., 1986. An isotopic study of paleosol carbonates from Oldovai Gorge. Quat. Res. 25, 63–78.

Cerling, T.E., Wang, Y., 1996. Stable carbon and oxygen isotopes in soil CO_2 and soil carbonate: theory, practice, and application to some prairie soils of upper Midwestern North America, in: Mass Spectrometry of Soils. Marcel Dekker, New York, pp. 113–132. https://doi.org/10.1017/CBO9781107415324.004

Cerling, T.E., 1992. Use of carbon isotopes in paleosols as an indicator of the $p(CO_2)$ of the paleoatmosphere. Global Biogeochem. Cycles 6, 307–314.

Cerling, T.E., 1984. The stable isotopic composition of modern soil carbonate and its relationship to climate. Earth Planet. Sci. Lett. 71, 229–240. https://doi.org/10.1016/0012-821X(84)90089-X

Cermak, V., Bodri, L., Kresl, M., Dedecek, P., Safanda, J., 2016. Eleven years of ground–air temperature tracking over different land cover types. Int. J. Climatol. 37, 1084–1099. https://doi.org/10.1002/joc.4764

Clark, I.D., Lauriol, B., 1992. Kinetic enrichment of stable isotopes in cryogenic calcites. Chem. Geol. 102, 217–228. https://doi.org/10.1016/0009-2541(92)90157-Z

Cotton, J.M., Sheldon, N.D., 2012. New constraints on using paleosols to reconstruct atmospheric pCO_2. Bull. Geol. Soc. Am. 124, 1411–1423. https://doi.org/10.1130/B30607.1

Courty, M., Marlin, C., Dever, L., Tremblay, P., Vachier, P., 1994. The properties, genesis and environmental significance of calcitic pendents from the High Arctic (Spitsbergen). Geoderma 61, 71–102.

da Silva, M.L., Batezelli, A., Ladeira, F.S.B., 2018. Genesis and paleoclimatic significance of palygorskite in the cretaceous paleosols of the Bauru Basin, Brazil. Catena. https://doi.org/10.1016/j.catena.2017.12.031

Daëron, M., Blamart, D., Peral, M., Affek, H.P., 2016. Absolute isotopic abundance ratios and the accuracy of Δ_{47} measurements. Chem. Geol. 442, 83–96. https://doi.org/10.1016/j.chemgeo.2016.08.014

Daëron, M., Guo, W., Eiler, J., Genty, D., Blamart, D., Boch, R., Drysdale, R., Maire, R., Wainer, K., Zanchetta, G., 2011. $^{13}C^{18}O$ clumping in speleothems: Observations

from natural caves and precipitation experiments. Geochim. Cosmochim. Acta 75, 3303–3317. https://doi.org/10.1016/j.gca.2010.10.032

de Winter, N.J., Goderis, S., Dehairs, F., Jagt, J.W.M., Fraaije, R.H.B., Van Malderen, S.J.M., Vanhaecke, F., Claeys, P., 2017. Tropical seasonality in the late Campanian (late Cretaceous): Comparison between multiproxy records from three bivalve taxa from Oman. Palaeogeogr. Palaeoclimatol. Palaeoecol. 485, 740–760. https://doi.org/10.1016/j.palaeo.2017.07.031

Deconto Brady, E.C., Bergengren, J., Hay, W.M., R.M., 2000. Late Cretaceous climate, vegetation, and ocean interactions, in: Warm Climates in Earth History. pp. 275–296.

DeConto, R.M., Hay, W.W., Thompson, S.L., Bergengren, J., 1999. Late Cretaceous climate and vegetation interactions: Cold continental interior paradox. Spec. Pap. 332 Evol. Cretac. Ocean. Syst. 391–406. https://doi.org/10.1130/0-8137-2332-9.391

Defliese, W.F., Hren, M.T., Lohmann, K.C., 2015. Compositional and temperature effects of phosphoric acid fractionation on Δ_{47} analysis and implications for discrepant calibrations. Chem. Geol. 396, 51–60. https://doi.org/10.1016/j.chemgeo.2014.12.018

Defliese, W.F., Lohmann, K.C., 2015. Non-linear mixing effects on mass-47 CO_2 clumped isotope thermometry: Patterns and implications. Rapid Commun. Mass Spectrom. 29, 901–909. https://doi.org/10.1002/rcm.7175

Dennis, K.J., Cochran, J.K., Landman, N.H., Schrag, D.P., 2013. The climate of the Late Cretaceous: New insights from the application of the carbonate clumped isotope

thermometer to Western Interior Seaway macrofossil. Earth Planet. Sci. Lett. 362, 51–65. https://doi.org/10.1016/j.epsl.2012.11.036

Dennis, K.J., Affek, H.P., Passey, B.H., Schrag, D.P., Eiler, J.M., 2011. Defining an absolute reference frame for 'clumped' isotope studies of CO_2. Geochim. Cosmochim. Acta 75, 7117–7131. https://doi.org/10.1016/j.gca.2011.09.025

Dennis, K.J., Schrag, D.P., 2010. Clumped isotope thermometry of carbonatites as an indicator of diagenetic alteration. Geochim. Cosmochim. Acta 74, 4110–4122. https://doi.org/10.1016/j.gca.2010.04.005

DePaolo, D.J., 2011. Surface kinetic model for isotopic and trace element fractionation during precipitation of calcite from aqueous solutions. Geochim. Cosmochim. Acta 75, 1039–1056. https://doi.org/10.1016/j.gca.2010.11.020

Devriendt, L.S., Watkins, J.M., McGregor, H. V., 2017. Oxygen isotope fractionation in the $CaCO_3$-DIC-H_2O system. Geochim. Cosmochim. Acta 214, 115–142. https://doi.org/10.1016/j.gca.2017.06.022

Diaz, N., King, G.E., Valla, P.G., Herman, F., Verrecchia, E.P., 2016. Pedogenic carbonate nodules as soil time archives: Challenges and investigations related to OSL dating. Quat. Geochronol. 36, 120–133. https://doi.org/10.1016/j.quageo.2016.08.008

Diefendorf, A.F., Mueller, K.E., Wing, S.L., Koch, P.L., Freeman, K.H., 2010. Global patterns in leaf ^{13}C discrimination and implications for studies of past and future climate. Proc. Natl. Acad. Sci. 107, 5738–5743. https://doi.org/10.1073/pnas.0910513107

Dietrich, F., Diaz, N., Deschamps, P., Ngounou Ngatcha, B., Sebag, D., Verrecchia, E.P., 2017. Origin of calcium in pedogenic carbonate nodules from silicate watersheds in the Far North Region of Cameroon: Respective contribution of in situ weathering source and dust input. Chem. Geol. 460, 54–69. https://doi.org/10.1016/j.chemgeo.2017.04.015

Dietzel, M., Tang, J., Leis, A., Köhler, S.J., 2009. Oxygen isotopic fractionation during inorganic calcite precipitation - Effects of temperature, precipitation rate and pH. Chem. Geol. 268, 107–115. https://doi.org/10.1016/j.chemgeo.2009.07.015

Ding, Z.L., Yang, S.L., 2000. C3/C4 vegetation evolution over the last 7.0 Myr in the Chinese Loess Plateau: eivdence from pedogenic carbonate d13C. Palaeogeogr. Palaeoclimatol. Palaeoecol. 160, 291–299. https://doi.org/http://dx.doi.org/10.1016/S0031-0182(00)00076-6

Donnadieu, Y., Pierrehumbert, R., Jacob, R., Fluteau, F., 2006. Modelling the primary control of paleogeography on Cretaceous climate. Earth Planet. Sci. Lett. 248, 411–422. https://doi.org/10.1016/j.epsl.2006.06.007

Drever, J.I., 1988. The geochemistry of natural waters, 2nd ed. Prentice Hall, Englewood Cliffs, New Jersey.

Dysli, M., Steiner, W., 2011. Correlations in Soil Mechanics. PPUR Polytechnic Press, Italy.

Eagle, R. a, Risi, C., Mitchell, J.L., Eiler, J.M., Seibt, U., Neelin, J.D., Li, G., Tripati, A.K., 2013. High regional climate sensitivity over continental China constrained by glacial-recent changes in temperature and the hydrological cycle. Proc. Natl. Acad. Sci. U. S. A. 110, 8813–8. https://doi.org/10.1073/pnas.1213366110

Eiler, J.M., 2011. Paleoclimate reconstruction using carbonate clumped isotope thermometry. Quat. Sci. Rev. 30, 3575–3588. https://doi.org/10.1016/j.quascirev.2011.09.001

Eiler, J.M., 2007. “Clumped-isotope” geochemistry—The study of naturally-occurring, multiply-substituted isotopologues. Earth Planet. Sci. Lett. 262, 309–327. https://doi.org/10.1016/j.epsl.2007.08.020

Eiler, J.M., Bergquist, B., Bourg, I., Cartigny, P., Farquhar, J., Gagnon, A., Guo, W., Halevy, I., Hofmann, A., Larson, T.E., Levin, N., Schauble, E. a., Stolper, D., 2014. Frontiers of stable isotope geoscience. Chem. Geol. 372, 119–143. https://doi.org/10.1016/j.chemgeo.2014.02.006

Eiler, J.M., Schauble, E., 2004. $^{18}O^{13}C^{16}O$ in Earth’s atmosphere. Geochim. Cosmochim. Acta 68, 4767–4777. https://doi.org/10.1016/j.gca.2004.05.035

Ekart, D.D., Cerling, T.E., Montañez, I.P., Tabor, N.J., 1999. A 400 million year carbon isotope record of pedogenic carbonate: Implications for paleoatmosperhic carbon dioxide. Am. J. Sci. 299, 805–827.

Fairchild, I.J., Bradby, L., Spiro, B., Project, I.G.C., 1994. Reactive carbonate in glacial systems: a preliminary synthesis of creation, dissolution and reincarnation. Earth’s Glacial Rec. 260, 176–192.

Fairchild, I.J., Frisia, S., Borsato, A., Tooth, A.F., 2007. Speleothems, in: Nash, D.J., McLaren, S.J. (Eds.), Geochemical Sediments and Landscapes. Blackwell Publishing, Malden, MA.

Falcon-Lang, H.J., 2003. Growth interruptions in silicified conifer woods from the Upper Cretaceous Two Medicine Formation, Montana, USA: Implications for

palaeoclimate and dinosaur palaeoecology. Palaeogeogr. Palaeoclimatol. Palaeoecol. 199, 299–314. https://doi.org/10.1016/S0031-0182(03)00539-X

Farke, A.A., Henn, M.M., Woodward, S.J., Xu, H.A., 2014. Leidyosuchus (Crocodylia: Alligatoroidea) from the Upper Cretaceous Kaiparowits Formation (late Campanian) of Utah, USA. PaleoBios 30, 72–88.

Feakes, C.R., Retallack, G.J., 1988. Recognition and chemical characterization of fossil soils developed on alluvium; A Late Ordovician example 35–48. https://doi.org/10.1130/SPE216-p35

Fiebig-Wittmaack, M., Astudillo, O., Wheaton, E., Wittrock, V., Perez, C., Ibacache, A., 2012. Climatic trends and impact of climate change on agriculture in an arid Andean valley. Clim. Change 111, 819–833. https://doi.org/10.1007/s10584-011-0200-z

Flaig, P.P., McCarthy, P.J., Fiorillo, A.R., 2013. Anatomy, Evolution, and Paleoenvironmental Interpretation of an Ancient Arctic Coastal Plain: Integrated Paleopedology and Palynology from the Upper Cretaceous (Maastrichtian) Prince Creek Formation, North Slope, Alaska, USA, New Frontiers in Paleopedology and Terrestrial Paleoclimatology: Paleosols and Soil Surface Analog Systems. https://doi.org/10.2110/sepmsp.104.14

Foley, K.K., 2005. Pedogenic carbonate distribution within glacial till in Taylor Valley, Southern Victoria Land, Antarctica. The Ohio State University.

Foreman, B.Z., FRICKE, H.C., Lohmann, K.C., Rogers, R.R., 2011. Reconstructing Paleocatchments By Integrating Stable Isotope Records, Sedimentology, and

Taphonomy: a Late Cretaceous Case Study (Montana, United States). Palaios 26, 545–554. https://doi.org/10.2110/palo.2010.p10-133r

Foreman, B.Z., Rogers, R.R., Deino, A.L., Wirth, K.R., Thole, J.T., 2008. Geochemical characterization of bentonite beds in the Two Medicine Formation (Campanian, Montana), including a new $^{40}Ar/^{39}Ar$ age. Cretac. Res. 29, 373–385. https://doi.org/10.1016/j.cretres.2007.07.001

Foreman, B.Z., Roberts, E.M., Tapanila, L., Ratigan, D., Sullivan, P., 2015. Stable isotopic insights into paleoclimatic conditions and alluvial depositional processes in the Kaiparowits Formation (Campanian, south-central Utah, U.S.A.). Cretac. Res. 56, 180–192. https://doi.org/10.1016/j.cretres.2015.05.001

Forman, S.L., Miller, G.H., 1984. Time-Dependent Soil Morphologies and Pedogenic Processes on Raised Beaches, Bröggerhalvöya, Spitsbergen, Svalbard Archipelago. Arct. Alp. Res. 16, 381–394. https://doi.org/10.2307/1550900

Fox, D.L., Koch, P.L., 2004. Carbon and oxygen isotopic variability in Neogene paleosol carbonates: Constraints on the evolution of the C4-grasslands of the Great Plains, USA. Palaeogeogr. Palaeoclimatol. Palaeoecol. 207, 305–329. https://doi.org/10.1016/j.palaeo.2003.09.030

Fricke, H.C., Foreman, B.Z., Sewall, J.O., 2010. Integrated climate model-oxygen isotope evidence for a North American monsoon during the Late Cretaceous. Earth Planet. Sci. Lett. 289, 11–21. https://doi.org/10.1016/j.epsl.2009.10.018

Gabitov, R.I., Watson, E.B., Sadekov, A., 2012. Oxygen isotope fractionation between calcite and fluid as a function of growth rate and temperature: An in situ study. Chem. Geol. 306–307, 92–102. https://doi.org/10.1016/j.chemgeo.2012.02.021

Gallagher, T.M., Sheldon, N.D., 2013. A new paleothermometer for forest paleosols and its implications for Cenozoic climate. Geology 41, 647–650. https://doi.org/10.1130/G34074.1

Gallagher, T.M., Sheldon, N.D., 2016. Combining soil water balance and clumped isotopes to understand the nature and timing of pedogenic carbonate formation. Chem. Geol. 435, 79–91. https://doi.org/10.1016/j.chemgeo.2016.04.023

Garreaud, R.D., Vuille, M., Compagnucci, R., Marengo, J., 2009. Present-day South American climate. Palaeogeogr. Palaeoclimatol. Palaeoecol. 281, 180–195. https://doi.org/10.1016/j.palaeo.2007.10.032

Garzione, C.N., Auerbach, D.J., Jin-Sook Smith, J., Rosario, J.J., Passey, B.H., Jordan, T.E., Eiler, J.M., 2014. Clumped isotope evidence for diachronous surface cooling of the Altiplano and pulsed surface uplift of the Central Andes. Earth Planet. Sci. Lett. 393, 173–181. https://doi.org/10.1016/j.epsl.2014.02.029

Garzione, C.N., Hoke, G.D., Libarkin, J.C., Withers, S., MacFadden, B., Eiler, J., Ghosh, P., Mulch, A., 2008. Rise of the Andes. Science 320, 1304–1307. https://doi.org/10.1126/science.1148615

Garzione, C.N., Quade, J., DeCelles, P.G., English, N.B., 2000. Predicting paleoelevation of Tibet and the Himalaya from $\delta^{18}O$ versus altitude gradients in meteoric water across the Nepal Himalaya. Earth Planet. Sci. Lett. 183, 215–229. https://doi.org/10.1016/S0012-821X(00)00252-1

Gates, T. a., Sampson, S.D., Zanno, L.E., Roberts, E.M., Eaton, J.G., Nydam, R.L., Hutchison, J.H., Smith, J. a., Loewen, M. a., Getty, M. a., 2010. Biogeography of terrestrial and freshwater vertebrates from the late Cretaceous (Campanian)

Western Interior of North America. Palaeogeogr. Palaeoclimatol. Palaeoecol. 291, 371–387. https://doi.org/10.1016/j.palaeo.2010.03.008

Gay, A.L., Grandstaff, D.E., 1980. Chemistry and mineralogy of Precambrian paleosols at Elliot Lake, Ontario, Canada. Precambrian Res. 12, 349–373. https://doi.org/10.1016/0301-9268(80)90035-2

Getty, M.A., Loewen, M.A., Roberts, E.M., Titus, A.L., Sampson, S.D., 2010. Taphonomy of horned dinosaurs (Ornithischia: Ceratopsidae) from the late Campanian Kaiparowits Formation, Grand Staircase-Escalante National Monument, Utah, in: Ryan, M., Chinney-Algeier, B., Eberth, D. (Eds.), New Perspectives on Horned Dinosaurs: The Royall Tyrrell Museum Ceratopsian Symposium. Indiana University Press, Bloomington, Indiana.

Ghosh, P., Adkins, J., Affek, H., Balta, B., Guo, W., Schauble, E. a., Schrag, D., Eiler, J.M., 2006. $^{13}C–^{18}O$ bonds in carbonate minerals: A new kind of paleothermometer. Geochim. Cosmochim. Acta 70, 1439–1456. https://doi.org/10.1016/j.gca.2005.11.014

Ghosh, P., Garzione, Carmala, N., Eiler, J.M., 2006. Rapid uplift of the Altiplano revealed through $^{13}C-^{18}O$ bonds in paleosol carbonates. Science (80-.). 311, 511–515.

Ghosh, P., Vasiliev, M. V., Ghosh, P., Sarkar, S., Ghosh, S., Yamada, K., Ueno, Y., Yoshida, N., Poulsen, C.J., 2016. Tracking the migration of the Indian continent using the carbonate clumped isotope technique on Phanerozoic soil carbonates. Sci. Rep. 6, 1–7. https://doi.org/10.1038/srep22187

Gile, L., Peterson, F., Grossman, R., 1966. Morphological and genetic sequences of carbonate accumulation in desert soils. Soil Sci.

Golani, P.R., 1989. Sillimanite-corundum deposits of Sonapahar, Meghalaya, India: A metamorphosed Precambrian paleosol. Precambrian Res. 43, 175–189. https://doi.org/10.1016/0301-9268(89)90055-7

Grandstaff, D.E., Edelman, M.J., Foster, R.W., Zbinden, E., Kimberley, M.M., 1986. Chemistry and mineralogy of Precambrian paleosols at the base of the Dominion and Pongola Groups (Transvaal, South Africa). Precambrian Res. 32, 97–131. https://doi.org/10.1016/0301-9268(86)90003-3

Greenwood, D.R., Wing, S.L., 1995. Eocene continental climates and latitudinal temperature gradients. Geology 23, 1044–1048. https://doi.org/10.1130/0091-7613(1995)023<1044:ECCALT>2.3.CO;2

Gregory-Wodzicki, K.M., 2000. Relationships between leaf morphology and climate, Bolivia: implications for estimating paleoclimate from fossil floras. Paleobiology 26, 668–688. https://doi.org/10.1666/0094-8373(2000)026<0668:RBLMAC>2.0.CO;2

Grosjean, M., Geyh, M., Messerli, B., 1998. A late-Holocene (<2600 BP) glacial advance in the south-central Andes (29 S), northern Chile. … 4, 473–479.

Gunal, H., Ransom, M.D., 2006. Clay illuviation and calcium carbonate accumulation along a precipitation gradient in Kansas. Catena 68, 59–69. https://doi.org/10.1016/j.catena.2006.04.027

Guo, W., 2009. Carbonate clumped isotope thermometry: application to carbonaceous chondrites and effects of kinetic isotope fractionation. California Institute of Technology.

Hagedorn, B., Sletten, R.S., Hallet, B., 2007. Sublimation and ice condensation in hyperarid soils: Modeling results using field data from Victoria Valley, Antarctica. J. Geophys. Res. Earth Surf. 112. https://doi.org/10.1029/2006JF000580

Hagedorn, B., Sletten, R.S., Hallet, B., McTigue, D.F., Steig, E.J., 2010. Ground ice recharge via brine transport in frozen soils of Victoria Valley, Antarctica: Insights from modeling $\delta^{18}O$ and δD profiles. Geochim. Cosmochim. Acta 74, 435–448. https://doi.org/10.1016/j.gca.2009.10.021

Hallam, A., 1984. Continental humid and arid zones during the jurassic and cretaceous. Palaeogeogr. Palaeoclimatol. Palaeoecol. 47, 195–223. https://doi.org/10.1016/0031-0182(84)90094-4

Hallam, A., 1985. A review of Mesozoic climates. J. Geol. Soc. London. 142, 433–445. https://doi.org/10.1144/gsjgs.142.3.0433

Hallet, B., 1976. Deposits formbed by subglacial precipitation of $CaCO_3$. Geol. Soc. Am. Bull. 87, 1003–1015.

Hanshaw, B.B., Hallet, B., 1978. Oxygen Isotope Composition of Subglacially Precipitated Calcite: Possible Paleoclimatic Implications. Science. 200, 1267 LP-1270.

Hay, W.W., 2008. Evolving ideas about the Cretaceous climate and ocean circulation. Cretac. Res. 29, 725–753. https://doi.org/10.1016/j.cretres.2008.05.025

He, B., Olack, G.A., Colman, A.S., 2012. Pressure baseline correction and high-precision CO_2 clumped-isotope (δ_{47}) measurements in bellows and micro-volume modes. Rapid Commun. Mass Spectrom. 26, 2837–2853. https://doi.org/10.1002/rcm.6436

Henkes, G.A., Passey, B.H., Grossman, E.L., Shenton, B.J., Pérez-Huerta, A., Yancey, T.E., 2014. Temperature limits for preservation of primary calcite clumped isotope paleotemperatures. Geochim. Cosmochim. Acta 139, 362–382. https://doi.org/10.1016/j.gca.2014.04.040

Henkes, G.A., Passey, B.H., Wanamaker, A.D., Grossman, E.L., Ambrose, W.G., Carroll, M.L., 2013. Carbonate clumped isotope compositions of modern marine mollusk and brachiopod shells. Geochim. Cosmochim. Acta 106, 307–325. https://doi.org/10.1016/j.gca.2012.12.020

Hill, P.S., Tripati, A.K., Schauble, E.A., 2014. Theoretical constraints on the effects of pH, salinity, and temperature on clumped isotope signatures of dissolved inorganic carbon species and precipitating carbonate minerals. Geochim. Cosmochim. Acta 125, 610–652. https://doi.org/10.1016/j.gca.2013.06.018

Hinkle, M.E., 1994. Environmental conditions affecting concentrations of He, CO_2, O_2 and N_2 in soil gases. Appl. Geochemistry 9, 53–63. https://doi.org/10.1016/0883-2927(94)90052-3

Hitchon, B., Krouse, H., 1972. Hydrogeochemistry of the surface waters of the Mackenzie River drainage basin, Canada–III . Stable isotopes of oxygen, carbon and sulphur. Geochim. Cosmochim. Acta 36, 1337 to 1357.

Hoke, G.D., Garzione, C.N., Araneo, D.C., Latorre, C., Strecker, M.R., Williams, K.J., 2009. The stable isotope altimeter: Do Quaternary pedogenic carbonates predict modern elevations? Geology 37, 1015–1018. https://doi.org/10.1130/G30308A.1

Horner, J.R., Schmitt, J.G., Jackson, F., Hanna, R., 2001. Bones and rocks of Upper Cretaceous Two Medicine-Judith River clastic wedge complex, Montana, in: Hill, C. (Ed.), Guidebook for Field Trips: Mesozoic and Cenozoic Paleontology in the Western Plains and Rocky Mountains, Museum of the Rockies Occasional Paper 3. Society of Vertebrate Paleontology, Bozeman, pp. 3–13.

Hough, B.G., Fan, M., Passey, B.H., 2014. Calibration of the clumped isotope geothermometer in soil carbonate in Wyoming and Nebraska, USA: Implications for paleoelevation and paleoclimate reconstruction. Earth Planet. Sci. Lett. 391, 110–120. https://doi.org/10.1016/j.epsl.2014.01.008

Huber, M., 2008. A hotter greenhouse? Climate change. 321, 353–354.

Huber, M., Caballero, R., 2011. The early Eocene equable climate problem revisited. Clim. Past 7, 603–633. https://doi.org/10.5194/cp-7-603-2011

Hunter, S.J., Haywood, A.M., Valdes, P.J., Francis, J.E., Pound, M.J., 2013. Modelling equable climates of the Late Cretaceous: Can new boundary conditions resolve data-model discrepancies? Palaeogeogr. Palaeoclimatol. Palaeoecol. 392, 41–51. https://doi.org/10.1016/j.palaeo.2013.08.009

Huntington, K.W., Eiler, J.M., Affek, H.P., Guo, W., Bonifacie, M., Yeung, L.Y., Thiagarajan, N., Passey, B., Tripati, a., Daëron, M., Came, R., 2009. Methods and limitations of “clumped” CO_2 isotope (Δ_{47}) analysis by gas-source isotope

ratiomass spectrometry. J. Mass Spectrom. 44, 1318–1329. https://doi.org/10.1002/jms.1614

Hyland, E.G., Sheldon, N.D., Cotton, J.M., 2017. Constraining the early Eocene climatic optimum: A terrestrial interhemispheric comparison. Bull. Geol. Soc. Am. 129, 244–252. https://doi.org/10.1130/B31493.1

Hyland, E., Sheldon, N.D., Van der Voo, R., Badgley, C., Abrajevitch, A., 2015. Geology A new paleoprecipitation proxy based on soil magnetic properties : Implications for expanding paleoclimate reconstructions A new paleoprecipitation proxy based on soil magnetic properties : Implications for expanding paleoclimate reconstructions. Geol. Soc. Am. Bull. 1–7. https://doi.org/10.1130/B31207.1

Jordan, G.J., Wing, S.L., Greenwood, D., 1996. Geology Eocene continental climates and latitudinal temperature gradients : Comment and Reply. Geology 24, 1054. https://doi.org/10.1130/0091-7613(1996)024<1054

Jordan, G.J., 1997. Contrasts between the Climatic Ranges of Fossil and Extant Taxa: Causes and Consequences for Palaeoclimatic Estimates. Aust. J. Bot. 45, 465–474.

Jordan, G.J., 1997. Uncertainty in palaeoclimatic reconstructions based on leaf physiognomy. Aust. J. Bot. 45, 669–678.

Kabala, C., Zapart, J., 2012. Initial soil development and carbon accumulation on moraines of the rapidly retreating Werenskiold Glacier, SW Spitsbergen, Svalbard archipelago. Geoderma 175–176, 9–20. https://doi.org/10.1016/j.geoderma.2012.01.025

Kaiser, J., Schefus, E., Lamy, F., Mohtadi, M., Hebbeln, D., 2008. Glacial to Holocene changes in sea surface temperature and coastal vegetation in north central Chile: high versus low latitude forcing. Quat. Sci. Rev. 27, 2064–2075. https://doi.org/10.1016/j.quascirev.2008.08.025

Kalliokoski, J., 1975. Chemistry and mineralogy of Precambrian paleosols in northern Michigan. Bull. Geol. Soc. Am. 86, 371–376. https://doi.org/10.1130/0016-7606(1975)86<371:CAMOPP>2.0.CO;2

Kang, S., Kim, S., Oh, S., Lee, D., 2000. Predicting spatial and temporal patterns of soil temperature based on topography, surface cover and air temperature. For. Ecol. Manage. 136, 173–184. https://doi.org/10.1016/S0378-1127(99)00290-X

Kauffman, E.G., Caldwell, W.G.E., 1993. The Western Interior Basin in space and time. GAC Spec. Publ. 39, 1–30.

Kelley, J.J., Weaver, D.F., 1969. Physical processes at the surface of the arctic tundra. Arctic 22, 425–437. https://doi.org/10.2307/40507880

Kelson, J.R., Huntington, K.W., Schauer, A.J., Saenger, C., Lechler, A.R., 2017. Toward a universal carbonate clumped isotope calibration: Diverse synthesis and preparatory methods suggest a single temperature relationship. Geochim. Cosmochim. Acta 197, 104–131. https://doi.org/10.1016/j.gca.2016.10.010

Kim, S.T., O'Neil, J.R., Hillaire-Marcel, C., Mucci, A., 2007. Oxygen isotope fractionation between synthetic aragonite and water: Influence of temperature and Mg^{2+} concentration. Geochim. Cosmochim. Acta 71, 4704–4715. https://doi.org/10.1016/j.gca.2007.04.019

Kim, S.-T., O'Neil, J.R., 1997. Equilibrium and nonequilibrium oxygen isotope effects in synthetic carbonates. Geochim. Cosmochim. Acta 61, 3461–3475. https://doi.org/10.1016/S0016-7037(97)00169-5

Kluge, T., Affek, H.P., 2012. Quantifying kinetic fractionation in Bunker Cave speleothems using Δ_{47}. Quat. Sci. Rev. 49, 82–94. https://doi.org/10.1016/j.quascirev.2012.06.013

Kluge, T., Affek, H.P., Zhang, Y.G., Dublyansky, Y., Spötl, C., Immenhauser, A., Richter, D.K., 2014. Clumped isotope thermometry of cryogenic cave carbonates. Geochim. Cosmochim. Acta 126, 541–554. https://doi.org/10.1016/j.gca.2013.11.011

Kluge, T., John, C.M., Jourdan, A.-L., Davis, S., Crawshaw, J., 2015. Laboratory calibration of the calcium carbonate clumped isotope thermometer in the 25–250 °C temperature range. Geochim. Cosmochim. Acta 157, 213–227. https://doi.org/10.1016/j.gca.2015.02.028

Koch, P.L., Zachos, J.C., Dettman, D.L., 1995. Stable isotope stratigraphy and paleoclimatology of the Paleogene Bighorn Basin (Wyoming, USA). Palaeogeogr. Palaeoclimatol. Palaeoecol. 115, 61–89. https://doi.org/10.1016/0031-0182(94)00107-J

Kohn, M.J., 2010. Carbon isotope compositions of terrestrial C3 plants as indicators of (paleo)ecology and (paleo)climate. Proc. Natl. Acad. Sci. U. S. A. 107, 19691–5. https://doi.org/10.1073/pnas.1004933107

Kowalski, E. a, Dilcher, D.L., 2003. Warmer paleotemperatures for terrestrial ecosystems. Proc. Natl. Acad. Sci. U. S. A. 100, 167–170. https://doi.org/10.1073/pnas.232693599

Kull, C., Grosjean, M., Veit, H., 2002. Modeling modern and late pleistocene glacio-climatological conditions in the north chilean andes (29–30 °S). Clim. Change 52, 359–381.

Kump, L.R., Slingerland, R.L., 1999. Circulation and stratification of the early Turonian Western Interior Seaway: Sensitivity to a variety of forcings, in: Special Paper 332: Evolution of the Cretaceous Ocean-Climate System. pp. 181–190. https://doi.org/10.1130/0-8137-2332-9.181

Lacelle, D., 2007. Environmental setting, (micro)morphologies and stable C–O isotope composition of cold climate carbonate precipitates—a review and evaluation of their potential as paleoclimatic proxies. Quat. Sci. Rev. 26, 1670–1689. https://doi.org/10.1016/j.quascirev.2007.03.011

Lachniet, M.S., 2009. Climatic and environmental controls on speleothem oxygen-isotope values. Quat. Sci. Rev. 28, 412–432. https://doi.org/10.1016/j.quascirev.2008.10.021

Lambert, M.G., Roberts, E., 1976. Aspect differences in an unimproved hill country pasture, 1. climatic differences. New Zeal. J. Agric. Res. 19, 459–467. https://doi.org/10.1080/00288233.1978.10427407

Lamy, F., Hebbeln, D., Wefer, G., 1999. High-resolution marine record of climatic change in mid-latitude Chile during the last 28,000 years based on terrigenous

sediment parameters. Quat. Res. 51, 83–93. https://doi.org/10.1006/qres.1998.2010

Landi, A., Mermut, A.., Anderson, D.., 2003. Origin and rate of pedogenic carbonate accumulation in Saskatchewan soils, Canada. Geoderma 117, 143–156. https://doi.org/10.1016/S0016-7061(03)00161-7

Latorre, C., Quade, J., McIntosh, W.C., 1997. The structure and rate of late Miocene expansion of C4plants: Evidence from lateral variation in stable isotopes in paleosols of the Siwalik Group, northern Pakistan. Earth Planet. Sci. Lett. 146, 83–96. https://doi.org/10.1130/B26064.1

Lechler, A.R., Niemi, N.A., 2012. The influence of snow sublimation on the isotopic composition of spring and surface waters in the southwestern United States: Implications for stable isotope-based paleoaltimetry and hydrologic studies. Bull. Geol. Soc. Am. 124, 318–334. https://doi.org/10.1130/B30467.1

Lee, Y. Il, 1999. Stable isotopic composition of calcic paleosols of the Early Cretaceous Hasandong Formation, Southeastern Korea. Palaeogeogr. Palaeoclimatol. Palaeoecol. 150, 123–133. https://doi.org/10.1016/S0031-0182(99)00010-3

Lehman, T.M., 2001. Late Cretaceous Dinosaur Provinciality, in: Tanke, D., Carpenter, K. (Eds.), Mesozoic Vertebrate Life. Indiana University Press, Bloomington, pp. 310–328.

Lehman, T.M., Mcdowell, F.W., Connelly, J.N., 2006. First isotopic (U-Pb) age for the Late Cretaceous Alamosaurus vertebrate fauna of west Texas, and its significance as a link between two faunal provinces. J. Vertebr. Paleontol. 26, 922–928. https://doi.org/10.1671/0272-4634(2006)26

Leier, A., McQuarrie, N., Garzione, C., Eiler, J., 2013. Stable isotope evidence for multiple pulses of rapid surface uplift in the central andes, bolivia. Earth Planet. Sci. Lett. 371–372, 49–58. https://doi.org/10.1016/j.epsl.2013.04.025

Leonards, G., 1962. Foundation Engineering. McGraw-Hill, New York.

Leslie, C.E., Peppe, D.J., Williamson, T.E., Heizler, M., Jackson, M., Atchley, S.C., Nordt, L., Standhardt, B., 2018. Revised age constraints for Late Cretaceous to early Paleocene terrestrial strata from the Dawson Creek section , Big Bend National Park , west Texas 1–21.

Li, Y., Song, Y., Zeng, M., Lin, W., Orozbaev, R., Cheng, L., Chen, X., Halmurat, T., 2018. Evaluating the paleoclimatic significance of clay mineral records from a late Pleistocene loess-paleosol section of the Ili Basin, Central Asia. Quat. Res. (United States) 89, 660–673. https://doi.org/10.1017/qua.2017.58

Licht, A., Quade, J., Kowler, A., De Los Santos, M., Hudson, A., Schauer, A., Huntington, K., Copeland, P., Lawton, T., 2017. Impact of the North American monsoon on isotope paleoaltimeters: Implications for the paleoaltimetry of the American southwest. Am. J. Sci. 317, 1–33. https://doi.org/10.2475/01.2017.01

Little, S. a., Kembel, S.W., Wilf, P., 2010. Paleotemperature proxies from leaf fossils reinterpreted in light of evolutionary history. PLoS One 5, 1–8. https://doi.org/10.1371/journal.pone.0015161

Liu, W., Ning, Y., An, Z., Wu, Z., Lu, H., Cao, Y., 2005. Carbon isotopic composition of modern soil and paleosol as a response to vegetation change on the Chinese Loess Plateau. Sci. China Ser. D – Earth Sci. 48, 93. https://doi.org/10.1360/02yd0148

Liu, B., Phillips, F., Campbell, A., 1996. Stable carbon and oxygen isotopes of pedogenic carbonates, Ajo Mountains, southern Arizona: implications for paleoenvironmental change. Palaeogeogr. Palaeoclimatol. … 124, 233–246.

Lucas, S.G., Sullivan, R.M., Lichtig, A.J., Dalman, S.G., Jasinski, S.E., 2016. Late Cretaceous dinosaur biogeography and endemism in the Western Interior basin, North America: A critical re-evaluation. New Mex. Museum Nat. Hist. Sci. Bull. 71, 195–213.

Machette, M.N., 1985. Calcic soils of the southwestern United States. Geol. Soc. Am. Spec. Pap. 203, 1–22.

Mack, G.H., James, W.C., Monger, H.C., 1993. Classification of paleosols. Geol. Soc. Am. Bull. 105, 129–136. https://doi.org/10.1130/0016-7606(1993)105<0129

Magaritz, M., Kaufman, A., Yaalon, D.H., 1981. Calcium carbonate nodules in soils: $^{18}O/^{16}O$ and $^{13}C/^{12}C$ ratios and ^{14}C contents. Geoderma 25, 157–172. https://doi.org/10.1016/0016-7061(81)90033-1

Mann, D.H., Sletten, R.S., Ugolini, F.C., 1986. Soil development at Kongsfjorden, Spitsbergen. Polar Res. 4, 1–16. https://doi.org/10.1111/j.1751-8369.1986.tb00513.x

Markwick, P.J., 1998. Fossil crocodilians as indicators of Late Cretaceous and Cenozoic climates: Implications for using palaeontological data in reconstructing palaeoclimate. Palaeogeogr. Palaeoclimatol. Palaeoecol. 137, 205–271. https://doi.org/10.1016/S0031-0182(97)00108-9

Marlier, J.F., O'Leary, M.H., 1984. Carbon Kinetic Isotope Effects on the Hydration of Carbon Dioxide and the Dehydration of Bicarbonate Ion. J. Am. Chem. Soc. 106, 5054–5057. https://doi.org/10.1021/ja00330a003

Marlin, C., Dever, L., Vachier, P., Courty, M.-A., 1993. Variations chimiques et isotopique de l'eau du sol lors de la reprise en gel d'une couche active sur perigélisol continu (Presqu'île de Brogger, Svalbard). Can. J. Earth Sci. 30, 806–813. https://doi.org/10.1139/e93-066

Marticorena, C., Marticorena, C., Squeo, F. a, Squeo, F. a, Arancio, G., Arancio, G., 2001. Catálogo de la Flora Vascular de la IV Región de Coquimbo, in: Squeo, F.A., Arancio, G., Gutiérrez, J.R. (Eds.), Libro Rojo de La Flora Nativa y de Los Sitios Prioritarios Para Su Conservación: Región de Coquimbo. Ediciones Universidad de La Serena, La Serena, pp. 105–142.

Matthews, H.D., Eby, M., Ewen, T., Friedlingstein, P., Hawkins, B.J., 2007. What determines the magnitude of carbon cycle-climate feedbacks? Global Biogeochem. Cycles 21, 1–12. https://doi.org/10.1029/2006GB002733

Maynard, J.B., 1992. Chemistry of Modern Soils as a Guide to Interpreting Precambrian Paleosols. J. Geol. 100, 279–289. https://doi.org/10.1086/629632

McCarthy, P.J., Plint, A.G., 2013. A pedostratigraphic approach to nonmarine sequence stratigraphy: a three-dimensional paleosol-landscape model from the Cretaceous (Cenomanian) Dunvegan Formation, Alberta and British Columbia, Canada, in: Driese, S.G., Nordt, L.C. (Eds.), New Frontiers in Paleopedology and Terrestrial Paleoclimatology; SEPM Special Publications No. 104. Society for Sedimentary Geology, pp. 159–177.

McCraw, J.D., 1967. Soils of Taylor Dry Valley, Victoria Land, Antarctica, with notes on soils from other localities in Victoria Land. New Zeal. J. Geol. Geophys. 10, 498–539. https://doi.org/10.1080/00288306.1967.10426754

McFadden, L.D., McDonald, E. V., Wells, S.G., Anderson, K., Quade, J., Forman, S.L., 1998. The vesicular layer and carbonate collars of desert soils and pavements: formation, age and relation to climate change. Geomorphology 24, 101–145. https://doi.org/10.1016/S0169-555X(97)00095-0

McInerney, F.A., Wing, S.L., 2011. The Paleocene-Eocene Thermal Maximum: A Perturbation of Carbon Cycle, Climate, and Biosphere with Implications for the Future. Annu. Rev. Earth Planet. Sci. 39, 489–516. https://doi.org/10.1146/annurev-earth-040610-133431

Meyer, N. a, Breecker, D.O., Young, M.H., Litvak, M.E., 2014. Simulating the Effect of Vegetation in Formation of Pedogenic Carbonate. Soil Sci. Soc. Am. 78, 914–924. https://doi.org/10.2136/sssaj2013.08.0326

Michel, L.A., Tabor, N.J., Montañez, I.P., 2016. Paleosol Diagenesis and Its Deep-Time Paleoenvironmental Implications, Pennsylvanian–Permian Lodève Basin, France. J. Sediment. Res. 86, 813–829. https://doi.org/10.2110/jsr.2016.41

Miller, I.M., Johnson, K.R., Kline, D.E., Nichols, D.J., Barclay, R.S., 2013. A Late Campanian flora from the Kaiparowits Formation, Southern Utah, and a brief overview of the widely sampled but little-known Campanian vegetation of the Western Interior of North America, in: Titus, A.L., Loewen, M.A. (Eds.), At the Top of the Grand Staircase. Indiana University Press, Bloomington, Indiana, pp. 107–131.

Mintz, J.S., Driese, S.G., Breecker, D.O., Ludvigson, G.A., 2011. Influence of Changing Hydrology on Pedogenic Calcite Precipitation in Vertisols, Dance Bayou, Brazoria County, Texas, U.S.A.: Implications for Estimating Paleoatmospheric pCO_2. J. Sediment. Res. 81, 394–400. https://doi.org/10.2110/jsr.2011.36

Monger, H.C., Cole, D.R., Gish, J.W., Giordano, T.H., 1998. Stable carbon and oxygen isotopes in Quaternary soil carbonates as indicators of ecogeomorphic changes in the northern Chihuahuan Desert, USA. Geoderma 82, 137–172. https://doi.org/10.1016/S0016-7061(97)00100-6

Monger, H.C., Wilding, L.P., 2006. Inorganic Carbon: Composition and formation, in: Lal, R. (Ed.), Encyclopedia of Soil Science. Taylor & Francis, New York, pp. 886–889.

Monteith, J.L., Unsworth, M.H., 2013. Principles of environmental physics. Plants, Animals and the atmosphere, Monteith, J. L. And M. H. Unsworth. Principles of Environmental Physics, Second Edition. Xii+291p. Routledge, Chapman and Hall: New York, New York, USA. Illus. Paper.

Mook, W.G., Bommerson, J.C., Staverman, W.H., 1974. Carbon isotope fractionation between dissolved bicarbonate and gaseous carbon dioxide. Earth Planet. Sci. Lett. 22, 169–176. https://doi.org/10.1016/0012-821X(74)90078-8

Mora, C.I., Driese, S.G., Colarusso, L.A., 1996. Middle to late Paleozoic atmospheric CO_2 levels from soil carbonate and organic matter. Science (80-.). 271, 1105–1107. https://doi.org/10.1126/science.271.5252.1105

Mora, C.I., Driese, S.G., 1993. A steep, mid- to late Paleozoic decline in atmospheric CO_2: evidence from the soil carbonate CO_2 paleobarometer. Chem. Geol. 107, 217–219. https://doi.org/10.1016/0009-2541(93)90177-K

Morrone, J.J., 2014. Parsimony analysis of endemicity (PAE) revisited. J. Biogeogr. 41, 842–854. https://doi.org/10.1111/jbi.12251

Myers, T.S., Tabor, N.J., Jacobs, L.L., Bussert, R., 2016. Effects of different organic-matter sources on estimates of atmosphric and soil pCO2 using peodgenic carbonate. J. Sediment. Res. 86, 800–812. https://doi.org/10.2110/jsr.2016.52

Nakai, N., Wada, H., Kiyosu, Y.A., 1975. Stable isotope studies on the origin and geological history of water and salts in the Lake Yanda area , Antarctica 9.

Niezgodzki, I., Knorr, G., Lohmann, G., Tyszka, J., Markwick, P.J., 2017. Late Cretaceous climate simulations with different CO_2 levels and subarctic gateway configurations: A model-data comparison. Paleoceanography 32, 980–998. https://doi.org/10.1002/2016PA003055

Nordt, L.C., Driese, S.D., 2010. New weathering index improves paleorainfall estimates from Vertisols. Geology 38, 407–410. https://doi.org/10.1130/G30689.1

Nordt, L.C., Dworkin, S.I., Atchley, S.C., 2011. Ecosystem response to soil biogeochemical behavior during the Late Cretaceous and early Paleocene within the western interior of North America. Geol. Soc. Am. Bull. 123, 1745–1762. https://doi.org/10.1130/B30365.1

Nordt, L., Atchley, S., Dworkin, S., 2003. Terrestrial evidence for two greenhouse events in the latest Cretaceous. GSA Today 13, 4–9. https://doi.org/10.1130/1052-5173(2003)013<4:TEFTGE>2.0.CO;2

Nordt, L., Orosz, M., Driese, S., Tubbs, J., 2006. Vertisol Carbonate Properties in Relation to Mean Annual Precipitation: Implications for Paleoprecipitation Estimates. J. Geol. 114, 501–510. https://doi.org/10.1086/504182

Nydam, R.L., Rowe, T.B., Cifelli, R.L., 2013. Lizards and snakes of the Terlingua Local Fauna (late Campanian), Aguja Formation, Texas, with comments on the distribution of paracontemporaneous squamates throughout the Western Interior of North America. J. Vertebr. Paleontol. 33, 1081–1099. https://doi.org/10.1080/02724634.2013.760467

Outcalt, S.I., Nelson, F.E., Hinkel, K.M., 1990. The zero‐curtain effect: Heat and mass transfer across an isothermal region in freezing soil. Water Resour. Res. 26, 1509–1516. https://doi.org/10.1029/WR026i007p01509

Ohmoto, H., 1997. Evidence in pre-2.2 Ga paleosols for the early evolution of atmospheric oxygen and terrestrial biota: comment and reply. Geology 25, 858–859. https://doi.org/10.1130/0091-7613(1996)

Paneth, P., O'Leary, M.H., 1985. Mechanism of the Spontaneous Dehydration of Bicarbonate Ion. J. Am. Chem. Soc. 107, 7381–7384. https://doi.org/10.1021/ja00311a027

Panin, P.G., Timireva, S.N., Morozova, T.D., Kononov, Y.M., Velichko, A.A., 2018. Morphology and micromorphology of the loess-paleosol sequences in the south of the East European plain (MIS 1–MIS 17). Catena 168, 79–101. https://doi.org/10.1016/j.catena.2018.01.032

Parker, A., 1970. Index of weathering for silicate rocks. Geol. Mag. 107, 501–504.

Parrish, J.T., Ziegler, A.M., Scotese, C.R., 1982. Rainfall patterns and the distribution of coals and evaporites in the Mesozoic and Cenozoic. Palaeogeogr. Palaeoclimatol. Palaeoecol. 40, 67–101. https://doi.org/http://dx.doi.org/10.1016/0031-0182(82)90085-2

Passey, B.H., Levin, N.E., Cerling, T.E., Brown, F.H., Eiler, J.M., 2010. High-temperature environments of human evolution in East Africa based on bond ordering in paleosol carbonates. Proc. Natl. Acad. Sci. 107, 11245–11249. https://doi.org/10.1073/pnas.1001824107

Passey, B.H., Henkes, G.A., 2012. Carbonate clumped isotope bond reordering and geospeedometry. Earth Planet. Sci. Lett. 351–352, 223–236. https://doi.org/10.1016/j.epsl.2012.07.021

Paulik, C., Melzer, T., Hahn, S., Bartsch, A., Heim, B., Elger, K., Wagner, W., 2014. Circumpolar surface soil moisture and freeze/thaw surface status remote sensing products (version 4) with links to geotiff images and netCDF files (2007-01 to 2013-12). https://doi.org/10.1594/PANGAEA.832153

Peppe, D.J., Baumgartner, A., Flynn, A., Blonder, B., 2017. Reconstructing paleoclimate and paleoecology using fossil leaves. PaleorXiv Pap. 1–78. https://doi.org/10.31233/osf.io/stzuc

Peppe, D.J., Royer, D.L., Cariglino, B., Oliver, S.Y., Newman, S., Leight, E., Enikolopov, G., Fernandez-Burgos, M., Herrera, F., Adams, J.M., Correa, E., Currano, E.D., Erickson, J.M., Hinojosa, L.F., Hoganson, J.W., Iglesias, A., Jaramillo, C. a., Johnson, K.R., Jordan, G.J., Kraft, N.J.B., Lovelock, E.C., Lusk, C.H., Niinemets, Ü., Peñuelas, J., Rapson, G., Wing, S.L., Wright, I.J., 2011.

Sensitivity of leaf size and shape to climate: Global patterns and paleoclimatic applications. New Phytol. 190, 724–739. https://doi.org/10.1111/j.1469-8137.2010.03615.x

Peppe, D.J., Royer, D.L., Wilf, P., Kowalski, E.A., 2010. Quantification of large uncertainties in fossil leaf paleoaltimetry. Tectonics 29. https://doi.org/doi.org/10.1029/2009TC002549

Peters, N. a., Huntington, K.W., Hoke, G.D., 2013. Hot or not? Impact of seasonally variable soil carbonate formation on paleotemperature and O-isotope records from clumped isotope thermometry. Earth Planet. Sci. Lett. 361, 208–218. https://doi.org/10.1016/j.epsl.2012.10.024

Poulsen, C.J., Barron, E.J., Johnson, C.C., Fawcett, P., 1999. Links between major climatic factors and regional oceanic circulation in the mid-Cretaceous, in: Evolution of the Cretaceous Ocean–Climate System, Special Paper Geological Society of America. pp. 73–90. https://doi.org/10.1130/0-8137-2332-9.73

Poulsen, C.J., Pollard, D., White, T.S., 2007. General circulation model simulation of the $\delta^{18}O$ content of continental precipitation in the middle Cretaceous: A model-proxy comparison. Geology 35, 199–202. https://doi.org/10.1130/G23343A.1

Quade, J., Breecker, D.O., Daeron, M., Eiler, J., 2011. The paleoaltimetry of Tibet: An isotopic perspective. Am. J. Sci. 311, 77–115. https://doi.org/10.2475/02.2011.01

Quade, J., Eiler, J., Daëron, M., Achyuthan, H., 2013. The clumped isotope geothermometer in soil and paleosol carbonate. Geochim. Cosmochim. Acta 105, 92–107. https://doi.org/10.1016/j.gca.2012.11.031

Quade, J., Garzione, C., Eiler, J., 2007. Paleoelevation Reconstruction using Pedogenic Carbonates. Rev. Mineral. Geochemistry 66, 53–87. https://doi.org/10.2138/rmg.2007.66.3

Quade, J., Breecker, D.O., Daëron, M., Eiler, J., 2011. The paleoaltimetry of Tibet: An isotopic perspective. Am. J. Sci. 311, 77–115. https://doi.org/10.2475/02.2011.01

Quade, J., Rech, J. a., Latorre, C., Betancourt, J.L., Gleeson, E., Kalin, M.T.K., 2007. Soils at the hyperarid margin: The isotopic composition of soil carbonate from the Atacama Desert, Northern Chile. Geochim. Cosmochim. Acta 71, 3772–3795. https://doi.org/10.1016/j.gca.2007.02.016

Quade, J., Cater, J.M.L., Ohja, T.P., Adam, J., Harrison, T.M., 1995. Late Miocene environmental change in Nepal and the northern Indian subcontinent: Stable isotopic evidence from paleosols. Bull. Geol. Soc. Am. 107, 1381–1397. https://doi.org/10.1130/0016-7606(1995)107<1381:LMECIN>2.3.CO;2

Raigemborn, M.S., Krapovickas, V., Beilinson, E., Gómez Peral, L.E., Zucol, A.F., Zapata, L., Kay, M.R.F., Bargo, M.S., Vizcaíno, S.F., Sial, A.N., 2018. Multiproxy studies of Early Miocene pedogenic calcretes in the Santa Cruz Formation of southern Patagonia, Argentina indicate the existence of a temperate warm vegetation adapted to a fluctuating water table. Palaeogeogr. Palaeoclimatol. Palaeoecol. 500, 1–23. https://doi.org/10.1016/j.palaeo.2018.03.037

Retallack, G.J., Krinsley, D.H., Fischer, R., Razink, J.J., Langworthy, K.A., 2016. Archean coastal-plain paleosols and life on land. Gondwana Res. 40, 1–20. https://doi.org/10.1016/j.gr.2016.08.003

Retallack, G.J., Sheldon, N.D., Carr, P.F., Fanning, M., Thompson, C. a., Williams, M.L., Jones, B.G., Hutton, A., 2011. Multiple Early Triassic greenhouse crises impeded recovery from Late Permian mass extinction. Palaeogeogr. Palaeoclimatol. Palaeoecol. 308, 233–251. https://doi.org/10.1016/j.palaeo.2010.09.022

Retallack, G.J., Wynn, J.G., Fremd, T.J., 2004. Glacial-interglacial-scale paleoclimatic change without large ice sheets in the Oligocene of central Oregon. Geology 32, 297–300. https://doi.org/10.1130/G20247.1

Retallack, G.J., Robinson, S.E., Krull, E.S., 1995. Middle Devonian paleosols and vegetation of the Lashly Mountains, Antarctica. Antarct. J. United States 63, 62–65.

Retallack, G.J., James, W.C., Mack, G.H., Monger, H.C., 1993. Geological Society of America Bulletin Classification of paleosols : Discussion and reply. Geol. Soc. Am. Bull. https://doi.org/10.1130/0016-7606(1993)105<1635

Retallack, G.J., James, W.C., Mack, G.H., Monger, H.C., 1993. Geological Society of America Bulletin Classification of paleosols : Discussion and reply. Geol. Soc. Am. Bull. https://doi.org/10.1130/0016-7606(1993)105<1635

Retallack, G.J., 2018. The oldest known paleosol profiles on Earth: 3.46 Ga Panorama Formation, Western Australia. Palaeogeogr. Palaeoclimatol. Palaeoecol. 489, 230–248. https://doi.org/10.1016/j.palaeo.2017.10.013

Retallack, G.J., 2013a. Early Cambrian Humid, Tropical, Coastal Paleosols from Montana, USA, in: New Frontiers in Paleopedology and Terrestrial Paleoclimatology: Paleosols and Soil Surface Analog Systems. pp. 257–272. https://doi.org/10.2110/sepmsp.104.09

Retallack, G.J., 2013b. Permian and Triassic greenhouse crises. Gondwana Res. 24, 90–103. https://doi.org/10.1016/j.gr.2012.03.003

Retallack, G.J., 2009. Refining a pedogenic-carbonate CO2 paleobarometer to quantify a middle Miocene greenhouse spike. Palaeogeogr. Palaeoclimatol. Palaeoecol. 281, 57–65. https://doi.org/10.1016/j.palaeo.2009.07.011

Retallack, G.J., 2007. Cenozoic Paleoclimate on Land in North America. J. Geol. 115, 271–294. https://doi.org/10.1086/512753

Retallack, G.J., 2005. Pedogenic carbonate proxies for amount and seasonality of precipitation in paleosols. Geology 33, 333. https://doi.org/10.1130/G21263.1

Retallack, G., 1999. Carboniferous fossil plants and soils of an early tundra ecosystem. Palaios 14, 324–336.

Retallack, G.J., 1995. Palaeosols of the Siwalik Group as a 15 Myr record of South Asian palaeoclimate. Mem. - Geol. Soc. India 32, 36–51.

Retallack, G.J., 1994. A pedotype approach to latest Cretaceous and earliest Tertiary paleosols in eastern Montana. Geol. Soc. Am. Bull. 106, 1377–1397. https://doi.org/10.1130/0016-7606(1994)106<1377:APATLC>2.3.CO;2

Retallack, G.J., Mindszenty, A., 1994. Well Preserved Late Precambrian Paleosols from Northwest Scotland. J. Sediment. Res. Sect. a-Sedimentary Petrol. Process. 64, 264–281. https://doi.org/10.1306/D4267D7A-2B26-11D7-8648000102C1865D

Ringham, M.C., Hoke, G.D., Huntington, K.W., Aranibar, J.N., 2016. Influence of vegetation type and site-to-site variability on soil carbonate clumped isotope records, Andean piedmont of Central Argentina (32-34 °S). Earth Planet. Sci. Lett. 440, 1–11. https://doi.org/10.1016/j.epsl.2016.02.003

Riquelme, R., Rojas, C., Aguilar, G., Flores, P., 2011. Late Pleistocene–early Holocene paraglacial and fluvial sediment history in the Turbio valley, semiarid Chilean Andes. Quat. Res. 75, 166–175. https://doi.org/10.1016/j.yqres.2010.10.001

Roberts, E.M., 2005. Stratigraphic, taphonomic, and paleoenvironmental analysis of the Upper Cretaceous Kaiparowits Formation, Grand Staircase-Escalante National Monument, Souther Utah. University of Utah. https://doi.org/10.1177/001088048102200214

Roberts, E.M., 2007. Facies architecture and depositional environments of the Upper Cretaceous Kaiparowits Formation, southern Utah. Sediment. Geol. 197, 207–233. https://doi.org/10.1016/j.sedgeo.2006.10.001

Roberts, E.M., Deino, A.L., Chan, M. a., 2005. $^{40}Ar/^{39}Ar$ age of the Kaiparowits Formation, southern Utah, and correlation of contemporaneous Campanian strata and vertebrate faunas along the margin of the Western Interior Basin. Cretac. Res. 26, 307–318. https://doi.org/10.1016/j.cretres.2005.01.002

Rodhe, A., 1998. Snowmelt-Dominated Systems, in: Kendall, C., McDonnell, J.J. (Eds.), Isotope Tracers in Catchment Hydrology. Elsevier, Amsterdam, p. 839.

Rogers, R.R., 1998. Sequence analysis of the Upper Cretaceous Two Medicine and Judith River formations, Montana; nonmarine response to the Claggett and Bearpaw marine cycles. J. Sediment. Res. 68, 615–631. https://doi.org/10.2110/jsr.68.604

Rogers, R.R., 1995. Sequence stratigraphy and vertebrate taphonomy of the Upper Cretaceous Two Medicine and Judith River Formations, Montana. https://doi.org/10.16953/deusbed.74839

Rogers, R.R., Swisher III, C.C., Horner, J.R., 1993. $^{40}Ar/^{39}Ar$ age and correlation of the nonmarine Two Medicine Formation (Upper Cretaceous), northwestern Montana, U.S.A. Can. J. Earth Sci. 30, 1066–1075. https://doi.org/10.1139/e93-090

Romanek, C.S., Grossman, E.L., Morse, J.W., 1992. Carbon isotopic fractionation in synthetic aragonite and calcite: Effects of temperature and precipitation rate. Geochim. Cosmochim. Acta 56, 419–430. https://doi.org/10.1016/0016-7037(92)90142-6

Romanovsky, V.E., Osterkamp, T.E., 2000. Effects of unfrozen water on heat and mass transport processes in the active layer and permafrost. Permafr. Periglac. Process. 11, 219–239. https://doi.org/10.1002/1099-1530(200007/09)11:3<219::AID-PPP352>3.0.CO;2-7

Ross, S.M., 2003. Peirce's criterion for the elimination of suspect experimental data. J. Eng. Technol. 20, 1–12.

Rowley, D.B., Pierrehumbert, R.T., Currie, B.S., 2001. A new approach to stable isotope-based paleoaltimetry: implications for paleoaltimetry and paleohypsometry of the High Himalaya since the Late Miocene. Earth Planet. Sci. Lett. 188, 253–268. https://doi.org/10.1016/S0012-821X(01)00324-7

Royer, D.L., 2012. Climate reconstruction from leaf size and shape: New developments and challenges. Paleontol. Soc. Pap. 18, 195–212.

Saenger, C., Affek, H.P., Felis, T., Thiagarajan, N., Lough, J.M., Holcomb, M., 2012. Carbonate clumped isotope variability in shallow water corals: Temperature dependence and growth-related vital effects. Geochim. Cosmochim. Acta 99, 224–242. https://doi.org/10.1016/j.gca.2012.09.035

Salomons, W., Mook, W.G., 1986. Isotope Geochemistry of Carbonates in the Weathering Zone, The Terrestrial Environment, B. https://doi.org/10.1016/B978-0-444-42225-5.50011-5

Sampson, S.D., Loewen, M.A., Farke, A.A., Roberts, E.M., Forster, C.A., Smith, J.A., Titus, A.L., 2010. New horned dinosaurs from Utah provide evidence for intracontinental dinosaur endemism. PLoS One 5, 1–12. https://doi.org/10.1371/journal.pone.0012292

Schauble, E. A., Ghosh, P., Eiler, J.M., 2006. Preferential formation of $^{13}C–^{18}O$ bonds in carbonate minerals, estimated using first-principles lattice dynamics. Geochim. Cosmochim. Acta 70, 2510–2529. https://doi.org/10.1016/j.gca.2006.02.011

Schauer, A.J., Kelson, J., Saenger, C., Huntington, K.W., 2016. Choice of ^{17}O correction affects clumped isotope (Δ_{47}) values of CO_2 measured with mass spectrometry. Rapid Commun. Mass Spectrom. 30, 2607–2616. https://doi.org/10.1002/rcm.7743

Schuurmans, E.D., Dale, J., Hersi, O.S., 2015. Preliminary Study of Paleosols in the Lower Cretaceous McLaren and Waseca Members of the Mannville Group in Saskatchewan. Summ. Investig. 2015, Saskatchewan Geol. Surv. 1, 1–12.

Schwertfeger, W., 1984. Weather and climate of Antarctica. New York.

Sewall, J.O., Fricke, H.C., 2013. Andean-scale highlands in the Late Cretaceous Cordillera of the North American western margin. Earth Planet. Sci. Lett. 362, 88–98. https://doi.org/10.1016/j.epsl.2012.12.002

Sewall, J.O., Sloan, L.C., 2006. Come a little bit closer: A high-resolution climate study of the early Paleogene Laramide foreland. Geology 34, 81–84. https://doi.org/10.1130/G22177.1

Sharkey, T.D., 2000. Some like it hot. Science (80-.). 287, 435.

Sheldon, N.D., Retallack, G.J., Tanaka, S., 2002. Geochemical Climofunctions from North American Soils and Application to Paleosols across the Eocene-Oligocene Boundary in Oregon. J. Geol. 110, 687–696. https://doi.org/10.1086/342865

Sheldon, N.D., Tabor, N.J., 2009. Quantitative paleoenvironmental and paleoclimatic reconstruction using paleosols. Earth-Science Rev. 95, 1–52. https://doi.org/10.1016/j.earscirev.2009.03.004

Sheldon, N.D., 2006. Precambrian paleosols and atmospheric CO_2 levels. Precambrian Res. 147, 148–155. https://doi.org/10.1016/j.precamres.2006.02.004

Shenton, B.J., Grossman, E.L., Passey, B.H., Henkes, G.A., Becker, T.P., Laya, J.C., Perez-Huerta, A., Becker, S.P., Lawson, M., 2015. Clumped isotope thermometry in deeply buried sedimentary carbonates: The effects of bond reordering and recrystallization. Bull. Geol. Soc. Am. 127, 1036–1051. https://doi.org/10.1130/B31169.1

Sikes, N.E., Ashley, G.M., 2007. Stable isotopes of pedogenic carbonates as indicators of paleoecology in the Plio-Pleistocene (upper Bed I), western margin of the Olduvai Basin, Tanzania. J. Hum. Evol. 53, 574–594. https://doi.org/10.1016/j.jhevol.2006.12.008

Sloan, L.C., Barron, E.J., 1990. “Equable” climates during Earth history? Geology 18, 489–492. https://doi.org/10.1130/0091-7613(1990)018<0489:ECDEH>2.3.CO;2

Sloan, L.C., Morrill, C., 1998. Orbital forcing and Eocene continental temperatures. Palaeogeogr. Palaeoclimatol. Palaeoecol. 144, 21–35. https://doi.org/10.1016/S0031-0182(98)00091-1

Smith, F.A., Wing, S.L., Freeman, K.H., 2007. Magnitude of the carbon isotope excursion at the Paleocene-Eocene thermal maximum: The role of plant community change. Earth Planet. Sci. Lett. 262, 50–65. https://doi.org/10.1016/j.epsl.2007.07.021

Smith, G.A., Yang Wang, Cerling, T.E., Geissman, J.W., 1993. Comparison of a paleosol-carbonate isotope record to other records of Pliocene-early Pleistocene climate in the western United States. Geology 21, 691–694. https://doi.org/10.1130/0091-7613(1993)021<0691:COAPCI>2.3.CO;2

Snell, K.E., Thrasher, B.L., Eiler, J.M., Koch, P.L., Sloan, L.C., Tabor, N.J., 2013. Hot summers in the Bighorn Basin during the early Paleogene. Geology 41, 55–58. https://doi.org/10.1130/G33567.1

Snell, K.E., Koch, P.L., Druschke, P., Foreman, B.Z., Eiler, J.M., 2014. High elevation of the “Nevadaplano” during the Late Cretaceous. Earth Planet. Sci. Lett. 386, 52–63. https://doi.org/10.1016/j.epsl.2013.10.046

Snell, K.E., Thrasher, B.L., Eiler, J.M., Koch, P.L., Sloan, L.C., Tabor, N.J., 2013. Hot summers in the Bighorn Basin during the early Paleogene. Geology 41, 55–58. https://doi.org/10.1130/G33567.1

Solomon, D.K., Cerling, T.E., 1987. The annual carbon dioxide cycle in a montane soil: Observations, modeling, and implications for weathering. Water Resour. Res. 23, 2257–2265. https://doi.org/10.1029/WR023i012p02257

Souchez, R.A., Lemmens, M., 1985. Subglacial carbonate deposition: An isotopic study of a present-day case. Palaeogeogr. Palaeoclimatol. Palaeoecol. 51, 357–364. https://doi.org/10.1016/0031-0182(85)90093-8

Spicer, R.A., Herman, A.B., Kennedy, E.M., 2005. The Sensitivity of CLAMP to Taphonomic Loss of Foliar Physiognomic Characters. Palaios 20, 429–438. https://doi.org/10.2110/palo.2004.P04-63

Spicer, R.A., Ahlberg, A., Herman, A.B., Hofmann, C.C., Raikevich, M., Valdes, P.J., Markwick, P.J., 2008. The Late Cretaceous continental interior of Siberia: A challenge for climate models. Earth Planet. Sci. Lett. 267, 228–235. https://doi.org/10.1016/j.epsl.2007.11.049

Spicer, R.A., Bera, S., De Bera, S., Spicer, T.E. V, Srivastava, G., Mehrotra, R., Mehrotra, N., Yang, J., 2011. Why do foliar physiognomic climate estimates sometimes differ from those observed? Insights from taphonomic information loss and a CLAMP case study from the Ganges Delta. Palaeogeogr. Palaeoclimatol. Palaeoecol. 302, 381–395. https://doi.org/10.1016/j.palaeo.2011.01.024

Spicer, R.A., Herman, A.B., Kennedy, E.M., 2004. Foliar Physiognomic Record of Climatic Conditions during Dormancy: Climate Leaf Analysis Multivariate Program (CLAMP) and the Cold Month Mean Temperature. J. Geol. 112, 685–702. https://doi.org/10.1086/424579

Spicer, R.A., Yang, J., 2010. Quantification of uncertainties in fossil leaf paleoaltimetry: Does leaf size matter? Tectonics 29, 1–13. https://doi.org/10.1029/2010TC002741

Spinola, D.N., Portes, R. de C., Schaefer, C.E.G.R., Solleiro-Rebolledo, E., Pi-Puig, T., Kühn, P., 2017. Eocene paleosols on King George Island, Maritime Antarctica: Macromorphology, micromorphology and mineralogy. Catena 152, 69–81. https://doi.org/10.1016/j.catena.2017.01.004

Sreenivas, B., Roy, A.B., Srinivasan, R., 2001. Geochemistry of sericite deposits at the base of the Paleoproterozoic Aravalli Supergroup, Rajasthan, India: Evidence for metamorphosed and metasomatised Precambrian Paleosol. Proc. Indian Acad. Sci. Earth Planet. Sci. 110, 39–61. https://doi.org/10.1007/BF02702229

Stern, L. a, Baisden, W.T., Amundson, R., 1999. Processes controlling the oxygen isotope ratio of soil CO_2: analytic and numerical modeling. Geochim. Cosmochim. Acta 63, 799–814.

Still, C.J., Berry, J.A., Collatz, G.J., DeFries, R.S., 2003. Global distribution of C3 and C4 vegetation: Carbon cycle implications. Global Biogeochem. Cycles 17, 6-1-6–14. https://doi.org/10.1029/2001GB001807

Stolper, D.A., Eiler, J.M., 2015. The kinetics of solid-state isotope-exchange reactions for clumped isotopes: A study of inorganic calcites and apatites from natural and experimental samples. Am. J. Sci. 315, 363–411. https://doi.org/10.2475/05.2015.01

Strauch, G., Oyarzun, J., Fiebig-Wittmaack, M., González, E., Weise, S.M., 2006. Contributions of the different water sources to the Elqui river runoff (northern

Chile) evaluated by H/O isotopes. Isotopes Environ. Health Stud. 42, 303–322. https://doi.org/10.1080/10256010600839707

Suarez, M.B., Ludvigson, G.A., Gonzalez, L.A., You, H.L., 2017. Continental paleotemperatures from an early cretaceous Dolomitic Lake, Gansu Province, China. J. Sediment. Res. 486–499. https://doi.org/10.2110/jsr.2017.31

Suarez, M.B., Passey, B.H., Kaakinen, A., 2011. Paleosol carbonate multiple isotopologue signature of active east asian summer monsoons during the late Miocene and Pliocene. Geology 39, 1151–1154. https://doi.org/10.1130/G32350.1

Swett, K., 1974. Calcrete Crusts in an arctic permafrost environment. Am. J. Sci. 274, 1059–1063.

Swiss Standard SN 670 010b, 1999. Characteristic coefficients of soils. Association of Swiss Road and Traffic Engineers

Tabor, N.J., Myers, T.S., Huffington, R.M., Sciences, E., Gulbranson, E., Rasmussen, C., Sheldon, N.D., 2013. Carbon stable isotope composition of modern calcareous soil profiles in California: implications for CO_2 reconstructions from calcareous paleosols. SEPM Sepecial Pulication 17–34. https://doi.org/10.2110/sepmsp.104.07

Tabor, N.J., Myers, T.S., Huffington, R.M., Sciences, E., Gulbranson, E., Rasmussen, C., Sheldon, N.D., 2013. Carbon stable isotope composition of mordern calcatrous soil profiles in California: implications for CO_2 reconstructions from calcareous paleosols. SEPM Sepecial Pulication 17–34. https://doi.org/10.2110/sepmsp.104.07

Takeuchi, A., Larson, P.B., Suzuki, K., 2007. Influence of paleorelief on the Mid-Miocene climate variation in southeastern Washington, northeastern Oregon, and western Idaho, USA. Palaeogeogr. Palaeoclimatol. Palaeoecol. 254, 462–476. https://doi.org/10.1016/j.palaeo.2007.06.023

Tedrow, J.C.F., Ugolini, F.C., 1966. Antarctic soils. Antarct. Res. Ser. 8.

Terry, D.O., 2001. Paleopedology of the Chadron Formation of northwestern Nebraska: Implications for paleoclimatic change in the North American midcontinent across the Eocene-Oligocene boundary. Palaeogeogr. Palaeoclimatol. Palaeoecol. 168, 1–38. https://doi.org/10.1016/S0031-0182(00)00248-0

Thrasher, B.L., Sloan, L.C., 2010. Land cover influences on the regional climate of western North America during the early Eocene. Glob. Planet. Change 72, 25–31. https://doi.org/10.1016/j.gloplacha.2010.02.002

Tidwell, W.D., Britt, B.B., Tidwell, L.S., 2007. A review of the Cretaceous floras of east-central Utah and western Colorado, in: Central Utah: Diverse Geology of a Dynamic Landscape, UGA Publication 36. Utah Geological Association publication, pp. 466–481.

Tobin, T.S., Schauer, A.J., Lewarch, E., 2011. Alteration of micromilled carbonate $\delta^{18}O$ during Kiel Device Analysis. Rapid Commun. Mass Spectrom. 25, 2149–2152. https://doi.org/10.1002/rcm.5093

Tripati, A.K., Eagle, R.A., Thiagarajan, N., Gagnon, A.C., Bauch, H., Halloran, P.R., Eiler, J.M., 2010. ^{13}C-^{18}O isotope signatures and “clumped isotope” thermometry in foraminifera and coccoliths. Geochim. Cosmochim. Acta 74, 5697–5717. https://doi.org/10.1016/j.gca.2010.07.006

Tripati, A.K., Hill, P.S., Eagle, R.A., Mosenfelder, J.L., Tang, J., Schauble, E.A., Eiler, J.M., Zeebe, R.E., Uchikawa, J., Coplen, T.B., Ries, J.B., Henry, D., 2015. Beyond temperature: Clumped isotope signatures in dissolved inorganic carbon species and the influence of solution chemistry on carbonate mineral composition. Geochim. Cosmochim. Acta 166, 344–371. https://doi.org/10.1016/j.gca.2015.06.021

Uchikawa, J., Zeebe, R.E., 2012. The effect of carbonic anhydrase on the kinetics and equilibrium of the oxygen isotope exchange in the CO_2-H_2O system: Implications for $\delta^{18}O$ vital effects in biogenic carbonates. Geochim. Cosmochim. Acta 95, 15–34. https://doi.org/10.1016/j.gca.2012.07.022

Uhl, D., Klotz, S., Traiser, C., Thiel, C., Utescher, T., Kowalski, E., Dilcher, D.L., 2007. Cenozoic paleotemperatures and leaf physiognomy - A European perspective. Palaeogeogr. Palaeoclimatol. Palaeoecol. 248, 24–31. https://doi.org/10.1016/j.palaeo.2006.11.005

Upchurch, G.R., Kiehl, J., Shields, C., Scherer, J., Scotese, C., 2015. Latitudinal temperature gradients and high-latitude temperatures during the latest Cretaceous: Congruence of geologic data and climate models. Geology 43, 683–686. https://doi.org/10.1130/G36802.1

Usdowski, E., Hoefs, J., 1993. Oxygen isotope exchange between carbonic acid, bicarbonate, carbonate, and water: A re-examination of the data of McCrea (1950) and an expression for the overall partitioning of oxygen isotopes between the carbonate species and water. Geochim. Cosmochim. Acta 57, 3815–3818. https://doi.org/10.1016/0016-7037(93)90159-T

Valdes, P., 2011. Built for stability. Nat. Geosci. 4, 414–416. https://doi.org/10.1038/ngeo1200

Varricchio, D.J., 1995. Taphonomy of Jack's Birthday Site, a diverse dinosaur bonebed from the Upper Cretaceous Two Medicine Formation of Montana. Palaeogeogr. Palaeoclimatol. Palaeoecol. 114, 297–323. https://doi.org/10.1016/0031-0182(94)00084-L

Vogt, T., Corte, a E., 1996. Secondary precipitates in Pleistocene and present cryogenic environments (Mendoza Precordillera, Argentina, Transbaikalia, Siberia, and Seymour Island, Antarctica). Sedimentology 43, 53–64. https://doi.org/10.1111/j.1365-3091.1996.tb01459.x

Wacker, U., Fiebig, J., Schoene, B.R., 2013. Clumped isotope analysis of carbonates: comparison of two different acid digestion techniques. Rapid Commun. Mass Spectrom. 27, 1631–42. https://doi.org/10.1002/rcm.6609

Wang, Y., McDonald, E., Amundson, R., McFadden, L., Chadwick, O., 1996. An isotopic study of soils in chronological sequences of alluvial deposits, Providence Mountains, California. Bull. Geol. Soc. Am. 108, 379–391. https://doi.org/10.1130/0016-7606(1996)108<0379:AISOSI>2.3.CO;2

Wang, Y., Amundson, R., Trumbore, S., 1994. A model for soil $_{14CO2}$ and its implications for using ^{14}C to date pedogenic carbonate. Geochim. Cosmochim. Acta 58, 393–399. https://doi.org/10.1016/0016-7037(94)90472-3

Wang, Y., Cerling, T.E., Effland, W.R., Wang, Y., Cerling, T.E., Effland, W.R., 1993. Stable isotope ratios of soil carbonate and soil organic matter as indicators of forest invasion of prairie near Ames, Iowa. Oecologia 95, 365–369.

Wang, Z., Gaetani, G., Liu, C., Cohen, A., 2013. Oxygen isotope fractionation between aragonite and seawater: Developing a novel kinetic oxygen isotope fractionation model. Geochim. Cosmochim. Acta 117, 232–251. https://doi.org/10.1016/j.gca.2013.04.025

Wang, Z., Schauble, E.A., Eiler, J.M., 2004. Equilibrium thermodynamics of multiply substituted isotopologues of molecular gases. Geochim. Cosmochim. Acta 68, 4779–4797. https://doi.org/10.1016/j.gca.2004.05.039

Watkins, J.M., Hunt, J.D., 2015. A process-based model for non-equilibrium clumped isotope effects in carbonates. Earth Planet. Sci. Lett. 432, 152–165. https://doi.org/10.1016/j.epsl.2015.09.042

Watkins, J.M., Hunt, J.D., Ryerson, F.J., DePaolo, D.J., 2014. The influence of temperature, pH, and growth rate on the $\delta^{18}O$ composition of inorganically precipitated calcite. Earth Planet. Sci. Lett. 404, 332–343. https://doi.org/10.1016/j.epsl.2014.07.036

Watkins, J.M., Nielsen, L.C., Ryerson, F.J., DePaolo, D.J., 2013. The influence of kinetics on the oxygen isotope composition of calcium carbonate. Earth Planet. Sci. Lett. 375, 349–360. https://doi.org/10.1016/j.epsl.2013.05.054

Watson, E.B., 2004. A conceptual model for near-surface kinetic controls on the trace-element and stable isotope composition of abiogenic calcite crystals. Geochim. Cosmochim. Acta 68, 1473–1488. https://doi.org/10.1016/j.gca.2003.10.003

Watson, E.B., Müller, T., 2009. Non-equilibrium isotopic and elemental fractionation during diffusion-controlled crystal growth under static and dynamic conditions. Chem. Geol. 267, 111–124. https://doi.org/10.1016/j.chemgeo.2008.10.036

West, T., 2010. Geology Applied to Engineering. Waveland Press, Long Grove, Illinois.

Wilf, P., 1997. When are Leaves Good Thermometers? A New Case for Leaf Margin Analysis. Paleobiology 23, 373–390.

Wing, S.L., Alroy, J., Hickey, L.J., 1995. Plant and mammal diversity in the Paleocene to early Eocene of the Bighorn Basin. Palaeogeogr., Palaeoclim., Palaeoecol. 115, 117–156. https://doi.org/10.1016/0031-0182(94)00109-L

Wing, S.L., Harrington, G.J., 2001. Floral response to rapid warming in the earliest Eocene and implications for concurrent faunal change. Paleobiology 27, 539–563. https://doi.org/10.1666/0094-8373(2001)027<0539:FRTRWI>2.0.CO;2

Wing, S.L., Harrington, G.J., Smith, F.A., Bloch, J.I., Boyer, D.M., Freeman, K.H., 2005. Paleontology: Transient floral change and rapid global warming at the Paleocene-Eocene boundary. Science (80-.). 310, 993–996. https://doi.org/10.1126/science.1116913

Wolfe, J.A., 1990. Paleobotantical evidence for a major temperature increase following the Cretaceous/Tertiary boundary. Nature 343, 153–156.

Wolfe, J.A., Upchurch, G.R., 1987. North American nonmarine climates and vegetation during the Late Cretaceous. Palaeogeogr. Palaeoclimatol. Palaeoecol. 61, 33–77. https://doi.org/10.1016/0031-0182(87)90040-X

Wynn, J.G., 2000. Paleosols, stable carbon isotopes, and paleoenvironmental interpretation of Kanapoi, Northern Kenya. J. Hum. Evol. 39, 411–432. https://doi.org/10.1006/jhev.2000.0431

Zaarur, S., Affek, H.P., Brandon, M.T., 2013. A revised calibration of the clumped isotope thermometer. Earth Planet. Sci. Lett. 382, 47–57. https://doi.org/10.1016/j.epsl.2013.07.026

Zech, R., Kull, C., Veit, H., 2006. Late Quaternary glacial history in the Encierro Valley, northern Chile (29 °S), deduced from 10Be surface exposure dating. Palaeogeogr. Palaeoclimatol. Palaeoecol. 234, 277–286. https://doi.org/10.1016/j.palaeo.2005.10.011

Zeebe, R.E., 2007. An expression for the overall oxygen isotope fractionation between the sum of dissolved inorganic carbon and water. Geochemistry, Geophys. Geosystems 8, 1–7. https://doi.org/10.1029/2007GC001663

Zeebe, R.E., 1999. An explanation of the effect of seawater carbonate concentration on foraminiferal oxygen isotopes. Geochim. Cosmochim. Acta 63, 2001–2007. https://doi.org/10.1016/S0016-7037(99)00091-5

Zeebe, R.E., Wolf-Gladrow, D.A., Jansen, H., 1999. On the time required to establish chemical and isotopic equilibrium in the carbon dioxide system in seawater. Mar. Chem. 65, 135–153. https://doi.org/10.1016/S0304-4203(98)00092-9

Zeebe, R.E., Wolfe-Gladrow, D., 2001. CO_2 in seawater : equilibrium , kinetics , isotopes, 1st ed. Elsevier, Amsterdam, The Netherlands.

Zhou, J., Chafetz, H.S., 2010. Pedogenic Carbonates in Texas: Stable-Isotope Distributions and Their Implications for Reconstructing Region-Wide

Paleoenvironments. J. Sediment. Res. 80, 137–150.

https://doi.org/10.2110/jsr.2010.018

Appendix A: Chapter 2 Supplementary Materials

The figures and tables in this section correspond to the materials presented in Chapter 2 of this dissertation.

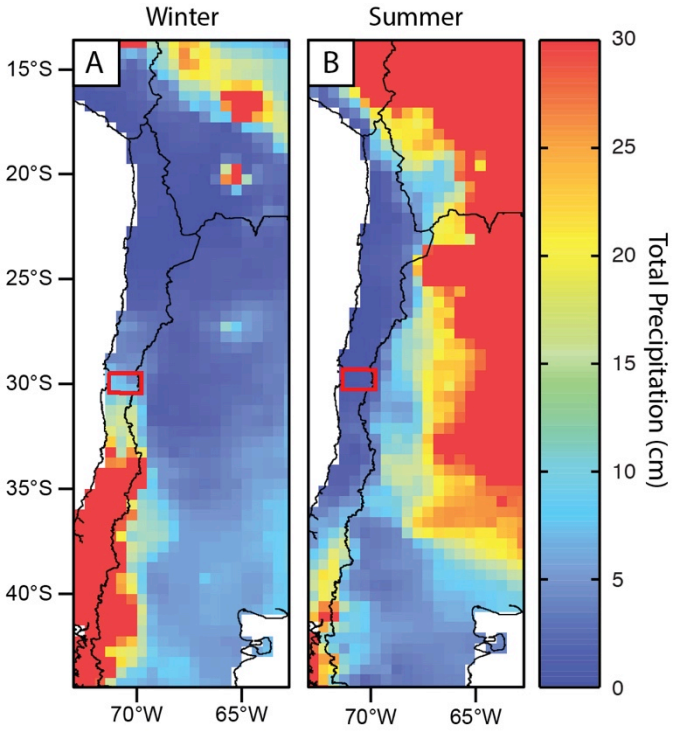

Supplementary Figure A1. Total seasonal precipitation (cm) for (A) austral winter (JJA), and (B) summer (DJF). The Elqui/Turbio study area is outlined by the red boundary. In the Elqui/Turbio drainage basin, more than 60% of total annual precipitation falls during austral winter (JJA), consistent with the findings of Kull et al. (2002).

Supplementary Table A1. Precipitation and surface water isotopic values

Station[a] or Sample ID	Station Name	Lat (°N)	Lon (°E)	δD (‰)	$\delta^{18}O$ (‰)	Sample Type	Mean Catchment Elevation (m)	Elevation (m)
NA	La Serena	-29.894	-71.244	-72.6	-9.9	Rain	NA	40
NA	La Serena (GNIP)	-29.894	-71.244	NA	-5.9	Rain	NA	40
1	Almendral	-29.982	-70.919	-64.9	-9.0	Rain	NA	400
3	Rividavia	-29.977	-70.562	-91.2	-12.3	Rain	NA	800
4	Huanta	-29.848	-70.385	-85.4	-10.2	Rain	NA	1300
ELQ13-01	NA	-29.842	-70.377	-100.3	-13.01	Tributary	3700	1400
ELQ13-16	NA	NA	NA	-109.2	-14.3	River	3855	1694
5	Las Juntas	-29.977	-70.094	-104.9	-13.5	Rain	NA	2100
ELQ13-02	NA	-30.169	-70.046	-115.6	-15.1	Tributary	4020	2900
ELQ13-03	NA	-30.188	-70.051	-120.2	-16.2	Tributary	3990	3100
ELQ13-05	NA	-30.258	-70.018	-125.4	-16.8	Trunk	4342	3100
ELQ13-06	NA	-30.230	-70.038	-116.4	-15.1	Tributary	4032	3100
6	La Laguna	-30.203	-70.042	-100.3	-13.6	Rain/Snow	NA	3100
ELQ13-04	NA	-30.261	-69.996	-121.8	-16.5	Tributary	4251	3190
ELQ13-15	NA	-30.204	-69.916	-128.7	-17.5	Trunk	4600	3795
ELQ13-07	NA	-30.190	-69.913	-127.9	-17.5	Tributary	4393	3860
ELQ13-08	NA	NA	NA	-125.1	-17.2	River	4513	3860
ELQ13-09	NA	-30.157	-69.879	-130.4	-17.9	Tributary	4689	4045
ELQ13-14	NA	-29.989	-70.249	-136.6	-18.1	Trunk	4614	4070
ELQ13-10	NA	-30.157	-69.865	-133.6	-17.9	Tributary	4755	4100
ELQ13-11	NA	-30.155	-69.857	-133.3	-18.0	Tributary	4772	4170
ELQ13-12	NA	-30.140	-69.832	-130.0	-17.6	Tributary	4841	4481
ELQ13-13	NA	-30.177	-69.831	-133.0	-17.6	Snowpack	4700	4700

Supplementary Table A2. Location, stable isotope, and replicate clumped isotope data for samples collected from the Elqui Valley, Chile

Sample ID	Elevation (m)	Depth (cm)	RF	$\delta^{13}C_{CO2}$ (‰) WG	$\delta^{13}C_{CO2}$ (‰) VPDB	$\delta^{18}O_{CO2}$ (‰) WG, measured	$\delta^{18}O_{CO2}$ (‰) VPDB, measured	δ^{47} (‰) VPDB	Δ_{47} (‰), ARF	Analytical Error	δ^{48} (‰) VPDB	Δ_{48} (‰), ARF	δ^{49} (‰) VPDB	Δ_{49} (‰), ARF	Avg. T(Δ_{47}) (°C) Kluge	Avg. T(Δ_{47}) (°C) Zaarur
Elq13-400-30	400	30	3	-6.8	-6.7	-4.7	-4.5	5.00	0.625	0.013	4.20	0.639	100.76	92.95	24	24
Elq13-400-30	400	30	3	-6.7	-6.7	-4.6	-4.4	5.12	0.639	0.011	4.30	0.590	55.96	48.29	20	21
Elq13-400-70	400	70	3	-7.6	-7.6	-3.4	-3.2	5.52	0.649	0.012	6.58	0.402	50.41	41.13	17	18
Elq13-400-70	400	70	4	-7.5	-7.4	-3.2	-3.2	5.73	0.589	0.016	6.55	0.049	29.78	20.27	37	33
Elq13-400-95	400	95	4	-8.7	-8.6	-3.5	-3.3	4.33	0.600	0.013	6.02	0.069	21.45	13.73	33	30
Elq13-400-95	400	95	4	-8.6	-8.6	-3.5	-3.3	4.44	0.642	0.011	5.96	-0.065	20.73	12.91	19	20
Elq13-400-95	400	95	4	-8.6	-8.5	-3.5	-3.5	4.35	0.615	0.015	5.80	-0.063	17.66	10.03	28	26
Elq13-400-95	400	95	3	-8.5	-8.5	-3.7	-3.5	4.34	0.661	0.012	6.02	0.422	49.91	42.20	13	16
Elq13-600-50	600	50	1	-5.9	-5.9	-7.8	-7.6	2.58	0.623	0.015	-2.06	0.727	33.37	31.70	25	24
Elq13-600-50	600	50	1	-6.0	-5.9	-7.8	-7.5	2.62	0.602	0.011	-2.13	0.506	42.13	40.32	32	30
Elq13-600-50	600	50	1	-5.9	-5.9	-7.9	-7.7	2.50	0.574	0.010	-2.70	0.182	7.56	6.03	42	37
Elq13-600-50	600	50	1	-6.0	-5.9	-7.9	-7.7	2.47	0.625	0.010	-2.32	0.637	77.95	76.43	24	24
Elq13-600-50	600	50	2	-6.1	-6.0	-7.5	-7.3	2.70	0.589	0.011	-2.09	0.072	22.74	20.63	37	33
Elq13-850-50	850	50	1	-3.2	-3.1	-6.5	-6.3	6.68	0.651	0.013	0.97	1.017	58.86	51.39	16	18
Elq13-850-50	850	50	1	-3.2	-3.1	-6.4	-6.3	6.67	0.569	0.014	0.82	0.803	37.30	29.87	44	38
Elq13-850-50	850	50	1	-3.1	-3.0	-6.4	-6.2	6.78	0.598	0.011	0.78	0.709	75.11	67.31	33	30
Elq13-850-50	850	50	1	-3.2	-3.1	-6.6	-6.4	6.60	0.650	0.010	0.35	0.608	35.61	28.48	17	18
Elq13-850-50	850	50	1	-3.1	-3.0	-6.5	-6.3	6.71	0.641	0.011	0.53	0.659	63.69	56.18	19	20
Elq13-850-50	850	50	3	-3.1	-3.0	-6.7	-6.5	6.51	0.623	0.012	-0.25	0.335	42.60	35.65	25	24
Elq13-850-50	850	50	3	-3.1	-3.0	-6.8	-6.6	6.43	0.608	0.012	-0.64	0.108	35.93	29.17	30	28

Supplementary Table A2. Continued 1

Sample ID	Elevation (m)	Depth (cm)	RF	$\delta^{13}C_{CO2}$ (‰) WG	$\delta^{13}C_{CO2}$ (‰) VPDB	$\delta^{18}O_{CO2}$ (‰) WG, measured	$\delta^{18}O_{CO2}$ (‰) VPDB, measured	δ^{47} (‰) VPDB	Δ_{47} (‰), ARF	Analytical Error	δ^{48} (‰) VPDB	Δ_{48} (‰), ARF	δ^{49} (‰) VPDB	Δ_{49} (‰), ARF	Avg. T(Δ_{47}) (°C) Kluge	Avg. T(Δ_{47}) (°C) Zaarur
Elq13-1300-20	1300	20	2	2.1	2.2	-6.2	-6.0	12.14	0.613	0.011	0.76	0.220	52.28	38.71	28	27
Elq13-1300-20	1300	20	2	2.0	2.2	-6.2	-6.0	12.11	0.612	0.011	0.98	0.448	74.54	60.73	29	27
Elq13-1300-20	1300	20	2	2.1	2.2	-6.2	-6.0	12.19	0.634	0.012	1.28	0.648	146.46	131.61	21	22
Elq13-1300-20	1300	20	2	2.0	2.1	-5.9	-5.7	12.38	0.620	0.011	1.63	0.457	59.98	45.75	26	25
Elq13-1300-20	1300	20	2	1.9	2.1	-6.2	-6.0	12.01	0.626	0.011	1.25	0.665	113.42	99.21	24	24
Elq13-1300-40	1300	40	2	0.2	0.3	-8.5	-8.3	7.81	0.598	0.011	-3.98	0.197	27.30	20.82	33	31
Elq13-1300-40	1300	40	2	0.2	0.4	-8.5	-8.3	7.90	0.623	0.010	-3.97	0.186	19.14	12.63	25	24
Elq13-1300-40	1300	40	2	0.1	0.2	-8.6	-8.4	7.70	0.603	0.012	-3.87	0.429	40.73	34.36	32	29
Elq13-1300-40	1300	40	2	0.2	0.3	-8.4	-8.2	7.92	0.607	0.012	-3.60	0.387	40.33	33.57	30	28
Elq13-1300-40	1300	40	2	0.1	0.2	-8.3	-8.1	7.99	0.623	0.012	-3.17	0.591	67.40	60.28	25	24
Elq13-1300-60	1300	60	1	-3.7	-3.6	-10.2	-9.9	2.39	0.594	0.011	-6.99	0.432	9.07	9.86	35	31
Elq13-1300-60	1300	60	1	-3.7	-3.6	-10.0	-9.8	2.55	0.629	0.011	-6.19	0.990	44.10	44.66	23	23
Elq13-1300-60	1300	60	1	-3.6	-3.5	-10.1	-9.8	2.64	0.646	0.010	-4.65	2.604	83.16	83.69	18	19
Elq13-1300-60	1300	60	1	-3.6	-3.6	-10.1	-9.8	2.56	0.643	0.012	-6.50	0.749	47.14	47.74	18	20
Elq13-1300-60	1300	60	2	-3.6	-3.5	-10.0	-9.7	2.62	0.595	0.011	-6.89	0.181	16.12	16.50	34	31
Elq13-1300-60	1300	60	2	-3.8	-3.7	-9.9	-9.7	2.56	0.616	0.011	-6.62	0.344	25.98	26.39	27	26
Elq13-1300-80	1300	80	2	-2.9	-2.8	-10.7	-10.4	2.62	0.601	0.012	-7.89	0.610	51.15	52.27	32	30
Elq13-1300-80	1300	80	2	-2.8	-2.7	-10.7	-10.5	2.60	0.591	0.010	-8.15	0.466	75.13	76.34	36	32
Elq13-1300-80	1300	80	2	-2.9	-2.8	-10.8	-10.6	2.46	0.639	0.013	-8.10	0.680	133.62	135.21	20	21
Elq13-1300-80	1300	80	2	-2.9	-2.8	-10.7	-10.4	2.64	0.607	0.011	-8.04	0.403	17.14	18.18	30	28

Supplementary Table A2. Continued 2

Sample ID	Elevation (m)	Depth (cm)	RF	$\delta^{13}C_{CO2}$ (‰) WG	$\delta^{13}C_{CO2}$ (‰) VPDB	$\delta^{18}O_{CO2}$ (‰) WG, measured	$\delta^{18}O_{CO2}$ (‰) VPDB, measured	δ^{47} (‰) VPDB	Δ_{47} (‰), ARF	Analytical Error	δ^{48} (‰) VPDB	Δ_{48} (‰), ARF	δ^{49} (‰) VPDB	Δ_{49} (‰), ARF	Avg. T(Δ_{47}) (°C) Kluge	Avg. T(Δ_{47}) (°C) Zaarur
Elq13-1300-100	1300	100	2	-3.3	-3.2	-10.9	-10.7	1.99	0.592	0.010	-8.73	0.267	11.34	13.30	35	32
Elq13-1300-100	1300	100	2	-3.3	-3.2	-10.9	-10.7	1.99	0.599	0.013	-8.78	0.215	-7.02	-5.09	33	30
Elq13-1300-100	1300	100	2	-3.3	-3.2	-11.0	-10.7	1.87	0.607	0.012	-8.43	0.666	54.86	57.11	30	28
Elq13-1300-100	1300	100	2	-3.6	-3.5	-10.8	-10.5	1.88	0.597	0.011	-8.30	0.334	15.75	17.67	34	31
Elq13-1500-50	1500	50	1	-0.4	-0.3	-9.9	-9.6	5.87	0.623	0.011	-5.85	1.060	51.55	48.39	25	24
Elq13-1500-50	1500	50	1	-0.4	-0.2	-9.9	-9.7	5.84	0.572	0.011	-6.59	0.396	7.64	4.64	43	37
Elq13-1500-50	1500	50	1	-0.4	-0.3	-10.0	-9.7	5.85	0.630	0.012	-6.22	0.792	40.59	37.54	23	23
Elq13-1500-50	1500	50	2	-0.4	-0.3	-9.9	-9.7	5.79	0.585	0.010	-6.43	0.528	59.44	56.33	38	34
Elq13-1500-50	1500	50	1	-0.3	-0.2	-10.1	-9.9	5.72	0.626	0.011	-6.38	0.978	81.94	79.09	24	24
Elq13-1500-50	1500	50	2	-0.5	-0.3	-9.8	-9.5	5.93	0.598	0.010	-6.09	0.569	77.23	73.77	33	30
Elq13-1700-50	1700	50	2	-3.5	-3.4	-11.8	-11.5	0.79	0.605	0.011	-9.83	0.916	64.29	68.57	31	29
Elq13-1700-50	1700	50	2	-3.4	-3.3	-12.1	-11.8	0.66	0.613	0.010	-11.32	-0.008	-1.93	2.51	28	27
Elq13-1700-50	1700	50	2	-3.5	-3.4	-12.1	-11.8	0.61	0.614	0.010	-10.78	0.573	121.76	126.84	28	26
Elq13-1700-50	1700	50	2	-3.3	-3.2	-12.1	-11.8	0.84	0.626	0.012	-11.10	0.123	15.77	20.07	24	24
Elq13-1924-20	1924	20	2	2.9	3.0	-8.5	-8.3	10.51	0.606	0.011	-3.84	0.278	37.86	28.45	31	28
Elq13-1924-20	1924	20	2	2.7	2.9	-8.8	-8.6	10.05	0.629	0.011	-4.07	0.642	62.72	53.91	23	23
Elq13-1924-20	1924	20	2	3.0	3.2	-8.7	-8.5	10.46	0.615	0.010	-3.90	0.554	61.62	52.23	28	26
Elq13-1924-20	1924	20	2	3.1	3.3	-8.5	-8.3	10.79	0.638	0.011	-3.64	0.410	56.50	46.63	20	21
Elq13-1924-20	1924	20	2	2.7	2.9	-8.7	-8.5	10.18	0.602	0.011	-3.71	0.764	76.93	67.71	32	30
Elq13-1924-40	1924	40	2	1.6	1.8	-9.1	-8.9	8.64	0.606	0.012	-2.47	0.573	195.08	46.57	31	29

Supplementary Table A2. Continued 3

Sample ID	Elevation (m)	Depth (cm)	RF	$\delta^{13}C_{CO2}$ (‰) WG	$\delta^{13}C_{CO2}$ (‰) VPDB	$\delta^{18}O_{CO2}$ (‰) WG, measured	$\delta^{18}O_{CO2}$ (‰) VPDB, measured	δ^{47} (‰) VPDB	Δ_{47} (‰), ARF	Analytical Error	δ^{48} (‰) VPDB	Δ_{48} (‰), ARF	δ^{49} (‰) VPDB	Δ_{49} (‰), ARF	Avg. T(Δ_{47}) (°C) Kluge	Avg. T(Δ_{47}) (°C) Zaarur
Elq13-1924-40	1924	40	2	1.6	1.8	-9.3	-9.1	8.44	0.592	0.010	-4.81	0.593	53.49	63.19	35	32
Elq13-1924-40	1924	40	2	1.6	1.8	-9.0	-8.8	8.74	0.608	0.011	-5.15	0.876	69.82	105.21	30	28
Elq13-1924-60	1924	60	1	-0.7	-0.6	-10.5	-10.3	4.95	0.613	0.011	-4.28	5.377	112.74	16.16	28	27
Elq13-1924-60	1924	60	1	-0.7	-0.6	-10.5	-10.2	4.94	0.596	0.010	-3.34	0.616	95.58	31.68	34	31
Elq13-1924-60	1924	60	1	-0.7	-0.5	-10.6	-10.3	4.95	0.621	0.010	-2.84	1.170	17.65	48.93	26	25
Elq13-1924-60	1924	60	2	-0.7	-0.6	-10.5	-10.2	4.98	0.607	0.011	-7.50	0.773	33.23	81.75	30	28
Elq13-1924-60	1924	60	2	-0.7	-0.6	-10.5	-10.2	4.95	0.607	0.010	-7.08	0.415	50.43	34.77	30	28
Elq13-1924-80	1924	80	2	-1.7	-1.6	-10.9	-10.6	3.58	0.585	0.010	-7.29	0.402	83.45	14.10	38	34
Elq13-1924-80	1924	80	2	-1.7	-1.6	-11.0	-10.7	3.45	0.596	0.010	-7.64	0.626	36.36	44.86	34	31
Elq13-1924-80	1924	80	2	-1.7	-1.6	-10.9	-10.7	3.52	0.610	0.011	-8.47	0.425	13.85	12.88	29	27
Elq13-1924-80	1924	80	2	-1.7	-1.6	-10.7	-10.4	3.77	0.607	0.011	-8.53	0.448	44.31	31.41	30	28
Elq13-1924-80	1924	80	2	-1.6	-1.5	-11.0	-10.7	3.51	0.575	0.011	-8.58	0.481	12.49	21.37	42	37
Elq13-1924-100	1924	100	2	-2.3	-2.2	-11.3	-11.0	2.54	0.605	0.011	-8.03	0.525	31.54	25.03	31	29
Elq13-1924-100	1924	100	2	-2.3	-2.2	-11.5	-11.2	2.31	0.582	0.011	-8.62	0.611	20.94	36.72	39	35
Elq13-1924-100	1924	100	2	-2.4	-2.3	-11.4	-11.1	2.39	0.601	0.010	-9.14	0.565	23.28	8.20	32	30
Elq13-1924-100	1924	100	2	-2.4	-2.3	-11.2	-11.0	2.52	0.585	0.010	-9.51	0.495	34.51	20.28	38	34
Elq13-2100-50	2100	50	2	0.1	0.2	-11.9	-11.6	4.31	0.599	0.011	-9.37	0.465	6.19	20.29	33	30
Elq13-2100-50	2100	50	2	0.1	0.2	-11.6	-11.4	4.43	0.610	0.011	-9.11	0.762	18.57	34.94	29	27
Elq13-2100-50	2100	50	2	0.1	0.3	-11.8	-11.5	4.40	0.602	0.013	-10.40	0.146	19.81	15.81	32	30
Elq13-2300-50	2300	50	2	0.1	0.2	-13.8	-13.4	2.40	0.628	0.011	-9.65	0.499	34.82	24.16	23	23

Supplementary Table A2. Continued 4

Sample ID	Elevation (m)	Depth (cm)	RF	$\delta^{13}C_{CO2}$ (‰) WG	$\delta^{13}C_{CO2}$ (‰) VPDB	$\delta^{18}O_{CO2}$ (‰) WG, measured	$\delta^{18}O_{CO2}$ (‰) VPDB, measured	δ^{47} (‰) VPDB	Δ_{47} (‰), ARF	Analytical Error	δ^{48} (‰) VPDB	Δ_{48} (‰), ARF	δ^{49} (‰) VPDB	Δ_{49} (‰), ARF	Avg. T(Δ_{47}) (°C) Kluge	Avg. T(Δ_{47}) (°C) Zaarur
Elq13-2300-50	2300	50	3	0.1	0.2	-13.8	-13.4	2.37	0.622	0.011	-10.58	0.290	15.50	16.35	25	25
Elq13-2300-50	2300	50	3	0.1	0.2	-13.7	-13.4	2.39	0.607	0.011	-14.13	0.397	19.80	19.06	30	28
Elq13-2700-20	2700	20	2	5.5	5.7	-8.8	-8.5	12.87	0.640	0.012	-14.34	0.766	12.00	145.11	20	20
Elq13-2700-20	2700	20	2	5.5	5.7	-8.7	-8.5	12.88	0.655	0.011	-14.14	0.949	14.79	157.22	15	17
Elq13-2700-20	2700	20	2	5.3	5.5	-9.0	-8.7	12.52	0.670	0.011	-3.86	0.635	158.03	55.57	11	14
Elq13-2700-20	2700	20	2	5.3	5.5	-9.0	-8.8	12.47	0.641	0.011	-3.59	0.718	170.32	62.67	19	20
Elq13-2700-20	2700	20	2	5.5	5.7	-9.2	-8.9	12.47	0.651	0.012	-4.37	0.641	66.88	53.47	16	18
Elq13-2700-40	2700	40	2	3.2	3.3	-12.1	-11.8	7.09	0.628	0.013	-4.36	0.749	73.99	46.62	23	23
Elq13-2700-40	2700	40	2	3.1	3.3	-12.2	-11.9	7.03	0.639	0.012	-4.75	0.925	64.52	87.27	20	21
Elq13-2700-40	2700	40	2	3.1	3.3	-11.9	-11.6	7.23	0.625	0.011	-10.58	0.800	48.86	41.30	24	24
Elq13-2700-40	2700	40	2	3.3	3.4	-12.2	-11.9	7.09	0.635	0.011	-10.49	0.545	89.47	29.77	21	22
Elq13-2700-60	2700	60	1	2.7	2.9	-12.9	-12.6	5.81	0.615	0.011	-10.18	1.237	43.85	64.06	27	26
Elq13-2700-60	2700	60	1	2.7	2.9	-13.0	-12.7	5.69	0.627	0.010	-10.99	1.151	31.86	54.31	24	24
Elq13-2700-60	2700	60	2	2.7	2.9	-12.9	-12.6	5.80	0.609	0.013	-11.68	0.746	64.13	35.68	30	28
Elq13-2700-60	2700	60	1	2.7	2.9	-13.0	-12.7	5.73	0.590	0.012	-11.99	1.718	54.13	16.81	36	32
Elq13-2700-80	2700	80	2	2.3	2.4	-13.9	-13.5	4.38	0.607	0.012	-12.16	0.709	35.75	31.66	30	28
Elq13-2700-80	2700	80	2	2.3	2.5	-13.8	-13.5	4.50	0.627	0.010	-11.40	0.871	16.72	66.44	24	23
Elq13-2700-80	2700	80	2	2.2	2.4	-13.7	-13.4	4.54	0.653	0.011	-14.12	1.090	29.27	96.09	16	17
Elq13-2700-80	2700	80	2	2.2	2.4	-13.6	-13.2	4.68	0.624	0.013	-13.89	0.550	64.12	95.33	25	24
Elq13-2700-80	2700	80	2	2.4	2.5	-14.0	-13.7	4.36	0.634	0.012	-13.47	0.852	93.82	66.59	21	22

Supplementary Table A2. Continued 5

Sample ID	Elevation (m)	Depth (cm)	RF	$\delta^{13}C_{CO2}$ (‰) WG	$\delta^{13}C_{CO2}$ (‰) VPDB	$\delta^{18}O_{CO2}$ (‰) WG, measured	$\delta^{18}O_{CO2}$ (‰) VPDB, measured	δ^{47} (‰) VPDB	Δ_{47} (‰), ARF	Analytical Error	δ^{48} (‰) VPDB	Δ_{48} (‰), ARF	δ^{49} (‰) VPDB	Δ_{49} (‰), ARF	Avg. T(Δ_{47}) (°C) Kluge	Avg. T(Δ_{47}) (°C) Zaarur
Elq13-2700-100	2700	100	2	2.3	2.5	-13.7	-13.4	4.57	0.606	0.010	-13.68	0.645	93.42	32.30	30	28
Elq13-2700-100	2700	100	2	2.3	2.4	-13.8	-13.4	4.49	0.601	0.010	-14.26	0.500	63.93	20.42	32	30
Elq13-2700-100	2700	100	2	2.3	2.5	-13.9	-13.6	4.39	0.609	0.013	-13.89	0.370	30.26	10.66	29	28
Elq13-3100-50	3100	50	2	-4.3	-4.2	-15.7	-15.4	-4.00	0.577	0.011	-14.13	0.101	18.29	-20.18	41	36
Elq13-3100-50	3100	50	2	-4.3	-4.2	-15.6	-15.2	-3.79	0.593	0.012	-14.53	0.156	8.30	-20.32	35	32
Elq13-3100-50	3100	50	3	-4.4	-4.3	-15.6	-15.3	-3.98	0.550	0.012	-18.46	0.173	-32.55	-15.70	52	43
Elq13-3100-50	3100	50	3	-4.4	-4.3	-15.5	-15.1	-3.89	0.548	0.011	-18.16	0.324	-32.39	0.53	53	44
Elq13-3100-50	3100	50	4	-4.5	-4.4	-15.4	-15.1	-3.80	0.584	0.012	-18.16	-0.190	-27.97	-20.07	38	34
Elq13-3300-50	3300	50	1	5.7	5.9	-10.4	-10.1	11.38	0.702	0.011	-17.77	1.376	-11.73	112.81	2	7
Elq13-3300-50	3300	50	1	5.6	5.8	-10.5	-10.2	11.25	0.717	0.013	-18.10	1.339	-31.95	100.15	-2	4
Elq13-3300-50	3300	50	2	5.6	5.8	-10.4	-10.1	11.35	0.665	0.012	-6.50	0.562	121.85	49.49	12	15
Elq13-3300-50	3300	50	1	5.5	5.7	-10.4	-10.2	11.19	0.668	0.011	-6.74	0.967	108.82	55.51	11	14
Elq13-3550-20	3550	20	2	2.8	2.9	-5.9	-5.7	13.20	0.644	0.011	-7.28	0.516	58.04	53.92	18	19
Elq13-3550-20	3550	20	2	2.8	3.0	-6.2	-6.0	12.91	0.651	0.011	-7.00	0.707	63.86	80.48	16	18
Elq13-3550-20	3550	20	2	2.8	2.9	-6.3	-6.1	12.76	0.663	0.011	1.73	0.561	69.15	49.42	13	15
Elq13-3550-20	3550	20	2	2.3	2.4	-6.3	-6.1	12.27	0.698	0.014	1.25	0.703	95.40	141.76	3	8
Elq13-3550-20	3550	20	2	3.1	3.3	-5.3	-5.2	14.12	0.689	0.014	0.93	0.785	63.66	84.01	5	10
Elq13-3550-40	3550	40	2	2.9	3.1	-8.5	-8.3	10.59	0.683	0.011	0.96	0.787	156.56	64.84	7	11
Elq13-3550-40	3550	40	2	2.8	3.0	-8.8	-8.5	10.26	0.675	0.011	3.05	0.892	101.19	87.46	9	13
Elq13-3550-40	3550	40	2	2.8	3.0	-8.6	-8.4	10.44	0.657	0.012	-3.36	0.564	74.57	51.55	14	17

Supplementary Table A2. Continued 6

Sample ID	Elevation (m)	Depth (cm)	RF	$\delta^{13}C_{CO2}$ (‰) WG	$\delta^{13}C_{CO2}$ (‰) VPDB	$\delta^{18}O_{CO2}$ (‰) WG, measured	$\delta^{18}O_{CO2}$ (‰) VPDB, measured	δ^{47} (‰) VPDB	Δ_{47} (‰), ARF	Analytical Error	δ^{48} (‰) VPDB	Δ_{48} (‰), ARF	δ^{49} (‰) VPDB	Δ_{49} (‰), ARF	Avg. T(Δ_{47}) (°C) Kluge	Avg. T(Δ_{47}) (°C) Zaarur
Elq13-3550-40	3550	40	2	2.8	2.9	-8.8	-8.6	10.11	0.646	0.010	-3.73	0.714	96.78	82.92	18	19
Elq13-3550-40	3550	40	2	2.5	2.7	-8.5	-8.3	10.26	0.674	0.011	-3.73	0.732	60.94	20.45	9	13
Elq13-3550-60	3550	60	1	1.0	1.1	-10.0	-9.8	7.13	0.654	0.014	-4.06	1.689	91.99	41.34	15	17
Elq13-3550-60	3550	60	1	1.4	1.6	-10.0	-9.7	7.64	0.709	0.010	-3.32	1.186	29.48	108.23	0	6
Elq13-3550-60	3550	60	1	1.3	1.4	-10.1	-9.9	7.35	0.678	0.013	-5.46	0.553	45.68	22.32	8	12
Elq13-3550-60	3550	60	2	1.1	1.3	-9.9	-9.7	7.37	0.650	0.012	-5.93	0.283	113.38	19.13	16	18
Elq13-3550-60	3550	60	2	1.0	1.1	-10.1	-9.9	7.03	0.646	0.012	-6.82	0.533	26.66	55.92	18	19
Elq13-3550-60	3550	60	1	0.5	0.6	-10.2	-10.0	6.51	0.714	0.011	-6.66	1.003	23.73	56.79	-1	5
Elq13-3550-80	3550	80	2	3.8	4.0	-9.2	-9.0	10.74	0.665	0.011	-6.82	0.681	60.11	70.96	12	15
Elq13-3550-80	3550	80	2	3.9	4.1	-8.8	-8.6	11.26	0.670	0.011	-6.55	0.518	60.25	48.28	11	14
Elq13-3550-80	3550	80	2	3.8	4.0	-9.2	-8.9	10.82	0.687	0.012	-4.82	0.576	80.23	44.35	6	10
Elq13-3550-80	3550	80	2	3.5	3.7	-9.4	-9.1	10.30	0.649	0.011	-4.23	0.532	58.29	45.82	17	18
Elq13-3550-100	3550	100	2	0.4	0.5	-11.6	-11.3	4.92	0.620	0.012	-4.87	0.651	53.48	56.75	26	25
Elq13-3550-100	3550	100	2	0.4	0.5	-11.4	-11.1	5.15	0.656	0.011	-5.27	0.575	54.26	42.44	15	17
Elq13-3550-100	3550	100	2	0.4	0.5	-11.9	-11.6	4.66	0.639	0.011	-9.64	0.445	57.18	25.30	20	21
Elq13-3550-100	3550	100	2	0.7	0.8	-11.5	-11.2	5.28	0.657	0.011	-9.34	0.575	43.28	45.27	14	17
Elq13-3750-50	3750	50	1	0.8	0.9	-12.0	-11.7	4.92	0.687	0.013	-10.36	1.244	25.18	100.19	6	10
Elq13-3750-50	3750	50	1	0.8	1.0	-11.9	-11.6	5.12	0.689	0.010	-9.57	1.270	46.13	56.15	5	10
Elq13-3750-50	3750	50	1	0.7	0.9	-11.9	-11.6	4.98	0.706	0.012	-9.85	1.468	100.15	92.31	1	7
Elq13-3750-50	3750	50	2	0.7	0.9	-11.5	-11.2	5.41	0.663	0.011	-9.55	0.677	56.47	173.37	13	15

Supplementary Table A2. Continued 7

Sample ID	Elevation (m)	Depth (cm)	RF	$\delta^{13}C_{CO2}$ (‰) WG	$\delta^{13}C_{CO2}$ (‰) VPDB	$\delta^{18}O_{CO2}$ (‰) WG, measured	$\delta^{18}O_{CO2}$ (‰) VPDB, measured	δ^{47} (‰) VPDB	Δ_{47} (‰), ARF	Analytical Error	δ^{48} (‰) VPDB	Δ_{48} (‰), ARF	δ^{49} (‰) VPDB	Δ_{49} (‰), ARF	Avg. T(Δ_{47}) (°C) Kluge	Avg. T(Δ_{47}) (°C) Zaarur
Elq13-3750-50	3750	50	1	0.6	0.7	-12.2	-11.9	4.57	0.685	0.011	-9.50	1.174	92.39	114.66	6	11
Elq13-4200-50	4200	50	1	6.7	6.9	-4.8	-4.6	18.26	0.678	0.012	-9.38	1.659	174.53	77.03	9	12
Elq13-4200-50	4200	50	1	6.6	6.8	-4.7	-4.5	18.20	0.691	0.011	-10.30	2.072	114.02	96.81	5	9
Elq13-4200-50	4200	50	1	6.7	7.0	-4.7	-4.5	18.40	0.691	0.012	5.13	1.082	99.34	93.95	5	9
Elq13-4200-50	4200	50	2	6.6	6.8	-4.9	-4.8	17.97	0.697	0.011	5.62	0.810	119.48	86.47	3	8
Elq13-4500-50	4500	50	1	9.0	9.2	-9.5	-9.2	15.64	0.742	0.011	4.75	1.955	116.85	192.19	-8	0
Elq13-4500-50	4500	50	1	8.9	9.1	-9.5	-9.2	15.54	0.737	0.011	3.93	1.546	108.44	121.88	-7	1
Elq13-4500-50	4500	50	1	8.9	9.1	-9.3	-9.1	15.63	0.710	0.011	-4.04	1.515	208.12	115.44	0	6
Elq13-4500-50	4500	50	1	8.8	9.0	-9.3	-9.1	15.60	0.722	0.010	-4.47	1.456	136.76	94.03	-3	3
Elq13-4500-50	4500	50	1	8.7	8.9	-9.4	-9.2	15.41	0.724	0.011	-4.23	1.935	130.51	195.28	-4	3
Elq13-4500-50	4500	50	2	9.1	9.3	-9.5	-9.2	15.62	0.664	0.011	-4.27	0.875	108.76	71.87	12	15
Elq13-4700-20	4700	20	2	9.2	9.4	-3.3	-3.2	22.19	0.683	0.013	-3.99	0.730	211.03	116.78	7	11
Elq13-4700-20	4700	20	2	9.3	9.5	-3.2	-3.0	22.25	0.665	0.011	-5.19	0.879	86.22	136.72	12	15
Elq13-4700-20	4700	20	2	9.3	9.5	-3.4	-3.2	22.24	0.665	0.011	7.11	0.969	146.01	133.12	12	15
Elq13-4700-40	4700	40	2	8.3	8.6	-4.1	-3.9	20.54	0.659	0.011	7.57	0.606	166.76	78.35	14	16
Elq13-4700-40	4700	40	2	8.3	8.6	-4.1	-3.9	20.50	0.637	0.012	7.25	0.645	162.80	123.75	20	21
Elq13-4700-40	4700	40	2	8.3	8.5	-4.1	-4.0	20.45	0.687	0.017	6.95	0.631	151.14	85.73	6	10
Elq13-4700-40	4700	40	2	8.4	8.6	-3.8	-3.6	20.73	0.639	0.013	5.45	0.594	103.96	83.87	20	21
Elq13-4700-60	4700	60	2	9.7	10.0	-4.4	-4.3	21.55	0.668	0.019	5.46	0.850	150.40	72.63	11	14
Elq13-4700-60	4700	60	2	9.8	10.0	-4.4	-4.3	21.59	0.652	0.012	5.39	0.948	111.34	182.25	16	18

Supplementary Table A2. Continued 8

Sample ID	Elevation (m)	Depth (cm)	RF	$\delta^{13}C_{CO2}$ (‰) WG	$\delta^{13}C_{CO2}$ (‰) VPDB	$\delta^{18}O_{CO2}$ (‰) WG, measured	$\delta^{18}O_{CO2}$ (‰) VPDB, measured	δ^{47} (‰) VPDB	Δ_{47} (‰), ARF	Analytical Error	δ^{48} (‰) VPDB	Δ_{48} (‰), ARF	δ^{49} (‰) VPDB	Δ_{49} (‰), ARF	Avg. T(Δ_{47}) (°C) Kluge	Avg. T(Δ_{47}) (°C) Zaarur
Elq13-4700-60	4700	60	2	9.8	10.0	-4.4	-4.2	21.65	0.678	0.011	6.05	0.844	110.19	97.59	8	12
Elq13-4700-60	4700	60	2	9.9	10.1	-4.2	-4.1	21.74	0.664	0.012	5.00	0.926	98.85	113.17	12	15
Elq13-4700-80	4700	80	2	10.3	10.5	-5.3	-5.1	20.97	0.673	0.012	5.12	0.885	211.23	148.20	10	13
Elq13-4700-80	4700	80	2	10.2	10.5	-5.3	-5.1	20.95	0.677	0.011	5.03	0.863	124.55	92.04	9	12
Elq13-4700-80	4700	80	2	10.1	10.4	-5.5	-5.3	20.83	0.663	0.011	5.51	1.050	140.87	95.41	12	15
Elq13-4700-80	4700	80	2	10.2	10.4	-5.5	-5.3	20.91	0.682	0.011	3.22	1.633	174.60	324.61	7	11
Elq13-4700-100	4700	100	2	9.1	9.4	-6.4	-6.3	18.71	0.674	0.011	3.19	1.107	117.11	141.31	10	13
Elq13-4700-100	4700	100	2	9.1	9.4	-6.4	-6.2	18.76	0.652	0.011	3.01	0.965	120.22	109.12	16	18
Elq13-4700-100	4700	100	2	8.9	9.2	-6.6	-6.4	18.56	0.678	0.012	3.64	0.805	354.70	86.91	8	12
Elq13-4700-100	4700	100	2	9.0	9.2	-6.8	-6.6	18.36	0.650	0.012	1.17	0.713	163.63	60.73	16	18
Elq13-4700-100	4700	100	2	9.1	9.4	-6.7	-6.5	18.58	0.665	0.013	1.17	0.861	130.96	80.48	12	15

Supplementary Table A3. Clumped Isotope Reference Frame Data

Reference Frame	Date	Acid Correction Factor[a]	C64[b] Mean Δ_{47} (‰)	C64 Δ_{47} Std. (‰)	Heated Gas Equilibration Temperature (°C)	n	Slope	Intercept (Δ_{47} [EGvsWG])	r^2	Empirical Transfer Function (ETF) Slope	ETF Intercept	ETF r^2	Bootstrapped Absolute Reference Frame (ARF) Slope	Bootstrapped ARF Intercept
1	Sep. 2013 - Dec. 2013	0.082	0.621	0.037	4	22	0.0020	0.1153	0.4756	1.0963	0.9189	1.0000	0.0020	0.11608
					60	14	0.0020	-0.1443	0.8328	1.0963	0.9189	1.0000	0.0020	-0.14409
					1000	75	0.0020	-0.8136	0.2145	1.0963	0.9189	1.0000	0.0020	-0.81359
2	Feb. 2014 - Oct. 2014	0.082	0.621	0.024	4	15	0.0021	0.1191	0.7773	1.0643	0.9155	1.0000	0.0021	0.11967
					60	17	0.0021	-0.1418	0.6748	1.0643	0.9155	1.0000	0.0021	-0.14154
					1000	49	0.0021	-0.8360	0.5952	1.0643	0.9155	1.0000	0.0021	-0.83587
3	Oct. 2014 - Apr. 2015	0.082	0.621	0.019	4	14	0.0027	0.0889	0.8384	1.0826	0.9343	0.9995	0.0028	0.088462
					60	17	0.0027	-0.1422	0.7299	1.0826	0.9343	0.9995	0.0028	-0.14247
					1000	35	0.0027	-0.8426	0.5522	1.0826	0.9343	0.9995	0.0028	-0.84277
4	Jul. 2015 -	0.082	0.621	0.033	4	7	-0.0010	0.0731	0.8497	1.2781	0.9420	0.9998	-0.0010	0.073111
					60	7	-0.0010	-0.1316	0.4179	1.2781	0.9420	0.9998	-0.0010	-0.1315
					1000	6	-0.0010	-0.7187	0.5737	1.2781	0.9420	0.9998	-0.0010	-0.71859

a. Acid correction factor taken from Wacker et al. (2014)

b. Isolab in-house standard

Appendix B: Chapter 3 Supplementary Materials

The figures and tables in this section correspond to the materials presented in Chapter 3 of this dissertation.

Supplementary Figure B1 (following page). Climate data for seven of the soil carbonate sampling sites: A1, A2) 4700 masl Elqui Valley, Chile; B1, B2) Ny-Ålesund, Svalbard; C1, C2) Scott Base, Antarctica; D1, D2) Victoria Valley, Antarctica; E1, E2) Lhasa, Tibet; F1, F2) T'u-ko-erh-ho-kung, Tibet; and G1, G2) Shigatse, Tibet. For each sample site, the solid black line shows mean monthly weather station air temperature, the dashed black line shows maximum monthly weather station air temperature, the solid red line shows mean monthly 50 cm weather station soil temperature, the dashed red line shows maximum monthly weather station 50 cm soil temperature, the solid blue line shows mean monthly air temperature from ERA-Interim climate reanalysis data, the dashed blue line shows maximum monthly air temperatures from ERA-Interim climate reanalysis data, the solid magenta line shows mean monthly 50 cm climate reanalysis soil temperature, and the dashed magenta line shows maximum monthly 50 cm climate reanalysis soil temperature. The blue triangles in the upper left of each plot mark the clumped isotope temperatures measured on soil carbonate pendants at each site, and the horizontal light blue lines show that value across the plot, for clarity. The dashed gray line marks 0 °C across each plot. The histograms in the large plots (A1, B1, C1, D1, E1, F1, G1) show mean monthly precipitation from weather stations (blue bars) and ERA-Interim climate reanalysis data (green bars). The histograms in the small plots (A2, B2, C2, D2, E2, F2, G2) show soil moisture values derived from weather stations (blue bars) and ERA-Interim climate reanalysis data (green bars).

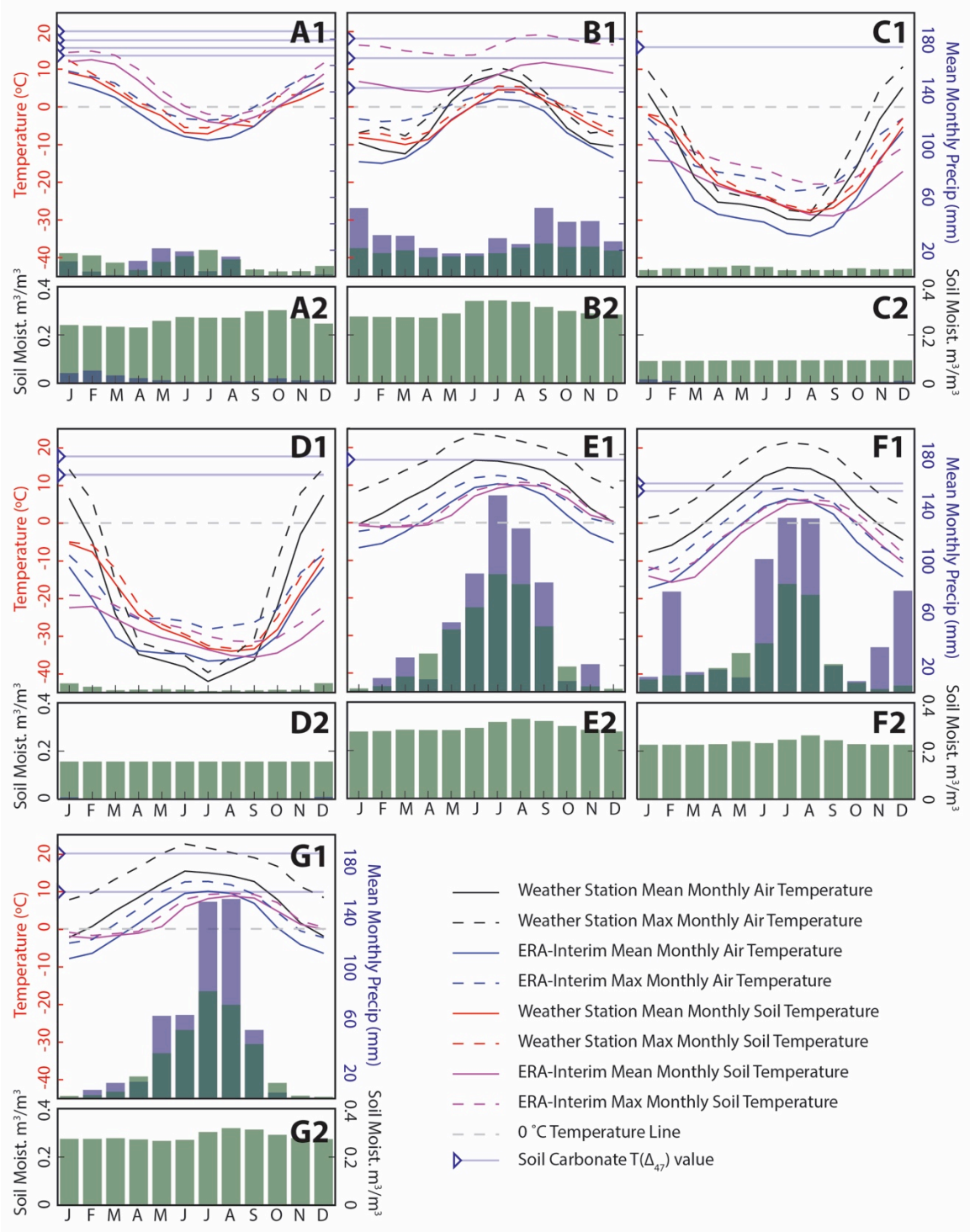
A1
B1
C1
A2
B2
C2
D1
E1
F1
D2
E2
F2
G1
G2
Temperature (°C)
Mean Monthly Precip (mm)
Soil Moist. m³/m³
J F M A M J J A S O N D
Weather Station Mean Monthly Air Temperature
Weather Station Max Monthly Air Temperature
ERA-Interim Mean Monthly Air Temperature
ERA-Interim Max Monthly Air Temperature
Weather Station Mean Monthly Soil Temperature
Weather Station Max Monthly Soil Temperature
ERA-Interim Mean Monthly Soil Temperature
ERA-Interim Max Monthly Soil Temperature
0 °C Temperature Line
Soil Carbonate T(Δ47) value

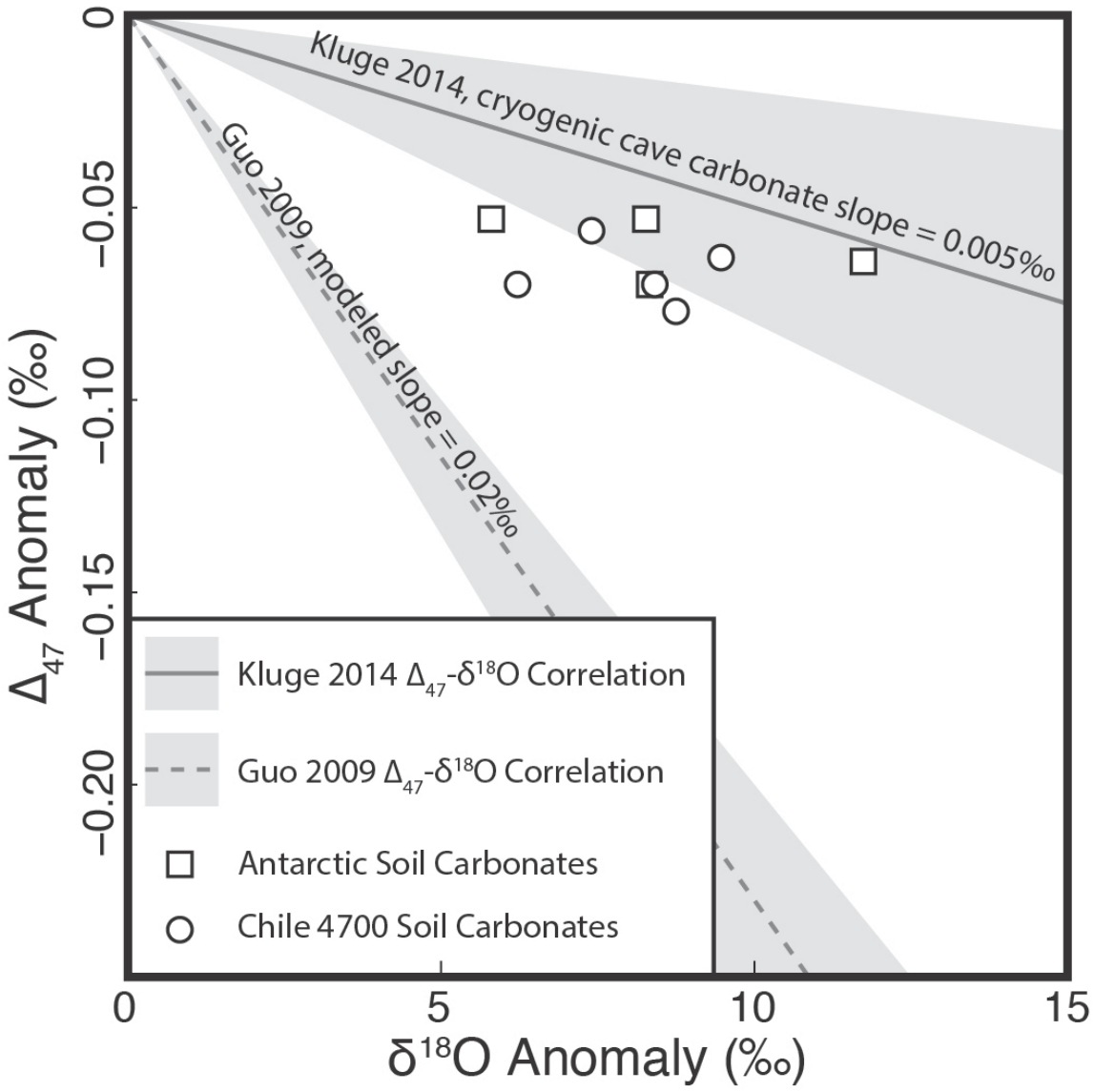

Supplementary Figure B2. Δ_{47} and $\delta^{18}O$ anomaly results for the Antarctic (squares) and 4700 masl Chilean (circle) soil carbonate samples, compared to the observed Δ_{47}- $\delta^{18}O$ correlation for cryogenic cave calcites from Kluge et al. (2014) (slope = -0.005‰) and the predicted bicarbonate dehydration Δ_{47}-$\delta^{18}O$ correlation from Guo (2009) (slope = -0.02‰).

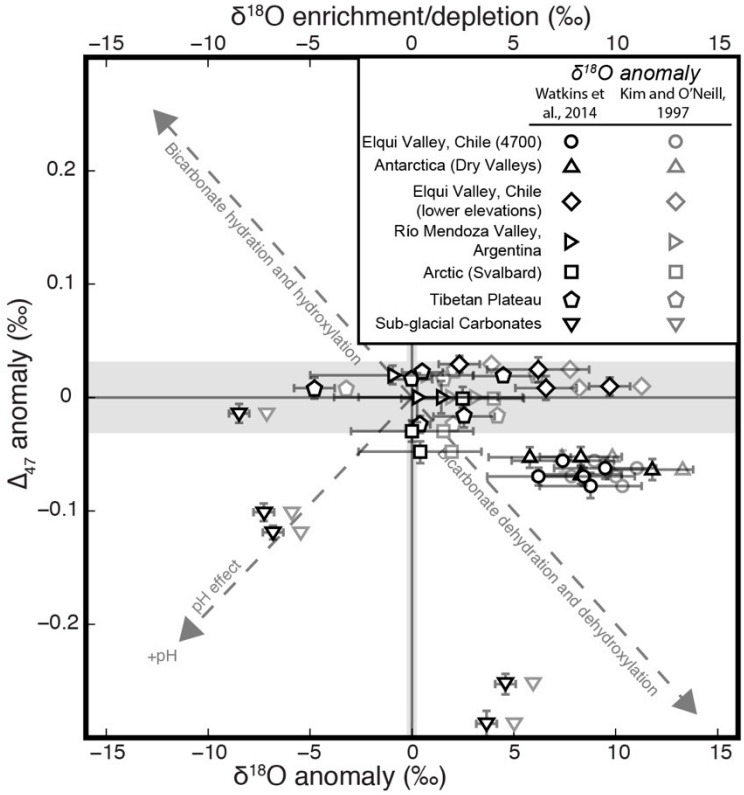

Supplementary Figure B3. Cross-plot of Δ_{47} and $\delta^{18}O$ anomalies as in Figure 7. Black markers represent $\delta^{18}O$ anomalies calculated using the Watkins et al. (2014) calcite-water $\delta^{18}O$ calibration. Gray markers represent $\delta^{18}O$ anomalies calculated using the Kim and O'Neil (1997) calcite-water $\delta^{18}O$ calibration.

Supplementary Table B1a. Clumped Isotope Standards[a]

Acid Correction Factor[b]	C64[c] Mean Δ_{47} (‰)	C64 Δ_{47} Std. (‰)	C2[c] Mean Δ_{47} (‰)	C2 Δ_{47} Std. (‰)	Coral[c] Mean Δ_{47} (‰)	Coral Δ_{47} Std. (‰)	ETH1[c] Mean Δ_{47} (‰)	ETH1 Δ_{47} Std. (‰)	ETH2[c] Mean Δ_{47} (‰)	ETH2 Δ_{47} Std. (‰)	ETH3[c] Mean Δ_{47} (‰)	ETH3 Δ_{47} Std. (‰)	ETH4[c] Mean Δ_{47} (‰)	ETH4 Δ_{47} Std. (‰)
0.082	0.621	0.037	0.548	0.025	0.629	0.031	0.214	0.034	0.219	0.030	0.612	0.017	0.444	0.016

a - For all samples except the Peters et al. (2013) samples, which were analyzed at Caltech from 2010-2011

b - Acid correction factor taken from Wacker et al. (2014)

c - Isolab in-house standard

Supplemental Table 1b. Clumped Isotope Reference Frame Data[a]

Heated Gas Equilibration Temperature (°C)	n	Slope	Intercept (Δ_{47} [EGvsWG])	r^2	Empirical Transfer Function (ETF) Slope	ETF Intercept	ETF r^2
4	6	-0.00034248	0.079404	-0.021864	1.047	0.93616	0.99844
60	6	-0.00034248	-0.13554	0.56117	1.047	0.93616	0.99844
1000	8	-0.00034248	-0.87565	-0.0339	1.047	0.93616	0.99844

Supplementary Table B2. Location, stable isotope, and replicate clumpe isotope data for all samples

Sample ID	$\delta^{13}C_{CO2}$ (‰) WG	$\delta^{13}C_{CO2}$ (‰) VPDB	$\delta^{18}O_{CO2}$ (‰) WG	$\delta^{18}O_{CO2}$ (‰) VPDB	δ^{47} (‰) VPDB	Δ_{47} (‰), ARF	Analytical Error	δ^{48} (‰) VPDB	Δ_{48} (‰), ARF	δ^{49} (‰) VPDB	Δ_{49} (‰), ARF
140520_1_Elq13_4700_20	9.20	9.42	-3.32	-3.13	22.19	0.650	0.010	7.11	0.730	146.01	116.752
140630_1_Elq13_4700_20	9.12	9.33	-3.16	-2.98	22.25	0.637	0.008	7.57	0.879	166.76	136.722
140726_1_Elq13_4700_20	9.33	9.55	-3.37	-3.19	22.24	0.631	0.008	7.25	0.969	162.80	133.087
140520_2_Elq13_4700_40	8.29	8.49	-4.12	-3.93	20.45	0.655	0.015	5.39	0.631	111.34	85.696
140630_2_Elq13_4700_40	8.25	8.45	-3.77	-3.58	20.73	0.612	0.010	6.05	0.594	110.19	83.865
140724_2_Elq13_4700_40	8.37	8.58	-4.08	-3.89	20.54	0.626	0.008	5.45	0.606	103.96	78.317
140726_2_Elq13_4700_40	8.36	8.57	-4.09	-3.90	20.50	0.605	0.008	5.46	0.645	150.40	123.719
140520_4_Elq13_4700_60	9.74	9.97	-4.43	-4.23	21.55	0.633	0.017	5.00	0.850	98.85	72.597
140630_3_Elq13_4700_60	9.72	9.94	-4.21	-4.02	21.74	0.635	0.008	5.51	0.926	140.87	113.170
140724_3_Elq13_4700_60	9.80	10.02	-4.41	-4.22	21.59	0.617	0.009	5.12	0.948	211.23	182.211
140726_3_Elq13_4700_60	9.82	10.05	-4.41	-4.21	21.65	0.644	0.007	5.03	0.844	124.55	97.559
140627_1_Elq13_4700_80	10.11	10.34	-5.33	-5.12	20.97	0.644	0.009	3.22	0.885	174.60	148.201
140630_5_Elq13_4700_80	10.08	10.31	-5.33	-5.12	20.95	0.647	0.008	3.19	0.863	117.11	92.035
140724_5_Elq13_4700_80	10.17	10.41	-5.51	-5.30	20.83	0.627	0.008	3.01	1.050	120.22	95.371
140726_5_Elq13_4700_80	10.22	10.45	-5.49	-5.28	20.91	0.647	0.007	3.64	1.633	354.70	324.566
140627_2_Elq13_4700_100	9.00	9.22	-6.45	-6.23	18.71	0.646	0.008	1.17	1.107	163.63	141.311
140630_7_Elq13_4700_100	9.00	9.22	-6.38	-6.16	18.76	0.625	0.008	1.17	0.965	130.96	109.117
140724_6_Elq13_4700_100	8.97	9.18	-6.56	-6.34	18.56	0.644	0.009	0.65	0.805	107.85	86.872
140726_6_Elq13_4700_100	8.93	9.15	-6.64	-6.41	18.39	0.585	0.008	0.58	0.889	107.57	86.803
140923_2_Elq13_4700_100	9.01	9.23	-6.77	-6.54	18.36	0.616	0.009	0.14	0.713	80.76	60.687
140923_8_Elq13_4700_100	9.18	9.40	-6.73	-6.50	18.58	0.630	0.010	0.37	0.861	101.16	80.443
160318_5_ANT1	6.82	7.05	-14.39	-14.10	8.25	0.649	0.008	-15.70	0.157	11.16	9.965
160627_2_ANT1	6.61	6.79	-14.93	-14.57	7.48	0.635	0.008	-16.65	0.289	30.10	30.227
160630_5_ANT1	6.55	6.73	-14.92	-14.55	7.44	0.631	0.008	-16.64	0.266	21.12	21.272
160318_4_ANT2	8.27	8.52	-17.90	-17.56	6.00	0.635	0.009	-22.54	0.295	4.94	9.469
160627_3_ANT2	8.08	8.28	-18.42	-18.02	5.30	0.645	0.008	-23.54	0.325	10.49	16.298
160630_4_ANT2	8.09	8.29	-18.26	-17.86	5.45	0.617	0.007	-23.12	0.436	36.80	42.411
160318_3_ANT3	8.81	9.07	-17.82	-17.48	6.63	0.658	0.008	-22.43	0.240	8.16	11.984
160627_4_ANT3	8.64	8.85	-18.51	-18.11	5.75	0.644	0.008	-23.61	0.442	24.99	30.499
160630_3_ANT3	8.57	8.77	-18.42	-18.02	5.77	0.647	0.007	-23.39	0.485	83.10	88.816
160318_1_ANT4	9.14	9.40	-20.43	-20.05	4.22	0.641	0.007	-27.50	0.369	55.22	64.530
160907_1_ANT4	9.08	9.29	-21.17	-20.65	3.41	0.658	0.008	-29.07	0.257	64.07	75.153

Supplementary Table B2. Continued.

Sample ID	$\delta^{13}C_{CO2}$ (‰) WG	$\delta^{13}C_{CO2}$ (‰) VPDB	$\delta^{18}O_{CO2}$ (‰) WG	$\delta^{18}O_{CO2}$ (‰) VPDB	δ^{47} (‰) VPDB	Δ_{47} (‰), ARF	Analytical Error	δ^{48} (‰) VPDB	Δ_{48} (‰), ARF	δ^{49} (‰) VPDB	Δ_{49} (‰), ARF
161130_1_ANT4	9.07	9.27	-21.37	-20.32	3.18	0.648	0.007	-29.70	0.012	167.62	180.285
140325_6_Elq13_3550_20	2.80	2.94	-5.86	-5.65	13.20	0.622	0.009	1.73	0.516	69.15	53.901
140327_6_Elq13_3550_20	2.85	2.99	-6.20	-5.98	12.91	0.628	0.008	1.25	0.707	95.40	80.456
140506_4_Elq13_3550_20	3.15	3.29	-5.35	-5.14	14.12	0.666	0.011	3.05	0.785	101.19	83.984
140812_1_Elq13_3550_20	2.30	2.44	-6.34	-6.12	12.27	0.676	0.012	0.96	0.703	156.56	141.730
140919_8_Elq13_3550_20	2.78	2.92	-6.29	-6.07	12.76	0.640	0.008	0.93	0.561	63.66	49.398
Peters_B15	NaN	-2.05	NaN	-10.63	4.595	0.685	0.008	8.969	2.482	NaN	NaN
Peters_B15	NaN	-2.13	NaN	-10.62	4.587	0.719	0.018	9.679	3.150	NaN	NaN
Peters_B15	NaN	-2.08	NaN	-10.78	4.427	0.651	0.020	10.717	4.518	NaN	NaN
Peters_B15	NaN	-2.07	NaN	-10.62	4.619	0.679	0.012	11.731	5.204	NaN	NaN
Peters_B30	NaN	-5.37	NaN	-11.88	0.029	0.662	0.0100	5.610	1.683	NaN	NaN
Peters_B30	NaN	-5.37	NaN	-11.77	0.180	0.705	0.0150	6.616	2.464	NaN	NaN
Peters_B45	NaN	-4.65	NaN	-12.82	-0.185	0.726	0.009	3.654	1.631	NaN	NaN
Peters_B45	NaN	-4.68	NaN	-12.81	-0.216	0.701	0.009	3.591	1.536	NaN	NaN
Peters_B45	NaN	-4.69	NaN	-12.87	-0.281	0.714	0.016	3.542	1.614	NaN	NaN
Peters_B45	NaN	-4.66	NaN	-12.86	-0.310	0.689	0.016	2.949	1.010	NaN	NaN
161008_3_KG_201a	-0.54	-0.45	-7.91	-7.53	7.79	0.649	0.010	-2.89	0.007	61.80	54.491
161014_1_KG_201a	-0.52	-0.42	-8.04	-7.67	7.67	0.649	0.010	-3.28	-0.103	40.83	33.928
161130_3_KG_201a	-0.49	-0.40	-8.09	-7.33	7.64	0.647	0.007	-3.65	-0.374	17.32	10.642
161008_4_KG_201b	0.45	0.55	-7.62	-7.26	9.03	0.632	0.008	-2.44	-0.113	26.40	17.738
161014_2_KG_201b	0.43	0.54	-7.67	-7.31	8.96	0.619	0.010	-2.48	-0.050	40.91	32.249
170126_3_KG_201b	0.44	0.49	-7.31	-6.78	9.34	0.641	0.007	-1.71	-0.010	24.86	15.579
161130_2_Cannes_62	5.33	5.49	-5.84	-5.12	15.65	0.620	0.006	0.75	-0.523	20.74	3.579
170124_4_Cannes_62	5.23	5.36	-5.44	-4.89	16.03	0.715	0.007	2.16	0.081	38.69	20.526
170126_2_Cannes_62	5.04	5.16	-5.68	-5.13	15.57	0.672	0.007	1.79	0.190	72.04	53.991
170127_3_Cannes_62	5.25	5.38	-5.60	-5.04	15.87	0.680	0.006	1.81	0.043	38.47	20.594
170128_3_Cannes_62	5.27	5.40	-5.47	-4.92	16.02	0.682	0.006	2.10	0.090	53.22	34.821
170107_1_TS19a	3.29	3.42	-15.42	-14.70	3.81	0.706	0.008	-17.11	0.820	121.23	126.229
170117_5_TS19a	3.25	3.32	-15.26	-14.56	3.88	0.657	0.007	-17.18	0.429	21.25	25.499
170119_3_TS19a	3.28	3.37	-15.38	-14.68	3.79	0.661	0.007	-17.35	0.493	23.11	27.580
170123_1_TS19a	3.11	3.21	-15.24	-14.91	3.75	0.654	0.006	-17.02	0.553	57.13	61.635
170117_1_TS19b	3.74	3.81	-14.98	-14.27	4.65	0.657	0.007	-16.52	0.521	61.57	64.847

Supplementary Table B2. Continued.

Sample ID	$\delta^{13}C_{CO2}$ (‰) WG	$\delta^{13}C_{CO2}$ (‰) VPDB	$\delta^{18}O_{CO2}$ (‰) WG	$\delta^{18}O_{CO2}$ (‰) VPDB	δ^{47} (‰) VPDB	Δ_{47} (‰), ARF	Analytical Error	δ^{48} (‰) VPDB	Δ_{48} (‰), ARF	δ^{49} (‰) VPDB	Δ_{49} (‰), ARF
170121_2_TS19b	3.56	3.66	-14.81	-14.13	4.66	0.660	0.006	-16.16	0.541	56.55	59.634
170107_2_TS21a	-2.92	-2.86	-12.41	-11.74	0.84	0.658	0.008	-11.24	0.700	110.73	115.817
170119_1_TS21a	-2.93	-2.92	-12.32	-11.62	0.91	0.670	0.009	-11.18	0.577	89.37	94.172
170121_3_TS21a	-2.96	-2.95	-12.25	-11.60	0.94	0.652	0.008	-11.24	0.387	43.39	47.881
170107_3_TS21b	-2.90	-2.84	-14.23	-13.53	-1.07	0.606	0.008	-15.20	0.378	41.69	50.311
170119_2_TS21b	-2.96	-2.95	-14.26	-13.56	-1.16	0.618	0.007	-15.32	0.315	15.78	24.302
170126_6_TS21b	-3.01	-3.02	-14.14	-13.67	-1.05	0.651	0.007	-15.02	0.374	15.28	23.599
170117_2_TS22	-1.37	-1.37	-16.37	-15.66	-1.81	0.600	0.008	-19.29	0.552	43.77	55.365
170123_4_TS22	-1.60	-1.58	-15.96	-15.64	-1.60	0.614	0.006	-18.53	0.492	23.48	34.223
170124_6_TS22	-1.45	-1.42	-16.20	-15.88	-1.68	0.630	0.008	-19.02	0.475	16.36	27.365
170126_7_TS22	-1.47	-1.44	-16.24	-15.79	-1.73	0.630	0.007	-19.03	0.542	18.86	29.988
170117_3_LH4	-3.88	-3.90	-17.88	-17.17	-5.75	0.642	0.007	-22.29	0.577	16.64	33.700
170123_5_LH4	-4.08	-4.09	-17.63	-17.34	-5.68	0.648	0.007	-21.84	0.518	13.67	30.353
170124_1_LH4	-3.96	-3.97	-17.77	-17.48	-5.73	0.617	0.007	-22.15	0.482	54.83	72.365
161130_6_GL1 (CG-1)	0.26	0.35	-11.24	-10.41	4.93	0.444	NaN	-10.39	-0.817	-16.39	-17.362
170124_5_GL1 (CG-1)	0.60	0.67	-10.33	-9.88	6.21	0.462	0.006	-7.56	0.190	31.61	28.339
170127_4_GL1 (CG-1)	0.51	0.57	-10.89	-10.39	5.52	0.430	0.008	-8.57	0.314	42.08	40.053
170124_7_GL2 (CG-2)	2.34	2.43	-11.62	-11.20	6.50	0.392	0.008	-10.19	0.134	16.49	14.134
170125_4_GL2 (CG-2)	2.34	2.43	-11.64	-11.14	6.50	0.408	0.007	-10.19	0.180	30.43	28.083
170126_8_GL2 (CG-2)	2.32	2.40	-11.63	-11.14	6.51	0.431	0.006	-9.92	0.445	62.88	60.480
170125_1_GL3a (BF-1)	-1.17	-1.13	-18.67	-18.23	-3.91	0.671	6.905	-23.58	0.836	91.43	108.486
170125_6_GL3a (BF-1)	-1.21	-1.18	-18.66	-18.24	-3.94	0.676	5.589	-23.71	0.691	33.55	49.736
170127_5_GL3a (BF-1)	-1.14	-1.11	-18.73	-18.31	-3.91	0.705	-1.827	-23.92	0.625	3.11	18.896
160108_3_GL3b (BF-2)	-0.83	-0.74	-17.15	-16.81	-2.09	0.578	35.168	-21.08	0.300	-2.04	10.083
170125_2_GL3b (BF-2)	-0.81	-0.77	-17.62	-17.18	-2.58	0.582	33.769	-21.81	0.524	26.27	39.731
170125_7_GL3b (BF-2)	-0.81	-0.77	-17.54	-17.10	-2.46	0.607	25.354	-21.59	0.571	23.49	36.727
170128_1_GL3b (BF-2)	-0.81	-0.78	-17.60	-17.16	-2.50	0.621	20.938	-21.43	0.852	99.04	113.387
160108_4_GL3c (BF-3)	-0.91	-0.81	-16.75	-16.41	-1.76	0.568	38.773	-20.22	0.368	2.89	14.327
170126_1_GL3c (BF-3)	-0.96	-0.93	-17.14	-16.70	-2.11	0.686	3.046	-20.22	1.161	188.15	202.728
170127_2_GL3c (BF-3)	-0.99	-0.96	-17.22	-16.79	-2.32	0.588	31.618	-20.99	0.545	33.80	46.683
170128_2_GL3c (BF-3)	-0.88	-0.85	-17.08	-16.64	-2.08	0.581	33.845	-20.75	0.503	29.26	41.675

Supplementary Table B3. Comparison of $\delta^{13}C$, $\delta^{18}O$, $T(\Delta_{47})$ results for

	$\delta^{13}C$			$\delta^{18}O$			$T(\Delta_{47})$		
Sample	**Burgener**	**Quade**	**Difference**	**Burgener**	**Quade**	**Difference**	**Burgener**	**Quade**	**Difference**
mean Tsangpo-19	3.55	5.25	-1.70	-14.46	-12.90	-1.56	10	11	-2
mean Tsangpo-21	-2.92	-4.45	1.53	-12.62	-19.00	6.38	15	23	-8
mean Tsangpo-22	-1.45	0.30	-1.75	-15.74	-18.35	2.61	22	20	2
mean Lhasa-4	-3.98	-1.95	-2.03	-17.33	-17.95	0.62	17	18	-1

Appendix C: Chapter 4 Supplementary Materials

The figures and tables in this section correspond to the materials presented in Chapter 4 of this dissertation.

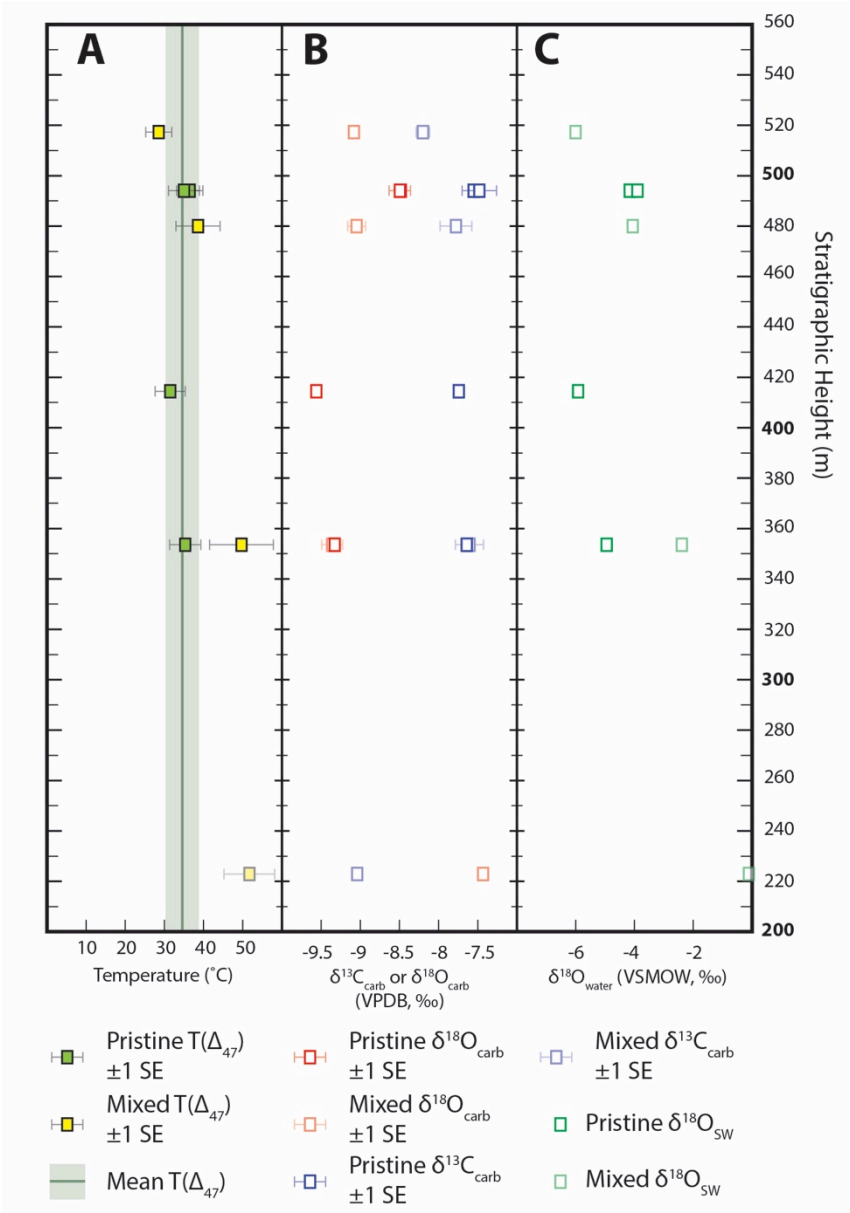

Supplementary Figure C1. Paleosol carbonate $T(\Delta_{47})$, $\delta^{18}O$, and $\delta^{13}C$ results for the Kaiparowits Formation, Blue Ceratopsian section (KBC). The $\delta^{18}O_{water}$ values in column C are calculated from the carbonate $\delta^{18}O$ and $T(\Delta_{47})$ values.

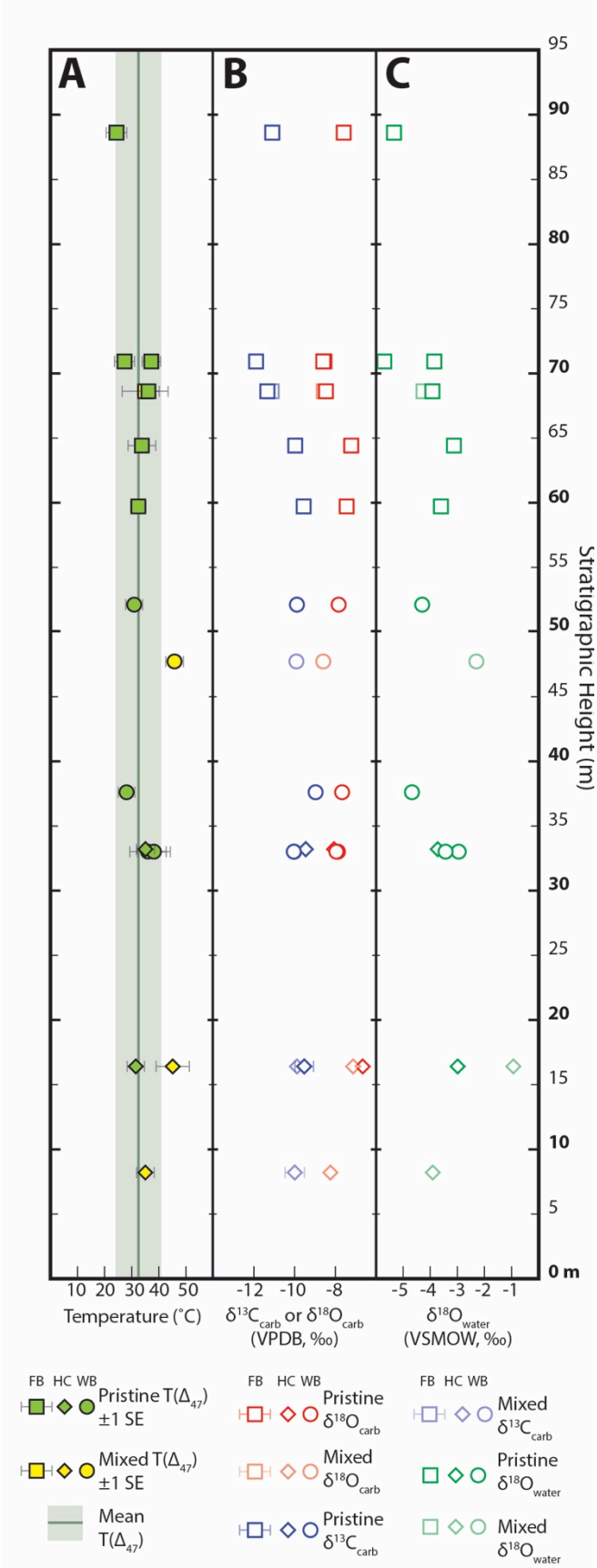

Supplementary Figure C2. Paleosol carbonate $T(\Delta_{47})$, $\delta^{18}O$, and $\delta^{13}C$ results for the Two Medicine Formation. FB = Flag Butte section, HC = Hagan's Crossing section, and WB = Western Butte section. The $\delta^{18}O_{water}$ values in column C are calculated from the carbonate $\delta^{18}O$ and $T(\Delta_{47})$ values. The $\delta^{18}O_{water}$ values in column C are calculated from the carbonate $\delta^{18}O$ and $T(\Delta_{47})$ values.

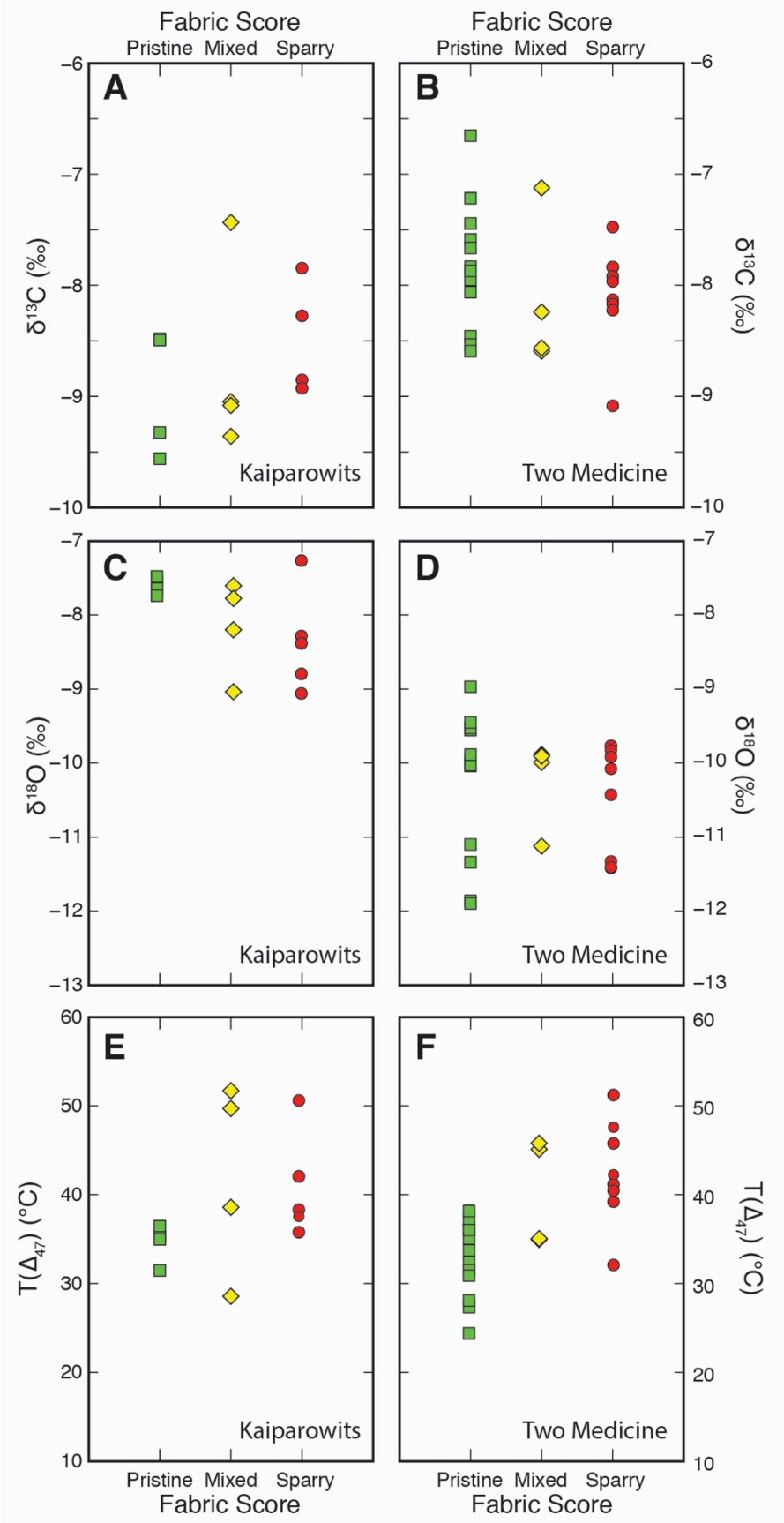
Fabric Score
Pristine Mixed Sparry
A
B
C
D
E
F
Kaiparowits
Two Medicine
δ13C (‰)
δ18O (‰)
T(Δ47) (°C)
−6
−7
−8
−9
−10
−11
−12
−13
60
50
40
30
20
10

Supplementary Figure C3 (previous page). Paleosol carbonate nodule $\delta^{13}C$ (A, B), $\delta^{18}O$ (C, D), and $T(\Delta_{47})$ (E, F) values plotted versus fabric score (FS 1 = micritic, FS 2 = mixed, FS 3 = sparry).

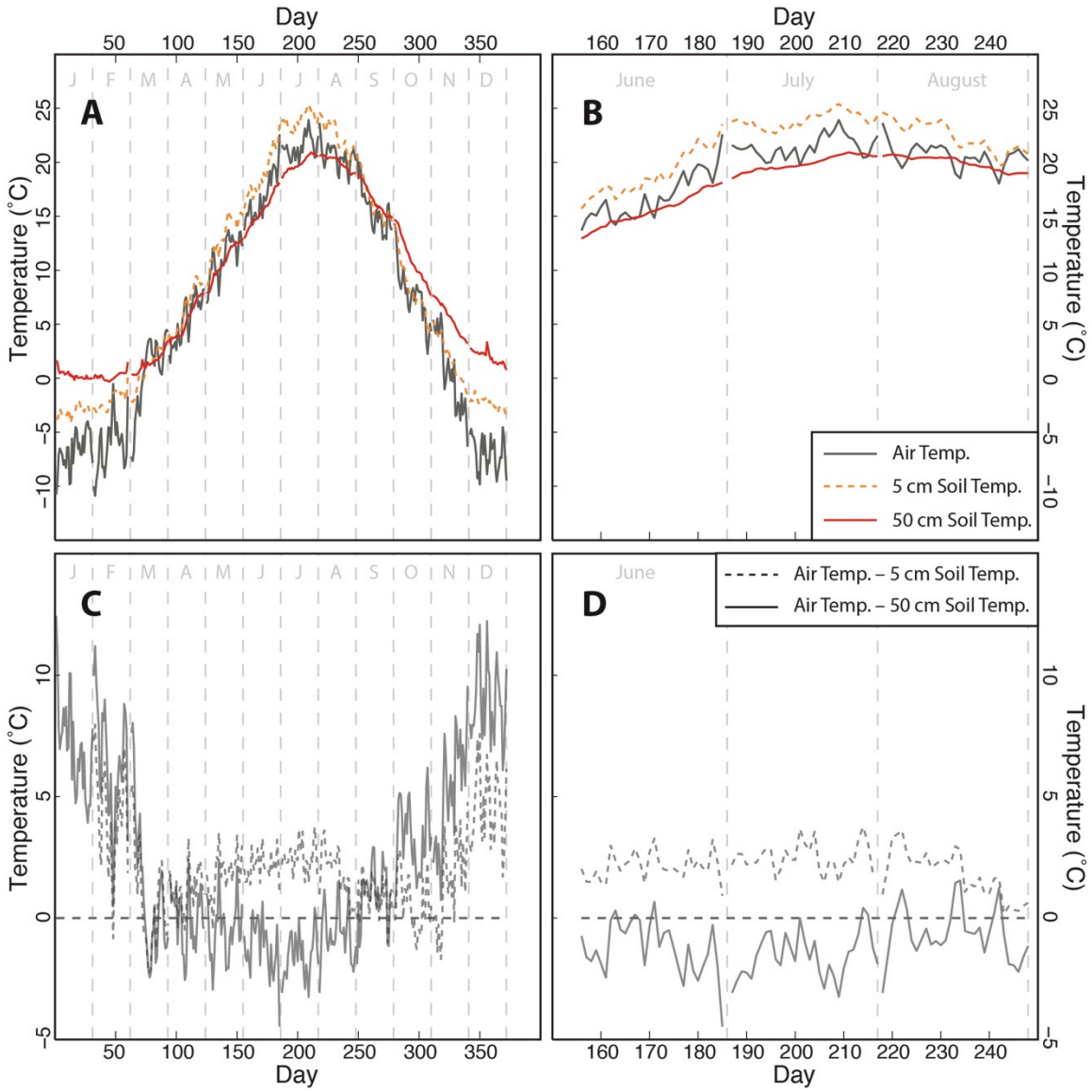

Supplementary Figure C4. Annual and summer (JJA) air, 10 cm soil, and 50 cm soil temperature data from SCAN station 581 (site name: Lindsay) in Dawson, MT. A and B show the time lag in warmest month mean air (~10 to 15 days). Note that for the entire summer period (JJA), STRH at 50 cm depth is near 0 °C, and always $\ll 5$ °C (panel D).

Supplementary Table C1. Paleosol measurements and descriptions.

Formation	Section	Paleosol[a]	Horizon	Thickness (cm)	Descriptive Features	Color[b]	Munsell Description	Stratigraphic Height (m)[c]	Depth to Bk (cm)[d]	Maximum Approx. Soil Age (ky)[e]	Minimum Approx. Soil Age (ky)[e]	Classification	
												Following Mack et al. (1993)	Following Retallack et al. (1993)
Two Medicine	Flag Butte (FB)	12	A	50	Orange red sandy silt, gray mottles	4/10GY	Dark Greenish Gray	33 (90)	155	3.9	2.3	Calcic Argillisol	Calcic Alfisol
			Bt	50	Red purple silt/clay, slickensides	10R 4/1	Dark Reddish Gray						
			Bk	70	Red brown silt, small peds, abundant nodules (<1 cm)	10YR 3/1	Dark Reddish Gray						
Two Medicine	Flag Butte (FB)	11	A	30	Red brown, no slickensides			32 (89)	47	5.4	3.5	Calcisol	Aridisol
			Bkt	90	Gray brown, some slickensides, some gray mottling	5Y 4/1	Dark Gray						
Two Medicine	Flag Butte (FB)	10	A	30	Same as underlying horizon but siltier, some Fe staining on ped edges	5YR 4/1	Dark Gray	20 (77)				Argillisol	Alfisol
			Bt	60	Gray/purple, rare slickensides, blocky angular peds (<1 cm)	10YR 4/1	Dark Gray						
Two Medicine	Flag Butte (FB)	9	A	30	Dark purple with large light green mottles (10 cm), some slickensides	7.5YR 4/1	Dark Gray	17 (74)	171	3.4	1.8	Calcic Argillisol	Calcic Alfisol
			Bt	80	Dark purple, slickensides	5YR 4/1	Dark Gray						
			Bkt	20	Carbonate nodules (<1 cm)	5YR 4/1	Dark Gray						
Two Medicine	Flag Butte (FB)	8	A	40	Purple, gray green root traces, rare slickensides	2.5Y 4/1	Dark Gray	16 (73)	62	3.0	1.8	Calcisol	Aridisol
			Bkt	50	Olive green gray, very small nodules (<2 mm), rare slickensides	6/10Y	Greenish Gray						

Supplementary Table C1. Continued 1.

Formation	Section	Paleosol[a]	Horizon	Thickness (cm)	Descriptive Features	Color[b]	Munsell Description	Stratigraphic Height (m)[c]	Depth to Bk (cm)[d]	Maximum Approx. Soil Age (ky)[e]	Minimum Approx. Soil Age (ky)[e]	Classification	
												Following Mack et al. (1993)	Following Retallack et al. (1993)
Two Medicine	Flag Butte (FB)	7	A	30	Siltier than underlying horizons, reddish purple color, green mottling, root traces	5YR 4/1	Dark Gray	14 (71)	187	5.7	3.3	Calcic Argillisol	Calcic Alfisol
			Bt	90	Dark brown/purple, slickensides, gray mottles	5YR 4/1	Dark Gray						
			Bk	80	Medium gray, carbonate nodules with incorporated sand grains (~1 cm)	5/5G	Greenish Gray						
Two Medicine	Flag Butte (FB)	6	A	30	Dark purple/brown, gray root traces	5YR 4/1	Dark Gray	13 (70)				Argillisol	Alfisol
			Bt	40	Light olive gray, slickensides, blocky angular peds	5/5GY	Greenish Gray						
Two Medicine	Flag Butte (FB)	5	A	50	Gray, slickensides, white root traces	4/10GY	Dark Greenish Gray	12 (69)	171	5.5	4.1	Calcic Argillisol	Calcic Alfisol
			Bt	20	Reddish brown, slickensides	10R 3/1	Dark Reddish Gray						
			Bk	50	Dark greenish gray, sandy at the base fining to silt/clay at the top, carbonate nodules (<3 cm), scattered slickensides at top	5/5G	Greenish Gray						
Two Medicine	Flag Butte (FB)	4	Bkt	60	Dark, small blocky angular peds (<2 cm), small carbonate nodules (<3 cm)	5/10GY	Greenish Gray	8 (65)	truncated	5.2	3.6		
Two Medicine	Flag Butte (FB)	3	Bk	40	Silty with slight clay accumulation, small blocky angular peds, carbonate nodules (2-3 cm)	5/10GY	Greenish Gray	7 (64)	truncated	4.9	3.9		

Supplementary Table C1. Continued 2.

Formation	Section	Paleosol[a]	Horizon	Thickness (cm)	Descriptive Features	Color[b]	Munsell Description	Stratigraphic Height (m)[c]	Depth to Bk (cm)[d]	Maximum Approx. Soil Age (ky)[e]	Minimum Approx. Soil Age (ky)[e]	Classification	
												Following Mack et al. (1993)	Following Retallack et al. (1993)
Two Medicine	Flag Butte (FB)	2	Bk	110	Gray silty sand, carbonate nodules (<1 cm)	5/10GY	Greenish Gray	4 (61)	truncated	4.8	3.1		
Two Medicine	Flag Butte (FB)	1	Bkt2	50	Slight clay accumulation, no slickensides, platy peds, carbonate nodules (<3 cm)	4/10GY	Dark Greenish Gray	2 (59)	truncated	5.2	3.6		
			Bkt1	100	Slight clay accumulation, no slickensides, blocky peds, carbonate nodules (<3 cm)	4/10GY	Dark Greenish Gray						
			C	70	Silty fine clay, thinly bedded	5Y 7/2	Light Gray						
Two Medicine	Western Butte (WB)	16	Bt	60	Gray with purple mottles, some clay accumulation	5Y 4/2	Olive Gray	41 (74)	truncated				
Two Medicine	Western Butte (WB)	15	A	40	Lighter gray, root traces, gray mottles			36 (69)				Argillisol	Alfisol
			Bt	70	Darkgray, clay accumulation	2.5Y 4/1	Dark Gray						
Two Medicine	Western Butte (WB)	14	A	30	Lighter purple gray, root traces, gray mottles			33 (66)				Argillisol	Alfisol
			Bt	70	Dark purple/brown, clay accumulation	10R 4/1	Dark Reddish Gray						

Supplementary Table C1. Continued 3.

Formation	Section	Paleosol[a]	Horizon	Thickness (cm)	Descriptive Features	Color[b]	Munsell Description	Stratigraphic Height (m)[c]	Depth to Bk (cm)[d]	Maximum Approx. Soil Age (ky)[e]	Minimum Approx. Soil Age (ky)[e]	Classification	
												Following Mack et al. (1993)	Following Retallack et al. (1993)
Two Medicine	Western Butte (WB)	13	A	30	Lighter purple gray			28 (61)				Argillisol	Alfisol
			Bt	80	Dark purple/gray, irregular peds, no slickensides	10R 4/1	Dark Reddish Gray						
Two Medicine	Western Butte (WB)	12	A	10	Lighter gray than underlying horizon			28 (61)				Argillisol	Alfisol
			Bt	70	Dark brown/purple, clay accumulation but no slickensides, indurated, possible incipient carbonate accumulation at bottom, but no nodules, small peds	10R 4/1	Dark Reddish Gray						
Two Medicine	Western Butte (WB)	11	A	20	Purple gray color, lighter than underlying horizon; siltier than underlying horizon	4/10Y	Dark Greenish Gray	27 (60)				Argillisol	Alfisol
			Bt	50	Large cm-scale purple-gray mottling, slickensides, 1 to 2 cm peds	5/5GY	Greenish Gray						
Two Medicine	Western Butte (WB)	10	A	60	Lighter gray and siltier than underyling horizon			23 (56)	109	3.6	2.3	Calcisol	Aridisol
			Bkt	160	Dark gray, slickensides, small nodules (<5 mm) mainly restricted to bottom 30 cm of horizon	5/5G	Greenish Gray						
Two Medicine	Western Butte (WB)	9	Bkt	60	Gray green with white mottles, orange/brown stainig, carbonate nodules (1-3 cm)	5/5GY	Greenish Gray	22 (55)	truncated	5.7	4.0		

Supplementary Table C1. Continued 4.

Formation	Section	Paleosol[a]	Horizon	Thickness (cm)	Descriptive Features	Color[b]	Munsell Description	Stratigraphic Height (m)[c]	Depth to Bk (cm)[d]	Maximum Approx. Soil Age (ky)[e]	Minimum Approx. Soil Age (ky)[e]	Classification	
												Following Mack et al. (1993)	Following Retallack et al. (1993)
Two Medicine	Western Butte (WB)	8	Bkt	130	Dark gray with green mottling and Fe/Mg staining, lare carbonate nodules (<10 cm)	4/10Y	Dark Greenish Gray	20 (53)	truncated	7.0	3.9		
Two Medicine	Western Butte (WB)	7	A	50	Light olive gray, small brown mottling, micaceous			19 (52)				Argillisol	Alfisol
			Bt	30	Dark green clay accumulation, brown mottling, small blocky peds	5/5GY	Greenish Gray						
Two Medicine	Western Butte (WB)	6	A	70	Siltier than underlying horizon, root traces, brown mottling	6/5GY	Greenish Gray	15 (48)	218	5.6	4.0	Calcic Argillisol	Calcic Alfisol
			Bt	70	Gray with rare purple staining, clay accumulation with minor slickensides	4/5G	Dark Greenish Gray						
			Bk	40	Dark gray green silty clay, incipient slickensides, carbonate nodules (<4 cm)	5/10 GY	Greenish Gray						
Two Medicine	Western Butte (WB)	5	Bt	120	Dark gray green, incipient slickensides	5/10GY	Greenish Gray	13 (46)	truncated	5.9	4.2		
			Bk	50	Dark gray green, silty with minor clay accumulation, possible incipient slickensides, flattened carbonate nodules	5/10GY	Greenish Gray						
Two Medicine	Western Butte (WB)	4	A	100	Light bluish gray, silty, minor white root traces, orange Fe staining, brown mottling	5Y 5/2	Olive Gray	8 (41)	249	4.9	3.5	Calcic Argillisol	Calcic Alfisol
			Bt	60	Dark greenish gray, rare small slickensides, clay accumulation	5Y 4/2	Olive Gray						
			Bk	40	Dark gray peds, carbonate nodules (<2 cm)	4/5GY	Dark Greenish Gray						

Supplementary Table C1. Continued 5.

Formation	Section	Paleosol[a]	Horizon	Thickness (cm)	Descriptive Features	Color[b]	Munsell Description	Stratigraphic Height (m)[c]	Depth to Bk (cm)[d]	Maximum Approx. Soil Age (ky)[e]	Minimum Approx. Soil Age (ky)[e]	Classification	
												Following Mack et al. (1993)	Following Retallack et al. (1993)
Two Medicine	Western Butte (WB)	3	Bkt	110	Green gray with weak clay accumulation, poorly consolidated with small peds, carbonate nodules (<5 cm)	5Y 5/2	Olive Gray	5 (38)	truncated	6.4	4.0		
Two Medicine	Western Butte (WB)	2	A	20	Siltier than underlying horizon, small peds and some mottling			4 (37)	31	5.9	4.7	Calcic Argillisol	Calcic Alfisol
			Bt	50	Ped surfaces coated in clay, orange mottling, no slickensides	5Y 4/2	Olive Gray						
			Bk	30	Greenish gray micaceous sandy silt, weakly developed peds, carbonate nodules (<5 cm)	2.5Y 7/2	Light Gray						
Two Medicine	Western Butte (WB)	1	Bk	80	Gray silt with minor clay accumulation, carbonate nodules (<1 cm)	2.5Y 6/2	Light Brownish Gray	0 (33)	truncated	5.4	3.0		
Two Medicine	Hagan's Crossing (HC)	15	Bkt	260	Truncated, dark green gray with scattered Fe staining, carbonate nodules (< 3cm)	5/10Y	Greenish Gray	73 (73)	truncated	5.4	3.0		
Two Medicine	Hagan's Crossing (HC)	14	A	20	Greener color than underyling layer, Fe/Mn staining			67 (67)				Argillisol	Alfisol
			Bt	110	Small (< 5 mm) blocky angular peds, dark red-brown color, Fe/Mn staining on ped surfaces	5Y 5/2	Olive Gray						

Supplementary Table C1. Continued 6.

Formation	Section	Paleosol[a]	Horizon	Thickness (cm)	Descriptive Features	Color[b]	Munsell Description	Stratigraphic Height (m)[c]	Depth to Bk (cm)[d]	Maximum Approx. Soil Age (ky)[e]	Minimum Approx. Soil Age (ky)[e]	Classification	
												Following Mack et al. (1993)	Following Retallack et al. (1993)
Two Medicine	Hagan's Crossing (HC)	13	A	30	Lighter in color than underlying horizon			61 (61)	47	5.1	2.9	Calcisol	Aridisol
			Bk	110	Brown-gray, carbonate nodules (<2 cm)	5Y 5/2	Olive Gray						
Two Medicine	Hagan's Crossing (HC)	12	A	40	Siltier than underlying horizon			55 (55)	62	3.7	2.4	Calcisol	Aridisol
			Bk	140	Carbonate nodules (<1 cm), weak clay accumulation, gray, large blocky peds, abundant shell material	5/10Y	Greenish Gray						
Two Medicine	Hagan's Crossing (HC)	11	A	130	Weak histosol, similar to paleosol 10			54 (54)				Histosol	Histosol
Two Medicine	Hagan's Crossing (HC)	10	A	300	Weak histosol, lignite with oxidized plant matter surrounded by halo of Fe/S mottling, 1 cm thick coal deposit at base of horizon, 20 cm thick plant and shell hash 140 cm from base of horizon			44 (44)				Histosol	Histosol
Two Medicine	Hagan's Crossing (HC)	9	A	30	Lighter gray and sandier than underlying horizon			38 (38)	47	6.4	3.0	Calcisol	Aridisol
			Bkt	130	Dark gray with small angular and blocky peds, rare carbonate nodules (<3 cm)	4/10Y	Dark Greenish Gray						

Supplementary Table C1. Continued 7.

Formation	Section	Paleosol[a]	Horizon	Thickness (cm)	Descriptive Features	Color[b]	Munsell Description	Stratigraphic Height (m)[c]	Depth to Bk (cm)[d]	Maximum Approx. Soil Age (ky)[e]	Minimum Approx. Soil Age (ky)[e]	Classification	
												Following Mack et al. (1993)	Following Retallack et al. (1993)
Two Medicine	Hagan's Crossing (HC)	8	Bkt	70	Gray with no mottling, carbonate nodules (0.1 to 1 cm)	6/10Y	Greenish Gray	34 (34)	truncated	5.8	3.8		
Two Medicine	Hagan's Crossing (HC)	7	Bkt	80	Abundant carbonate nodules (<5 cm), medium gray color, weak clay accumulation, no slickensides	5/5GY	Greenish Gray	33 (33)	truncated	5.9	2.9		
Two Medicine	Hagan's Crossing (HC)	6	A	60	Lighter gray, small peds, siltier than underlying horizon	5/5GY	Greenish Gray	28 (28)				Argillisol	Alfisol
			Bt	100	Dark gray, clay accumulation with no slickensides, small, angular and blocky peds	4/10GY	Dark Greenish Gray						
Two Medicine	Hagan's Crossing (HC)	5	A	30	Lighter gray and siltier than underyling horizon			23 (23)	47	3.3	2.3	Calcisol	Aridisol
			Bkt	80	Very weak clay accumulation, no slickensides, very small carbonate nodules (<2 mm), brown gray with Fe staining	4/5GY	Dark Greenish Gray						
Two Medicine	Hagan's Crossing (HC)	4	A	30	Light purple/gray			18 (18)				Argillisol	Alfisol
			Bt	80	Green silt with weak clay accumulation, no slickensides	5/5GY	Greenish Gray						

Supplementary Table C1. Continued 8.

Formation	Section	Paleosol[a]	Horizon	Thickness (cm)	Descriptive Features	Color[b]	Munsell Description	Stratigraphic Height (m)[c]	Depth to Bk (cm)[d]	Maximum Approx. Soil Age (ky)[e]	Minimum Approx. Soil Age (ky)[e]	Classification	
												Following Mack et al. (1993)	Following Retallack et al. (1993)
Two Medicine	Hagan's Crossing (HC)	3	A	30	Slightly lighter gray than underlying horizons, red-orange root traces			16 (16)	47	5.0	3.6	Calcisol	Aridisol
			Bkt	40	Dark gray green, clay accumulation, no slickensides, carbonate nodules (<3 cm)	5Y 5/1	Olive Gray						
			C	100	Dark gray, some dark purple staining, calcareous clay/silt								
Two Medicine	Hagan's Crossing (HC)	2	A	80	Gray green sandy silt, gray mottles	4/5GY	Dark Greenish Gray	10 (10)				Agrillisol	Alfisol
			Bt	20	Dark brown with distinct clay accumulation, Fe staining on ped surfaces, no slickensides	5Y 4/1	Dark Gray						
			C	90	Calcareous silt, dark gray brown, abundant mica grains	5Y 4/1	Dark Gray						
Two Medicine	Hagan's Crossing (HC)	1	A	30	Lighter gray and sandier than underyling horizon	6/10GY	Greenish Gray	8 (8)	47	5.5	3.7	Calcisol	Aridisol
			Bkt	100	Dark gray, blocky angular peds (1-2 cm), carbonate nodules (<3 cm)	6/10GY	Greenish Gray						
Kaiparowits	Blue Ceratopsian (KBC)	197	Bt	220	Dark green to dark brown (varies on ~10 m scale, weak and rare slickensides	5Y 4/2	Olive Gray	623	truncated				
Kaiparowits	Blue Ceratopsian (KBC)	157	A	50	Dark, olive gray with orange staining, organic carbon			526	171	4.0	2.7	Calcic Argillisol	Calcic Alfisol
			Bt	60	Dark brown with red slickensides	5Y 3/1	Very Dark Gray						
			Bk	90	Brown gray silty clay, orange and dark purple staining, carbonate nodules (< 1 cm)								

Supplementary Table C1. Continued 9.

Formation	Section	Paleosol[a]	Horizon	Thickness (cm)	Descriptive Features	Color[b]	Munsell Description	Stratigraphic Height (m)[c]	Depth to Bk (cm)[d]	Maximum Approx. Soil Age (ky)[e]	Minimum Approx. Soil Age (ky)[e]	Classification	
												Following Mack et al. (1993)	Following Retallack et al. (1993)
Kaiparowits	Blue Ceratopsian (KBC)	150	A	20	Light gray silty sand			517	202	5.1	3.3	Calcic Argillisol	Calcic Alfisol
			Bt	110	Dark gray silty clay, slickensides	5Y 4/2	Olive Gray						
			Bk	30	Gray green silty sand, carbonate nodules								
Kaiparowits	Blue Ceratopsian (KBC)	146b	A	40	Light gray, sandy silt			511	109	4.5	2.7	Calcic Argillisol	Calcic Alfisol
			Bt	40	Dark gray, silty clay, scattered slickensides	5Y 6/2	Light Olive Gray						
			Bk	90	Gray green, large peds (>10 cm) near top of horizon, smaller (<1 cm) peds near bottom of horizon, large carbonate nodules (<2 cm)								
Kaiparowits	Blue Ceratopsian (KBC)	145	A	20	Dark gray, silty			501	109	4.0	2.3	Calcic Argillisol	Calcic Alfisol
			Bt	50	Dark gray, silty clay, slickensides	5Y 4/2	Olive Gray						
			Bk	50	Green gray, some slickensides, silty, carbonate nodules (<1 cm)								
Kaiparowits	Blue Ceratopsian (KBC)	142	A	60	Upper contact grades into sand			494	202	4.7	3.5	Calcic Argillisol	Calcic Alfisol
			Bt	70	Darker gray than A and Bk horizon, abundant slickensides	5Y 6/2	Light Olive Gray						
			Bk	50	Gray brown, medium sized nodules, silty								
Kaiparowits	Blue Ceratopsian (KBC)	137	Bk	80	Green gray to brown, sandy silt with orange staining, large carbonate nodules (<2 cm), indurated, truncated	5Y 6/2	Light Olive Gray	480	truncated	5.3	4.5		

Supplementary Table C1. Continued 10.

Formation	Section	Paleosol[a]	Horizon	Thickness (cm)	Descriptive Features	Color[b]	Munsell Description	Stratigraphic Height (m)[c]	Depth to Bk (cm)[d]	Maximum Approx. Soil Age (ky)[e]	Minimum Approx. Soil Age (ky)[e]	Classification	
												Following Mack et al. (1993)	Following Retallack et al. (1993)
Kaiparowits	Blue Ceratopsian (KBC)	133	A	30	Light gray/brown, sandier than underyling horizons			476	249	3.8	3.0	Calcic Argillisol	Calcic Alfisol
			Bt	130	Top 30 cm green, middle 80 cm brown, bottom 20 cm green; large slickensides, manganese staining, root traces and carbonized plant material near top	5Y 4/2	Olive Gray						
			Bk	20	Green/brown, shell material, rare carbonate nodules								
Kaiparowits	Blue Ceratopsian (KBC)	125	A	30	Dark gray, organic carbon, siltier/sandier than underlying horizons			461	156	4.4	2.9	Calcic Argillisol	Calcic Alfisol
			Bt	70	Dark gray, abundant slickensides	5Y 4/1	Dark Gray						
			Bk	70	Light gray, silty with some slickensides, small carbonate nodules (<1 cm)								
Kaiparowits	Blue Ceratopsian (KBC)	112	A	10	Abundant plan material, siltier than underlying horizon			424	16	4.7	3.2	Calcic Protosol	Calcic Inceptisol
			Bkt	90	Abundant nodules (< 1cm), slickensides, plant impressions and preserved material	5Y 4/1	Dark Gray						
Kaiparowits	Blue Ceratopsian (KBC)	110	A	10	Light gray, small peds			423				Argillic Protosol	Argillic Inceptisol
			Bt	30	Light greenish gray, no slickensides, weak clay accumulation	5Y 5/1	Gray						
Kaiparowits	Blue Ceratopsian (KBC)	107	A	20	Organic material			420	31	4.1	2.7	Calcic Protosol	Calcic Inceptisol
			Bkt	110	Small carbonate nodules (< 5 mm), some slickensides, dark gray	5Y 5/2	Olive Gray						

Supplementary Table C1. Continued 11.

Formation	Section	Paleosol[a]	Horizon	Thickness (cm)	Descriptive Features	Color[b]	Munsell Description	Stratigraphic Height (m)[c]	Depth to Bk (cm)[d]	Maximum Approx. Soil Age (ky)[e]	Minimum Approx. Soil Age (ky)[e]	Classification	
												Following Mack et al. (1993)	Following Retallack et al. (1993)
Kaiparowits	Blue Ceratopsian (KBC)	105	A	30	Darker and sandier than underlying horizon, small peds			414	47	4.2	2.7	Calcic Protosol	Calcic Inceptisol
			Bkt	70	Dark gray, scattered concentrations of small carbonate nodules (<1 cm), Fe/Mg staining (black and shiny), Fe staining (red), roots and organic matter	5Y 5/2	Olive Gray						
Kaiparowits	Blue Ceratopsian (KBC)	96	A	30	Siltier than underlying horizon			393	47	3.7	2.4	Calcic Protosol	Calcic Inceptisol
			Bk	120	Weak clay accumulation, small carbonate nodules (< 5 mm)	5Y 5/2	Olive Gray						
Kaiparowits	Blue Ceratopsian (KBC)	80	A	20	Darker gray than underlying horizon, smaller peds, organic plant matter			365	31	3.9	2.6	Calcic Protosol	Calcic Inceptisol
			Bk	80	Small carbonate nodules (<5 mm), light gray, no slickensides, bottom grades to sand	5Y 5/2	Olive Gray						
Kaiparowits	Blue Ceratopsian (KBC)	78	A	30	Slightly lighter in color than underyling horizon, siltier with weaker ped development			362	47	2.7	2.1	Calcic Protosol	Calcic Inceptisol
			Bkt	90	Dark gray, bright red staining on ped surfaces, very small carbonate nodules (<5 mm), some gastropod fossils	5Y 5/1	Gray						

Supplementary Table C1. Continued 12.

Formation	Section	Paleosol[a]	Horizon	Thickness (cm)	Descriptive Features	Color[b]	Munsell Description	Stratigraphic Height (m)[c]	Depth to Bk (cm)[d]	Maximum Approx. Soil Age (ky)[e]	Minimum Approx. Soil Age (ky)[e]	Classification	
												Following Mack et al. (1993)	Following Retallack et al. (1993)
Kaiparowits	Blue Ceratopsian (KBC)	69	A	30	Darker gray, sandy			354	124	3.9	2.9	Calcic Argillisol	Calcic Alfisol
			Bt	50	Lighter gray color, orange ped staining, slickensides	5Y 6/2	Light Olive Gray						
			Bk	150	Small carbonate nodules (<1 cm), 1-3 cm angular peds, dark brownish gray, iron manganese staining								
Kaiparowits	Blue Ceratopsian (KBC)	50	A	60	Green-gray, gastropod fossils, manganese staining			322	264	3.9	2.9	Calcic Argillisol	Calcic Alfisol
			Bt	110	Dark gray green, slickensides	5Y 4/2	Olive Gray						
			Bk	80	Dark gray, no slickensides, carbonate nodules (<1 cm)								
Kaiparowits	Blue Ceratopsian (KBC)	15	A	70	Darker gray, carbonaceous plant material, siltier than underlying horizon			223	202	4.0	2.4	Calcic Argillisol	Calcic Alfisol
			Bt	60	Clay accumulation, darker gray, slickensides	5Y 4/1	Dark Gray						
			Bk	90	Light gray green, carbonate nodules (<1 cm), yellow mottling, silty								

Supplementary Table C2. Replicate data for all clumped isotope analyses.

Sample Name	Sample Number	Replicate ID	Analysis Date	Mass (mg)	$\delta^{13}C$ (‰) VPDB	±1 SE (‰)	$\delta^{18}O$ (‰) VPDB	±1 SE (‰)	Δ_{47} (‰)	±1 SE (‰)	Δ_{48} (‰)	±1 SE (‰)	Δ_{49} (‰)	±1 SE (‰)
TM-FB-1	1	170209_6_FB_1_Bk2	170209	7.043	-7.382	0.004	-9.598	0.007	0.5733	0.0069	0.1683	0.0305	19.6040	1.6543
TM-FB-1	1	170307_2_TM_FB_1	170307	8.291	-7.557	0.005	-9.568	0.007	0.6023	0.0079	0.2520	0.0294	32.0857	1.9283
TM-FB-1	1	170606_3_TM_FB_1	170606	9.267	-7.469	0.005	-9.551	0.008	0.5828	0.0060	-0.0054	0.0339	9.3199	1.5343
TM-FB-1	1	170629_6_TM_FB_1	170629	9.711	-7.363	0.005	-9.503	0.007	0.5844	0.0065	0.2319	0.0258	21.1647	1.6531
TM-FB-3	2	170530_4_TM_FB_3	170530	8.193	-7.261	0.005	-9.874	0.006	0.5806	0.0080	0.1270	0.0319	17.7040	1.6627
TM-FB-3	2	170629_1_TM_FB_3	170629	8.913	-7.201	0.004	-9.986	0.007	0.5585	0.0072	0.4048	0.0342	72.8837	2.0118
TM-FB-3	2	170711_3_TM_FB_3	170711	8.500	-7.183	0.004	-10.052	0.006	0.6083	0.0063	0.1123	0.0272	8.6249	1.7215
TM-FB-5	3	170307_1_TM_FB_5	170307	7.298	-8.654	0.004	-11.115	0.008	0.5551	0.0065	0.4983	0.0298	102.1216	1.9887
TM-FB-5	3	170209_5_FB_5_Bk	170209	7.222	-8.475	0.003	-11.129	0.007	0.6034	0.0074	0.2458	0.0293	13.0592	2.0457
TM-FB-5b	4	170706_5_TM_FB_5b	170706	8.792	-8.239	0.004	-11.302	0.007	0.5493	0.0070	0.2765	0.0319	16.7407	2.0134
TM-FB-5b	4	170711_5_TM_FB_5b	170711	8.173	-8.020	0.004	-11.355	0.007	0.5674	0.0068	0.2241	0.0335	17.3985	1.7506
TM-FB-5c	5	170629_4_TM_FB_5b	170629	9.242	-8.212	0.004	-11.496	0.007	0.5799	0.0061	0.2493	0.0321	24.8561	1.4956
TM-FB-5c	5	170802_1_TM_FB_5b	170802	8.175	-8.707	0.004	-11.183	0.007	0.5701	0.0072	0.6120	0.0327	72.9719	2.0543
TM-FB-7	6	161014_6_TM_FB_7_Bk	161014	10.812	-8.664	0.004	-12.124	0.006	0.5923	0.0083	0.1126	0.0353	18.1512	1.6128
TM-FB-7	6	170209_1_TM_FB_7_Bk	170209	6.871	-8.402	0.004	-11.598	0.006	0.6096	0.0063	0.4997	0.0310	80.4171	2.0381
TM-FB-7b	7	170530_3_TM_FB_7b	170530	7.282	-8.650	0.004	-11.774	0.007	0.5956	0.0065	0.2922	0.0315	23.9337	2.0786
TM-FB-7b	7	170802_2_TM_FB_7b	170802	8.041	-8.582	0.005	-11.630	0.006	0.5552	0.0061	0.5192	0.0356	56.8503	2.1574
TM-FB-7b	7	170808_1_TM_FB_7b	170808	8.178	-8.586	0.004	-12.591	0.007	0.5603	0.0081	0.5498	0.0446	95.0517	3.3418
TM-FB-7b	7	170811_4_TM_FB_7b	170811	8.109	-8.554	0.004	-11.583	0.006	0.5780	0.0073	0.5455	0.0362	42.4787	1.7441
TM-FB-11b	8	170526_3_TM_FB_11b	170526	9.098	-7.588	0.004	-11.184	0.007	0.6050	0.0076	0.4599	0.0293	49.4321	1.5502
TM-FB-11b	8	170629_5_TM_FB_11b	170629	10.179	-7.535	0.004	-11.068	0.007	0.6471	0.0072	0.5778	0.0392	45.4798	2.2445
TM-FB-11b	8	170706_4_TM_FB_11b	170706	11.298	-7.553	0.003	-11.022	0.006	0.6222	0.0073	0.4559	0.0328	41.1873	2.5300
TM-FB-11b	8	170711_6_TM_FB_11b	170711	11.037	-7.641	0.004	-11.115	0.006	0.5789	0.0075	0.3331	0.0334	28.0000	1.8896
TM-FB-11b	8	170715_5_TM_FB_11b	170715	9.363	-7.615	0.004	-11.108	0.008	0.6012	0.0085	0.5072	0.0350	48.5995	2.5759
TM-HC-1	9	170209_3_HC_1_Bk	170209	7.219	-7.758	0.004	-9.803	0.007	0.5540	0.0073	0.1002	0.0248	13.2299	1.4752
TM-HC-1	9	170213_3_HC_1	170213	7.327	-7.916	0.003	-9.854	0.006	0.5723	0.0071	0.2187	0.0300	21.3201	1.9609
TM-HC-1b	10	170530_2_TM_HC_1b	170530	7.183	-8.382	0.004	-9.504	0.008	0.5775	0.0067	0.2342	0.0305	25.6204	1.5805
TM-HC-1b	10	170802_4_TM_HC_1b	170802	7.450	-8.163	0.004	-9.534	0.008	0.5821	0.0075	0.5223	0.0357	48.9104	1.7963
TM-HC-1b	10	170808_2_TM_HC_1b	170808	7.356	-8.175	0.004	-10.936	0.007	0.5745	0.0070	0.4610	0.0295	52.8349	1.8664
TM-HC-1s	11	170213_4_HC_1s	170213	5.592	-6.520	0.004	-12.405	0.007	0.5035	0.0070	0.3706	0.0362	32.0246	2.1354
TM-HC-1s	11	170209_4_HC_1_Bks	170209	6.717	-6.263	0.004	-12.238	0.006	0.6081	0.0074	0.3862	0.0334	21.6227	1.6255
TM-HC-3	12	170211_6_TM_HC_3	170211	7.253	-7.121	0.004	-9.884	0.007	0.5507	0.0061	0.2238	0.0297	27.0668	1.3006
TM-HC-3c	13	170630_3_TM_HC_3c	170630	10.067	-8.187	0.004	-9.858	0.006	0.6132	0.0073	0.2437	0.0285	19.0461	1.6744
TM-HC-3c	13	170711_1_TM_HC_3c	170711	9.360	-8.152	0.004	-9.976	0.006	0.5262	0.0063	0.2933	0.0331	67.0554	1.9072
TM-HC-3c	14	170802_5_TM_HC_3c	170802	9.102	-6.736	0.004	-9.083	0.007	0.5806	0.0074	0.4378	0.0367	47.1562	2.0902

Supplementary Table C2. Continued 1.

Sample Name	Sample Number	Replicate ID	Analysis Date	Mass (mg)	$\delta^{13}C$ (‰) VPDB	±1 SE (‰)	$\delta^{18}O$ (‰) VPDB	±1 SE (‰)	Δ_{47} (‰)	±1 SE (‰)	Δ_{48} (‰)	±1 SE (‰)	Δ_{49} (‰)	±1 SE (‰)
TM-HC-3c	14	170808_5_TM_HC_3c	170808	9.035	-6.660	0.004	-10.438	0.007	0.5855	0.0070	0.6099	0.0382	54.9932	1.9257
TM-HC-3c	14	170824_2_TM_HC_3c	170824	9.987	-6.556	0.004	-9.060	0.007	0.5991	0.0074	0.6382	0.0376	61.7106	2.3599
TM-HC-7	15	170630_5_TM_HC_7	170630	8.951	-8.075	0.004	-9.352	0.007	0.5673	0.0073	0.1400	0.0249	15.0625	1.5303
TM-HC-7	15	170711_2_TM_HC_7	170711	7.640	-8.053	0.004	-9.514	0.007	0.5969	0.0066	0.3286	0.0322	33.6653	1.8218
TM-HC-7	15	170802_6_TM_HC_7	170802	8.152	-8.057	0.005	-9.496	0.007	0.5705	0.0076	0.3133	0.0388	22.5982	28.0768
TM-HC-7s	16	170715_4_TM_HC_7s	170715	8.771	-4.485	0.005	-15.892	0.007	0.4540	0.0071	0.3249	0.0293	20.0145	1.7715
TM-HC-7s	16	170802_7_TM_HC_7s	170802	7.520	-4.679	0.004	-15.643	0.007	0.4763	0.0063	0.5267	0.0298	26.7569	1.6080
TM-HC-9	17	170419_2_TM_HC_9	170419	7.505	-9.092	0.004	-10.257	0.010	0.5575	0.0074	0.1732	0.0296	19.3706	1.6622
TM-HC-9b	17	170804_2_TM_HC_9b	170804	7.783	-9.086	0.004	-10.040	0.007	0.5690	0.0070	0.3765	0.0353	42.7962	2.3773
TM-HC-9b	17	170811_1_TM_HC_9b	170811	7.651	-9.084	0.004	-9.943	0.008	0.5571	0.0071	0.4461	0.0310	111.7953	1.5260
TM-HC-13	18	170213_6_TM_HC_13	170213	7.104	-7.988	0.004	-10.366	0.006	0.5353	0.0068	0.3314	0.0328	25.0270	1.5728
TM-HC-13	18	170211_2_TM_HC_13	170211	7.206	-7.941	0.004	-10.493	0.006	0.5635	0.0076	0.1846	0.0289	10.3044	1.8983
TM-HC-13b	19	170630_6_TM_HC_13b	170630	8.558	-8.490	0.004	-9.910	0.006	0.5268	0.0073	0.2701	0.0312	23.7335	1.8454
TM-HC-13c	19	170804_3_TM_HC_13c	170804	7.669	-7.958	0.004	-9.627	0.007	0.5632	0.0074	0.2744	0.0306	31.2498	1.7264
TM-HC-15	20	170714_1_TM_HC_15	170714	9.324	-7.424	0.004	-11.476	0.007	0.5860	0.0065	0.8513	0.0324	221.1433	2.2185
TM-HC-15	20	170805_2_TM_HC_15	170805	10.192	-7.529	0.004	-11.458	0.007	0.5903	0.0068	0.5723	0.0361	54.6259	2.2284
TM-HC-15	20	170811_2_TM_HC_15	170811	10.276	-7.476	0.004	-11.285	0.007	0.5834	0.0074	0.5681	0.0335	56.7242	1.7402
TM-WB-1a	21	170211_5_TM_WB_1a	170211	6.952	-7.999	0.004	-10.173	0.006	0.5583	0.0079	0.2072	0.0263	27.8901	1.6967
TM-WB-1a	21	170213_2_TM_WB_1a	170213	7.356	-8.019	0.004	-10.140	0.006	0.6045	0.0071	0.3430	0.0297	30.0556	1.7556
TM-WB-1a	21	170824_4_TM_WB_1a	170824	9.745	-7.750	0.005	-9.926	0.011	0.5871	0.0076	0.3009	0.0333	35.9392	2.8577
TM-WB-1a	21	170829_5_TM_WB_1a	170829	8.364	-7.714	0.004	-9.917	0.007	0.5325	0.0066	0.0759	0.0325	7.6382	2.1361
TM-WB-1b	22	170714_2_TM_WB_1b	170714	8.648	-7.975	0.004	-10.149	0.006	0.5807	0.0062	0.4132	0.0324	69.2778	1.7598
TM-WB-1b	22	170824_5_TM_WB_1b	170824	8.115	-7.932	0.004	-9.934	0.007	0.6059	0.0072	0.5700	0.0478	51.0057	3.1100
TM-WB-1b	22	170830_1_TM_WB_1b	170830	8.974	-7.944	0.004	-9.999	0.006	0.5427	0.0055	0.2274	0.0267	58.6691	1.9692
TM-WB-3	23	170714_3_TM_WB_3	170714	8.790	-7.642	0.005	-8.816	0.007	0.6026	0.0060	0.3705	0.0278	72.7047	1.7134
TM-WB-3	23	170805_3_TM_WB_3	170805	8.062	-7.671	0.004	-9.039	0.007	0.6071	0.0065	0.5309	0.0322	42.6070	1.7409
TM_WB_3	23	170811_3_TM_WB_3	170811	8.672	-7.678	0.005	-9.053	0.007	0.5863	0.0064	0.3737	0.0290	41.0189	1.4951
TM-WB-5	24	170714_4_TM_WB_5	170714	8.406	-7.919	0.004	-11.417	0.008	0.5355	0.0074	0.3307	0.0265	29.0679	1.4832
TM-WB-6	25	170715_1_TM_WB_6	170715	8.231	-8.487	0.004	-10.102	0.007	0.5654	0.0064	0.5352	0.0294	88.7570	1.6035
TM-WB-6	25	170805_4_TM_WB_6	170805	8.239	-8.539	0.004	-10.216	0.006	0.5374	0.0068	0.2196	0.0315	21.3079	2.2327
TM-WB-6	25	170811_6_TM_WB_6	170811	8.635	-8.695	0.004	-9.578	0.007	0.5597	0.0059	0.2718	0.0294	28.1987	1.7766
TM-WB-6	25	170825_1_TM_WB_6	170825	8.466	-8.650	0.004	-9.737	0.007	0.5347	0.0072	0.0701	0.0262	36.2643	1.5913
TM-WB-6s	26	170812_2_TM_WB_6s	170812	8.789	-7.258	0.004	-13.071	0.006	0.5269	0.0071	0.4029	0.0370	31.8806	1.9915
TM-WB-6s	26	170825_2_TM_WB_6s	170825	8.359	-7.119	0.004	-13.345	0.006	0.5212	0.0071	0.3042	0.0302	26.6114	1.9412
TM-WB-8	27	170213_1_TM_WB_8	170213	7.066	-7.875	0.005	-9.706	0.008	0.5847	0.0063	0.4123	0.0314	99.1121	1.7395

Supplementary Table C2. Continued 2.

Sample Name	Sample Number	Replicate ID	Analysis Date	Mass (mg)	$\delta^{13}C$ (‰) VPDB	±1 SE (‰)	$\delta^{18}O$ (‰) VPDB	±1 SE (‰)	Δ_{47} (‰)	±1 SE (‰)	Δ_{48} (‰)	±1 SE (‰)	Δ_{49} (‰)	±1 SE (‰)
TM-WB-8	27	170308_1_TM_WB_8	170308	7.846	-7.926	0.004	-10.036	0.007	0.5960	0.0074	0.3601	0.0305	79.2980	2.0421
TM-WB-8	27	170715_2_TM_WB_8	170715	8.233	-7.698	0.005	-9.918	0.007	0.5898	0.0077	0.3256	0.0281	36.8608	2.0589
KBC-15	28	160817_6_KBC_15_Bk	160817	12.930	-6.520	0.005	-10.011	0.007	0.5452	0.0083	0.0481	0.0399	13.0504	2.5071
KBC-15	28	160810_6_KBC_15_Bk	160810	11.641	-6.284	0.004	-10.076	0.007	0.5569	0.0086	0.2414	0.0410	91.8087	2.4648
KBC-15	29	170523_7_KBC_15b*	170523	8.103	-7.433	0.004	-9.039	0.007	0.5342	0.0067	0.2420	0.0307	27.3275	2.0918
KBC-50	30	160817_5_KBC_50_Bk	160817	14.575	-9.865	0.004	-7.972	0.006	0.5479	0.0085	0.1488	0.0334	28.9420	2.5675
KBC-50	30	160810_7_KBC_50_Bk	160810	11.583	-9.868	0.005	-8.010	0.006	0.5581	0.0077	0.2229	0.0341	88.8633	2.4402
KBC-69	31	160817_4_KBC_69_Bk	160817	12.724	-8.970	0.004	-8.583	0.007	0.5634	0.0080	0.1587	0.0371	49.7983	2.6730
KBC-69	31	160810_8_KBC_69_Bk	160810	12.432	-9.046	0.004	-8.598	0.006	0.5777	0.0081	0.3404	0.0334	84.4152	2.7970
KBC-69b	32	170428_1_KBC_69b*	170428	7.438	-9.493	0.004	-7.427	0.008	0.5600	0.0076	0.1550	0.0361	58.6365	2.3011
KBC-69b	32	170523_1_KBC_69c*	170523	8.528	-9.225	0.004	-7.786	0.007	0.5197	0.0069	0.0762	0.0309	109.3474	2.3193
KBC-69b	33	170825_3_KBC_69b	170825	7.704	-9.389	0.004	-7.697	0.006	0.5765	0.0073	0.0453	0.0373	11.3019	2.6892
KBC-69b	33	170830_2_KBC_69b	170830	8.400	-9.263	0.004	-7.584	0.007	0.5780	0.0067	0.0595	0.0257	14.9848	1.4834
KBC-80	34	160818_5_KBC_80_Bk	160818	14.576	-8.713	0.004	-8.442	0.006	0.5043	0.0086	0.0465	0.0342	17.6910	2.5765
KBC-80	34	160811_7_KBC_80_Bk	160811	12.037	-7.784	0.005	-8.170	0.007	0.5241	0.0087	0.0855	0.0292	58.6488	3.0744
KBC-80b	35	160905_2_KBC_80b_Bk	160905	13.400	-8.413	0.004	-7.847	0.005	0.5611	0.0072	0.0060	0.0371	17.6404	2.5388
KBC-80b	35	160907_6_KBC_80b_Bk	160907	13.636	-8.324	0.004	-7.898	0.007	0.5567	0.0086	0.0365	0.0289	8.7021	2.5698
KBC-96	36	170421_1_KBC_96_Bk	170421	9.282	-8.942	0.004	-8.311	0.009	0.5333	0.0066	-0.0086	0.0256	20.9824	1.5635
KBC-96	36	170624_3_KBC_96	170624	9.049	-8.964	0.004	-8.333	0.007	0.5909	0.0071	0.0698	0.0368	18.7034	2.3362
KBC-96	36	170630_1_KBC_96	170630	8.608	-8.978	0.004	-8.241	0.006	0.5448	0.0068	0.1355	0.0290	40.6843	1.6952
KBC-96	36	170824_1_KBC_96	170824	8.318	-8.968	0.005	-8.352	0.007	0.5837	0.0064	0.3590	0.0294	74.3602	2.0926
KBC-105	37	160811_4_KBC_105_Bk	160811	11.271	-9.739	0.004	-8.519	0.007	0.5907	0.0086	0.3221	0.0349	100.0061	2.5313
KBC-105	37	160818_2_KBC_105_Bk	160818	13.101	-9.634	0.004	-8.318	0.007	0.5697	0.0086	0.1169	0.0374	41.2973	2.3941
KBC-105	37	170421_3_KBC_105_Bk	170421	11.671	-9.625	0.004	-7.804	0.007	0.5819	0.0075	0.0042	0.0254	16.4912	1.6020
KBC-105b	38	170428_4_KBC_105b*	170428	7.501	-9.520	0.004	-7.729	0.008	0.6250	0.0069	0.1039	0.0328	28.5096	2.0164
KBC-105b	38	170523_2_KBC_105b*	170523	7.503	-9.620	0.004	-7.817	0.007	0.5731	0.0062	0.2306	0.0326	43.5748	1.9524
KBC-105b	38	170603_2_KBC_105b*	170603	8.227	-9.504	0.005	-7.828	0.007	0.5623	0.0053	-0.0256	0.0336	12.7194	1.6283
KBC_105b	38	170811_7_KBC_105b	170811	8.220	-9.575	0.004	-7.601	0.006	0.5957	0.0073	0.3718	0.0358	33.9897	2.4875
KBC-105b	38	170825_5_KBC_105b	170825	9.166	-9.583	0.005	-7.735	0.006	0.5895	0.0081	-0.0394	0.0251	7.1498	1.2738
KBC-107	39	160818_1_KBC_107_Bk	160818	13.238	-9.228	0.005	-9.373	0.006	0.5518	0.0085	0.1292	0.0357	86.2092	3.0619
KBC-107	39	160811_3_KBC_107_Bk	160811	13.222	-9.275	0.003	-9.635	0.006	0.5671	0.0090	0.1297	0.0373	49.0965	2.8012
KBC-107	39	160907_5_KBC_107_Bk	160907	11.542	-9.186	0.004	-9.100	0.007	0.6011	0.0086	0.0273	0.0368	2.8071	3.2979
KBC-107	39	160905_4_KBC_107_Bk	160905	12.524	-9.206	0.005	-8.943	0.007	0.6099	0.0071	0.0736	0.0314	7.4739	2.1819
KBC-107	39	170609_2_KBC_107	170609	9.210	-9.189	0.004	-8.711	0.006	0.5714	0.0069	0.0341	0.0316	10.4073	1.9658
KBC-107	39	170624_2_KBC_107	170624	9.331	-9.199	0.004	-9.045	0.007	0.5827	0.0075	0.1134	0.0316	13.8908	1.6988

Supplementary Table C2. Continued 3.

Sample Name	Sample Number	Replicate ID	Analysis Date	Mass (mg)	$\delta^{13}C$ (‰) VPDB	±1 SE (‰)	$\delta^{18}O$ (‰) VPDB	±1 SE (‰)	Δ_{47} (‰)	±1 SE (‰)	Δ_{48} (‰)	±1 SE (‰)	Δ_{49} (‰)	±1 SE (‰)
KBC-112	40	161014_3_KBC_112_Bk	161014	13.105	-7.867	0.005	-9.157	0.006	0.5257	0.0091	-0.0946	0.0337	22.5752	1.4465
KBC-112	40	161008_1_KBC_112_Bk	161008	9.015	-7.841	0.004	-8.967	0.007	0.5487	0.0071	0.1263	0.0263	82.4284	1.6916
KBC-112	41	170523_3_KBC_112b	170523	7.801	-8.277	0.004	-8.569	0.008	0.5450	0.0064	0.2865	0.0347	62.4210	1.7288
KBC-112b	41	170825_6_KBC_112b	170825	8.615	-8.258	0.004	-8.851	0.007	0.5779	0.0058	0.2399	0.0318	27.9567	2.0126
KBC-112b	41	170830_4_KBC_112b	170830	8.103	-8.290	0.004	-8.968	0.007	0.5542	0.0068	0.1309	0.0299	14.3842	1.5860
KBC-125	42	160817_2_KBC_125_Bk	160817	12.990	-9.041	0.005	-8.072	0.007	0.5262	0.0095	0.1553	0.0341	77.4686	2.8020
KBC-125	42	160905_3_KBC_125_Bk	160905	15.968	-8.929	0.004	-7.608	0.007	0.5548	0.0079	-0.0126	0.0328	5.0874	1.9701
KBC-125	42	160811_2_KBC_125_Bk	160811	12.041	-9.179	0.004	-8.142	0.007	0.6051	0.0071	0.4995	0.0323	207.9078	2.3638
KBC-125	42	160907_4_KBC_125_Bk	160907	12.886	-8.928	0.003	-7.690	0.007	0.6095	0.0072	0.0825	0.0359	14.0152	2.1450
KBC-125b	43	170501_1_KBC_125b	170501	7.899	-8.918	0.004	-7.188	0.007	0.6015	0.0061	0.5184	0.0345	89.0845	1.8483
KBC-125b	43	170825_7_KBC_125b	170825	10.858	-8.770	0.004	-7.308	0.006	0.5612	0.0069	0.0607	0.0273	13.6913	1.4595
KBC-125b	43	170830_5_KBC_125b	170830	8.411	-9.095	0.004	-7.302	0.008	0.5525	0.0059	0.2436	0.0312	27.3605	1.4314
KBC-137	44	161118_1_KBC_137_Bk	161118	8.770	-8.901	0.004	-8.432	0.008	0.5438	0.0080	-0.3438	0.0264	75.0400	1.4991
KBC-137	44	160721_4_KBC_137_Bk	160721	10.571	-8.803	0.005	-8.400	0.009	0.5735	0.0093	0.3386	0.0648	41.7844	2.5088
KBC-137	44	160716_2_KBC_137_Bk	160716	11.921	-8.852	0.004	-8.319	0.006	0.5913	0.0070	0.1949	0.0302	78.4265	2.0516
KBC-137b	45	170502_3_KBC_137b	170502	8.932	-9.233	0.005	-7.393	0.007	0.5709	0.0072	0.0390	0.0326	24.6430	2.3731
KBC-137b	45	170523_4_KBC_137c	170523	8.289	-9.073	0.005	-8.078	0.007	0.5418	0.0068	0.0187	0.0272	18.3382	1.6889
KBC-137b	45	170829_4_KBC_137b	170829	8.254	-8.837	0.005	-7.864	0.006	0.5940	0.0062	0.0566	0.0312	17.8901	2.1673
KBC-137s	46	161118_5_KBC_137_Bks	161118	8.170	-8.563	0.005	-7.907	0.007	0.5833	0.0078	-0.3949	0.0291	6.6456	1.5451
KBC-142	47	161008_2_KBC_142_Bka	161008	9.950	-8.482	0.004	-7.519	0.007	0.5806	0.0081	0.0823	0.0299	67.6550	2.1230
KBC-142	47	161014_4_KBC_142_Bka	161014	12.495	-8.480	0.004	-7.582	0.007	0.5758	0.0090	-0.0543	0.0404	14.8506	1.9675
KBC-142b	48	170706_1_KBC_142	170706	9.051	-8.233	0.005	-7.326	0.006	0.5691	0.0076	0.2241	0.0366	75.1696	2.3989
KBC-142b	48	170828_3_KBC_142b	170828	10.717	-8.692	0.003	-7.200	0.007	0.5890	0.0073	0.0139	0.0284	11.8024	1.9305
KBC-142b	48	170906_2_KBC_142b	170906	10.507	-8.561	0.004	-7.915	0.008	0.5646	0.0069	0.2142	0.0356	32.7159	1.5590
KBC-145	49	160905_5_KBC_145_Bk	160905	14.245	-10.515	0.004	-7.516	0.006	0.6095	0.0080	-0.0079	0.0365	7.2089	2.7324
KBC-145	49	170530_5_KBC_145	170530	7.018	-10.553	0.004	-7.340	0.007	0.6044	0.0083	0.1431	0.0300	22.3472	1.8230
KBC-145	49	170606_4_KBC_145	170606	7.399	-10.534	0.004	-7.340	0.007	0.6117	0.0078	0.0587	0.0309	19.2780	2.1046
KBC-146	50	160905_6_KBC_146b_Bk	160905	15.869	-9.113	0.004	-9.657	0.005	0.5648	0.0090	0.1432	0.0357	16.9313	2.6507
KBC-146	50	170606_5_KBC_146b	170606	8.508	-9.150	0.004	-9.501	0.007	0.5277	0.0075	-0.0032	0.0277	8.3349	1.7299
KBC-150	51	160705_3_KBC_150_Bk	160705	8.638	-7.930	0.004	-8.167	0.006	0.5627	0.0078	0.1375	0.0297	32.5832	2.0918
KBC-150	51	160721_3_KBC_150_Bk	160721	10.178	-7.770	0.004	-8.435	0.007	0.5596	0.0081	0.1073	0.0333	37.5994	2.8859
KBC-150	51	161118_3_KBC_150_Bk	161118	9.330	-7.835	0.005	-8.280	0.008	0.6079	0.0081	-0.3235	0.0271	14.4251	1.3369
KBC-150b	52	170505_2_KBC_150b	170505	7.520	-9.153	0.005	-8.149	0.008	0.6141	0.0070	0.3996	0.0345	85.3187	1.7623
KBC-150b	52	170523_5_KBC_150b	170523	8.517	-9.079	0.004	-8.083	0.008	0.5798	0.0068	0.6612	0.0293	175.5912	2.1101
KBC-150b	52	170624_5_KBC_150b	170624	9.540	-9.013	0.004	-8.368	0.007	0.5984	0.0064	0.2134	0.0321	25.4247	1.8332
KBC-157	53	160907_2_KBC_157_Bk	160907	12.937	-9.647	0.005	-8.355	0.006	0.6049	0.0088	0.0585	0.0270	5.3687	2.3204
KBC-157	53	170606_1_KBC_157	170606	9.941	-9.716	0.004	-8.085	0.007	0.5598	0.0067	0.1685	0.0332	59.3642	1.8804
KBC-157	53	170609_3_KBC_157	170609	9.210	-9.660	0.004	-8.006	0.008	0.6105	0.0072	0.1003	0.0311	20.6354	1.9045
KBC-157	53	170624_1_KBC_157	170624	9.544	-9.631	0.005	-8.238	0.007	0.5550	0.0063	0.2098	0.0288	56.2791	1.5079
KBC-157	53	170630_2_KBC_157	170630	9.843	-9.644	0.004	-8.085	0.007	0.6043	0.0065	0.1218	0.0282	16.2068	1.7865

Supplemental Table C3a. Clumped Isotope Standards

C64[c] Mean Δ_{47} (‰)	C64 Δ_{47} Std. (‰)	C2[c] Mean Δ_{47} (‰)	C2 Δ_{47} Std. (‰)	Coral[c] Mean Δ_{47} (‰)	Coral Δ_{47} Std. (‰)	ETH1[d] Mean Δ_{47} (‰)	ETH1 Δ_{47} Std. (‰)	ETH2[d] Mean Δ_{47} (‰)	ETH2 Δ_{47} Std. (‰)	ETH3[d] Mean Δ_{47} (‰)	ETH3 Δ_{47} Std. (‰)	ETH4[d] Mean Δ_{47} (‰)	ETH4 Δ_{47} Std. (‰)
0.5250	0.0160	0.5337	0.0326	0.6274	0.0239	0.2089	0.0361	0.2458	0.0550	0.6236	0.0282	0.4513	0.0215

c - Isolab in-house standard

d - Interlaboratory clumped isotope standard

Supplemental Table C3b. Clumped Isotope Reference Frame Data[a]

Heated Gas Equilibration Temperature (°C)	n	Slope	Intercept (Δ_{47} [EGvsWG])	r^2	Empirical Transfer Function (ETF) Slope	ETF Intercept	ETF r^2
4	11	-0.00052174	0.10566	0.50501	1.0237	0.92412	0.99962
60	12	-0.00052174	-0.14271	0.62228	1.0237	0.92412	0.99962
1000	17	-0.00052174	-0.8807	0.30485	1.0237	0.92412	0.99962

a - Reference frame data for the period July 2016 to September 2017

Supplementary Table C4. Soil and air temperature data from various studies.

Reference	Location	Lat. (°N)	Depth (cm)	Season	Surface Type	Min. ST_{excess} (°C)[a]	Max. ST_{excess} (°C)	Mean ST_{excess} (°C)	Notes
Passey et al. (2010)	Hohot, China	40.8	10	MAT	bare soil	-1.4	4.3	1.45	Assuming this is a bare soil, paper doesn't specify
	Ileret, Kenya	4.3	26	MAT	bare soil	4.1	4.1	4.1	Assuming this is a bare soil, paper doesn't specify
	Ileret, Kenya	4.3	35	MAT	bare soil	4	4	4	Assuming this is a bare soil, paper doesn't specify
	Ileret, Kenya	4.3	50	MAT	bare soil	3.9	3.9	3.9	Assuming this is a bare soil, paper doesn't specify
	Narok, Kenya	-1.13	NA	Summer	NA	2.7	2.7	2.7	No info provided on depth of soil temp probe or vegetation cover
	Awash, Ethiopia	8.9	NA	Summer	NA	-1.4	-1.4	-1.4	No info provided on depth of soil temp probe or vegetation cover
	Mile, Ethiopia	11.42	NA	Summer	NA	-1.3	-1.3	-1.3	No info provided on depth of soil temp probe or vegetation cover
	Lucerne Valley, California	34.4	NA	Summer	NA	-0.4	-0.4	-0.4	No info provided on depth of soil temp probe or vegetation cover
Cermak et al. (2016)	Prague	50.1	2	MAT	asphalt	4.1	4.1	4.1	mean values
		50.1	2	MAT	bare clay soil	1.4	1.4	1.4	mean values
		50.1	2	MAT	bare sandy soil	1.6	1.6	1.6	mean values
		50.1	2	MAT	short grass	0.2	0.2	0.2	mean values
		50.1	2	Summer	asphalt	6	8	7	from figure 3
		50.1	2	Summer	bare clay soil	1	2	1.5	from figure 3
		50.1	2	Summer	bare sandy soil	2	3	2.5	from figure 3
		50.1	2	Summer	short grass	-1	0	-0.5	from figure 3
Bartlett et al. (2006)	Emigrant Pass Observatory	49.5	2.5	MAT	scrub/grass	1	1	1	Ground Sensors 1 and 4
		49.5	2.5	MAT	Trees/shrubs	1	1	1	Ground Sensor 3
		49.5	2.5	MAT	bare rock	2.3	2.3	2.3	Ground sensors 2 and 5
		49.5	5	MAT	scrub/grass	1	1	1	Ground Sensors 1 and 4
		49.5	5	MAT	Trees/shrubs	1.1	1.1	1.1	Ground Sensor 3
		49.5	5	MAT	bare rock	2.2	2.2	2.2	Ground sensors 2 and 5
		49.5	10	MAT	scrub/grass	1.2	1.2	1.2	Ground Sensors 1 and 4
		49.5	10	MAT	Trees/shrubs	1.2	1.2	1.2	Ground Sensor 3
		49.5	10	MAT	bare rock	2.5	2.5	2.5	Ground sensors 2 and 5
		49.5	50	MAT	scrub/grass	1.4	1.4	1.4	Ground Sensors 1 and 4
		49.5	50	MAT	Trees/shrubs	1.3	1.3	1.3	Ground Sensor 3
		49.5	50	MAT	bare rock	2.6	2.6	2.6	Ground sensors 2 and 5
		49.5	100	MAT	scrub/grass	1.7	1.7	1.7	Ground Sensors 1 and 4
		49.5	100	MAT	Trees/shrubs	1.5	1.5	1.5	Ground Sensor 3
		49.5	100	MAT	bare rock	2.9	2.9	2.9	Ground sensors 2 and 5
		49.5	2.5	Summer	scrub/grass	2.4	2.4	2.4	Ground Sensors 1 and 4; http://thermal.gg.utah.edu/facilities/epo/aboutEPO.html
		49.5	2.5	Summer	Trees/shrubs	2.2	2.2	2.2	Ground Sensor 3
		49.5	2.5	Summer	bare rock	3.8	3.8	3.8	Ground sensors 2 and 5
		49.5	5	Summer	scrub/grass	1	1	1	Ground Sensors 1 and 4
		49.5	5	Summer	Trees/shrubs	0.8	0.8	0.8	Ground Sensor 3
		49.5	5	Summer	bare rock	2.7	2.7	2.7	Ground sensors 2 and 5
		49.5	10	Summer	scrub/grass	-0.1	-0.1	-0.1	Ground Sensors 1 and 4
		49.5	10	Summer	Trees/shrubs	-0.3	-0.3	-0.3	Ground Sensor 3
		49.5	10	Summer	bare rock	2.7	2.7	2.7	Ground sensors 2 and 5
		49.5	50	Summer	scrub/grass	-2	-2	-2	Ground Sensors 1 and 4
		49.5	50	Summer	Trees/shrubs	-2.4	-2.4	-2.4	Ground Sensor 3
		49.5	50	Summer	bare rock	1.3	1.3	1.3	Ground sensors 2 and 5
		49.5	100	Summer	scrub/grass	-4.5	-4.5	-4.5	Ground Sensors 1 and 4
		49.5	100	Summer	Trees/shrubs	-5	-5	-5	Ground Sensor 3
		49.5	100	Summer	bare rock	-1.3	-1.3	-1.3	Ground sensors 2 and 5

a - ST_{excess} is equal to the difference between soil and air temperature. A positive ST_{excess} means soil temperature is higher than air temperature.